



University of  
**Strathclyde**  
**Glasgow**

**Department of Physics**

Marine Optics and Remote  
Sensing Group

# **Ocean Colour Remote Sensing of Zooplankton Swarms**

By

**Cait McCarry**

2024

*A thesis submitted in accordance with the requirements  
for the degree*

Doctor of Philosophy

## Declaration of Authenticity and Authors Rights

This thesis is the result of the author's original research. It has been composed by the author and has not been previously submitted for examination which has lead to the award of a degree.

The copyrights of this thesis belongs to the author under the terms of the United Kingdom Copyright Acts as qualified by the University of Strathclyde regulation 3.50. Due acknowledgement must always be made of the use of any material contained in, or derived from, this thesis.

Signed:

Date:

# Abstract

Zooplankton are keystone organisms in the marine environment, providing a crucial link between primary production and high order predators, as well as playing a critical role in biogeochemical cycling within the ocean. Many zooplankton groups also represent considerable economic interest, both by serving as a primary food source for many commercially harvested fish species and being directly harvested for the development of aquaculture feed and human health supplements. In this context, there is considerable interest in the accurate monitoring and characterisation of zooplankton populations, for the successful management of these organisms.

Despite this interest, relatively little is known about wide-scale distributions of these organisms, largely due to their patchy population dynamics and the challenges associated with ship-based sampling. To help address this issue, this thesis explores the potential for the detection of surface swarms of zooplankton from satellite derived ocean colour data. This work presents the first attempt to remotely identify and characterise surface swarms of the copepod species *Calanus finmarchicus* using a novel enhanced RGB colour matching technique developed throughout this work. With this framework, surface concentration estimates of these copepods were determined from space for the first time. However, application of these methods to optically complex environments led to concerns regarding the quality of remote sensing reflectance data retrievals, resulting in the development of a novel per-pixel atmospheric correction optimisation method. This showed considerable improvement in data quality when compared to the NASA standard atmospheric correction scheme. With increased confidence in the spectral information, a spectral matching technique was developed as an alternative method to the colour matching approach for the detection of zooplankton, to allow for the inclusion of more spectral information. Whilst results were comparable, the spectral matching method provides more flexibility and can be consistently applied to both coastal and open water environments, making this methodology the most favourable. Finally, to explore the

potential of remote detection of other key zooplankton groups, the spectral absorption properties of 7 groups of zooplankton were measured in a Point Source Integrating Cavity Absorption Meter (PSICAM). Results indicate that several different zooplankton groups have the potential to be identified and characterised through ocean colour if present in sufficient quantities. Further, intra-species variance was also preliminarily explored to determine the impact of life stage and seasonality on absorption properties, which provided evidence that considerable variance in absorption within organisms of the same species is possible.

## Acknowledgements

Starting my PhD just six weeks before the onset of a global pandemic made an already challenging undertaking even more difficult. Despite this, I was able to learn and achieve a lot in the last four years and overall I had a great PhD experience. However, without the professional and personal support I received throughout this period, I would have likely not made it past my first year. So here I would like to sincerely thank all of the people that helped to make this PhD possible.

Firstly, I would like to express my deepest gratitude to my supervisor David McKee. Thank you for all of the advice, guidance and copious amounts of coffee over the past four years. I am grateful for all your encouragement, support and generally making my PhD experience such a great one. I would also like to thank my co-supervisors, Sünnje Basedow at the Arctic University of Norway and Emlyn Davies at SINTEFF Ocean, for all the knowledge and experience shared with me, both remotely and in person, throughout my PhD.

I would like to sincerely thank Kim Last at SAMs for helping me to collect some 'emergency' zooplankton samples from Loch Etive, when COVID-19 made it very difficult to carry out any field research. I would also like to thank all of the scientists and crew on board the R/V Helmar Hanssen during the June 2022 SFI Harvest cruise.

I would like to thank all of my office mates over the years, from Stacey and Madjid who welcomed me into the group, to Anna G., Håkon and Ru who have kept me company in the final stages of my PhD. I would also like to thank all of my friends across the UK, especially Anna B., Devina, Georgie and Megan for not giving up on me and providing lots of laughs throughout the years! Thank you to the best boy Ralph who provided lots of (begrudging) emotional support cuddles. A very special thank you also goes to Vay, for providing endless support, delicious food and joyful moments during the later stages, I am forever grateful. Lastly, I would like to express my gratitude to my parents, without whom I would not have been able to pursue a PhD. Thank you for all of your love and unshakeable support, I am so grateful that you encouraged me to pursue my passions.

# Table of Contents

<b>1</b>	<b>Introduction .....</b>	<b>1</b>
1.1	Optical Theory .....	1
1.1.1	<i>Radiometry .....</i>	<i>2</i>
1.1.2	<i>Inherent Optical Properties .....</i>	<i>3</i>
1.1.3	<i>Optically important constituents .....</i>	<i>5</i>
1.2	Satellite derived remote sensing of ocean colour .....	8
1.2.1	<i>Basic principles and background .....</i>	<i>8</i>
1.2.2	<i>Atmospheric correction .....</i>	<i>10</i>
1.2.3	<i>Phytoplankton monitoring .....</i>	<i>12</i>
1.3	Zooplankton and their potential impact on ocean colour.....	14
1.3.1	<i>Why are zooplankton important? .....</i>	<i>15</i>
1.3.2	<i>Current in situ methods for monitoring zooplankton .....</i>	<i>17</i>
1.3.3	<i>Indirect remote sensing methods for estimating zooplankton abundances.....</i>	<i>20</i>
1.3.4	<i>Can zooplankton be directly identified from space? .....</i>	<i>22</i>
1.3.5	<i>Challenges associated with determining zooplankton IOPs.....</i>	<i>28</i>
1.4	Thesis structure and aims .....	29
<b>2</b>	<b>Materials and Methods .....</b>	<b>31</b>
2.1	Field data- Sea Patches 2017 .....	31
2.1.1	<i>Chlorophyll concentrations.....</i>	<i>32</i>
2.1.2	<i>CDOM absorption measurements.....</i>	<i>32</i>
2.1.3	<i>C. finmarchicus sampling and abundance.....</i>	<i>33</i>
2.2	Zooplankton absorption measurements .....	34
2.2.1	<i>Determination of absorption in the PSICAM .....</i>	<i>35</i>
2.2.2	<i>PSICAM setup .....</i>	<i>38</i>
2.2.3	<i>PSICAM calibration.....</i>	<i>39</i>
2.2.4	<i>Zooplankton absorption measurement procedure.....</i>	<i>40</i>

2.3	Radiative transfer simulations.....	42
2.3.1	<i>Bio-optical model</i> .....	42
2.3.2	<i>Ecolight set-up</i> .....	45
2.4	Satellite data processing.....	46
2.4.1	<i>Standard eRGB image processing</i> .....	47
<b>3</b>	<b>Estimating surface concentrations of <i>Calanus finmarchicus</i> using standardised satellite derived enhanced RGB imagery .....</b>	<b>49</b>
3.1	Introduction .....	49
3.2	Standardised eRGB imagery.....	51
3.3	eRGB colour simulation .....	56
3.4	Quantification of perceived colour difference .....	57
3.5	Bio-optical anomaly detection.....	59
3.6	Impact of <i>C. finmarchicus</i> absorption on reflectance signals.....	61
3.6.1	<i>Estimating surface C. finmarchicus concentrations from eRGB imagery</i> .....	63
3.7	Impact of <i>C. finmarchicus</i> absorption on OC3M algorithm performance .....	66
3.8	Application of the colour matching method to the Gulf of Maine	69
3.9	Conclusions .....	74
<b>4</b>	<b>A per -pixel approach to atmospheric correction implementation using a Case 2 spectral matching technique .....</b>	<b>77</b>
4.1	Introduction .....	77
4.2	The Gulf of Maine test image .....	79
4.3	Selection of an appropriate spectral matching technique .....	80
4.3.1	<i>Testing the suitability of RRMSD for identifying optical anomalies</i> .....	85
4.4	Atmospheric correction selection.....	88
4.4.1	<i>The effect of atmospheric correction on spectral information</i> .....	88
4.5	A per-pixel approach to atmospheric correction selection .....	92
4.5.1	<i>Spectral matching generated constituent concentration estimates</i> .....	97
4.6	Conclusions .....	98

<b>5</b>	<b>Development of a spectral matching approach to identify surface swarms of <i>C. finmarchicus</i> from satellite derived ocean colour data</b>	<b>101</b>
5.1	Introduction	101
5.2	$\Delta E_{2000}$ anomaly mapping on the Gulf of Maine dataset with pixel specific atmospheric correction applied	103
5.3	The development of an alternative spectral matching approach.	108
5.3.1	<i>Selection of optimal wavebands for anomaly mapping using a spectral matching approach</i>	108
5.3.2	<i>Identification of in-water anomalies and estimation of <i>C. finmarchicus</i> concentrations in the Gulf of Maine</i>	112
5.3.3	<i>Application of spectral matching approach to the northern Norwegian Sea</i>	115
5.4	Comparison of <i>C. finmarchicus</i> concentration estimates derived from the $\Delta E_{2000}$ and the RRMSD spectral matching approaches	118
5.5	Establishment of an anomaly threshold for the targeted application of the <i>C. finmarchicus</i> model to ocean colour data	120
5.6	Conclusions	126
<b>6</b>	<b>Experimental determination of the absorption properties of select zooplankton groups</b>	<b>130</b>
6.1	Introduction	130
6.2	Zooplankton sampling	132
6.2.1	<i>Loch Etive</i>	132
6.2.2	<i>Northern Norwegian Sea (SFI Harvest)</i>	133
6.3	The absorption properties of select zooplankton groups	134
6.3.1	<i>Calanus finmarchicus</i>	135
6.3.2	<i>Calanus hyperboreus</i>	142
6.3.3	<i>Paraeuchaeta norvegica</i>	144
6.3.4	<i>Meganyctiphanes norvegica</i>	147
6.3.5	<i>Limacina spp.</i>	150
6.3.6	<i>Parathemisto spp.</i>	153

6.3.7	<i>Aurelia aurita</i> .....	156
6.3.8	<i>Comparison of zooplankton spectral absorption properties</i> .....	160
6.4	Modelled impact of zooplankton on remote sensing reflectance signals .....	162
6.4.1	<i>Concentrations of zooplankton required to reach the RRMSD threshold of optical anomaly</i> .....	168
6.5	Uncertainties associated with the PSICAM serial addition approach .....	172
6.6	Conclusions .....	174
<b>7</b>	<b>Conclusions</b> .....	<b>179</b>
7.1	Summary of key findings.....	179
7.2	Future directions .....	186
7.2.1	<i>Development of remote detection methods and application to other zooplankton and large particles</i> .....	187
7.2.2	<i>Application of methods for remote detection of phytoplankton functional types</i> .....	190
7.2.3	<i>Characterisation of variability in spectral absorption within zooplankton species</i> .....	191
7.2.4	<i>Characterisation of the spectral scattering properties of zooplankton</i> .....	192
7.2.5	<i>In situ zooplankton monitoring and characterisation of evasion behaviour</i> .....	193
7.2.6	<i>Development of the per-pixel atmospheric correction method</i> .....	195
<b>8</b>	<b>References</b> .....	<b>197</b>

## List of Figures

Figure 1.1 Schematic of the radiance signal components measured by a satellite mounted ocean colour sensor. Schematic created with BioRender.com.....	2
Figure 1.2 The SIOP spectra used for the radiative transfer simulations in this study: specific absorption ( $a^*$ , blue), scattering ( $b^*$ , orange) and backscattering ( $b_b^*$ , green) of (a) phytoplankton (CHL), (b) material suspended sediment (MSS) and (c) coloured dissolved organic matter (CDOM). .....	7
Figure 1.3 Schematic of the key processes associated with the Biological Carbon Pump. Schematic created in Biorender. ....	16
Figure 1.4 (a) Image of <i>Calanus finmarchicus</i> . Free use, image credit: Michael Bok, licence: <a href="https://creativecommons.org/licenses/by-nc-sa/2.0/">https://creativecommons.org/licenses/by-nc-sa/2.0/</a> . (b) Concentration specific per- individual absorption spectrum of <i>C. finmarchicus</i> measured in a Point Source Integrating Cavity Absorption Meter (PSICAM) by K. Lefering, published in Basedow et al. 2019. ....	24
Figure 1.5 Image of the Antarctic krill species <i>Euphausia Superba</i> . Free use, image credit: Uwe kils on wikimedia commons. Licence: <a href="https://creativecommons.org/licenses/by-nc-sa/2.0/">https://creativecommons.org/licenses/by-nc-sa/2.0/</a> .....	27
Figure 2.1 Map of stations samples during the Sea Patches cruise in the northern Norwegian Sea on board the R/V Helmar Hansen between 28th April and 4th May 2017. ....	32
Figure 2.2 Schematic cross-section of the PSICAM set-up, showing the central light source at the centre of the integrating sphere and the light detector with its field of view (dashed line) that does not include the light source. Schematic from the operation procedures documentation for PSICAM (Röttgers, 2011). ....	35
Figure 3.1 Remote sensing reflectance spectra ( $R_{rs}$ ) for (a) the open water, (b) inside the swarm and (c) coastal waters, previously identified in Basedow et al. (2019). Original VIIRS processing produced anomalously low reflectance values in the blue-green that have largely been eliminated after the 2018 VIIRS reprocessing. Reprocessed VIIRS data broadly correlates with corresponding MODIS data.....	50
Figure 3.2 MODIS enhanced RGB images of the Norwegian Sea from the (a) 28 April and (b,c) 29 April 2017. These images were processed with the 443 nm, 488 nm and	

555 nm remote sensing reflectance data, and each waveband was stretched to include 95% of all pixels. Standard eRGB image processing results in significant variations in observed colours that are not reflective of changes in the optical characteristics of the water column. .... 52

Figure 3.3 Data distribution of remote sensing reflectance ( $R_{rs}$ ) values for (a) 443 nm  $\pm$  5 nm (b) 488 nm  $\pm$  5 nm (c) and 555 nm  $\pm$  5 nm from the global bio-optical dataset collated by Valente et al. (2022). The red dashed lines denote the lower limit of 0 and the upper limit of the 90th percentile of each band. These ranges informed the contrast stretch applied to standardise the eRGB imagery used in this study..... 54

Figure 3.4 MODIS enhanced RGB images of the Norwegian Sea from (a) the 28 April and (b,c) 29 April 2017. These images were processed with the 443 nm, 488 nm and 555 nm remote sensing reflectance data, and each waveband was stretched using a standardised range developed in this study. Three regions of interest are identified in (c): within the patch (red), coastal (green) and offshore (yellow). .... 55

Figure 3.5 Simulated remote sensing reflectance ( $R_{rs}$ ) spectra with (a) increasing chlorophyll (CHL), (b) coloured dissolved organic matter (CDOM), and (c) material suspended sediment (MSS) concentrations. CDOM concentrations are defined by its absorption at 440 nm. Each spectrum is coloured using its associated eRGB colour coordinate..... 57

Figure 3.6 Minimum delta E 2000 ( $\Delta E_{2000}$ ) anomaly map derived through eRGB colour matching, with the inside patch (red), coastal (green), and offshore (yellow) regions of interest depicted. Satellite eRGB pixels were compared to an eRGB look-up table (LUT) that represented the standard bio-optical model. The minimum  $\Delta E_{2000}$  derived from this comparison was extracted and mapped. Higher  $\Delta E_{2000}$  values signify a greater visual difference between the measured and modelled colour coordinates. 59

Figure 3.7 Estimated constituent concentrations derived from the delta E 2000 colour matching method using the standard case 2 bio-optical model of (a) chlorophyll (CHL), (b) coloured dissolved organic matter (CDOM- concentrations are denoted as absorption at 440 nm), and (c) material suspended sediment (MSS). These concentrations are required to provide the best optical closure using the standard bio-optical model alone..... 60

Figure 3.8 Comparison of median satellite ( $\pm 1$  standard deviation) and modelled remote sensing reflectance spectra with increasing concentrations of *Calanus finmarchicus* (a,c,e) with associated delta E 2000 ( $\Delta E_{2000}$ ) values (b,d,f) of each region of interest. The spectra are coloured with their associated eRGB coordinates. Initial

modelled spectra (without the addition of *C. finmarchicus*) were modelled using chlorophyll concentrations informed by satellite data and coloured dissolved organic matter concentrations informed by in situ measurements. An MSS value of  $0.03 \text{ gm}^{-3}$  was used across all three regions of interest to provide the best fit..... 62

Figure 3.9 (a) Minimum delta E 2000 ( $\Delta E_{2000}$ ) anomaly maps derived through eRGB colour matching with the inside patch (red), coastal (green), and offshore (grey) regions of interest are depicted. Satellite eRGB pixels were compared to an eRGB look-up table (LUT) that represented the standard bio-optical model, with *Calanus finmarchicus* absorption added as well. The minimum  $\Delta E_{2000}$  derived from this comparison was extracted and mapped. (b) An estimation of CDOM concentrations (CDOM concentrations are denoted as absorption at 440 nm) and (c) surface concentrations of *C. finmarchicus* produced using the identified minimum  $\Delta E_{2000}$  value for each pixel in the image (concentrations are expressed as individuals  $\text{m}^3$ ).64

Figure 3.10 Comparison estimates of chlorophyll derived from (a) the minimum delta E 2000 ( $\Delta E_{2000}$ ) colour matching technique and (b) the MODIS standard chlorophyll product calculated using the OC3M algorithm. .... 67

Figure 3.11 Impact of increasing *Calanus finmarchicus* concentrations on the MODIS OC3M chlorophyll algorithm output from the inside patch (red triangle), offshore (blue circle), and coastal (green cross) ROIs..... 68

Figure 3.12 (a) MODIS enhanced RGB image and (b) Minimum delta E 2000 ( $\Delta E_{2000}$ ) anomaly map derived through eRGB colour matching of the Gulf of Maine from 17<sup>th</sup> June 2009. The eRGB image was processed with the 443 nm, 488 nm and 555 nm waveband and stretched using the standardised range developed in this study. For anomaly identification, satellite eRGB pixels were compared to an eRGB look-up table (LUT) that represented the standard bio-optical model. The minimum  $\Delta E_{2000}$  derived from this comparison was extracted and mapped. .... 71

Figure 3.13 (a) Minimum delta e 2000 ( $\Delta E_{2000}$ ) and estimated (b) *C. finmarchicus* concentrations derived through eRGB colour matching of the Gulf of Maine from 17<sup>th</sup> June 2009. For anomaly identification, satellite eRGB pixels were compared to an eRGB look-up table (LUT) that represented the standard bio-optical model with the addition of *C. finmarchicus* absorption. The minimum  $\Delta E_{2000}$  derived from this comparison and the *C. finmarchicus* concentrations required to reach that minimum were extracted and mapped. .... 72

Figure 3.14 Estimated constituent concentrations required to reach minimum delta e 2000 ( $\Delta E_{2000}$ ) values with (a,c,e) the full Case 2 model and (b,d,f) the case two model

with the addition of <i>C. finmarchicus</i> absorption. Estimates are derived from the $\Delta E_{2000}$ colour matching technique. ....	74
Figure 4.1 Standardised MODIS eRGB image from the 17 <sup>th</sup> June 2009. The location of spectra used in analysis from the coastal (green), inside potential patch of <i>C. finmarchicus</i> (red) and open water (blue) regions of interest are denoted with a cross. ....	80
Figure 4.2 Two best spectral match ups for the inside patch (red) and offshore (blue) pixel spectra with the application of (a) spectral information divergence (SID), (b) normalised spectral similarity (NS <sup>3</sup> ) and (c) relative root mean square difference (RRMSD).....	83
Figure 4.3 Comparison of the (a) quality water index polynomial (QWIP) score and (b) relative root mean square difference (RRMSD) methods of spectral anomaly detection. It is recommended that any pixel with an absolute QWIP score of 0.3 or greater (depicted in black in panel a) is removed from spectral analysis. This anomaly detection had been conducted on the Gulf of Maine image from 17 <sup>th</sup> June 2009, and processed using standard atmospheric correction. ....	87
Figure 4.4 Remote sensing reflectance ( $R_{rs}$ ) values at 412 nm for the Gulf of Maine image processed using (a) the NASA standard atmospheric correction, as well as (b-h) 7 variants of the MUMM atmospheric correction, each with a different multiple scattering aerosol reflectance ratio ( $\epsilon_m$ ). ....	90
Figure 4.5 The impact of varying atmospheric correction methods in remote sensing reflectance ( $R_{rs}$ ) spectra in the (a) offshore, (b) coastal and (c) inside patch regions of interest. The arrow direction denotes the evolution from the NASA standard atmospheric correction, to the MUMM atmospheric correction with an aerosol reflectance ratio ( $\epsilon_m$ ) of 0.8. ....	91
Figure 4.6 Gulf of Maine maps of minimum relative root mean square difference (RRMSD) for the comparison of (a) the NASA standard and (b-h) the MUMM atmospheric correction with varying the aerosol reflectance ratio ( $\epsilon_m$ ) parameter to the standard case two spectral look up table (LUT).....	93
Figure 4.7 The Gulf of Maine (a) Index of atmospheric correction selection for each pixel and (b) relative root mean square difference (RRMSD) and (c) quality water index polynomial (QWIP) score for the corrected data. ....	95

Figure 4.8 Constituent concentrations of (a) chlorophyll (CHL), (b) coloured dissolved organic matter (CDOM) and (c) material suspended sediment (MSS) required to reach minimum relative root mean square difference (RRMSD) values derived from the comparison of fully corrected satellite data and a standard case two bio-optical model.....	98
Figure 5.1 Minimum Delta E 2000 ( $\Delta E_{2000}$ ) map derived by comparing eRGB colour values from the Gulf of Maine MODIS image on 17 <sup>th</sup> June 2009 to (a) a standard Case 2 bio-optical model and (b) a Case 2 bio-optical model with the addition of <i>C. finmarchicus</i> absorption. As well as (c) the estimated surface concentrations of <i>C. finmarchicus</i> produced from the minimum $\Delta E_{2000}$ value for each pixel in the image (concentrations are expressed as individuals $m^{-3}$ ). This data has been corrected using the per-pixel atmospheric correction approach outlined in Chapter 4. ....	104
Figure 5.2 Estimated constituent concentrations required to reach minimum delta E 2000 ( $\Delta E_{2000}$ ) values with (a,c,e) a full Case 2 model and (b,d,f) a Case 2 model with the addition of <i>C. finmarchicus</i> absorption. This data has had the per-pixel atmospheric correction method applied to it, following the procedure outlined in Chapter 4. ....	107
Figure 5.3 Minimum relative root mean square difference (RRMSD) maps for satellite spectral matching with a standard Case 2 bio-optical model using different spectral information. Spectral matching variants include (a) all 8 wavebands available (412, 443, 469, 488, 531, 547, 555 and 645 nm), (b) all wavebands except 412 nm (443, 469, 488, 531, 547, 555, 645 nm), (c) the ocean colour wavebands without 412 nm (443, 488, 531, 555, 645 nm) and (d) the three wavebands used in the $\Delta E_{2000}$ approach (443, 488 and 555 nm).....	110
Figure 5.4 Minimum RRMSD map for spectral matching of the Gulf of Maine image with (a) a standard Case 2 spectral LUT and (b) a Case 2 spectral LUT with the addition of <i>C. finmarchicus</i> and (c) the <i>C. finmarchicus</i> concentrations estimates required to reach minimum RRMSD values.....	113
Figure 5.5 Constituent concentrations required to reach minimum RRMSD values with (a,c,e) the full Case 2 model and (b,d,f) the Case 2 model with the addition of <i>C. finmarchicus</i> absorption in the Gulf of Maine. Estimates are derived from the RRMSD 4 waveband spectral matching technique.....	114
Figure 5.6 Minimum RRMSD map for spectral matching of the northern Norwegian Sea image (29 <sup>th</sup> April 2017) with (a) a standard Case 2 spectral LUT and (b) a Case 2 spectral LUT with the addition of <i>C. finmarchicus</i> and (c) the <i>C. finmarchicus</i>	

concentrations estimates required to reach minimum RRMSD values. Data has been corrected using the NASA standard atmospheric correction. .... 116

Figure 5.7 Constituent concentrations required to reach minimum RRMSD values with (a,c,e) the full Case 2 model and (b,d,f) the Case 2 model with the addition of *C. finmarchicus* absorption in the Northern Norwegian Sea. Estimates are derived from the RRMSD 4 waveband spectral matching technique. The data has been corrected using the NASA standard atmospheric correction. .... 117

Figure 5.8 Normalised difference maps for the comparison of *C. finmarchicus* concentration estimates derived from the RRMSD spectral matching and the Delta E 2000 ( $\Delta E_{2000}$ ) colour matching approach (RRMSD- $\Delta E_{2000}$ ) in (a) the Gulf of Maine and (b) the northern Norwegian Sea..... 119

Figure 5.9 (a) Minimum RRMSD map for spectral matching of the Gulf of Maine (GoM) image with a standard Case 2 spectral LUT applied. The anomaly threshold of 0.095 was calculated using the mean value of the offshore area denoted by the yellow box (0.053) + 2 standard deviations (0.021). (b) Image of the GoM showing all pixels that exceed the anomaly threshold of 0.095 in yellow. All pixels that are 'solved' using a standard Case 2 model are represented in black. Pixels representing a coastal (green), in patch (red) and offshore (yellow) region are denoted by crosses. .... 122

Figure 5.10 Satellite spectra for the (a) offshore, (b) coastal and (c) in patch pixels with all simulated spectral solutions for each pixel plotted in grey. The cross markers denote the location of the wavebands used in the spectral matching process. .... 124

Figure 5.11 Constituent concentration estimates for the in patch pixel derived from all spectral match ups with a RRMSD value below the anomaly threshold of 0.095. Spectral matching was conducted using a Case 2 model with the addition of *C. finmarchicus* absorption..... 125

Figure 6.1 Map of Loch Etive, with the location of the sampled station RE5 denoted by a red star..... 133

Figure 6.2 Map of stations sampled during the SFI Harvest cruise in the northern Norwegian Sea on board the R/V 'Helmar Hannsen' between 7th and 14th June 2022. .... 134

Figure 6.3 (a,c,e,g) Four *C. finmarchicus* serial addition experiments conducted on samples collected from Loch Etive on 7<sup>th</sup> March 2022 with (b,d,f,h) associated

regression analysis between absorption and number of individuals at 440 nm. The slope of this regression represents the per-individual absorption value at 440 nm.136

Figure 6.4 Two images of the same sample of *C. finmarchicus* obtained from station 9 during the SFI Harvest cruise on 12<sup>th</sup> June 2022. Image (a) was taken at 10:39 pm, just after the sample had been collected and image (b) was taken at 9:10 am on the 13<sup>th</sup> June 2022, after the sample had been placed in a refrigerator at 6 degrees..... 138

Figure 6.5 (a,c) Two *C. finmarchicus* serial addition experiments conducted at station 9 (ST09) on the 12<sup>th</sup> June 2022 during the SFI Harvest cruise in the northern Norwegian Sea, with associated (b, d) regression analysis between absorption and number of individuals at 440 nm. The slope of this regression represents the per-individual absorption value at 440 nm..... 139

Figure 6.6 The per individual absorption spectra (per m<sup>3</sup>) derived from the four *C. finmarchicus* serial addition experiments conducted on samples from Loch Etive collected on 7<sup>th</sup> March 2022 (solid blue lines), as well as two conducted on samples from the Northern Norwegian Sea during the SFI Harvest cruise in June 2022 (dot-dashed lines). The black dashed line represents the historic *C. finmarchicus* absorption measurement taken during the Sea Patches cruise in May 2017, which has been plotted for comparison..... 140

Figure 6.7 (a) *C. hyperboreus* serial addition experiment conducted at station 9 on 12<sup>th</sup> June 2022 during the SFI Harvest cruise in the Northern Norwegian Sea, with associated (b) regression analysis between absorption and number of individuals at 440 nm. The slope of this regression represents the per-individual absorption value at 440 nm. .... 143

Figure 6.8 The concentration specific per-individual absorption spectra (per m<sup>3</sup>) derived from the *C. hyperboreus* serial addition experiment conducted on samples from station 9 (ST09) on 12<sup>th</sup> June 2022 during the SFI Harvest cruise in the Norwegian Sea in June 2022. .... 144

Figure 6.9 *P. norvegica* serial addition experiments conducted at Loch Etive on 7<sup>th</sup> March 2022. Serial addition experiments were divided into (a) larger females with egg sacs and (c) smaller individuals, with associated (b and d) regression analysis between absorption and number of individuals at 440 nm. The slope of this regression represents the per-individual absorption value at 440 nm. .... 145

Figure 6.10 The per individual absorption spectra (per m<sup>3</sup>) derived from the *P. norvegica* serial addition experiment conducted on samples from Loch Etive collected

on 7<sup>th</sup> March 2022. The solid line represents the absorption spectra from mature females with an attached egg sac and the dashed line represents smaller individuals without an egg sac. .... 146

Figure 6.11 Image of *M. norvegica* sample retrieved from 300 m depth on 13<sup>th</sup> June 2022 during the SFI Harvest cruise in the northern Norwegian Sea. .... 148

Figure 6.12 The mean per individual absorption spectra (per m<sup>3</sup>) of *M. norvegica* on samples from station 11 of the SFI Harvest cruise in the northern Norwegian Sea collected on 13<sup>th</sup> June 2022. The mean is derived from 11 individual absorption spectra and the shaded area represents  $\pm 1$  standard deviation from the mean. .... 150

Figure 6.13 *Limacina* spp. serial addition experiments conducted on samples from (a) station 2 on the 8<sup>th</sup> June 2022 (c) station 4 on 9<sup>th</sup> June 2022 and (e) station 6 on 10<sup>th</sup> June 2022 during the SFI Harvest cruise in the northern Norwegian Sea. (b, d and f) represent regression analysis between absorption and number of individuals at 440 nm. The slope of this regression represents the per-individual absorption value at 440 nm..... 152

Figure 6.14 The per individual absorption spectra (per m<sup>3</sup>) derived from the three *Limacina* serial addition experiments conducted on samples from station 2 (*limacina* 1) station 4 (*limacina* 2) and station 6 (*limacina* 3) during the SFI Harvest cruise in the northern Norwegian Sea in June 2022..... 153

Figure 6.15 Image of a *Parathemisto* sample taken from station 4 (ST04) on 9<sup>th</sup> June 2022 during the SFI Harvest cruise in the northern Norwegian Sea. .... 154

Figure 6.16 *Parathemisto* spp. serial addition experiments conducted on samples from (a) station 2 on the 8<sup>th</sup> June 2022 (c) station 4 on 9<sup>th</sup> June 2022 and (e) station 6 on 10<sup>th</sup> June 2022 during the SFI Harvest cruise in the northern Norwegian Sea. (b, d and f) represent regression analysis between absorption and number of individuals at 440 nm. The slope of this regression represents the per-individual absorption value at 440 nm. .... 155

Figure 6.17 The per individual absorption spectra (per m<sup>3</sup>) derived from the three *Parathemisto* serial addition experiments conducted on samples from ST02, ST04 and ST06 during the SFI Harvest cruise in the northern Norwegian Sea in June 2022. . 156

Figure 6.18 Image of cultivated *A. aurita* ephyra/ medusa sample used for serial addition experiments. Samples were cultivated by the Evolution of Early Branching

Metazoans Research Group at the Maine Biological Association in Plymouth, UK. .....	158
Figure 6.19 (a) Serial addition of the cultivated <i>A. aurita</i> sample and (b) regression analysis between absorption and number of individuals at 440 nm. The slope of this regression represents the per-individual absorption value at 440 nm. ....	159
Figure 6.20 The per individual absorption spectra (per m <sup>3</sup> ) derived from cultivated <i>A. aurita</i> serial addition experiment.....	160
Figure 6.21 . Comparison of (a) absolute and (b) normalised absorption spectra of all the zooplankton groups in this study. Species with multiple absorption spectra are represented by the mean with the shaded region depicting $\pm 1$ standard deviation. .....	161
Figure 6.22 Modelled remote sensing reflectance spectra with increasing concentrations of (a, c) <i>C. finmarchicus</i> , (e) <i>C. hyperboreus</i> , (g, i) <i>P. norvegica</i> , (k) <i>M. norvegica</i> , (m) <i>A. aurita</i> , (o) <i>Parathemisto</i> spp. and (q) <i>Limacina</i> spp., with associated (b, d, f, h, j, l, n, p, r) relative root mean square difference values for comparison between each modelled spectrum with the initial spectrum where no zooplankton were present.....	164
Figure 7.1 (a) MODIS Enhanced RGB image of the South Orkney Islands from 15 <sup>th</sup> February 2016, showing an extensive red feature in the same region that a British Antarctic Survey (BAS) lead research cruise (cruise extent indicated by red dotted line) recorded large surface swarms of <i>E. superba</i> . (b) The red feature was highlighted as optically anomalous when compared to a standard Case 2 model. (c) This anomaly was resolved with the addition of an astaxanthin absorbing component into the model. ....	189

## List of Tables

Table 2.1 Summary of field data from the Sea Patches 2017 cruise used to inform the modelling work conducted in this thesis.....	34
Table 5.1 Spectral information available from MODIS Aqua data for the waveband range used in this study, along with the signal to noise ratio (SNR) requirement for each waveband. ....	109
Table 5.2 Summary of possible solutions below the anomaly threshold for the offshore, coastal and in patch pixels using the Case 2 (C2) and Case 2 + C. finmarchicus (C2+Cal) bio-optical model. ....	123
Table 6.1 Concentrations of each zooplankton group required to produce a strong enough signal to be identified through satellite imagery. ....	168

## List of abbreviations

<b>a</b>	Absorption
<b>AC</b>	Atmospheric Correction
<b>AOP</b>	Apparent Optical Property
<b>AVW</b>	Apparent Visible Wavelength
<b>b</b>	Scattering
<b>b<sub>b</sub></b>	Backscattering
<b>c</b>	Attenuation
<b>CDOM</b>	Coloured Dissolved Organic Matter
<b>CHL</b>	Chlorophyll- <i>a</i>
<b>DVM</b>	Diel Vertical Migration
<b>eRGB</b>	Enhanced Red Green Blue imagery
<b>GoM</b>	Gulf of Maine
<b>IOP</b>	Inherent Optical Property
<b>LUT</b>	Look-up Table
<b>L<sub>w</sub></b>	Water-leaving Radiance
<b>LWCC</b>	Liquid Waveguide Capillary Cell
<b>MODIS</b>	The Moderate Resolution Imaging Spectroradiometer
<b>MSS</b>	Mineral Suspended Sediment
<b>MUMM</b>	The Management Unit of the North Seas Mathematical Models atmospheric correction
<b>NAP</b>	Non-Algal Particulates
<b>NASA</b>	The National Aeronautics and Space Administration
<b>NIR</b>	Near-Infra Red
<b>NS<sup>3</sup></b>	Normalised Spectral Similarity Score
<b>OC3M</b>	Ocean Colour 3M algorithm
<b>OCI</b>	Ocean Colour Index
<b>PACE</b>	Plankton Aerosol, Cloud, ocean Ecosystem (satellite mission)

<b>PFT</b>	Phytoplankton Functional Type
<b>PSICAM</b>	Point Source Integrating Cavity Absorption Meter
<b>QWIP</b>	Quality Water Index Polynomial
<b>ROI</b>	Region of Interest
<b>R<sub>rs</sub></b>	Remote Sensing Reflectance
<b>RT</b>	Radiative Transfer
<b>SID</b>	Spectral Information Divergence
<b>SIOP</b>	Specific Inherent Optical Properties
<b>SNR</b>	Signal-to-Noise Ratio
<b>TOA</b>	Top of Atmosphere
<b>VIIRS</b>	The Visible Infrared Imaging radiometer Suite
<b><math>\Delta E_{2000}</math></b>	Delta E 2000 metric
<b><math>\epsilon_m</math></b>	Aerosol reflectance ratio

## Publications

McCarry, C.L., Basedow, S.L., Davies, E.J. and McKee, D., 2023. Estimating surface concentrations of *Calanus finmarchicus* using standardised satellite-derived enhanced RGB imagery. *Remote Sensing*, 15(12), p.2987.

# 1 Introduction

## 1.1 Optical Theory

The largest proportion of solar electromagnetic radiation that hits the surface of the ocean is in the range of visible light (between 400-700 nm). This visible light drives the photosynthetic processes of primary producers, thereby facilitating the foundation of the marine food web. Solar energy that passes through the earth's atmosphere and reaches the ocean is either reflected back into the atmosphere through direct Fresnel reflectance, or penetrates the water column, where it is absorbed or scattered, with some of the scattered light reaching the sea surface and passing back through the atmosphere (Figure 1.1). Distinguishing this light scattered from within the water column from other sources of light reaching satellite sensors in orbit around the Earth is a key challenge for ocean colour remote sensing applications. The way in which light travels through the water column is described by radiative transfer (RT) theory, which provides a framework for calculation of the spectral distribution and angular structure of underwater and water-leaving light fields. RT in the oceanic environment is dependent on the Inherent Optical Properties (IOPs) of the water body, which can be defined as optical properties that are independent of the angular structure of the incident light field. IOPs are therefore the sum of contributions from water itself, as well as the dissolved and particulate materials within it. As a result, characterising the IOPs of the water column not only provides information on the biogeochemical properties of the water body but allows for the accurate parameterisation of RT models to simulate oceanic light fields. The optical theory outlined in this section is summarised from the account detailed by Mobley (1994) unless otherwise referenced.

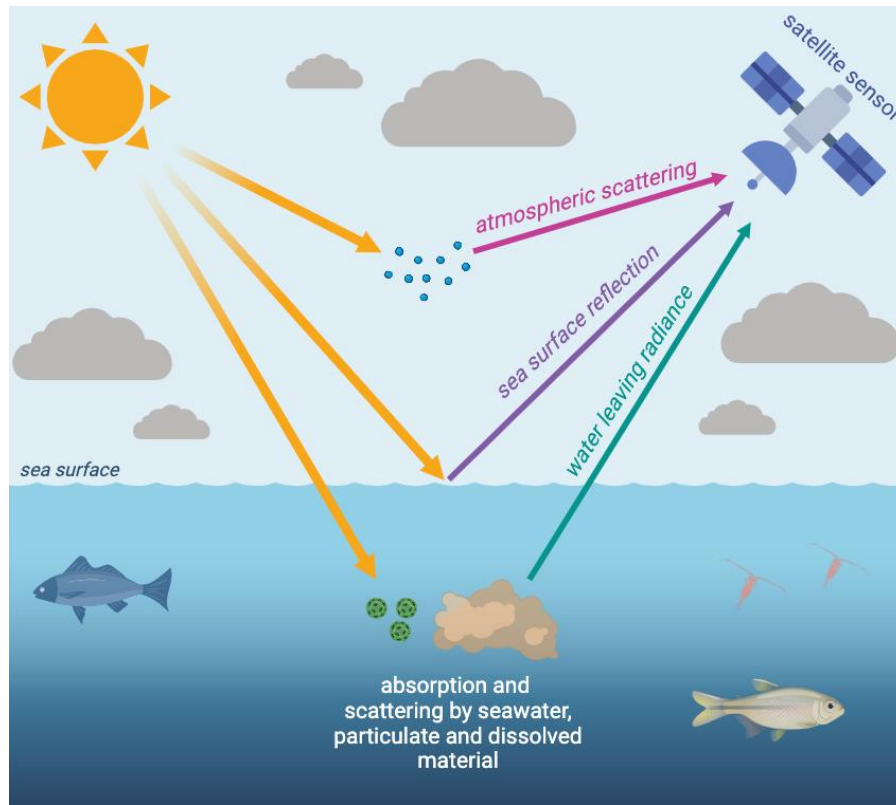


Figure 1.1 Schematic of the radiance signal components measured by a satellite mounted ocean colour sensor. Schematic created with BioRender.com.

### 1.1.1 Radiometry

The fundamental parameter used to describe the underwater light field in RT theory is the spectral radiance ( $L(\lambda)$ ).  $L(\lambda)$  is defined as the amount of radiant energy ( $Q$ ), per unit area ( $A$ ) per unit solid angle ( $\Omega$ ):

$$L(\lambda, z, \theta, \phi) = \frac{dQ}{dA d\Omega d\lambda} \quad [\text{Wm}^{-2} \text{sr}^{-1} \text{nm}^{-1}] \quad (1.1)$$

for a given depth ( $z$ ), zenith ( $\theta$ ) and azimuthal ( $\phi$ ) angle of incoming light. All other radiometric quantities can be derived from radiance. However, due to instrumental constraints and because complete radiance distribution information is not required for most practical applications, the most commonly measured radiometric quantity

is spectral irradiance ( $E(\lambda)$ ). The downwards planar irradiance ( $E_d(\lambda)$ ) describes all radiance travelling in the downward direction ( $\theta=0-\pi/2$ ) per unit area. Conversely, the upwelling planar irradiance describes all light travelling in the general upwards direction ( $\theta=\pi/2-\pi$ ), per unit area. These irradiances are expressed as:

$$E_d(\lambda, z) = \int_{\phi=0}^{2\pi} \int_{\theta=0}^{\pi/2} L(\lambda, z, \theta, \phi) \cos\theta \sin\theta \, d\theta d\phi$$

[W m<sup>-2</sup> nm<sup>-1</sup>] (1.2)

$$E_u(\lambda, z) = \int_{\phi=0}^{2\pi} \int_{\theta=\pi/2}^{\pi} L(\lambda, z, \theta, \phi) \cos\theta \sin\theta \, d\theta d\phi$$

[W m<sup>-2</sup> nm<sup>-1</sup>] (1.3)

Note that planar irradiances have a cosine dependence on the zenith angle, with maximal sensitivity orthogonal to the sea surface and zero sensitivity parallel to the sea surface. Similar definitions exist for scalar irradiances in the upwards and downwards direction, the difference being the absence of any angular dependence as scalar irradiances are integrated across all angles of light.

### 1.1.2 Inherent Optical Properties

When light travels through a volume of water of a certain thickness ( $\Delta r$ ), some of the incident radiant energy is absorbed ( $I_A$ ) within the volume of water, some will be scattered ( $I_B$ ) out of the beam path and the remaining will be transmitted through the volume. The spectral absorption coefficient ( $a(\lambda)$ ) is defined as the fraction of incident power ( $I_0$ ) that is absorbed within the volume:

$$a(\lambda) = \lim_{\Delta r \rightarrow 0} \frac{I_A(\lambda) / I_0(\lambda)}{\Delta r}$$

[m<sup>-1</sup>] (1.4)

Similarly, the spectral scattering coefficient ( $b(\lambda)$ ) is defined as the total fraction of incident power scattered, regardless of angular distribution, per unit distance:

$$b(\lambda) = \lim_{\Delta r \rightarrow 0} \frac{I_b(\lambda) / I_0(\lambda)}{\Delta r} \quad [\text{m}^{-1}] \quad (1.5)$$

The spectral attenuation coefficient ( $c(\lambda)$ ) is defined as the sum of the spectral absorption and scattering coefficients:

$$c(\lambda) = a(\lambda) + b(\lambda) \quad [\text{m}^{-1}] \quad (1.6)$$

The angular distribution of the scattered radiant power within the water volume is described by the spectral volume scattering function or VSF ( $\beta(\Psi, \lambda)$ ). VSF is expressed as the fraction of incident light scattered at an angle ( $\Psi$ ), into a solid angle ( $\Delta\Omega$ ):

$$\beta(\Psi, \lambda) = \lim_{\Delta r \rightarrow 0} \lim_{\Delta\Omega \rightarrow 0} \frac{I_B(\Psi, \lambda) / I_0(\lambda)}{\Delta r \Delta\Omega} \quad [\text{m}^{-1} \text{ sr}^{-1}] \quad (1.7)$$

Integrating the VSF over all directions (solid angles), gives the total scattered power per unit of incident radiant power, or the spectral scattering coefficient ( $b$ ):

$$b(\lambda) = \int_{\Xi} \beta(\Psi, \lambda) d\Omega = 2\pi \int_0^{\pi} \beta(\Psi, \lambda) \sin \Psi d\Psi \quad [\text{m}^{-1}] \quad (1.8)$$

For practical applications, it is useful to partition the spectral scattering coefficient into the spectral forward scattering coefficient ( $b_f(\lambda)$ ) and the spectral backscattering coefficient ( $b_b(\lambda)$ ), which are respectively expressed as:

$$b_f(\lambda) = 2\pi \int_0^{\pi/2} \beta(\Psi, \lambda) \sin \Psi d\Psi \quad (1.9a)$$

$$b_b(\lambda) = 2\pi \int_{\pi/2}^{\pi} \beta(\Psi, \lambda) \sin \Psi d\Psi \quad (1.9b)$$

### 1.1.3 *Optically important constituents*

The IOPs of marine waters are driven by the dissolved and particulate material within a water body, as well as the water itself. The spectral absorption of pure water is well described within the literature (Buiteveld et al., 1994; Pope & Fry, 1997), absorbing weakly in the blue and strongly in the red/ near infrared (NIR) part of the spectrum. However, marine waters contain various dissolved salts, with an average concentration of around 35 parts per thousand. Water absorption is sensitive to changes in salinity and temperature in red/ NIR wavelengths. Corrections are necessary to account for these effects when making high quality absorption measurements *in situ* (Zaneveld & Pegau, 1993). Remote sensing signals are, however, relatively insensitive to these effects. Conversely, dissolved salts increase the scattering of marine waters by around 30% compared to pure freshwater (X. Zhang et al., 2009), thereby influencing remote sensing signals to a considerable degree.

Particulate matter within the marine environment can be sub-divided into two categories based on the origin: organic and inorganic. Of all the organic particulates, phytoplankton are arguably the most influential. Phytoplankton are marine primary producers that are ubiquitous in the global ocean and consist of many different species with a particle diameter variation of 0.5  $\mu\text{m}$  to  $>50 \mu\text{m}$ . The IOPs of these organisms vary between species due to the variation in pigment composition, size and physiological state of the organism. Despite this, all phytoplankton share the main light-harvesting pigment called chlorophyll-*a* (CHL). Because of this, CHL is often used as a proxy for phytoplankton biomass. Extracted CHL pigment absorption shows strong peaks in absorption at around 430 nm and 665 nm. For many phytoplankton species, CHL dominates the species-specific absorption spectrum. However, some species such as cyanobacteria rely more heavily on auxiliary pigments, and as a result can have significantly different spectral absorption features (Neveux, 2008). Despite this, for the purposes of RT modelling, phytoplankton are often varied with respect to CHL concentration. Phytoplankton also scatter light with

the angular and spectral distributions being a function of size, complex refractive index and shape, including internal cellular structures.

Another organic component of particulate matter that can influence the optics of the water column are non-algal particulates (NAP). These are defined as particles that do not have extractable (via solvents such as acetone or methanol) pigments. This can include the non-pigmented parts of phytoplankton cells, detrital material, heterotrophic bacteria and viruses. In some cases, NAPs can also include inorganic particles of biogenic origin, such as diatom frustules and calcite coccoliths.

Inorganic particles generally consist of sediments suspended in the surface layer. These sediments can vary from fine silts and clays up to larger aggregates or 'flocs' of inorganic particles bound together by organic material. Generally, the effects of these particles are grouped together and are known as mineral suspended sediments (MSS). Generally, MSS is very effective at scattering light at the red/ NIR end of the spectrum, as well as absorbing light in the blue.

Dissolved material within the marine environment is generally characterised by any material that passes through a 0.2  $\mu\text{m}$  filter. Coloured dissolved organic matter (CDOM) is the photoactive fraction of dissolved organic matter (DOM) and can have a considerable impact on the optical properties of the water column. CDOM is derived from decaying phytoplankton cells and other organic material, as well as terrestrial sources (riverine input of biological material) and is typically yellow/brown in colour. As CDOM is dissolved, its effect on overall scattering in marine waters is usually considered to be negligible. Therefore, CDOM predominantly impacts absorption, absorbing strongly in the shorter wavelengths. The specific IOPs (SIOPs) of the optical constituents that informed the bio-optical model used in this thesis are presented in Figure 1.2. These SIOPs were measured in the Ligurian Sea in 2009 and are fully described in Chapter 2. In this case, the CHL component describes both phytoplankton pigment and biogenic detritus associated with algal material.

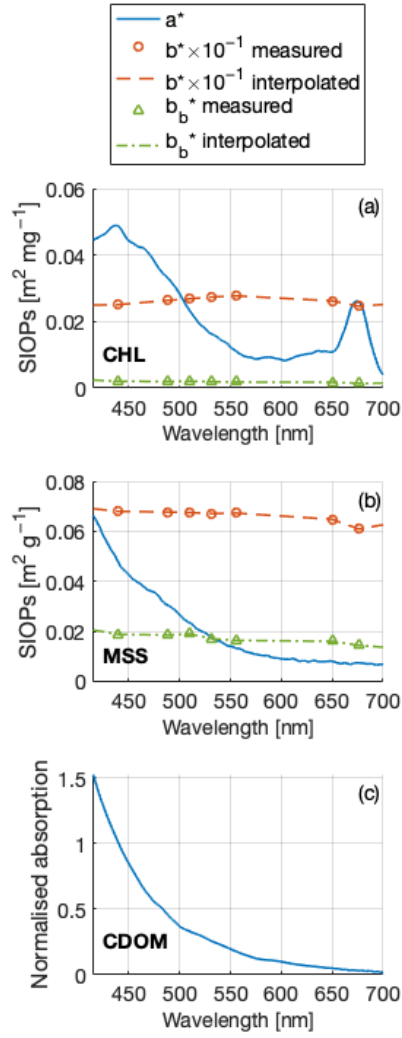


Figure 1.2 The SIOP spectra used for the radiative transfer simulations in this study: specific absorption ( $a^*$ , blue), scattering ( $b^*$ , orange) and backscattering ( $b_b^*$ , green) of (a) phytoplankton (CHL), (b) material suspended sediment (MSS) and (c) coloured dissolved organic matter (CDOM).

Taken all together, the bulk IOPs of the water column and can be expressed as:

$$a(\lambda) = a_w(\lambda) + a_{\text{CHL}}(\lambda) + a_{\text{NAP}}(\lambda) + a_{\text{MSS}}(\lambda) + a_{\text{CDOM}}(\lambda) \quad (1.10)$$

$$b(\lambda) = b_w(\lambda) + b_{\text{CHL}}(\lambda) + b_{\text{NAP}}(\lambda) + b_{\text{MSS}}(\lambda) \quad (1.11)$$

$$b_b(\lambda) = b_{bw}(\lambda) + b_{bCHL}(\lambda) + b_{bNAP}(\lambda) + b_{bMSS}(\lambda) \quad (1.12)$$

Marine waters are often classified according to the dominant constituents influencing the bulk IOPs of the water column. Originally defined by Morel and Prieur (1977), the aquatic environment can be broadly divided into Case 1 and Case 2 waters. Case 1 waters are typically open ocean environments, where bulk IOPs are primarily influenced by phytoplankton and co-varying materials e.g. CDOM and NAP. Conversely, Case 2 waters are more optically complex coastal and inland environments, where CDOM and MSS make a contribution to bulk IOPs that is independent of the CHL. Whilst characterising Case 1 waters is often relatively simple, coastal and inland Case 2 waters are typically more challenging, largely due to the diverse and variable optical signatures within these environments.

## 1.2 Satellite derived remote sensing of ocean colour

Satellite derived ocean colour is routinely used to remotely identify the optically important constituents in the water column, as the composition of these constituents can provide important information on marine biogeochemical processes. Since the launch of the Coastal Zone Colour Scanner (CZCS) in 1978, a sequence of satellite ocean colour sensors have supplied daily global coverage of natural waters, providing unprecedented ability to monitor marine biogeochemistry over large spatio-temporal scales.

### 1.2.1 *Basic principles and background*

Satellite observation of ocean colour involves the detection of spectral variance in water-leaving radiance ( $L_w$ ). Backscattering from interactions of the underwater light field with the optically important constituents result in light being diverted back to the surface and then into the atmosphere. It is this signal that is of interest to optical oceanographers and can be obtained from sensors on board

satellites, after the removal of the atmospheric and surface effects through the atmospheric correction (AC) process.

Since the launch of CZCS, which marked the beginning of ocean colour remote sensing, there have been several ocean colour sensors launched by multiple agencies. The European Space Agency's (ESA) missions include the Medium Resolution Imaging Spectrometer (MERIS), as well as the Copernicus program's Sentinel 2 and 3. The National Aeronautics and Space Administration (NASA) has two sensors currently in operation: the Moderate Resolution Imaging Spectrometer (MODIS) on board the Aqua satellite and the Visible Infrared Imaging Radiometer Suite (VIIRS) Suomi National Polar-orbiting Partnership (NPP). In addition, NASA's first hyperspectral sensor the Plankton Aerosol Cloud ocean Ecosystem (PACE) recently launched in February 2024. The PACE mission will provide 5 nm resolution data between 350 and 800 nm at 1 km spatial resolution, which will be particularly useful for resolving fine scale optical features.

The data used for this thesis is from the MODIS sensor, which was chosen because it has the most spectral bands available in the visible/ NIR region of the spectrum. MODIS is a 36 band spectroradiometer that was launched in 2002 and completes a sun-synchronous orbit around the Earth every 99 minutes, covering the planet every 1-2 days. The sensor has a swath width of 2330km, producing ocean colour data with a spatial resolution of 1 km.

MODIS data is used to determine  $L_w$ , which is then used to calculate a fundamental parameter known as Remote Sensing Reflectance ( $R_{rs}$ ).  $R_{rs}$  is categorised as an Apparent Optical Property (AOP), as it is dependent on both the composition of the water column and the directional structure of the ambient light field.  $R_{rs}$  is the ratio of in air  $L_w$  and downwelling solar irradiance ( $E_d$ ) at the surface, and can be expressed as:

$$R_{rs} = \frac{L_w(\text{in air}, \theta, \phi, \lambda)}{E_d(\text{in air}, \lambda)} \quad [\text{sr}^{-1}] \quad (1.13)$$

### 1.2.2 Atmospheric correction

Upwelling radiance reaching an ocean colour sensor includes a signal from the atmosphere as well as the ocean (Figure 1.1). In fact, as the ocean is a strong absorber, it only contributes around 10% to the overall signal received by the satellite (Zhang et al., 1999). The signal therefore must be processed from top of atmosphere (TOA) to bottom of atmosphere (BOA) reflectance or water leaving radiance ( $L_w$ ) through a process called atmospheric correction (AC). During this process, the data is corrected for Rayleigh and aerosol scattering, absorption by atmospheric gases and atmospheric transmittances, as well as correcting for reflection/ refraction at the air-sea interface. However, AC is difficult to achieve in practice, and accurately determining the relative contribution of the atmospheric signal to total radiance received by the satellite can be a considerable source of error in determining  $L_w$ . This error is amplified in optically complex coastal environments, where the optical properties of the water and atmosphere can be influenced by increased turbidity and proximity to land.

The standard approach to AC was first suggested by Gordon (1978) and relied on what is known as 'the black pixel assumption'. This method consists of estimating the aerosol reflectance contribution in the red/ NIR wavebands where the ocean is assumed to be totally absorbing (i.e. black). This would then be extrapolated to the shorter wavelengths in order to correct the spectrum. This approach, further developed in Gordon and Wang (1994), forms the foundation of many AC algorithms still in use today and generally works well in open ocean environments. However, this assumption breaks down in coastal environments, where waters can be highly turbid and contain more inorganic particles from terrigenous sources. This MSS efficiently scatters light in the red/ NIR, thereby creating a signal from the water body at this end of the spectrum. As a result, this approach can often lead to an over-correction in coastal waters, especially at shorter wavelengths.

The current NASA default AC scheme developed by Bailey et al. (2010) attempted to address this issue by using an iterative correction to remove non-negligible NIR radiance from the NIR signal prior to aerosol determination. This method uses an iterative bio-optical model to estimate NIR  $L_w$  in optically complex waters. Following this, the effects of aerosols at the two NIR bands is extrapolated and removed from the spectrum. This method provides marked improvements on the traditional AC algorithms. However, the use of an empirically derived bio-optical model with a small number of spectra relative to the natural variability of the ocean results in limitations, especially in optically complex environments.

Another improvement to the original black pixel assumption was suggested by Ruddick et al. (2000). This scheme replaced the assumption of no  $L_w$  in the NIR by the assumption of spatial homogeneity of aerosol type within the region of interest, as well as homogeneity in NIR seawater spectral shape. It requires the determination of normalised reflectance ratios for water and aerosols at two NIR bands on a per-image basis. This AC algorithm is commonly referred to as the Management Unit of the North Sea Mathematical Models (MUMM) algorithm. Whilst this method has led to improvements of spectral  $L_w$  retrievals from turbid coastal waters, the assumption of a spatially homogenous atmosphere breaks down over significant spatial scales (basin wide), which presents a key limitation with the application of this method to images of a significant size.

An alternative approach is the use of short wave infrared (SWIR) bands instead of red/ NIR to establish the atmospheric contribution to TOA signal in optically complex environments, as the black pixel assumption is most robust at these wavelengths (Shi & Wang, 2009; Wang & Shi, 2005). MODIS Aqua has the SWIR bands 1240, 1640 and 2130 nm that have been used for the development of AC in highly turbid coastal and inland waters. However, as MODIS SWIR bands are preliminarily used for land and atmospheric applications, they have a low signal to noise ratio (SNR). As a result, they perform poorly compared to standard NIR methods in more optically clear coastal regions, as well as non-turbid open ocean environments, due to the noise introduced to the derived products (Wang, 2007). As a result, combination

NIR-SWIR approaches were developed for the application of AC to images containing highly turbid coastal waters, providing improvements to the traditional NIR techniques (Chen et al., 2014; Shi & Wang, 2012).

Aside from methods derived from the black pixel assumption, other novel techniques using spectral matching (Steinmetz et al., 2011) and direct inversion approaches using artificial neural networks (NN) (Schroeder et al., 2007) have been developed to help achieve high quality  $L_w$  retrieval, with varying levels of success. A more detailed outline of all the AC methods available can be found in the review Emberton et al. (2016) and Frouin et al. (2019). Despite considerable progress within this field since the initial CZCS mission, the complex problem of AC remains. Some of the remaining problems that need to be addressed for operational use include accounting for adjacency effects (land, sea ice, clouds etc) and cloud shadow, absorbing aerosols and whitecaps (Frouin et al., 2019). In particular, these issues can manifest in highly turbid, optically complex coastal environments, where a number of different factors are influencing the water-leaving optical signal. The current protocol is to flag regions where the AC has obviously failed (e.g. non-physical negative reflectance values) to be removed from analysis. This results in large regions, particularly in coastal environments, where sufficient quality  $L_w$  data is not available.

### 1.2.3 *Phytoplankton monitoring*

The remote sensing of ocean colour has greatly contributed to the effort of monitoring the marine environment, as it supplies data on large spatio- temporal scales, yielding resolution that would not be possible with traditional ship-based sampling techniques. One of the most significant advancements since the advent of ocean colour remote sensing is the wide scale monitoring of phytoplankton dynamics in the global ocean. There has been considerable historic focus on the remote sensing of phytoplankton, largely due to their place as the foundation of the marine food web, as well as their importance in the global carbon cycle. Despite containing a diverse number of taxonomic groups, all phytoplankton contain the photosynthetic pigment

chlorophyll-*a* (CHL), through which energy from the sunlight is synthesised. As a result, CHL is commonly used as a proxy for phytoplankton biomass.

To infer CHL concentrations from ocean colour signals, *in situ* data is used to develop algorithms and models. The numerous CHL algorithms described within the literature (a detailed review of which can be found in O'Reilly & Werdell (2019)) can be broadly divided into two categories: empirical and semi-analytical algorithms. Of these, the most widely used are empirical band ratio algorithms, in which blue/ green wavelength ratios are constructed by a regression of *in situ* observations. As CHL absorbs much more strongly in the blue relative to the green, the ratio of these wavelengths can be used to estimate CHL concentrations. For example, standard CHL retrievals from MODIS are determined using the Ocean Colour Index (OCI) algorithm, which combines a band difference approach (Hu et al., 2019) and a band ratio approach (Hu et al., 2012) for determining low and high CHL concentrations respectively. Whilst these algorithms continue to be widely used, the variability in material composition within natural waters can lead to retrieval errors, especially in optically complex Case 2 waters. An alternative approach is the use of semi-analytical methods that employ radiative transfer theory to infer optically important constituents from the bulk IOPs of the water column. As these methodologies can account for other optical constituents such as CDOM or detrital material, they can perform better, especially in optically complex environments (Carder et al., 2004). Whilst the methodology of these approaches vary considerably, they all rely on accurate *in situ* IOP measurements to produce reliable results and for ground truthing purposes.

A more recent development within this field is the identification of different groups or 'functional types' of phytoplankton (PFTs) from satellite ocean colour data. PFTs are groups of phytoplankton classified according to their ecological function and can have considerably different impacts on biogeochemical cycling within the marine environment (Nair et al., 2008). Some key PFTs include nitrogen fixers (e.g. *Trichodesmium* spp.), calcifiers (e.g. Coccolithophores), silicifiers (e.g. Diatoms) and dimethylsulfide producers (e.g. Phaeocystis). Due to their unique physiology, some

of these groups have distinctive optical characteristics, making it potentially possible to distinguish their signal from ocean colour data. For example, coccolithophores form external calcium carbonate scales or 'liths' that produce a strong backscattering signal across the visible spectrum. This can turn the water a milky white or turquoise colour, and can be detected from ocean colour data (Brown & Podestá, 1997; Loveday & Smyth, 2018; Moore et al., 2012; Shutler et al., 2010). However, this feat becomes more challenging when the optical signal from a particular group is less distinguishable. In this case, alternative approaches have been developed, including the use of artificial NNs that incorporate geographical and ecological knowledge alongside ocean colour (Raitsos et al., 2008) and the use of optical characteristics to distinguish different phytoplankton groups as a function of size (Brewin et al., 2011).

This is a continually developing field of research and as such, a global consensus on remote monitoring of phytoplankton PFTs has yet to emerge. However, with the launch of the new hyperspectral satellite PACE, which will soon provide open access high spectral resolution data to the community, the ability to distinguish between optically important constituents with differing spectral characteristics should improve. Therefore, the establishment of spectral libraries containing the optical characteristics of these PFTs, as well as other potentially important constituents, is vital for the future development of the field.

### 1.3 Zooplankton and their potential impact on ocean colour

Zooplankton are the heterotrophic component of the planktonic community and comprise a diverse group of organisms ranging from 2  $\mu\text{m}$  to 20 mm or larger in size. As they are planktonic, they are classed as drifters or weak swimmers, and as a result their distributions are primarily influenced by oceanic currents and physical processes. These organisms are broadly classified into two groups according to their life cycle. These include holoplanktonic zooplankton, or organisms that remain within the zooplankton assemblage throughout their life cycle and meroplanktonic

zooplankton, which include organisms such as fish eggs and larvae that spend only part of their life cycle as zooplankton.

### 1.3.1 *Why are zooplankton important?*

Zooplankton are a keystone group of organisms in the marine environment, due to their sheer abundance and vital ecosystem roles. Indeed, the class of zooplankton Copepoda are the most abundant multicellular organisms on Earth, outnumbering insects by three orders of magnitude (Schminke, 2007). Because of this, zooplankton represent an essential component of the marine food web, serving as an intermediary for the transfer of energy between primary producers (phytoplankton) and higher order predators. As a result, they directly support many commercially harvested species of fish, as well as many charismatic marine mammal species. Additionally, zooplankton themselves represent an important economic resource, as these organisms are regularly harvested for the production of aquaculture feed, as well as supplements for human consumption. For example, growing interest surrounding health and wellbeing has resulted in increasing numbers of krill being fished for omega 3 as an alternative to fish oil, generating over 256.7 million USD in 2019 (Botterell et al., 2023).

Additionally, zooplankton are integral in the regulation of the biological carbon pump (BCP). The BCP is a collection of processes through which carbon is transported from the surface ocean to deep waters, a schematic of which is presented in Figure 1.3. Whilst the majority of carbon returns to the surface ocean and is exchanged with the atmosphere through processes such as respiration, a portion of it is exported to deeper waters, where it is sequestered from years to centuries. A study by Nowicki et al. (2022) quantified the carbon export and different sequestration pathways, finding the ocean responsible for the export of 10.2 Pg C yr<sup>-1</sup>. Of this, the gravitational pump, or sinking particle export, is responsible for 70% of total global carbon export. Fast sinking zooplankton faecal pellets are a very efficient form of export contributing around 85% of the gravitational pump, compared to only 15% of

sinking material by phytoplankton. In addition to this, diel vertical migration (DVM) is a behaviour commonly associated with many zooplankton species, where organisms will ascend from the depths to the surface at night to feed on phytoplankton. Once these organisms have fed, they return to the depths where they remain during the day, to avoid predation by visual predators (Iwasa, 1982). This migration is responsible for a further 10% of total export, with physical mixing making up the remaining 20%. As key regulators of the BCP, zooplankton facilitate carbon capture and storage, thereby allowing the ocean to act as a critical buffer against the impacts of climate change.

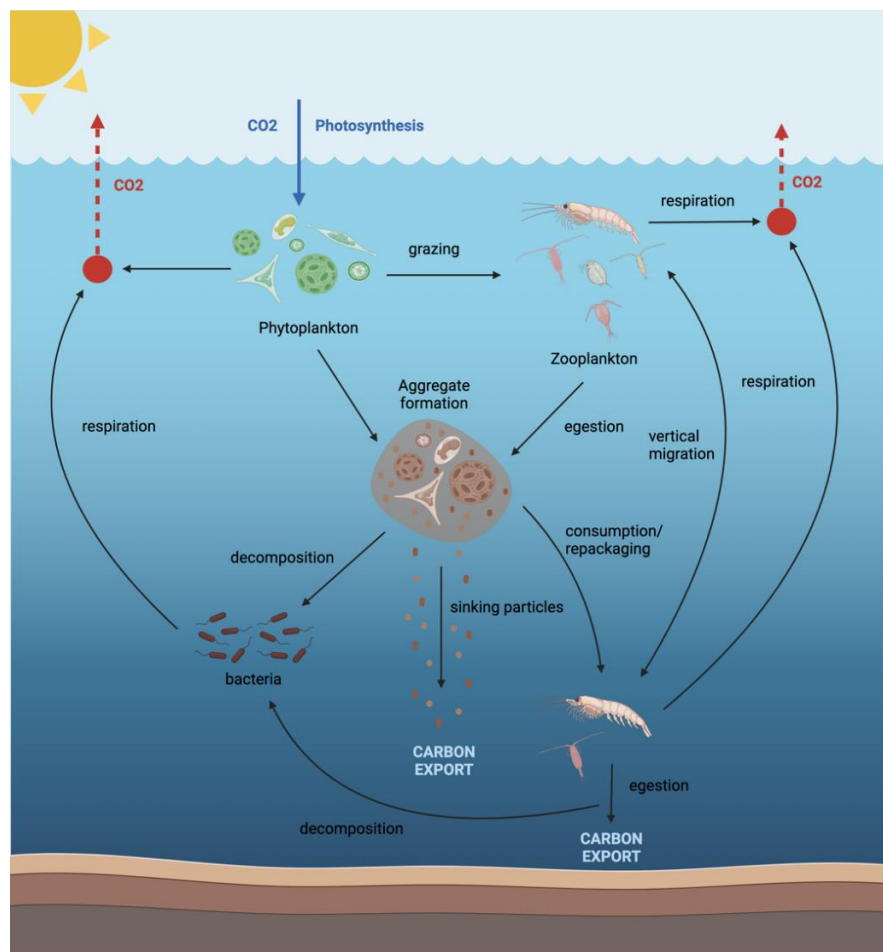


Figure 1.3 Schematic of the key processes associated with the Biological Carbon Pump. Schematic created in Biorender.

Additionally, many zooplankton species can act as bioindicators for ecosystem health due to their relatively short life cycles and responsiveness to environmental change. Due to their sensitivity, species richness and abundance of zooplankton assemblages can provide information of the degree of anthropogenic pollution within an ecosystem (Drira et al., 2018; Marcus, 2004). Further, the physiological processes of many zooplankton species are highly sensitive to temperature and coupled with their short life cycles (many species live less than 1 year), zooplankton can represent more effective indicators of environmental change than the environmental variables themselves. This is because the high sensitivity of these organisms can serve to amplify the signals of change (Richardson, 2008).

Indeed, zooplankton provide numerous critical ecosystem services, a comprehensive review of which can be found in Botterell et al. (2023). As a result, they hold significant value and have been the focus of considerable scientific effort over the last century. Despite this, the advancement in knowledge of *in situ* population dynamics is modest (Marine Zooplankton Colloquium 2, 2001). Traditional ship-based monitoring techniques likely contribute to the disparity between research effort and knowledge, as zooplankton populations are patchy by nature, making targeted sampling efforts challenging. Therefore, being able to remotely identify zooplankton from ocean colour, in a similar way to current remote phytoplankton monitoring methods, would likely lead to significant advancement in the community's understanding of these organisms. Considering their importance in the marine food web, their regulatory role in the BCP and their potential to act as bioindicators for anthropogenic climate change, the spatial and temporal coverage provided by satellite derived ocean colour data would be an invaluable resource for monitoring the marine environment and projecting change.

### 1.3.2 *Current in situ methods for monitoring zooplankton*

As a result of the critical roles zooplankton play within the marine environment, considerable scientific effort has been focused on the *in situ* study of

their abundance and distributions. Zooplankton represent such a diverse group of organisms with differing behavioural patterns and as such many techniques have been developed to better understand natural populations. Perhaps the most traditional and widely used method for zooplankton sampling are nets with various mesh sizes, which can partition samples according to size (for example MultiNet, WP2, Bongo nets and tucker trawls). These can either be towed vertically or horizontally, and can sample specific depth ranges using trigger mechanisms or pressure- meter activated release. Net sampling can provide information on species abundance composition, community size structure, as well as spatial distributions (especially in the vertical). However, net sampling has some significant limitations. Delicate zooplankton can often be damaged by net sampling, especially when nets are towed at high speeds. This is especially true for gelatinous zooplankton groups, such as jellyfish, which are highly delicate and often destroyed in the sampling process. Another limitation is the integrative nature of net sampled data, as population estimates are often integrated over tens of metres. This could lead to averaged concentration estimates that may not reflect natural vertical distributions or resolve surface swarm features. As well as this, net sampling techniques could be introducing bias into *in situ* population estimates simply due to the patchy distributions of these organisms. Net sampling methods are designed to sample one station at a time, broadly representing one point in the ocean. Therefore, if a large aggregation of zooplankton were located just out of the stations' sampling range, these organisms would not be represented in population estimates, despite potentially contributing significantly to the total zooplankton abundances in this region. Conversely, a net could sample a particularly dense, but spatially small patch of zooplankton at a certain station, leading to an overestimation of population size within the region.

Another well-established method for sampling zooplankton is the Continuous Plankton Recorder (CPR) Survey. This survey has been operating since 1931 and is managed by the Marine Biological Association in Plymouth. Water passes through the CPR and plankton are filtered onto a slow-moving band of silk, which is

then spooled in a storage tank containing formalin, to preserve the sample for later identification. The CPR is towed on ships of opportunity and represents one of the longest running, most geographically comprehensive ecological surveys in the world. As a result, extensive CPR datasets represent powerful tools that can be used to analyse long term spatio-temporal trends in zooplankton abundance. However, the CPR only samples open water environments and can only be towed at 5 to 10 m depth, therefore it cannot provide information on vertical distributions or coastal populations. As well as this, the mesh size of the silk within the CPR is fixed at 270  $\mu\text{m}$ , and thus smaller individuals (microzooplankton and juvenile/ small mesozooplankton) may be missed. Further, studies have reported that the CPR consistently under-estimates zooplankton populations relative to net estimates (Dippner & Krause, 2013; John et al., 2001), likely due to both the lack of vertical sampling and the narrow aperture of the CPR allowing zooplankton to easily evade capture.

The increasing need for zooplankton data to improve both monitoring and modelling efforts has driven the development of new technologies for characterising zooplankton dynamics. These include acoustic sensors such as echosounders that can partition zooplankton biomass according to size based on backscatter frequencies, as well as *in situ* imagers including the Imaging FlowCytobot (Olson & Sosik, 2007), the PlanktoScope (Pollina et al., 2022) and the Underwater Vision Profiler (Picheral et al., 2022). These sensors can be deployed over the side of a ship, mounted on static moorings or autonomous underwater vehicles (AUVs) to obtain high spatio temporal resolution over vast oceanic areas. Further, the autonomous Zooglider instrument combines both optical and acoustic sensors to provide fully autonomous *in situ* measurements of mesozooplankton distributions, together with information on the three-dimensional orientation of organisms in relation to other physical properties of the water column (Ohman et al., 2019). Whilst these advances can greatly add to our understanding of zooplankton dynamics, these methods can often not resolve zooplankton samples to species level. Further, acoustic sensors are not able to resolve

populations in the surface waters due to the presence of bubbles at the surface producing too much noise in the signal.

As evident, all of the sampling methods discussed have associated advantages and limitations and no single method is suitable for sampling such a diverse group of organisms. In fact, a recent review on monitoring and modelling zooplankton conducted by Ratnarajah et al. (2023) highlighted the importance of moving forward with an integrated approach, using the traditional methods with newer technologies to increase monitoring efforts, especially in under-sampled regions. This allows for historic time series that have been conducted using traditional methods to be sustained, whilst simultaneously allowing for the development that new technologies provide.

### 1.3.3 *Indirect remote sensing methods for estimating zooplankton abundances*

As discussed in the previous section, many methods have been developed to characterise zooplankton populations *in situ*. However, to further advance our understanding of these organisms and accurately parameterise biogeochemical models, routine acquisition of globally distributed observations is necessary. This feat is near impossible using ships and other marine platforms. Fortunately, satellite-borne ocean colour sensors can provide a regular, synoptic view of the earth's oceans and as a result represent a critical resource for better understanding zooplankton distribution and variability. Whilst satellite ocean colour data is routinely utilised to directly monitor marine primary productivity, its use as a method for directly identifying and characterising zooplankton assemblages is yet to be fully explored, and forms one of the main aims of this thesis. However, as zooplankton are primary and secondary consumers, their numbers are tightly coupled with primary production. Because of this, a number of studies have developed methods to derive zooplankton abundance estimates from satellite derived CHL data, which serves as a proxy for primary production.

One such study was conducted by Jennings et al. (2008), and developed an approach to estimate global trophic consumer biomass using satellite derived primary production (CHL) and sea surface temperature (SST) estimates. Biomass and production of consumer communities (portioned as a function of size) were calculated from estimated of primary production availability, whilst factors that influence the rate and efficiency of energy processing were accounted for (temperature, predator-prey mass ratios and trophic transfer efficiency). This was utilised to produce global biomass estimates for fish populations.

Similarly, Strömberg et al. (2009), developed a model to relate the flow of energy from primary production to zooplankton biomass, in order to produce global estimates of zooplankton abundance. This model was parameterised using the SeaWiFS satellite ocean colour record and a subset of the Coastal and Oceanic Plankton Ecology, Production and Observation Database (COPEPOD). The model was then validated with the remaining COPEPOD data. The relatively simple model performed well on a global scale, producing clear features such as higher zooplankton biomass in upwelling regions and on continental shelves, relative to the oligotrophic gyres. However, the model performed less well on a regional scale, likely due to its simplicity, as it did not take into account factors like ontogenetic diet shifts (from juvenile to adults stages), community structure and physical processes. These factors can all influence the propagation of zooplankton and therefore have the potential to influence biomass estimates. Thus, whilst this approach provided a good overview of global zooplankton biomass, it did not have the power to resolve fine-scale regional features.

More recently, Druon et al. (2019) investigated the utility of productivity fronts as an indicator for global mesozooplankton biomass. These fronts are generally meso-scale features that persist long enough to sustain zooplankton production and can be identified from satellite imagery through horizontal gradients of CHL concentration. These CHL gradients were used as the main proxy for food availability and characterised the environmental envelope for mesozooplankton, through matchups with CPR data. The results showed a general increase in productivity in the North

Atlantic from 2003 to 2017, which was hypothesised to be linked to atmospheric drivers (increase of latitudinal oscillation between low and high pressure systems generating unusual wind, evaporation and precipitation events) increasing the vertical turbulence and hence the frequency of productivity fronts across the region.

On a regional scale, Mahesh et al. (2018) developed an empirical approach to derive zooplankton biomass estimates in the Bay of Bengal a 3D multiple regression model using field measurements of mesozooplankton biomass, CHL concentration and sea surface temperature. Both seasonal and annual algorithms were developed, and the best was applied to MODIS derived SST and CHL products and validated with *in situ* data, yielding statistically significant relationships. The seasonal algorithms performed better than the annual, likely due to the high degree of seasonal variability in the Bay of Bengal resulting in error when the model was standardised on the annual scale.

#### 1.3.4 *Can zooplankton be directly identified from space?*

Ocean colour remote sensing signals are traditionally thought to be generated by mixtures of small (<100  $\mu\text{m}$ ) relatively abundant particles, as well as dissolved coloured materials (described in Section 1.1.3). However, a recent theoretical study demonstrated that larger, less abundant particles (>1 mm) may have an influence on ocean colour signals if present in sufficient concentrations (Davies et al., 2021). Using Mie Theory, Davies et al. (2021) illustrated that particles in the millimetre size class (which could include zooplankton, fish eggs, fish larvae and non-biogenic particulate material) can influence bulk IOPs, and in particular spectral absorption. This provides theoretical evidence to support the concept of identifying zooplankton through ocean colour remote sensing.

To successfully identify zooplankton from satellite  $R_{rs}$  signals, several conditions must be satisfied. Most importantly, the zooplankton group need to be pigmented enough to be optically identifiable. The pigmentation of these organisms will influence how they absorb light, which is the IOP likely to be most significantly

impacted by particles of this size (Davies et al., 2021). Further, this signal must contain distinct spectral features, to allow the zooplankton group to be distinguished from the other optically important constituents within the water column. Additionally, the target group need to be present in the surface waters, and in significant enough concentrations to impact the bulk IOPs of the water column. This concentration threshold will likely vary according to the physiology and pigmentation of the target zooplankton species. Finally, surface aggregations of these organisms need to be of a considerable spatial extent, as the spatial resolution of satellite data is often limited to around 1 km<sup>2</sup>. Zooplankton aggregations significantly smaller than the pixel size will not be resolved.

With the continuing development of new technologies, remote sensing as a method for direct zooplankton detection is starting to be explored. A recent study conducted by Behrenfeld et al. (2019) explored the use of a satellite mounted light detection and ranging (Lidar) sensor to detect an optical signal associated with organisms in the water column undergoing DVM. The study found that the organisms undergoing DVM contributed enough to the bulk backscattering ( $b_b$ ) signal to be identifiable by lidar. Further, due to the significant spatial and temporal coverage afforded by satellite mounted systems, the study was able to identify global trends in DVM biomass, with a greater proportion of the plankton biomass undergoing DVM within the sub-tropical gyres relative to higher latitudes. In addition, long term trends in DVM biomass were resolved, and a correlation between variation in DVM biomass and changes in phytoplankton production was identified. This work illustrates the power of using remote observations to assess populations on a large scale.

The first attempt to directly identify zooplankton from ocean colour  $R_{rs}$  was presented in Basedow et al. (2019) and forms the foundation work for this thesis. The Basedow et al. study was conducted in the northern Norwegian Sea, where the copepod species *Calanus finmarchicus* (Figure 1.4a) dominates the zooplankton assemblage. During this work, which was conducted in 2017, significant surface concentrations of *C. finmarchicus* were observed *in situ*. Concurrently, a satellite

derived enhanced RGB (eRGB) image captured a large red feature within the region, which was hypothesised to be influenced by a *C. finmarchicus* signal. When the satellite spectra at each sampled station was compared to spectra derived from a radiative transfer model with bio-optical constituent concentrations matching those measured, the blue reflectance derived from satellite data were consistently lower than the modelled reflectance. As the measured *C. finmarchicus* absorption spectrum showed an absorption feature in the blue wavelengths (Figure 1.4b), it was hypothesised that the lower blue reflectance from the satellite data was the result of *C. finmarchicus* absorption at these wavelengths. However, work conducted throughout the course of this thesis, and further explored in Chapter 3, indicates that the low blue satellite reflectance was primarily caused by previously unresolved satellite calibration issues, and when recalibration was applied, this disparity decreased considerably. As a result, the question surrounding the impact of zooplankton on ocean colour  $R_{rs}$  remained.

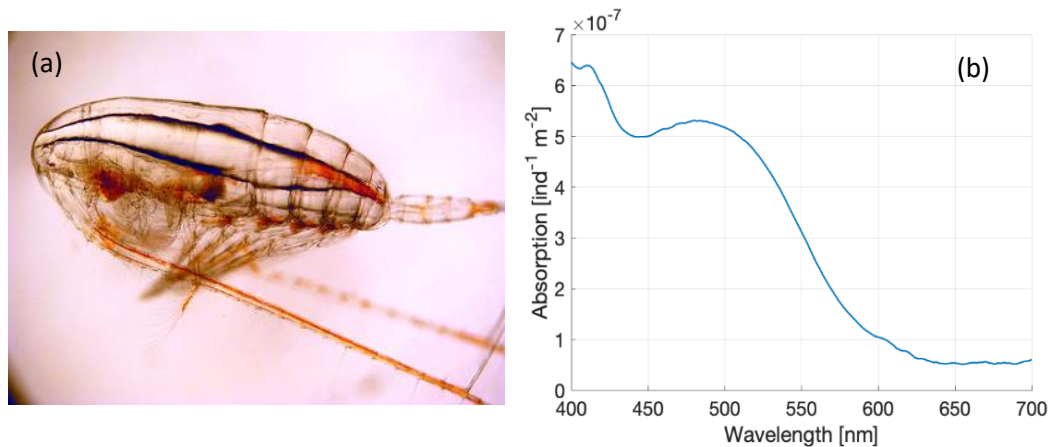


Figure 1.4 (a) Image of *Calanus finmarchicus*. Free use, image credit: Michael Bok, licence: <https://creativecommons.org/licenses/by-nc-sa/2.0/>. (b) Concentration specific per-individual absorption spectrum of *C. finmarchicus* measured in a Point Source Integrating Cavity Absorption Meter (PSICAM) by K. Lefering, published in Basedow et al. 2019.

Following on from the initial work conducted by Basedow et al. (2019), *C. finmarchicus* is the focus of the main body of work presented in this thesis. *C. finmarchicus* is a keystone species of the North Atlantic and Sub-Arctic ecosystem, serving as a nutritional food source for higher order predators in the region (Melle et al., 2014). These copepods are also commercially harvested for their high content of omega-3-rich oil, applications of which include incorporation into fish food for aquaculture and preparation of health supplements (Eilertsen et al., 2012; Pedersen et al., 2014; Wiborg, 1976). Whilst this is a relatively new fishery, a total annual quota of 240,000 tonnes has now been implemented in Norway (Botterell et al., 2023). In this context, there is considerable interest in establishing robust stock estimates to support sustainable management of this fishery.

*C. finmarchicus* are a good candidate species for remote identification, largely due to their physiology and behavioural patterns. Like many Crustacea species, the millimetre sized *C. finmarchicus* contain the red carotenoid pigment astaxanthin. It is synthesised from phytoplankton pre-cursors, with pigment expression varying considerably on both spatial and temporal scales. Due to the plasticity of this functional trait, understanding the main ecological benefit of pigmentation accumulation can be a challenge. However, a leading hypothesis within the scientific community suggests that amongst other uses, the strong antioxidant power of astaxanthin provides protection from oxidative damage caused by UV radiation (Vilgrain et al., 2023). This is suggested to prevent the degradation of the organisms' lipid sac when feeding on phytoplankton in surface waters. Much like CHL, the absorption generated by this pigment may be detectable from ocean colour signals if present in sufficient concentrations. As *C. finmarchicus* exhibit swarming behaviour, with anecdotal evidence of surface swarms visibly turning the water a 'reddish hue' or 'yellowish tint' in the Norwegian Sea (Bullen, 1913; Sars, 1903), it is possible that high concentration events such as these will have a considerable impact on  $R_{rs}$  signals.

As well as *C. finmarchicus*, other zooplankton groups may be good candidates for remote detection using ocean colour. The Antarctic krill species *Euphausia superba* are a critical organism in the Southern Ocean, serving as an important food source for

a wide range of protected Antarctic species, including seabirds, marine mammals, and fish. Further, *E. superba* represent a globally important economic resource, supporting the Southern Ocean's largest and continually expanding fishery (Botterell et al., 2023). Similar to *C. finmarchicus*, *E. superba* are largely transparent but contain varying concentrations of carotenoid pigments, including astaxanthin (Figure 1.5). These organisms also exhibit swarming behaviour, with swarms ranging tens to thousands of meters (Tarling et al., 2009; Tarling & Fielding, 2016). Antarctic krill swarms have even been characterised as 'super swarms', a term first used to describe *E. superba* by Cram et al. (1979) during a krill survey in the Southern Ocean. Here, super swarms were defined as 'swarms of large horizontal dimension (of the order of thousands of meters or greater) and perhaps more important, very high densities.' Since then, super swarms of varying sizes and densities (always on the order of several kilometres) have been recorded within the literature (Holm-Hansen & Huntley, 1982; Mathisen & Macaulay, 1983; Shulenberger, 1983; Tarling & Thorpe, 2017). These swarms have also been reported in surface waters, visually turning the water pink (Harrison et al., 2020; E. J. Miller et al., 2019; Nicol, 2018). Therefore, it is likely that these high concentration events will have a significant influence of  $R_{rs}$  signals. These organisms represent a considerable biological and economic interest, and as a result large scale monitoring efforts of stock level is critical. In fact, as Tarling & Fielding (2016) identified in a review of swarming and behaviour of Antarctic krill, 'the ability to detect and measure krill instantaneously over large spatial areas remains one of the ultimate challenges in krill science.' Due to the patchy population dynamics of these organisms, as well as the challenges associated with sampling in the Southern Ocean, traditional techniques may not provide accurate abundance estimates. Ocean colour remote sensing could help address this problem, by providing unparalleled spatio-temporal coverage for monitoring purposes.



Figure 1.5 Image of the Antarctic krill species *Euphausia Superba*. Free use, image credit: Uwe Kils on wikimedia commons. Licence: <https://creativecommons.org/licenses/by-nc-sa/2.0/>

Indeed, any pelagic zooplankton species has the potential to be detectable through ocean colour remote sensing if they meet the conditions described above. As a result, characterising the optical properties of dominant groups of zooplankton is an important scientific endeavour. This will achieve a more complete understanding of their role in influencing the bulk IOPs of the water column to better parameterise radiative transfer models.

However, when analysing the potential for using ocean colour remote sensing to identify zooplankton populations, limitations must be considered. Most notably, zooplankton live throughout the water column and can reach depths of thousands of meters. As ocean colour observations are limited to surface waters, due to the absorption properties of natural waters limiting light propagation to depth, satellite ocean colour data will not capture zooplankton populations that dwell below the surface waters. Despite this, satellite remote sensing provides a potentially useful tool for the identification of surface populations that can be utilised alongside other methods (such as those outlined in Section 1.3.2) as part of a holistic approach to monitoring.

### 1.3.5 Challenges associated with determining zooplankton IOPs

To achieve remote identification of zooplankton from satellite derived spectral  $R_{rs}$  signals, the IOPs of these organisms must first be accurately determined. This, however, presents a significant challenge, largely due to the bias of IOP measurements towards small particles. As *in situ* optical sensors are developed for the purpose of measuring small, relatively abundant particulates and dissolved materials, they typically have a sample volume on the order of 1 to 100 ml. This sample volume is too small to accurately determine the contribution of larger, less numerically abundant particles to bulk optical properties (Davies et al., 2021).

To overcome this issue, Basedow et al. (2019) first developed an approach to measuring the spectral absorption of *C. finmarchicus* in a Point-Source Integrating Cavity Absorption Meter (PSICAM). The PSICAM is a benchtop instrument with a 400 ml sample volume and high measurement sensitivity, providing results relatively free from scattering error (Röttgers et al., 2005). Whilst the sample volume of the PSICAM would still be too small to measure the absorption of natural zooplankton assemblages, due to the relative sparsity of these populations, Basedow et al. (2019) developed a serial addition method to determine per- individual absorption spectra. Using this method, 7 to 8 live *C. finmarchicus* per step were sequentially added to a seawater sample, with an absorption measurement at each step. Following this, the slope of a regression between number of individuals and absorption at each wavelength determined a per-individual absorption spectra. This value can then be scaled according to concentration to determine the absorption of an assemblage of a given density. Within the Basedow et al. (2019) paper, a *C. finmarchicus* absorption spectrum was measured, that displayed a peak in absorption that was characteristic of the pigment astaxanthin (Figure 1.4b).

Whilst this provides accurate zooplankton absorption measurements, there are currently no methods to determine the contribution of zooplankton to total spectral scattering ( $b$ ) or backscattering ( $b_b$ ), meaning the complete IOP profile of *C. finmarchicus* remains unknown. Whilst Davies et al. (2021) determined that due to the

size of these organisms, their spectral backscattering will have a much smaller contribution to bulk IOPs than that of absorption, this must be taken into consideration when using only absorption to represent the optical influence of zooplankton. As Davies et al. (2021) stated, it is evident that new approaches to *in situ* IOP sensing, in particular spectral backscattering sensors, need to be developed to properly account for the contribution of larger particles such as zooplankton to bulk IOPs.

#### 1.4 Thesis structure and aims

Larger millimetre sized ‘particles’, such as zooplankton, have traditionally been overlooked when considering optically important constituents within the marine environment. However, recent studies have theoretically established (Davies et al., 2021) and preliminarily explored (Basedow et al., 2019; Behrenfeld et al., 2019) the possibility of high concentration events having a considerable impact on the bulk IOPs of the water column, to an extent that their signal could be detectable from space. As many zooplankton species hold significant biological and economic value, and traditional ship-based monitoring techniques are unable to fully characterise their patchy population dynamics, being able to remotely monitor these populations would be of significant utility for monitoring purposes.

The ultimate aim of this thesis is to establish the potential for identification and characterisation of zooplankton assemblages from satellite derived ocean colour data. In particular, it attempts to quantify the extent to which zooplankton can influence spectral  $R_{rs}$  signals and develop methods to estimate surface concentrations of these organisms from space.

This thesis is structured in the following way:

- **Chapter 2** presents an outline of the common methods and materials used throughout the thesis, with further relevant methodological development within each of the results chapters.

- **Chapter 3** follows on from Basedow et al. (2019), presenting a method for the identification of surface swarms of *C. finmarchicus* in the northern Norwegian Sea using eRGB imagery. This chapter describes the development of a colour matching technique to identify regions of optical anomaly associated with *C. finmarchicus* absorption from ocean colour imagery. Further, remote estimations of surface concentrations within the *C. finmarhicus* features are presented and discussed for the first time.
- **Chapter 4** describes the development of an alternative approach to AC for optically complex waters. This method ensured best quality spectral reflectance data for the identification of optical anomaly associated with zooplankton.
- **Chapter 5** introduces an alternative spectral matching approach to identify and produce concentration estimates of *C. finmarchicus*. This method is compared to the results achieved using the colour matching approach developed in Chapter 3. Further, a threshold of optical anomaly is established to identify pixels not well described by a standard bio-optical model.
- **Chapter 6** presents the spectral absorption properties of 7 groups of zooplankton, measured in a PSICAM. Here, the influence of each group on spectral  $R_{rs}$  is modelled and concentrations required to reach the detection threshold established in Chapter 5 are estimated.
- **Chapter 7** presents the conclusions of the work in this thesis, as well as suggestions for the future direction of study.

## 2 Materials and Methods

This chapter provides an outline of the common materials and methodologies utilised throughout this thesis, including satellite image processing, collecting zooplankton absorption measurements and radiative transfer modelling. Further methodological development for the remote detection of zooplankton is presented as part of the results of this work and can be found in Chapters 3, 4 and 5.

### 2.1 Field data- Sea Patches 2017

The foundation work for this thesis was conducted by Basedow et al. (2019) during the Sea Patches cruise on board the R/V 'Helmar Hanssen' in the northern Norwegian Sea between 28<sup>th</sup> April and 3<sup>rd</sup> May 2017. Here, relatively large concentrations of *C. finmarchicus* were recorded in the surface waters at the same time that a satellite image captured a distinctly red feature. The measurements made during this cruise informed the modelling work conducted in Chapter 3. Further, the *C. finmarchicus* sampled during this cruise yielded the absorption spectrum (measured by K. Lefering) used for the majority of the *C. finmarchicus* modelling throughout this thesis (Figure 1.4b).

Amongst other measurements, CHL concentrations, CDOM absorption and *C. finmarchicus* abundance were taken at a total of 8 stations (Figure 2.1). The full information can be found in Basedow et al. (2019) but sampling of the data used in this work is summarised here for convenience and the results presented in Table 2.1.

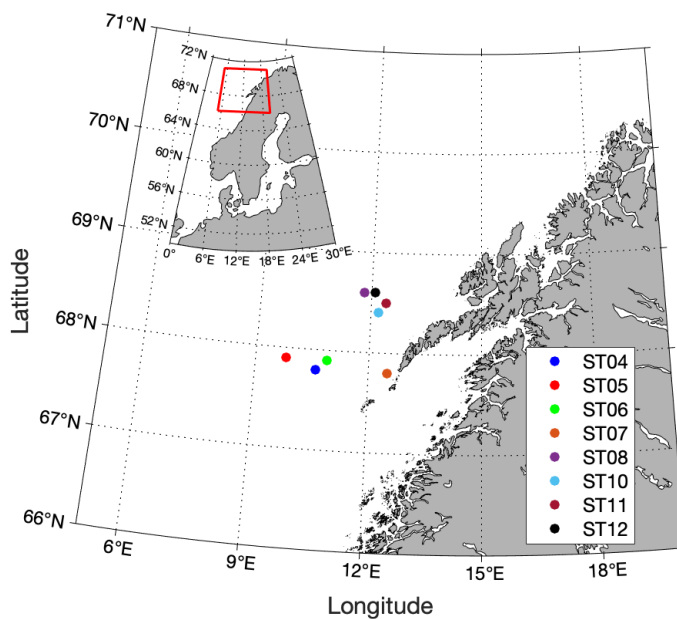


Figure 2.1 Map of stations samples during the Sea Patches cruise in the northern Norwegian Sea on board the R/V Helmar Hansen between 28th April and 4th May 2017.

### 2.1.1 Chlorophyll concentrations

CHL concentrations were measured using a 10-AU fluorometer (Turner designs, USA) from pigment extracts in methanol, obtained from filtered seawater samples (triplicates of 50 to 150 ml, GF/F filters, Whatman Inc., USA) from 0 m depth. These water samples were collected from Niskin bottles, filtered on board and frozen at -80 °C before analysis onshore immediately after the cruise.

### 2.1.2 CDOM absorption measurements

The proportion of light absorbed by CDOM was measured using a liquid waveguide capillary cell (LWCC, World Precision Instruments Inc., US) system with a 100 cm pathlength. The LWCC is a long pathlength system that provides high sensitivity absorption measurements. The cell was illuminated with a Deuterium/Halogen lamp with an internal shutter (DH-2000-BAL, Ocean Optics Inc., US) within the UV/VIS/NIR spectral region. The light from the lamp was directed to the LWCC

and the photo-diode mini spectrometer (AvaSpec ULS2048XL, Avantes, Netherlands) through fibre optic bundles (Ocean Optics Inc.).

Samples were injected into the system through spartan syringe filters (Whatman, Germany) with a 25 mm diameter and an 0.2  $\mu\text{m}$  pore size, in order to separate the suspended matter in the sample from the dissolved matter (i.e. CDOM). Absorption spectra were determined in triplicate against purified water as the reference measurement.

### 2.1.3 *C. finmarchicus* sampling and abundance

The abundance of *Calanus* spp. at each station was quantified based on vertically stratified net samples collected by a Multinet Midi (0.5 m s<sup>-1</sup> hauling speed, 180  $\mu\text{m}$  mesh size, 0.25 m<sup>2</sup> mouth opening, Hydro-Bio, Germany). Samples were preserved in a solution of 80% seawater and 20% fixing agent (75% formaldehyde buffered with hexamine, 25% anti-bactericide propane-1,2-diol). Sub-samples taken from depths of 30 to 4 m, 4 to 2 m and 2 m to surface (0 m) were enumerated under a microscope. Abundance was calculated based on the filtered volume obtained from the MultiNet flow meter.

Live *Calanus* species were collected for absorption measurements from the upper 15 m of the water column. Samples were collected using a Bongo net (mouth opening 0.28 m<sup>2</sup>, mesh size 200 and 500  $\mu\text{m}$ ) that was towed for 10 minutes at 2 knots.

Table 2.1 Summary of field data from the Sea Patches 2017 cruise used to inform the modelling work conducted in this thesis.

Station number	CHL [mg m <sup>-3</sup> ]	CDOM (abs at 440 nm) [m <sup>-1</sup> ]	<i>C. finmarchicus</i> concentration in surface 5 m [ind m <sup>-3</sup> ]
4	1.3	0.053	16,740
5	1.65	0.019	428
6	1.69	-	1,889
7	0.3	0.054	970
8	5.63	-	3,200
10	1.11	0.047	2,968
11	0.60	0.044	2,520
12	1.29	0.027	640

## 2.2 Zooplankton absorption measurements

The zooplankton absorption spectra generated in this study were calculated following the methodology briefly outlined in Basedow et al. (2019). The Basedow et al. study describes the absorption spectrum collected from *C. finmarchicus* during the Sea Patches 2017 cruise that was used for the majority of *C. finmarchicus* modelling conducted in this thesis (Figure 1.4b). This method was then applied with minor adaptations to the collection of other zooplankton absorption spectra, which are presented in Chapter 6 of this thesis. These measurements were conducted using a Point Source Integrating Cavity Absorption Meter (PSICAM), which is an instrument particularly suited to the measurements of particulate matter such as zooplankton, producing absorption measurements largely free from scattering error (Röttgers et al., 2005).

The PSICAM was first theoretically proposed as an instrument to produce high quality total absorption measurements by Kirk (1997) and later implemented (Leathers et al., 2000; Lerebourg et al., 2002; Röttgers et al., 2005). Generally, it consists of a spherical cavity illuminated with an isotropic light source placed at the centre (Figure 2.2). This integrating sphere produces multiple reflections at the cavity walls, resulting in long pathlengths and high measurement sensitivity. With the addition of

a homogenous, diffuse light source, scattering effects are minimised. The measurements are however, very sensitive to changes in the reflectivity of the cavity wall, and as a result calibration of the PSICAM using a known calibration solution is required to achieve accurate results.

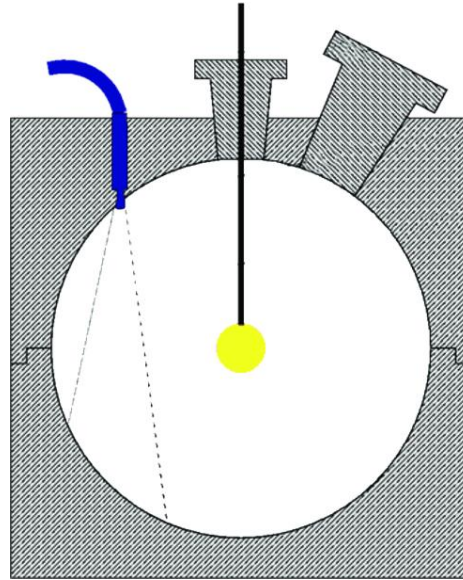


*Figure 2.2 Schematic cross-section of the PSICAM set-up, showing the central light source at the centre of the integrating sphere and the light detector with its field of view (dashed line) that does not include the light source. Schematic from the operation procedures documentation for PSICAM (Röttgers, 2011).*

### *2.2.1 Determination of absorption in the PSICAM*

The calculations used to derived spectral absorption coefficients from the PSICAM were developed by Kirk (1997) and Leathers et al. (2000) using radiative transfer theory. However, the nomenclature follows that of K. Lefering (2016) as it better reflects the measurement procedure and processing. The processing of PSICAM measurements was conducted in MATLAB (2022b) utilising a variation of the processing scripts originally developed by Lefering (2016).

All absorption measurements in the PSICAM are characterised by the light intensity at the cavity wall when it is filled with either a reference ( $R$ ), or a sample ( $S$ ) fluid. The ratio of these reflected irradiances ( $I_s/I_r$ ) is defined as the transmission,  $T_{sr}$  (Eq. 2.1).  $I$  is proportional to the number of times a photon collides with the cavity wall,  $N_c$ , before being absorbed by the wall or solution within the cavity:

$$T_{SR} = \frac{I_S}{I_R} = \frac{N_C^S}{N_C^R} \quad (2.1)$$

$N_c$  is dependent on both the probability that a photon coming from the central light source reaches the wall directly ( $P_0$ ) and the probability that a reflected photon will reach the wall again ( $P_s$ ), as well as the reflectivity of the wall itself ( $\rho$ ). This can be expressed as the sum of the number of photons reaching the wall directly and the number of photons returning to the wall for the second, third, fourth etc. time:

$$N_c = P_0 \sum_{n=1}^{\infty} (\rho P_s)^n = \frac{\rho P_0 P_s}{1 - \rho P_s} \quad (2.2)$$

As the transmission ( $T_{SR}$ ) is proportional to the ratio of  $N_c$  in the sample and reference solution (Eq. 2.1),  $T_{SR}$  can be expressed as:

$$T_{SR} = \frac{P_0^S P_s^S (1 - \rho P_s^R)}{P_0^R P_s^R (1 - \rho P_s^S)} \quad (2.3)$$

The diffuse light field inside a cavity with radius  $r$  (m) is generated by a spherical light source with radius  $r_s$  (m). Thus, the probability that a photon will reach the wall directly ( $P_0$ ) is calculated:

$$P_0(a, r_0) = \exp(-ar_0) \quad (2.4)$$

where  $r_0 = r - r_s$  and  $a$  is the absorption co-efficient of the fluid  $R$ . For a non-scattering solution  $P_s$  can be obtained using:

$$P_S(a, r) = \frac{1}{2a^2r^2} [1 - \exp(-2ar) (2ar + 1)] \quad (2.5)$$

From the components in Eq. 2.3 to 2.5, the transmission can be related to the absorption coefficients of a sample and reference solution:

$$T_{SR} = \exp[-r_0(a_S - a_R)] \left[ \frac{1 - \rho P_S(a_R, r) P_S(a_S, r)}{1 - \rho P_S(a_S, r) P_S(a_R, r)} \right] \quad (2.6)$$

In order to obtain the absorption co-efficient for a sample ( $a_s$ ), the reflectivity ( $\rho$ ) must be determined during instrument calibration, following the protocol outlined in Leathers et al. (2000). For calibration, the light intensity of a calibration solution ( $I_A$ ) and a reference solution ( $I_B$ ) are measured in the PSICAM to determine the transmittance  $T_{AB}$  following Eq. 2.1. The absorption coefficients of the calibration and reference solutions ( $a_A$  and  $a_B$  respectively) must be determined before calculating the reflectivity ( $\rho$ ). As the reference solution is generally purified water, the absorption coefficient ( $a_B$ ) is that of pure water and is taken from Pope & Fry (1997). The absorption coefficient of the calibration solution ( $a_A$ ) is determined using a Liquid Waveguide Capillary Cell (LWCC). Once these coefficients are obtained, the reflectivity of the wall ( $\rho$ ) can be calculated as:

$$\rho = \frac{T_{AB} \exp(-a_B r_0) P_S(a_B, r) - \exp(-a_A r_0) P_S(a_A, r)}{T_{AB} \exp(-a_B r_0) P_S(a_A, r) P_S(a_B, r) - \exp(-a_A r_0) P_S(a_B, r) P_S(a_A, r)} \quad (2.7)$$

With  $\rho$  calculated, the absorption coefficient of a sample of interest ( $a_s$ ) can be mathematically determined from solution of Eq. 2.6.

To summarise, determination of the absorption coefficient of a sample of interest ( $a_s$ ) in the PSICAM requires the following steps:

1. Calibration of the PSCIAM is first conducted, where irradiance is measured at the cavity walls when the PSICAM is filled with a calibration solution, most commonly nigrosine ( $I_A$ ) and a reference solution, namely pure water ( $I_B$ ). The absorption coefficients of both solutions are known (with pure water

absorption taken from the literature (Pope and Fry, 1997) and nigrosine absorption being determined in the LWCC). The ratio of these two irradiances ( $T_{AB}$ , Eq. 2.1) is used to determine the reflectivity of the cavity walls ( $\rho$ ) with Eq. 2.7.

2. The irradiance at the cavity walls is then measured again, this time with the cavity filled with a sample of interest ( $I_s$ ) and with a reference solution ( $I_A$ ), typically pure water, with a known absorption coefficient ( $a_R$ ). The ratio of these measurements is used to determine the transmission ( $T_{SR}$ ) following Eq. 2.1.
3. With  $T_{SR}$  and  $\rho$ , the absorption coefficient of the sample of interest ( $a_s$ ) can then be determined numerically using Eq. 2.6.

### 2.2.2 PSICAM setup

The PSICAM set-up used throughout this work follows the description in (Röttgers et al., 2005, 2007). The cavity was made from OP.DI.MA (Gigahertz-Optic, Germany), a highly diffuse reflective material. According to the manufacturer, the reflectivity is approximately 98% and is water repellent for a limited period of time so particulate material can be washed off easily. The light source consisted of a 10 mm diameter quartz- glass sphere placed in the centre of the cavity which has an inner radius of 4.5 cm. An electronically stabilised 150 W halogen lamp (CF1000, Illumination Technology) was connected to the scattering sphere using a glass fibre bundle. The light inside the cavity was collected by another quartz-glass fibre bundle, entering the cavity parallel to the central light source. This bundle was attached to the detector, a photo-diode mini spectrometer (AvaSpec ULS2048XL, Avantes, Netherlands). As any sample can eventually enter the porous cavity walls, the instrument was pre-soaked with ultra pure Milli Q water (water purification system: Simplicity UV, Millipore) 12 hours before any measurements took place. In addition, the halogen lamp was allowed to stabilise for at least one hour after being turned on before experiments were conducted.

### 2.2.3 PSICAM calibration

A limiting factor of the accuracy of the PSICAM is the determination of reflectivity of the cavity walls. As a result, careful calibration is required. In order to calibrate the system, a few drops of a black dye called Nigrosine (Aldrich Chemistry, USA) were placed into 1 litre of ultrapure Milli-Q water. As Nigrosine absorbs broadly across the UV/visible spectrum, it is a good solution for calibration across all wavebands. The stock was first filtered through a 25 mm Spartan filter with an 0.2  $\mu\text{m}$  pore size using a glass syringe. A few drops were then added to the Milli-Q. The solution was sufficiently diluted, with no visible colouration when placed into the purified water, to ensure the Nigrosine does not permanently stain the PSICAM walls.

Before any calibration took place, the PSICAM cavity was first bleached using a sodium hypochlorite solution (6-14% NaOCl, Sigma Aldrich co.) for 15 minutes. After this, the cavity was thoroughly rinsed under a running tap, and then three times with Milli-Q water. The PSICAM was then completely filled with a fresh sample of Milli-Q water, and the lamp intensity and integration time were adjusted so a maximum signal of 50,000 counts was achieved. The intensity inside the cavity was then measured twice, with the Milli-Q water acting as a reference, and then the nigrosine solution. After the nigrosine solution was taken out, the cavity was again bleached and rinsed thoroughly, to ensure the dye did not stick to the cavity walls. This process was repeated twice more, to produce one measurement averaged to compensate for any drift of the light intensity inside the cavity. Throughout these measurements, the PSICAM was covered in a thick black cloth, to minimise ambient light entering the sphere from the outside. The temperature of the reference and calibration solution was recorded before each replication for retroactive temperature correction.

During the 2017 Sea Patches cruise, the reflectivity of the PSICAM was determined three times a day throughout experimentation. However, the process of

calibration is very time consuming and the reflectivity of the cavity wall appeared to change very little with each measurement. As a result, for time efficiency, this approach was revised for the 2022 Loch Etive and 2022 SFI Harvest cruise work (presented in Chapter 6) to less regular calibrations, once a day before any samples were measured. Each reflectivity measurement was added to a database of cavity reflectivity (from historical data as well as during the cruise) and the average was taken for data processing. This reduced the possibility of any erroneous single calibrations affecting data quality. No long term trends in cavity reflectivity changes have been observed and therefore the average of an ensemble of calibrations was assumed to be an appropriate choice.

For each calibration conducted, the absorption coefficient of the nigrosine solution was determined in the LWCC. The system set-up for the 2017 calibrations was the same as that of the CDOM absorption measurements taken during the Sea Patches 2017 cruise (Section 2.1.2). For the absorption measurements presented in Chapter 6 of this thesis, the sample and reference solution was continuously pumped through the system using a mini peristaltic pump (World Precision Instruments, Florida, USA) instead of the previous sample injection method. This meant it was possible to continuously monitor the absorption inside the cell. A measurement was taken once the absorption spectrum had settled (after roughly one minute). Unlike the CDOM absorption measurements, the nigrosine solution was not passed through a 0.2  $\mu\text{m}$  filter, as this removed the absorbing material from the solution. The absorption was measured in triplicate, alternating between nigrosine and the Milli-Q reference. Between each nigrosine absorption measurement, bleach was pumped through the system to reduce the risk of contamination. After bleach had been pumped through, the cell was thoroughly rinsed with Milli-Q water.

#### 2.2.4 *Zooplankton absorption measurement procedure*

Once the PSICAM was appropriately calibrated, zooplankton absorption measurements could be taken. Per-individual zooplankton absorption spectra were

determined in the PSICAM using a serial addition approach, whereby a known number of live zooplankton were sequentially added to a filtered seawater sample, with Milli-Q purified water as a reference. Each experiment consisted of 6-11 additions, depending on the number of individuals available.

Similar to the calibration procedure, the lamp intensity and integration time were adjusted to a maximum of 50,000 count output when filled with the Milli-Q purified water. Again, two intensity measurements were taken, once with the reference Milli-Q water, and then with a seawater sample that had been filtered using a 47 mm GF/F filter to remove large particulate matter. For every measurement, the PSICAM was covered in a black cloth. A known number of live organisms were then added to the seawater sample (the number varied depending on size and pigmentation of the organism) and a new measurement was taken. This addition process was repeated several times (up to 11), each time adding a known number of live organisms and taking a corresponding measurement. The temperature of the reference fluid, as well as sample at each addition, was recorded using a waterproof thermometer (Hanna Instruments, UK) for temperature correction in the subsequent data processing.

Each measurement was corrected for temperature and salinity artefacts, which occur due to changes in the refractive index, using instrument specific temperature and salinity coefficients previously determined by Lefering (2016). Once the absorption spectra were determined from the intensity measurements using the equations presented in Section 2.3.1. and corrected for temperature and salinity effects, regression analysis was conducted between the number of individuals and the absorption measurements at each band from 400- 700 nm. The slope of each regression yielded the per individual absorption value, producing an absorption spectrum representative of an individual of the measured zooplankton group. This spectrum was then divided by the volume of the PSICAM (384 ml) to produce a concentration-specific absorption spectrum. This allowed for the spectrum to be integrated into a bio-optical model for radiative transfer modelling purposes.

## 2.3 Radiative transfer simulations

Above surface spectral remote sensing reflectance ( $R_{rs}$ ) was simulated using the Ecolight (version 5.2 Sequoia Scientific Inc., USA) radiative transfer model. Ecolight was used over Hydrolight, as Ecolight solved the azimuthally averaged radiative transfer equation, as opposed to full radiance distribution, which is less computationally expensive for the simulation of spectral  $R_{rs}$ . The total IOPs of standard Case 2 waters were assumed to be a function of three main optically important constituents, which include CHL, CDOM and MSS.

The IOPs of each constituent were modelled assuming a linear relationship between the constituent concentration and the spectral material-specific inherent optical properties (SIOPs). These were provided by the chosen bio-optical model (described below). To produce spectral look-up tables representative of Case 2 waters, the model was populated with a range of log spaced constituent concentrations for each optically important constituent. CHL was varied from 0.01 to 50 mg m<sup>-3</sup>, MSS from 0.01 to 25 g m<sup>-3</sup> and CDOM between 0.01 to 0.5 m<sup>-1</sup> (CDOM concentrations are denoted by associated absorption at 440 nm). This produced a total of 1008 unique constituent concentration combinations that broadly captured the natural optical variability in the ocean.

### 2.3.1 Bio-optical model

A bio-optical model provides SIOPs that are necessary to facilitate the simulation of water column IOPs from different optical constituent concentrations. In this thesis, a linear bio-optical model from the Ligurian Sea was used. All *in situ* data for the development of this bio-optical model were collected from the 13th-29th March 2009 during a cruise campaign in the Ligurian Sea on board the NR/V Alliance. A full description of the sampling locations, data acquired and methods used can be found in Bengil et al. (2016) but is summarised here. *In situ* non-water absorption ( $a_n$ ) and attenuation ( $c_n$ ) measurements were taken with a WETLabs 25 cm path length

AC-9 instrument, operating at nine wavebands (10 nm FWHM) across the visible-NIR (412, 440, 488, 510, 532, 555, 650, 676 and 715nm). Corrections were applied for the temperature and salinity dependence of pure seawater using data from temperature and salinity sensors mounted on a Seabird SBE 19 plus CTD. Absorption measurements were corrected for scattering error using the proportional method (Zaneveld & Pegau, 1993). *In situ* backscattering measurements ( $b_b$ ) were made with a WETLabs BB-9 backscattering meter operating at nine wavebands centred on 412, 440, 488, 510, 595, 650, 676 and 715nm. The data were corrected for path length absorption using the corrected AC-9 absorption data and the backscattering of pure water was subtracted to obtain the particulate backscattering coefficient as detailed by Lefering, Bengil, et al. (2016). BB-9 data were linearly interpolated to match AC-9 wavelengths.

The absorption of all dissolved and suspended components were measured using the PSICAM. Measurements of absorption by CDOM ( $a_{CDOM}$ ) were made using a 1 m LWCC and an Ocean Optics USB2000 mini spectrometer. Total particulate absorption ( $a_p$ ) was derived from subtracting  $a_{CDOM}$  from the PSICAM's non-water absorption measurements. Total particulate absorption was also obtained from the filter pad method (Ferrari & Tassan, 1999) using a Shimadzu UV-2501 PC benchtop spectrophotometer. Absorption by phytoplankton ( $a_{ph}$ ) was obtained through bleaching the samples to remove algal pigments, measuring the non-algal particulate absorption  $a_{nap}$  and subtracting this from  $a_p$ . PSICAM and LWCC data was utilised to determine path length amplification factors and scattering offset corrections through linear regression (Lefering, Bengil, et al., 2016; McKee et al., 2014). The filter pad corrections were applied to both bleached and unbleached absorption spectra.

CHL and total suspended solids (TSS) were measured in triplicate by colleagues from Management unit of the North Sea mathematical models (MUMM), with final values expressed as averages. Triplicate High Performance Liquid Chromatography (HPLC) samples were analysed by the marine chemistry laboratory of the MUMM using a reversed phase, acetone-based method with a C18 column and a Jasco FP-1520 fluorescence detector. TSS concentration estimates were collected

using pre-ashed, rinsed and pre-weighed 47 mm GF/F filters. Samples were carefully rinsed with ultrapure water, to minimise salt retention. Filters were stored frozen and returned to the lab where they were dried and re-weighed. TSS was numerically partitioned into bio-genic (OSS) and mineral (MSS) components using the technique outlined in Bengil et al. (2016).

The dataset collected during the Ligurian Sea cruise were from a total of 34 stations (after quality control) both onshore and offshore. The offshore stations consisted of deep, relatively clear waters, whereas the onshore stations were shallower and more turbid. Furthermore, onshore stations closer to the coast were influenced by fluvial sediments from the Arno River. As the offshore stations fit the criteria for Case 1 waters, it was assumed that no MSS would be present at these stations and thus CHL specific IOPs were derived from them. The CHL-specific IOPs were then used to further partition the onshore IOPs, which contained both biogenic particulates (CHL), as well as MSS. This allowed for the determination of mineral specific IOPs. CDOM was measured directly at each station.

The SIOPs were determined by a linear regression forced through zero of the partitioned IOPs against the associated constituent concentrations from surface water samples and is fully described by Lo Prejato et al. (2020). The SIOPs of each constituent used in this study are shown in Figure 1.2. The CHL component includes both the phytoplankton pigment absorption ( $a_{ph}$ ) and biogenic detritus ( $a_{det}$ ) (Figure 1.2a).

In order to model the impact of *C. finmarchicus*, and later other zooplankton species, on spectral  $R_{rs}$  signals, absorption spectra determined from the serial addition experiments were input into the bio-optical model as a separately varying constituent. Zooplankton were also varied linearly with concentration to determine concentration-specific absorption spectra. The *C. finmarchicus* absorption spectrum (determined by I. Lefering in Basedow et al., 2019) that was used for the majority of modelling work presented in this thesis is presented in Figure 1.4b.

### 2.3.2 *Ecolight set-up*

Ecolight was populated with a range of constituent concentrations in the surface layer (0 m depth), modelled with a homogenous water column and infinite depth. Ecolight was provided with latitude and longitude coordinates of the Norwegian Sea study area, as well as the time and date the satellite data was collected, in order to calculate the solar zenith angle. The model was set up with zero cloud cover, a windspeed of  $7.9 \text{ m s}^{-1}$ , a refractive index of 1.34 for seawater, water temperature of  $5.5 \text{ }^{\circ}\text{C}$  and a salinity of 34 psu. Note that the surface reflectance presented here do not include sun glint effects. Simulations were conducted between 412 nm and 714 nm at 2 nm intervals. Input files containing the IOPs generated from varying constituent concentrations and the bio-optical model described above, were generated using a bespoke MATLAB script. The partitioned IOPs from the Ligurian Sea were added together to produce total absorption ( $a_{tot}$ ), attenuation ( $c_{tot}$ ) and backscattering ( $b_{btot}$ ) spectra. These were then presented to Ecolight in the form of synthesised AC and BB instrument files. Raman scattering was the only form of inelastic scattering included the model, as CHL and CDOM fluorescence were not included. Whilst it would be optimal to include these effects, modelling fluorescence effects requires a quantification of quantum yields. This is a highly variable and difficult parameter to accurately characterise and therefore beyond the scope of this study. To minimise the effect of CHL fluorescence, all the matching techniques developed in this thesis did not include wavebands greater than 650 nm, as chlorophyll fluorescence typically peaks at around 676 nm. CDOM fluorescence has a wider wavelength range but has a minimal impact over most low to moderate CDOM waters (the concentrations associated with this study), on the order of a few percent at most (Mobley, 2022).

## 2.4 Satellite data processing

The satellite data used in this work were collected by the MODIS Aqua sensor. MODIS was chosen instead of VIIRS as it has increased spectral resolution in the visible light region of the spectrum. Level 1A MODIS Aqua data were acquired from the NASA Ocean Color archive (<https://oceancolor.gsfc.nasa.gov/>), with the R2018 calibration applied. Level 1A datasets contain reconstructed unprocessed instrument data at full resolution. Relatively cloud-free scenes of the chosen study area were downloaded and processed to level 2 using the tool 'l2gen' at 1 km resolution in the satellite data processing software package SeaDAS 7.5.1. Level 2 data consists of derived geophysical variables at the same resolution as the source Level 1 data. The default two-band aerosol model with an iterative near infrared correction was the chosen AC scheme (Bailey et al., 2010). For this study, bands 412, 443, 469, 488, 531, 547, 555, 645, 667, 678 and 745 nm were processed. For each band, spectral remote sensing reflectance ( $R_{rs}$ ) was downloaded (Eq. 1.13).

MODIS' standard chlorophyll product 'chlor\_a' was also processed. CHL estimations are calculated through the OCI algorithm, which combines a band difference approach for low chlorophyll concentrations (Hu et al., 2019), and a band ratio approach at higher chlorophyll concentrations (Hu et al., 2012). Chlorophyll concentrations are first calculated using the three-band reflectance difference CI algorithm specified by Hu et al. (2019):

$$\text{CHL} = 10^{(a_{0CI} + a_{1CI} \times \text{CI})} \quad (2.8)$$

where the coefficients  $a_{0CI} = -0.4287$  and  $a_{1CI} = 230.47$  and CI is calculated as:

$$\text{CI} = R_{rs555} - \left[ R_{rs443} + \left( \frac{R_{rs555} - R_{rs443}}{R_{rs667} - R_{rs443}} \right) \times (R_{rs667} - R_{rs443}) \right] \quad (2.9)$$

CHL is then calculated using the fourth-order polynomial ocean colour algorithm for the MODIS Aqua sensor (OC3M) (Hu et al., 2019):

$$\text{CHL} = 10^{(a+bR+cR^2+dR^5+eR^4)} \quad (2.10)$$

where  $R$  is calculated as:

$$R = \log_{10} \left\{ \max \left[ \left( \frac{R_{rs} 433}{R_{rs} 547} \right), \left( \frac{R_{rs} 488}{R_{rs} 547} \right) \right] \right\} \quad (2.11)$$

with  $a=0.2424$ ;  $b=-2.7423$ ,  $c=1.8017$ ,  $d=0.0015$  and  $e=-1.228$ . For CHL retrievals below  $0.25 \text{ mg m}^{-3}$  and above  $0.35 \text{ mg m}^{-3}$  the CI and the OC3M algorithm are used respectively. For retrievals in between these two values the CI and OC3M algorithm is combined using a weighted approach where:

$$\text{CHL} = \frac{\text{CHL}_{\text{CI}}(t_2 - \text{CHL}_{\text{CI}})}{t_2 - t_1} + \frac{\text{CHL}_{\text{OC3M}}(\text{CHL}_{\text{CI}} - t_1)}{t_2 - t_1} \quad (2.12)$$

where  $t_1 = 0.25$  and  $t_2 = 0.35$ .

The data were then re-projected using the Mercator 1SP projection. Single scene data were used as opposed to composites to maintain the temporal resolution, which reduces the potential of missing zooplankton swarm events that can occur over short time-periods. Land and cloud masks were applied, as well as a mask to remove any pixels with negative values in the spectra, as this is an indication of AC failure.

#### 2.4.1 Standard eRGB image processing

For each scene, eRGB images were generated in MATLAB (version R2022b) using three  $R_{rs}$  wavebands: 443 nm for the blue, 488 nm for the green and 555 nm for the red channel. eRGB imagery was utilised because it offers greater contrast to allow for more optical features to be visually identifiable. A standard image processing procedure was implemented, where each band was stretched to include 95% of all pixels through the percentile stretching technique:

$$\text{RGB}^{\text{out}}(\lambda) = A \left[ \frac{R_{rs}^{\text{in}}(\lambda) - R_{rs}^{\text{min}}(\lambda)}{R_{rs}^{\text{max}}(\lambda) - R_{rs}^{\text{min}}(\lambda)} \right] \quad (2.13)$$

where at a given waveband, the  $R_{rs}^{\text{in}}$  is the  $R_{rs}$  value of a pixel, and  $R_{rs}^{\text{min}}$  and  $R_{rs}^{\text{max}}$  represent the lower and upper stretch ranges. In this case,  $R_{rs}^{\text{min}}$  and  $R_{rs}^{\text{max}}$  are determined by the 2.5 and 97.5 percentiles of all pixels at each waveband. For these images  $A = 1$ , as the RGB co-ordinates are scaled within the range 0-1. This calculation is conducted for each channel, producing a three number RGB co-ordinate, representing the red, green and blue component of each pixel. Further, a gamma correction of 0.7 was applied to the blue channel to improve contrast:

$$B_{\text{out}} = AB_{\text{in}}^{\gamma} \quad (2.14)$$

where again  $A = 1$ ,  $B_{\text{in}}$  represents the calculated blue component of the RGB co-ordinate for each pixel and  $\gamma$  represents the chosen gamma correction value (in this case 0.7).

### 3 Estimating surface concentrations of *Calanus finmarchicus* using standardised satellite derived enhanced RGB imagery

#### 3.1 Introduction

Traditionally, ocean colour remote sensing signals are thought to be influenced by the optical properties of abundant, yet relatively small particles. This includes phytoplankton and associated material (CHL), material suspended sediments (MSS) and coloured dissolved organic material (CDOM). However, more recent theoretical studies have demonstrated the potential impact of larger, less abundant particles, such as the millimetre sized zooplankton species *Calanus finmarchicus* on the optics of the water column (Davies et al., 2021). As these organisms are known to exhibit swarming behaviour and have been visually reported to turn the surface waters a ‘reddish hue’ or yellowish tint’ (Bullen, 1913; Sars, 1903), it follows that high concentration events may influence surface reflectance signals. As *C. finmarchicus* are known for patchy population dynamics, it can be difficult to monitor distributions via traditional ship-based techniques. As a result, satellite-based monitoring could prove invaluable for management applications.

In the Norwegian Sea in 2017, large ‘red patches’ were identified from enhanced RGB (eRGB) imagery (Figure 3.2c) in a region where relatively high surface concentrations of *C. finmarchicus* were concurrently recorded during the Sea Patches cruise (28<sup>th</sup> April to 3<sup>rd</sup> May 2017) (Basedow et al., 2019). Here the absorption spectrum of *C. finmarchicus* was measured using a PSICAM (Figure 1.4b), and results indicated that the observed low satellite reflectance in the blue-green relative to spectra simulated using a standard Case 2 model could potentially be attributed to the effect of *C. finmarchicus* absorption at these wavelengths. However, since the publication of that paper, a recalibration of the VIIRS Suomi-NPP sensor (Weng et al., 2017) has led to a correction of the VIIRS spectra used in that study. Re-examination of the spectra

from the three different water types identified in Basedow et al. (2019) shows that the previously observed low reflectance in the blue-green has increased significantly in the recalibrated VIIRS spectra. The recalibrated VIIRS spectra also appear to broadly agree with the corresponding MODIS instrument data for each location (Figure 3.1). As a result of this re-analysis, the impact of *C. finmarchicus* on ocean colour data requires further analysis. Notably, the corresponding data from MODIS within the red patch (Figure 3.1b) has a peak at 676 nm associated with sun induced chlorophyll *a* fluorescence, which indicates the presence of raised levels of CHL. Therefore, it now seems possible that the red signatures within the image could potentially be explained by phytoplankton features.

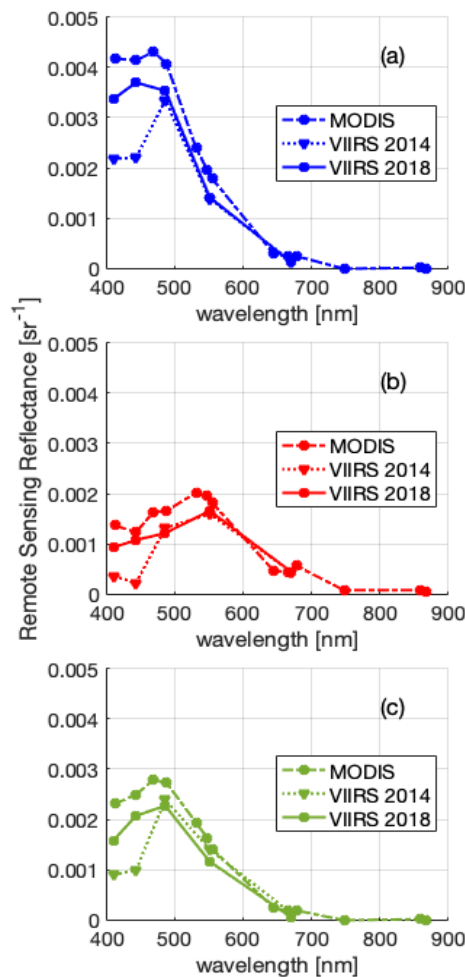


Figure 3.1 Remote sensing reflectance spectra ( $R_{rs}$ ) for (a) the open water, (b) inside the swarm and (c) coastal waters, previously identified in Basedow et al. (2019). Original VIIRS

*processing produced anomalously low reflectance values in the blue -green that have largely been eliminated after the 2018 VIIRS reprocessing. Reprocessed VIIRS data broadly correlates with corresponding MODIS data.*

This chapter aims to assess the extent to which *C. finmarchicus* absorption impacts ocean colour signals and ascertain if the ‘red patches’ identified by Basedow et al. (2019) are influenced by surface swarms of *C. finmarchicus*. To achieve this, a novel eRGB colour matching technique was developed, using the following methodology:

1. Images are standardised using a global range of *in situ*  $R_{rs}$  for each waveband to ensure colour consistency.
2. Images are compared to a look-up table (LUT) of eRGB colour values produced by varying constituents of a standard bio-optical model and simulating reflectance using the radiative transfer model Ecolight.
3. If the results indicate regions that deviate from the standard bio-optical model, images are then compared to a new LUT with the addition of *C. finmarchicus* absorption to address the anomaly.
4. Constituent concentrations required for optimal optical closure are extracted, providing concentration maps for the images.

The majority of this work has been published in a similar format in McCarry et al. (2023) Further, as a ‘proof of concept’ study, this chapter also presents results from the application of this method to an image from the Gulf of Maine. Whilst no *in situ* validation data is available, this is a useful exercise to test the performance of the method in a more optically complex environment.

### 3.2 Standardised eRGB imagery

Firstly, two scenes from the Norwegian Sea on the 28<sup>th</sup> and 29<sup>th</sup> April 2017 were downloaded and processed using a standard method outlined in Section 2.4.1. The images produced from the stretching method of excluding 5% of pixels in each band are visually inconsistent (Figure 3.2). Despite being only one day apart, the colour of

the offshore water varies significantly, as do the red pixels that appear along the coast. Furthermore, when the image is cropped to enlarge the suspected patch of *C. finmarchicus* (Figure 3.2c) and the same stretching method is applied, the colour of the sub-scene varies significantly. This is because the range applied to each of the bands is dependent on the information within the image (or cropped image) itself. This makes it difficult to distinguish variance caused by the optical properties of the water column from that caused by the processing method applied.

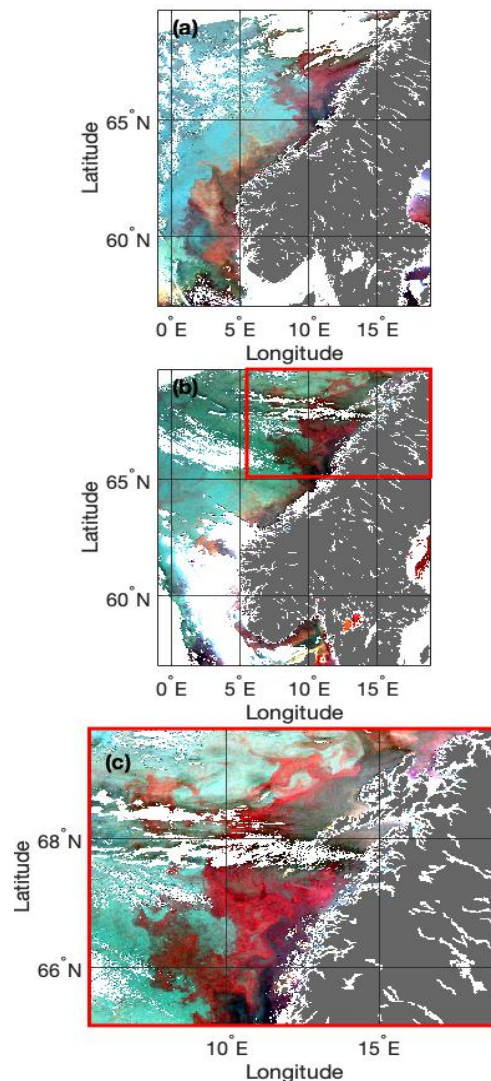


Figure 3.2 MODIS enhanced RGB images of the Norwegian Sea from the (a) 28 April and (b,c) 29 April 2017. These images were processed with the 443 nm, 488 nm and 555 nm remote sensing reflectance data, and each waveband was stretched to include 95% of all pixels.

*Standard eRGB image processing results in significant variations in observed colours that are not reflective of changes in the optical characteristics of the water column.*

To overcome this issue, a standardised stretch range was developed using an *in situ* dataset of global  $R_{rs}$  values compiled by Valente et al. (2022). All measurements  $\pm 5$  nm of each waveband were included to maximise data coverage (Figure 3.3). The minimum of the range was set to 0 and the maximum was determined by the 90th percentile of each band. In addition, a gamma correction of 0.8 applied in MATLAB to the blue band was determined to provide optimal visual contrast (Eq. 2.14). Whilst this *in situ* dataset nominally had global coverage, the upper 90<sup>th</sup> percentile range was selected to provide the best visual results for the Norwegian Sea images. Therefore, this range may need alteration depending on the selected study region. For example, in clear Case 1 waters, it is likely that the 443 nm and 488 nm wavebands would have high reflectance relative to the Norwegian Sea and would exceed the ranges applied in this study. Further, a lower limit of 0 is likely to be too low for satisfactory visual representation in Case 1 waters, where blue reflectance is unlikely to fall to these values. Whilst this range was determined to be visually optimal for the Norwegian Sea, it may need alteration if applied to optically clear, Case 1 waters.

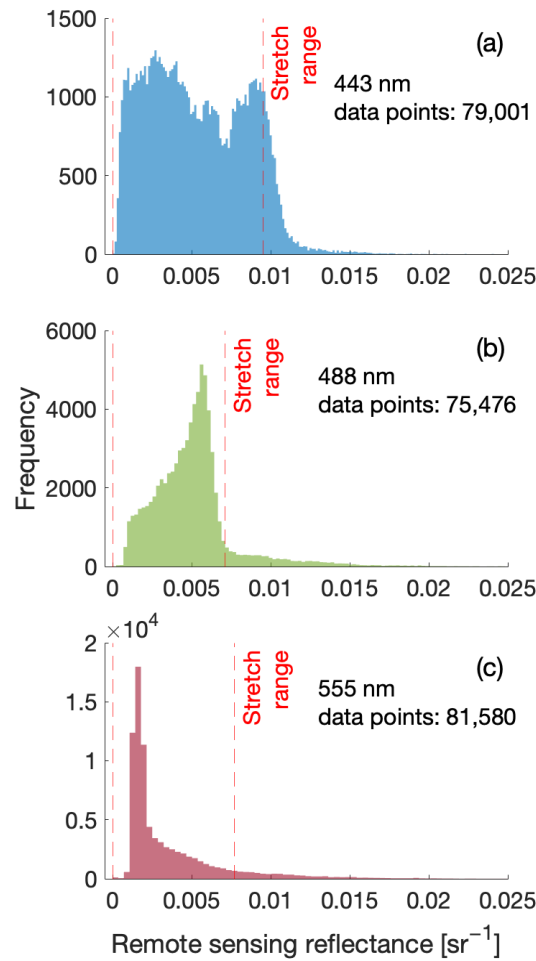


Figure 3.3 Data distribution of remote sensing reflectance ( $R_{rs}$ ) values for (a)  $443 \text{ nm} \pm 5 \text{ nm}$  (b)  $488 \text{ nm} \pm 5 \text{ nm}$  (c) and  $555 \text{ nm} \pm 5 \text{ nm}$  from the global bio-optical dataset collated by Valente et al. (2022). The red dashed lines denote the lower limit of 0 and the upper limit of the 90th percentile of each band. These ranges informed the contrast stretch applied to standardise the eRGB imagery used in this study.

Once the optimal ranges were determined and applied to the images using Eq. 2.13, the visual inconsistency between the images was largely removed (Figure 3.4). This essentially removed variance due to the processing method applied, and allowed for the derivation of more quantitative information, including the identification of persistent optical features of interest. From the re-processed sub-scene from 29<sup>th</sup> April 2017, there is still evidence of a red patch, which required further

analysis. For this, three regions of interest (ROIs) were identified for analysis. These three regions represent an area inside the suspected patch of *C. finmarchicus*, as well as an offshore region and a coastal area (Figure 3.4 c).

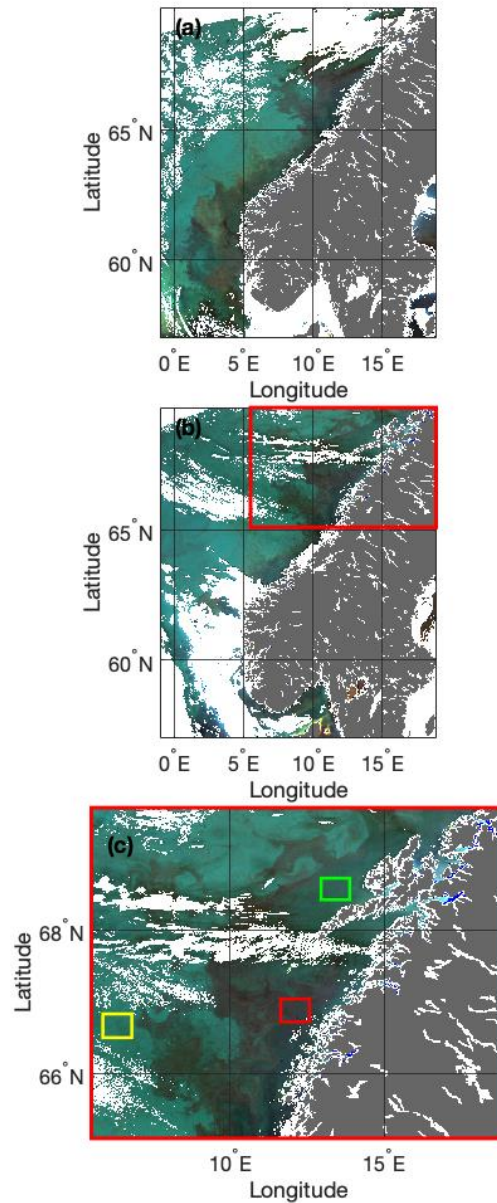


Figure 3.4 MODIS enhanced RGB images of the Norwegian Sea from (a) the 28 April and (b,c) 29 April 2017. These images were processed with the 443 nm, 488 nm and 555 nm remote sensing reflectance data, and each waveband was stretched using a standardised range developed in this study. Three regions of interest are identified in (c): within the patch (red), coastal (green) and offshore (yellow).

### 3.3 eRGB colour simulation

Once a meaningful eRGB colour space was established, it became possible to investigate the impacts of different optically important constituents on eRGB colour values. To facilitate this, a total of 1008 unique  $R_{rs}$  spectra were generated by varying constituent concentration combinations of a standard bio-optical model (CHL, MSS and CDOM). These were then converted into their associated standardised eRGB coordinates. Simulated  $R_{rs}$  values at wavelengths 442 nm, 488 nm and 554 nm (following the MODIS eRGB image processing method described above) were extracted and converted to eRGB coordinates using Eq. 2.13, with the standardised range applied. A gamma correction of 0.8 was also applied to the blue channel as per Eq. 2.14. Some of the RGB coordinates derived from the simulated spectra exceeded the standard 0–1 range of the RGB colour space. This is because the highest constituent concentrations simulated are likely not represented by the 0–90th percentile range of the *in situ* dataset. For these coordinates, minimum–maximum normalisation was applied.

From this, a look-up table (LUT) of eRGB colours associated with the standard bio-optical model was generated. Figure 3.5 shows the impact of varying each of these constituents in isolation on both the spectra and the associated eRGB colour value. It is evident from Figure 3.5a that high CHL concentrations alone ( $>10 \text{ mg m}^{-3}$ ) produce red hues in this colour space, through reduced blue reflectance and increased green/red reflectance. This is likely because the ‘red’ waveband used to create these images is actually a green waveband (555 nm). As a result, large phytoplankton blooms may produce red pixels in images such as the ones in the study.

Furthermore, the addition of high concentrations of MSS ( $>5 \text{ g m}^{-3}$ ) increases reflectance across the spectrum, especially in the green/red, and produces orange hues (Figure 3.5c). Conversely, CDOM acts to suppress reflectance across the spectrum, resulting in dark, brown/black hues at high concentrations (Figure 3.5b). CDOM acts differently to the other two standard constituents as it is considered dissolved and, therefore, does not scatter light.

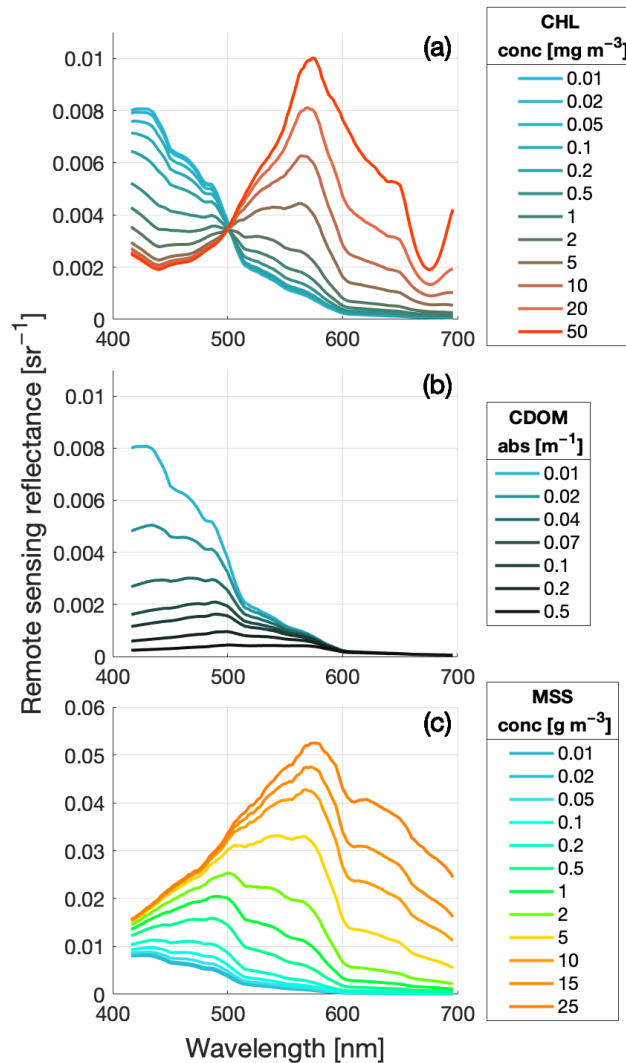


Figure 3.5 Simulated remote sensing reflectance ( $R_{rs}$ ) spectra with (a) increasing chlorophyll (CHL), (b) coloured dissolved organic matter (CDOM), and (c) material suspended sediment (MSS) concentrations. CDOM concentrations are defined by its absorption at 440 nm. Each spectrum is coloured using its associated eRGB colour coordinate.

### 3.4 Quantification of perceived colour difference

One of the objectives of this work was to determine if the of contribution zooplankton to ocean colour signals was visually identifiable. Therefore, in order to quantify perceived difference in eRGB colour co-ordinates, the International

Commission on Illumination (CIE) Delta E 2000 ( $\Delta E_{2000}$ ) metric was utilised. This metric quantifies the visual similarity between two different coordinates in the  $L^*a^*b$  (LAB) colour space, with higher  $\Delta E_{2000}$  values signalling more visually different colours. The LAB colour space is a three dimensional colour space defined by CIE in 1976. Similar to RGB, a LAB colour is defined by three co-ordinates, however instead of representing a red, green and blue value, the LAB co-ordinates represent a lightness value ( $L^*$ ) and two chromacity values ( $a^*$  and  $b^*$ ). A positive  $a^*$  indicates colours in the red direction, a negative  $a^*$  indicates colours in the green, whereas a positive  $b^*$  indicates colours in the yellow direction and a negative  $b^*$  indicates colours in the blue. The first  $\Delta E$  colour difference algorithm developed was  $\Delta E_{1976}$ , which provided a difference value derived from the Euclidian distance between two coordinates in the  $L^*a^*b$  colour space. However, this does not take into account the perceptual non-uniformity of the human eye response to colour, especially with highly saturated colour values. Thus, the newer iterations of the algorithm include weighting factors for lightness, chroma and hue value, which are all important when considering visual perception. The  $\Delta E_{2000}$  algorithm is the most sophisticated and accurate adaptation of  $\Delta E$  to date, providing significant improvements to the lightness calculation, and enhancing performance for the blue and grey colours (Luo et al., 2001). This is of potential importance for images of clear blue, Case 1 waters.

The MATLAB function 'imcolordiff' from the image processing toolbox was used to implement this algorithm. This function first converts RGB colour co-ordinates to their associated  $L^*a^*b$  co-ordinates using the function 'rgb2lab'. The  $\Delta E_{2000}$  algorithm is then applied to the co-ordinates following the formulae described in the implementation document by Sharma et al. (2005). The output is a  $\Delta E_{2000}$  value from 0 to 100, with 0 being no visual difference between the two input colours and 100 signifying colours that are opposite on the colour wheel. Colour difference thresholds can vary according to application, however the printing industry's  $\Delta E_{2000}$  threshold of 4 can be used as a guideline (Liu et al., 2013). Therefore, colour comparisons that yield  $\Delta E_{2000}$  values below 4 can be considered visually insignificant to the untrained eye.

### 3.5 Bio-optical anomaly detection

Each pixel in the sub-scene image was compared to the standard eRGB coordinate LUT (a total of 1008 eRGB coordinates) using the  $\Delta E_{2000}$  colour difference algorithm described in Section 3.4. This allowed for the identification of regions where the optics of the water column are not well described by the standard bio-optical model alone. For every pixel, the minimum  $\Delta E_{2000}$  value was extracted and mapped, producing an anomaly map where regions not well described by the standard bio-optical model are highlighted by relatively large minimum  $\Delta E_{2000}$  values (Figure 3.6). It is clear that the coastal and offshore ROIs have a low minimum  $\Delta E_{2000}$  relative to inside the red patch, suggesting that the red patch is not well described by the standard bio-optical model alone.

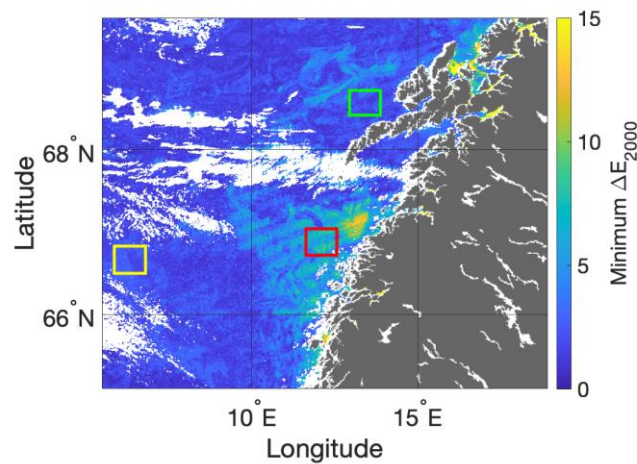


*Figure 3.6 Minimum delta E 2000 ( $\Delta E_{2000}$ ) anomaly map derived through eRGB colour matching, with the inside patch (red), coastal (green), and offshore (yellow) regions of interest depicted. Satellite eRGB pixels were compared to an eRGB look-up table (LUT) that represented the standard bio-optical model. The minimum  $\Delta E_{2000}$  derived from this comparison was extracted and mapped. Higher  $\Delta E_{2000}$  values signify a greater visual difference between the measured and modelled colour coordinates.*

The concentrations of each constituent required to produce the best  $\Delta E_{2000}$  colour matches were extracted and mapped (Figure 3.7).  $\Delta E_{2000}$  estimated CHL concentrations reached a high of  $2 \text{ mg m}^{-3}$  within the red patch (Figure 3.7a). CDOM concentrations were unexpectedly high, at  $0.2 \text{ m}^{-1}$  (absorption at 440 nm) in and around the patch (Figure 3.7b). As *in situ* measurements of CDOM during the 2017 Sea Patches cruise reached a maximum of  $0.06 \text{ m}^{-1}$ , these estimates are most likely erroneous. Finally, MSS remained broadly uniform and low throughout the region, with a median value of  $0.03 \text{ g m}^{-3}$  (Figure 3.7c).

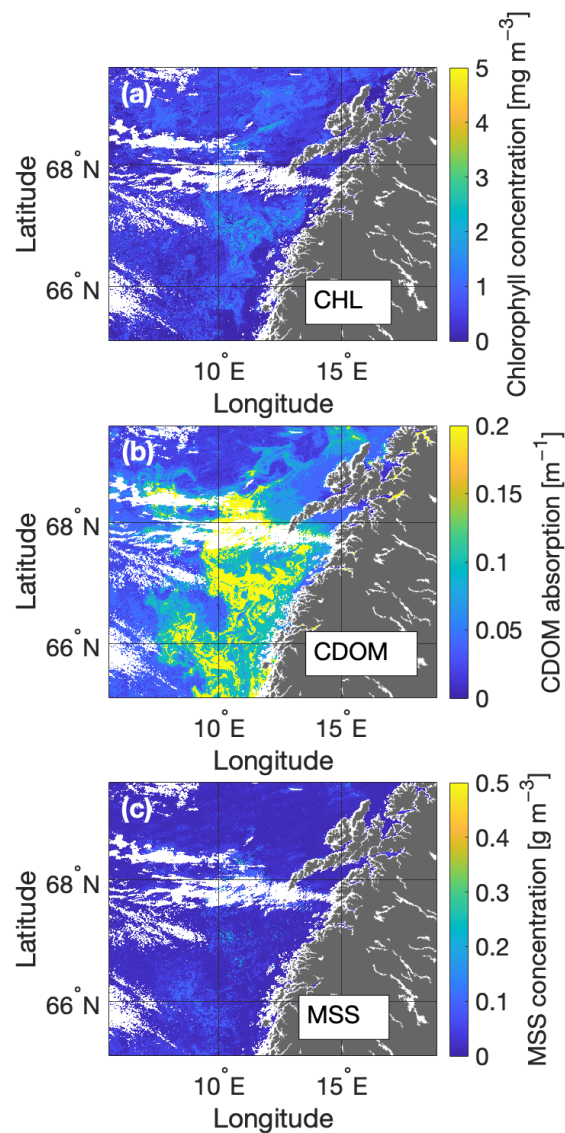


Figure 3.7 Estimated constituent concentrations derived from the delta E 2000 colour matching method using the standard case 2 bio-optical model of (a) chlorophyll (CHL), (b)

coloured dissolved organic matter (CDOM- concentrations are denoted as absorption at 440 nm), and (c) material suspended sediment (MSS). These concentrations are required to provide the best optical closure using the standard bio-optical model alone.

### 3.6 Impact of *C. finmarchicus* absorption on reflectance signals

*In situ* measurements from the Sea Patches cruise in 2017 indicated that *C. finmarchicus* were present at relatively high concentrations in the surface waters (Table 2.1) during the time period that these images were taken (Basedow et al., 2019). Further, analysis of the IOPs of the water column along with the phytoplankton assemblage indicate no other material present excluded from the standard bio-optical model (e.g. dinoflagellates) that would result in a red signal similar to *C. finmarchicus*. Therefore, *C. finmarchicus* absorption was introduced into the model to address the anomaly. The impact of *C. finmarchicus* on satellite reflectance signals was simulated in Ecolight and compared to the median satellite reflectance spectra of the three identified ROIs (Figure 3.8). Median spectra were used to represent the ROIs instead of individual pixel spectra to reduce the potential error associated with the high degree of variability in this region. For the initial spectra without the presence of *C. finmarchicus*, an MSS value of  $0.03 \text{ g m}^{-3}$  was used for all ROIs, along with the median CHL estimate derived from the satellite data ( $0.3 \text{ mg m}^{-3}$ ,  $0.6 \text{ mg m}^{-3}$ , and  $2 \text{ mg m}^{-3}$  for offshore, coastal, and inside patch ROIs, respectively). The CDOM input for the coastal and inside patch areas was set to  $0.05 \text{ m}^{-1}$ , as this was the median value obtained from *in situ* measurements in 2017 (Table 2.1). A CDOM value of  $0.04 \text{ m}^{-1}$  was used for the offshore ROI to provide the best spectral match with the median satellite spectra.

Overall, *C. finmarchicus* absorption acts to reduce  $R_{rs}$  across the blue/green part of the spectrum (from 412 nm to around 580 nm), which is a similar effect to that of CDOM (Figure 3.5b). However, the spectral absorption profile of these constituents does differ. The results also indicate that for the offshore and coastal ROIs, the spectral match is worsened and  $\Delta E_{2000}$  values increase with the addition of *C.*

*finmarchicus* (Figure 3.8a–d). Conversely, for the inside patch ROI, both the spectral shape and magnitude were improved with the addition of *C. finmarchicus*, and  $\Delta E_{2000}$  analysis indicated that 100,000 individuals  $m^{-3}$  provided the best colour match in this region (Figure 3.8e,f). This suggests that in order for optical closure to be achieved within the patch ROI, a *C. finmarchicus* component must be included within the bio-optical model.

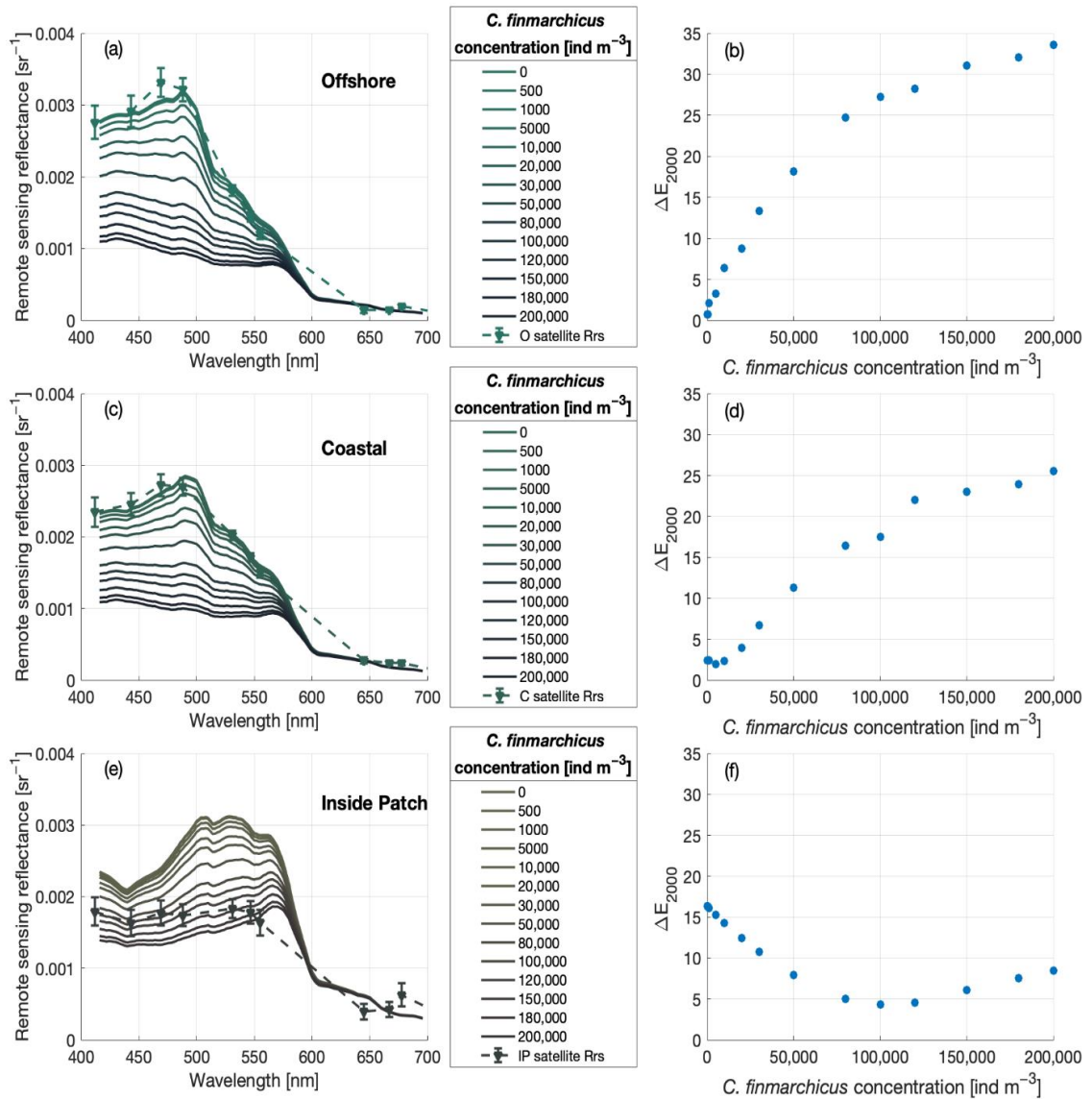


Figure 3.8 Comparison of median satellite ( $\pm 1$  standard deviation) and modelled remote sensing reflectance spectra with increasing concentrations of *Calanus finmarchicus* (a,c,e) with associated delta E 2000 ( $\Delta E_{2000}$ ) values (b,d,f) of each region of interest. The spectra are

coloured with their associated eRGB coordinates. Initial modelled spectra (without the addition of *C. finmarchicus*) were modelled using chlorophyll concentrations informed by satellite data and coloured dissolved organic matter concentrations informed by in situ measurements. An MSS value of  $0.03 \text{ gm}^{-3}$  was used across all three regions of interest to provide the best fit.

### 3.6.1 Estimating surface *C. finmarchicus* concentrations from eRGB imagery

To provide an estimate of patch extent and surface concentrations, *C. finmarchicus* were added as a varying constituent to the model. To facilitate this and reduce computation time, MSS concentrations were set to  $0.03 \text{ g m}^{-3}$ , as MSS appears to remain low and relatively stable in this region (Figure 3.7c). As a result, a new RGB LUT with a total of 1176 unique constituent concentration combinations was created. The new anomaly map shows a much lower minimum  $\Delta E_{2000}$  across the entire image, especially for the inside patch ROI (Figure 3.9a). Furthermore, anomaly remains low in the coastal and offshore ROIs. Thus, the lack of *C. finmarchicus* absorption in the original model potentially accounts for a large amount of the anomaly present in the image, especially within the red patch. Although still high, estimated concentrations of CDOM have been significantly reduced with the addition of *C. finmarchicus* absorption (Figure 3.9b). Notably, within the red patch where CDOM concentrations have significantly reduced, concentrations of *C. finmarchicus* appear to be high (Figure 3.9c). Surface concentration estimates of the copepod in this patch range from 80 to 150,000 individuals  $\text{m}^{-3}$ , with maximum values reaching 200,000 individuals  $\text{m}^{-3}$ .

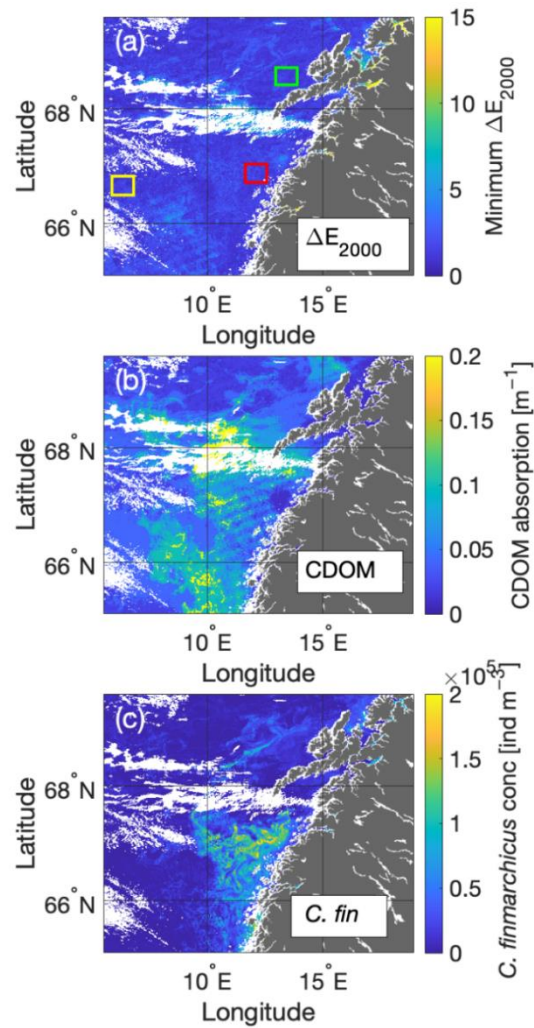


Figure 3.9 (a) Minimum delta E 2000 ( $\Delta E_{2000}$ ) anomaly maps derived through eRGB colour matching with the inside patch (red), coastal (green), and offshore (grey) regions of interest are depicted. Satellite eRGB pixels were compared to an eRGB look-up table (LUT) that represented the standard bio-optical model, with *Calanus finmarchicus* absorption added as well. The minimum  $\Delta E_{2000}$  derived from this comparison was extracted and mapped. (b) An estimation of CDOM concentrations (CDOM concentrations are denoted as absorption at 440 nm) and (c) surface concentrations of *C. finmarchicus* produced using the identified minimum  $\Delta E_{2000}$  value for each pixel in the image (concentrations are expressed as individuals  $m^{-3}$ ).

These concentrations are an order of magnitude greater than those measured using nets in the 2017 Sea Patches cruise, during which the maximum reached was

16,000 individuals  $\text{m}^{-3}$  at the surface (Table 2.1). There are two potential reasons for this apparent mismatch. Firstly, the zooplankton abundance estimates during the 2017 Sea Patches cruise were derived from Multinet samples, which sample the surface 5 m of the water column. Abundances are calculated over the surface 5 m, however it is not possible to tell where in the water column these organisms were distributed. If they were concentrated in the surface metre for example, surface abundances would be 80,000 individuals  $\text{m}^{-3}$ , which correlates more closely with the concentration maps derived from satellite data.

Another possible reason for the mismatch between satellite concentration estimates and *in situ* samples is animal evasion. Traditional zooplankton sampling techniques (i.e. net sampling or trawls) are invasive and likely disturb the community that they are attempting to sample. Unlike phytoplankton, *C. finmarchicus* have the ability to swim, and as a result may evade capture. A recent study conducted on fish and zooplankton populations in the Arctic during polar night found that a normal working-light from a ship could disrupt populations down to 200 m depth and up to 0.125  $\text{km}^2$  around the ship (Berge et al., 2020). Although data collected during the polar night are not directly transferable to the northern Norwegian sea in spring (ca. 20 hours daylight end of April), this study highlights the sensitivity of these organisms to disturbances. Therefore, the possibility that ship engine noise and disturbance from net sampling will also result in animal evasion must be considered. In fact, a recent study by Bandara et al. (2022) conducted in the Norwegian Sea found concentrations of up to 165,000 individuals  $\text{m}^{-3}$  of *C. finmarchicus* at 10 m depth. This study collected high frequency acoustic data in 2018 by means of a silent autonomous surface glider (Sailbuoy). This far less invasive method of data collection is likely to cause much lower disturbance to animal behaviour and has potential to therefore return more accurate results. Taken together, all of these results point to a potential problem with under-estimation of population densities for these mobile copepods using traditional ship-board sampling techniques, which could have significant implications for both management strategies and ecological modelling.

It is important to note that satellite data only has the ability to resolve surface populations of *C. finmarchicus*, and no information on populations at significant depths can be retrieved. The optical depth is primarily determined by the constituents in the water column and is typically between 5-10 m. Whilst we cannot resolve populations at depth, these results are useful for providing a non-invasive method to identify and quantify surface populations, as well as track the spatio-temporal variation of these large-scale features. Additionally, the optical characterisation of *C. finmarchicus* in this study is limited to absorption alone, as no data is currently available on backscattering effects. Whilst Davies et al. (2021) theoretically demonstrated that the impact of larger millimetre sized particles on backscattering is likely to be negligible, it may still impact satellite reflectance signals to an unknown degree. Thus, future work is required to better understand the optical properties of these organisms.

The addition of *C. finmarchicus* absorption, especially within the identified patch, significantly improved the CDOM concentration estimates (Figure 3.9). This highlights the importance of looking at not just the anomaly maps, but also the constituent concentrations providing the best match up. Further, knowledge of the typical concentrations of CDOM within the region of study is useful. In this case, *in situ* measurements of CDOM made during the Sea Patches cruise allowed for the identification of erroneously high estimates. Although it is clear that this method has the ability to discern somewhat between CDOM and *C. finmarchicus*, it is possible that there is still a degree of underestimation of *C. finmarchicus* populations due to limited ability to distinguish their optical signal from that of CDOM using only three wavebands.

### 3.7 Impact of *C. finmarchicus* absorption on OC3M algorithm performance

When the colour matching technique is applied with *C. finmarchicus* included, the  $\Delta E_{2000}$  CHL estimates increased (Figure 3.10a) compared to that produced by the standard bio-optical model (Figure 3.7a). However, estimates are generally lower

than the standard MODIS 'chlor\_a' product generated using the OCI algorithm (Figure 3.10b). For the inside patch ROI, the median CHL value predicted from the  $\Delta E_{2000}$  method is  $1 \text{ mg m}^{-3}$ , whereas the satellite CHL product predicts a median value of  $2 \text{ mg m}^{-3}$ . Furthermore, OCI predicts maximum values of  $5 \text{ mg m}^{-3}$  within the red patch, whereas these maximum values are much less frequently reached using the  $\Delta E_{2000}$  approach.

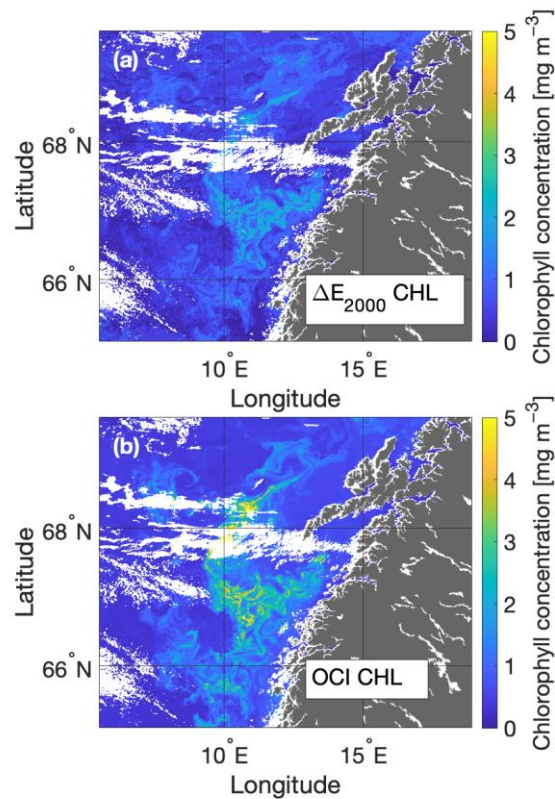


Figure 3.10 Comparison estimates of chlorophyll derived from (a) the minimum delta E 2000 ( $\Delta E_{2000}$ ) colour matching technique and (b) the MODIS standard chlorophyll product calculated using the OC3M algorithm.

In order to investigate the impact of *C. finmarchicus* absorption on MODIS' CHL retrievals, simulated spectra from each ROI with increasing *C. finmarchicus* concentrations were put through OC3M (Eq. 2.10 and 2.11). The impact of *C. finmarchicus* on OC3M specifically was tested as these copepods graze on phytoplankton and are, therefore, likely to be found at the surface when

concentrations of CHL are greater than  $0.35 \text{ mg m}^{-3}$  (for example, during the spring bloom) (Falk-Petersen et al., 2009; Madsen et al., 2008).

The results indicate that across all three ROIs, increasing *C. finmarchicus* concentrations lead to an increase in CHL estimates, despite the modelled CHL remaining constant during the simulations (Figure 3.11). Estimates of CHL in the coastal and offshore ROIs more than doubled with the addition of 200,000 individuals  $\text{m}^{-3}$ . Within the patch ROI, estimates increased by  $1 \text{ mg m}^{-3}$ . This explains the lower CHL values predicted through the  $\Delta E_{2000}$  method relative to the standard satellite CHL product. *C. finmarchicus* absorbs strongly in the blue part of the spectrum and peaks at around 480 nm (Figure 2d). As the OC3M algorithm relies on the ratio of the blue (443 nm or 488 nm band depending on water type) to green (547 nm) bands to estimate chlorophyll (Eq. 2.8, 2.9 and 2.10), greater reflectance in the green relative to the blue will lead to an overestimation in CHL concentrations. This is important to consider in regions where surface *C. finmarchicus* populations are significant.

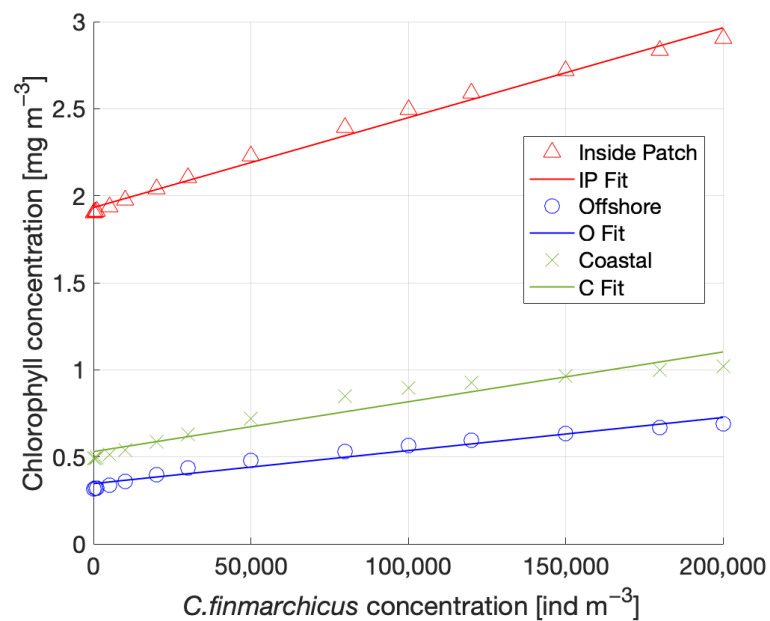


Figure 3.11 Impact of increasing *Calanus finmarchicus* concentrations on the MODIS OC3M chlorophyll algorithm output from the inside patch (red triangle), offshore (blue circle), and coastal (green cross) ROIs.

### 3.8 Application of the colour matching method to the Gulf of Maine

The  $\Delta E_{2000}$  method was applied to an image from the Gulf of Maine (GoM) to test its performance in a more optically complex environment. This provided a 'proof of concept' test, and whilst no *in situ* validation data is available for this image, previous modelling studies on *C. finmarchicus* habitat suitability helped to inform interpretation (Ross et al., 2023).

The GoM was chosen as a test location because this region is known to be an important feeding ground for the critically endangered North Atlantic right whale (*Eubalaena glacialis*). These organisms feed on *C. finmarchicus*, and even appear to select their feeding grounds based on whether copepod abundance reaches a critical feeding threshold (Kenney & Wishner, 1995). Therefore, both their population density and distributions are closely tied to that of *C. finmarchicus*. In 2010, the GoM underwent an unprecedented regime shift, where climate-driven changes to the Gulf Stream, resulted in warm slope waters entering the region and producing a less favourable habitat for *C. finmarchicus*. This led to a northward shift in foraging grounds for *E. glacialis*, which resulted in increased mortality risk from ship-strikes and fishing gear entanglement (Meyer-Gutbrod et al., 2021). Current management strategies for the preservation of *E. glacialis* rely on forecasting models to predict foraging areas, and therefore being able to remotely resolve and monitor surface populations of these organisms would be invaluable for informing these predictive models.

A cloud free MODIS Aqua scene of the GoM from 17<sup>th</sup> June 2009 was downloaded at level 1 and processed to level 2 following the general method described in Section 2.4. Following this, a standardised eRGB image was generated using the method described in Section 3.2 (Figure 3.12a). From this image, it is clear that the region has a significant amount of optical complexity, spanning from the Case 2 waters of the Bay of Fundy to clear blue Case 1 waters in the south of the scene. This provides a test for algorithm performance and allows for the identification of any potential issues for algorithm development.

Before the  $\Delta E_{2000}$  method was applied to this image, spectral quality control was conducted. Following the same method as applied to the Norwegian Sea image, all spectra with a negative value are removed from analysis. As evident from the resulting  $\Delta E_{2000}$  anomaly map of the region (Figure 3.12b), this removes a large amount of data along the coast, including the entirety of the Bay of Fundy. This is likely the result of poor AC in these optically complex Case 2 waters, leading to an overcorrection of spectra in this region.

When the  $\Delta E_{2000}$  method was applied to the remaining pixels available, two patches of anomaly become evident, one south of Nova Scotia (reaching  $\Delta E_{2000}$  values of 10) and some anomaly associated with the Georges Bank (Figure 3.12b). It is important to consider that the Georges Bank is a shallow submarine plateau between 3- 150 m depth. In this region, standard AC may fail due to increased reflectance signals as a result of an increase in turbidity, suspension of particles from the elevated seafloor, or a bottom reflectance feature. Whilst no spectra are being flagged as negative in this region, it is possible that there is a persistent issue with AC on the Georges Bank. However, the feature off the coast of Nova Scotia and that on Georges Bank also correlate with regions where dense aggregations of *C. finmarchicus* are expected at this time of year and fall into the regions of critical habitat in the Gulf of Maine (Ross et al., 2023).

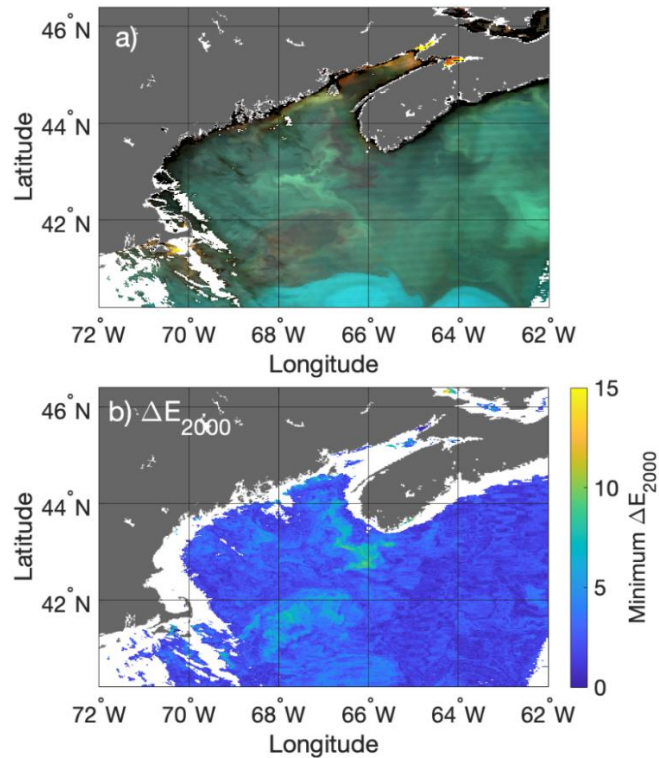


Figure 3.12 (a) MODIS enhanced RGB image and (b) Minimum delta E 2000 ( $\Delta E_{2000}$ ) anomaly map derived through eRGB colour matching of the Gulf of Maine from 17<sup>th</sup> June 2009. The eRGB image was processed with the 443 nm, 488 nm and 555 nm waveband and stretched using the standardised range developed in this study. For anomaly identification, satellite eRGB pixels were compared to an eRGB look-up table (LUT) that represented the standard bio-optical model. The minimum  $\Delta E_{2000}$  derived from this comparison was extracted and mapped.

When applying the Case 2 model with the addition of *C. finmarchicus*, the MSS value needs to vary in order to capture the optical complexity within the Gulf of Maine. Therefore, a new LUT was devised with CHL varying from 0.01-5 mg m<sup>-3</sup>, CDOM values of 0.01-0.5 m<sup>-1</sup> (absorption at 440 nm) and MSS values of 0.01-1 g m<sup>-3</sup>, with a total of 4410 unique constituent concentration combinations. CHL values were constrained to reduce the processing power required.

The newly generated  $\Delta E_{2000}$  map shows a significant reduction in anomaly, especially within the Georges Bank and south Nova Scotia patches (Figure 3.13a). This

reduction coincides with high surface concentrations of *C. finmarchicus* (Figure 3.13b). In both these potential patches, estimated *C. finmarchicus* concentrations are between the range of 60000-100000 ind m<sup>-3</sup>. These patches spatially correlate with projections of high density *C. finmarchicus* patches in the GoM in June, which were modelled using data from the National Oceanic and Atmospheric Administration (NOAA) Fisheries Ecosystem Monitoring Program (Ross et al., 2023). Interestingly, there is an artefact in the centre of the image that appears to be erroneously associated with high *C. finmarchicus* concentrations. This actually appears to correlate with a milky white feature on the eRGB image (Figure 3.12a), possibly associated with a coccolithophore bloom, which are common in the Gulf of Maine at this time of year (Balch et al., 1991). However, it is not currently possible to resolve the impact of coccolithophores on ocean colour signals, as coccolithophore IOP measurements have not been conducted.

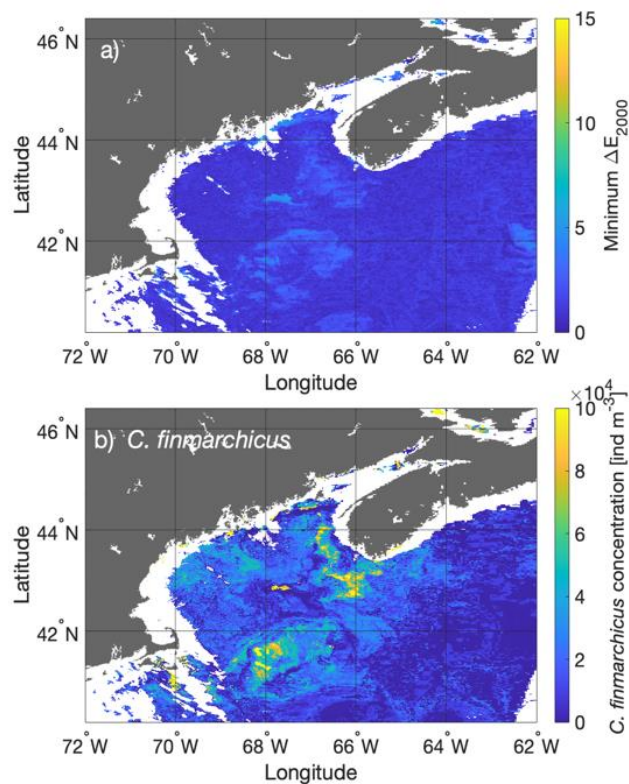


Figure 3.13 (a) Minimum delta e 2000 ( $\Delta E_{2000}$ ) and estimated (b) *C. finmarchicus* concentrations derived through eRGB colour matching of the Gulf of Maine from 17<sup>th</sup> June

2009. For anomaly identification, satellite *eRGB* pixels were compared to an *eRGB* look-up table (LUT) that represented the standard bio-optical model with the addition of *C. finmarchicus* absorption. The minimum  $\Delta E_{2000}$  derived from this comparison and the *C. finmarchicus* concentrations required to reach that minimum were extracted and mapped.

A comparison of the constituent concentrations required to reach the minimum  $\Delta E_{2000}$  in both the full Case 2 and Case 2 with the addition of *C. finmarchicus* is presented in Figure 3.14. Similar to the Norwegian sea estimates, CHL concentrations appear to broadly correlate with presence of *C. finmarchicus* (Figure 3.14a, b), and high CDOM estimates are reduced with the addition of the copepod, especially within the patches (Figure 3.14c, d). Interestingly, the milky white patch within the middle of the Gulf of Maine image is initially attributed to higher MSS concentrations relative to surrounding waters (Figure 3.14e). This is potentially erroneous, as it is unlikely that there would be increased sediment in the middle of the Gulf of Maine. It is more plausible that this feature can be attributed to coccolithophores, however in the absence of coccolithophore IOP data within the model, it is incorrectly attributing the signal to MSS. With the addition of *C. finmarchicus* absorption, MSS estimates rise across the entire image (Figure 3.14f). It is important to note that whilst the constituent concentrations appear to be reasonable, there is currently no *in situ* data to validate these estimates.

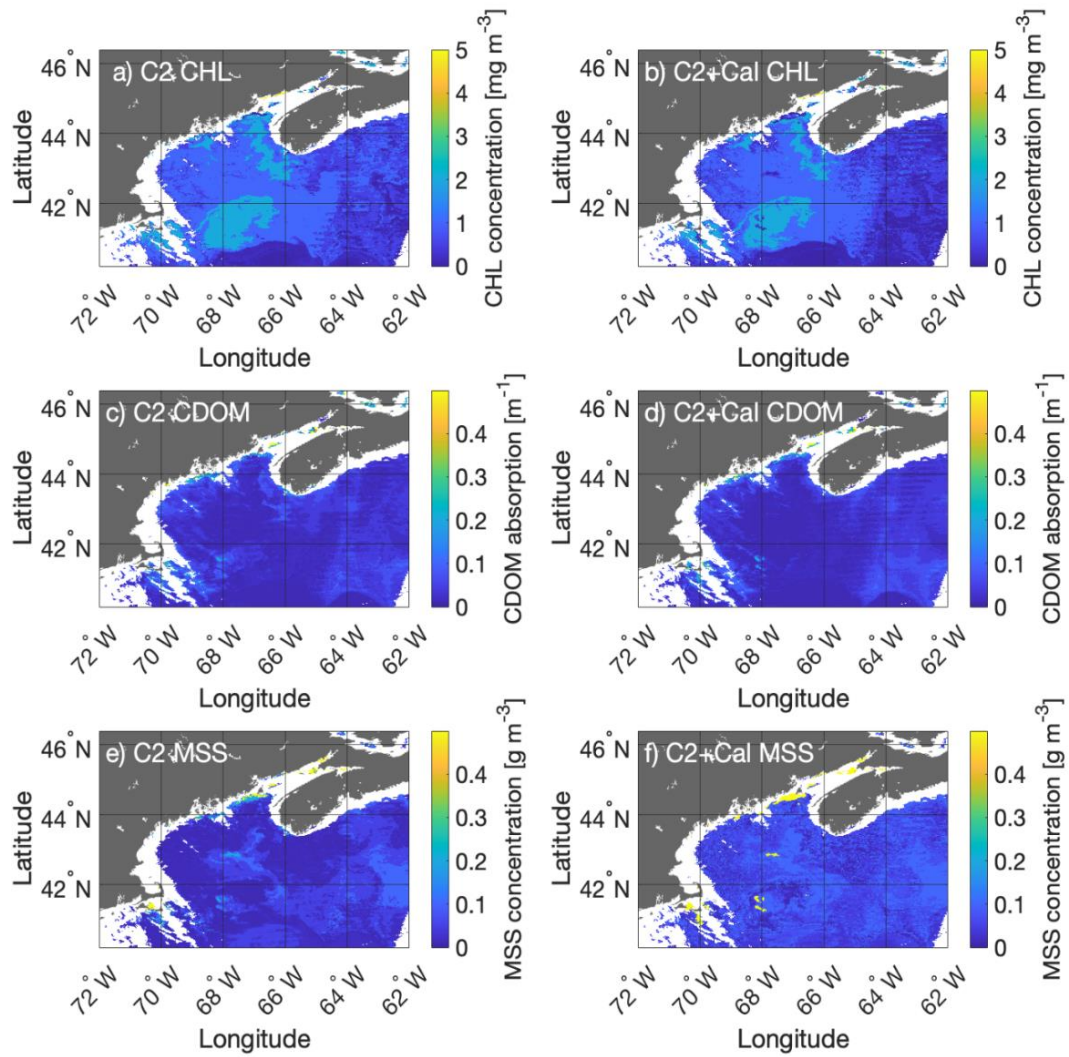


Figure 3.14 Estimated constituent concentrations required to reach minimum delta  $e$  2000 ( $\Delta E_{2000}$ ) values with (a,c,e) the full Case 2 model and (b,d,f) the case two model with the addition of *C. finmarchicus* absorption. Estimates are derived from the  $\Delta E_{2000}$  colour matching technique.

### 3.9 Conclusions

This chapter demonstrated, through the use of a novel eRGB colour matching technique, the ability to identify and characterise dense surface aggregations of the zooplankton species *C. finmarchicus* in the northern Norwegian Sea from satellite

derived ocean colour imagery. The use of eRGB coordinates and minimum  $\Delta E_{2000}$  as a method of anomaly detection allows for greater understanding of how these features present in RGB imagery. In the case of *C. finmarchicus* specifically, eRGB coordinates resolve the impact of these organisms well, as the 488 nm waveband is used, which corresponds with their absorption peak of 480 nm. In a wider context, this method can be generally applied to identify regions or features that deviate from the standard bio-optical model. This could be a valuable tool to support targeted sampling efforts for optically complex regions.

Concentration estimates of *C. finmarchicus* derived from the patch in the northern Norwegian Sea were an order of magnitude greater than those measured *in situ*, which points to a potential animal evasion issue, due to the invasive nature of traditional ship-based techniques. This could lead to significant population underestimations, and therefore more work is required both to characterize potential evasion behaviour, as well as develop less invasive sampling methods that will reduce population disturbance for ground truthing.

The results in this chapter indicate that *C. finmarchicus* and CDOM appears to have a similar effect on  $R_{rs}$  signals. Whilst it is clear that this method has the ability to discern somewhat between CDOM and *C. finmarchicus*, it is possible that there is still a degree of underestimation of *C. finmarchicus* populations due to limited ability to distinguish their optical signal from that of CDOM using only three wavebands. A potential solution to this is a spectral matching approach using more or even all of the current multispectral data available, extendable in the future to hyperspectral data. The use of more of the spectral information available may aid in resolving finer scale optical features such as this and will form the subject of further work in this area. This possibility will be explored more in Chapter 5.

This chapter also presented a 'proof of concept' study for the  $\Delta E_{2000}$  method in the Gulf of Maine (GoM), a critical habitat for *C. finmarchicus*. The GoM image provided a good test for the algorithm as it spans a larger geographical area and contains significantly more optical complexity than that of the northern Norwegian Sea. The resulting *C. finmarchicus* concentration estimates derived from an image

taken on the 17<sup>th</sup> June 2009 broadly correlate with previously modelled distributions in this region in June. However, there is an interesting artefact in the centre of the GoM image that was erroneously attributed to high *C. finmarchicus* concentrations. This feature appears to be milky-white in colour and is more likely the result of a coccolithophore bloom, which are common in this region at this time of year. However, without the appropriate IOP data for coccolithophores, this hypothesis cannot be tested. This, along with *in situ* constituent concentration measurements, will form the foundation of future work in the region.

Critically, the GoM image highlighted the issues surrounding appropriate AC procedures for data that spans both Case 1 and Case 2 waters. When all spectra with negative values were flagged and removed, this eliminated a lot of coastal data, including the entirety of the Bay of Fundy. Whilst it is easy to flag pixels where AC has obviously failed, it does not allow for the identification of poorly applied AC that has not resulted in negative reflectance values. This is a significant issue when applying a spectral matching technique that relies on high quality  $R_{rs}$  data in order to obtain accurate constituent estimates. This is a problem that will be addressed in the following chapter of this thesis.

## 4 A per -pixel approach to atmospheric correction implementation using a Case 2 spectral matching technique

### 4.1 Introduction

The use of a colour / spectral matching technique to identify in- water anomalies (and indeed any bio-optical modelling method) is reliant on high quality  $R_{rs}$  data. The quality of  $R_{rs}$  data is heavily dependent on the selection of an appropriate atmospheric correction (AC) method for the environment being studied. For example, in optically clear Case 1 waters (open ocean), a standard AC procedure that builds on the assumption of zero water-leaving radiance ( $L_w$ ) in the NIR (the black pixel assumption) (Gordon, 1978; Gordon & Wang, 1994) may be suitable. However, in optically complex Case 2 (coastal) waters, this assumption breaks down due to increased riverine sediment input and turbidity. Many specialised AC algorithms have been developed for this purpose, including the modified NIR correction model that assumes homogeneity of the aerosol reflectance and  $L_w$  in the NIR bands (MUMM) (Ruddick et al., 2000). However, this algorithm can only be applied to a small- scale region of interest, due to the assumption of homogenous aerosol reflectance.

The Gulf of Maine (GoM) image from 17<sup>th</sup> June 2009, which was processed in the previous chapter, is an example of an optically complex region. The swath spans both coastal waters and clear open ocean and as a result presents a challenge for appropriate AC selection. As apparent from the previous chapter, the use of the NASA standard AC method leads to negative reflectance spectra along the coast and in the Bay of Fundy. However, the blanket application of a coastal AC method like MUMM is likely to overcorrect and result in erroneous spectra in the optically clear regions of the image.

An obvious solution to this is to select regions where standard AC fails and it is appropriate to apply a Case 2 specific algorithm. However, it can be a challenge to identify poor quality spectra beyond those that have negative values. There are methods for assessing the data quality of a water spectrum, including work by Wei et al. (2016) that provided a means of scoring a spectrum based on 23 different simulated water types, and the quality water index polynomial (QWIP) method (Dierssen et al., 2022), which is calculated using apparent visible wavelength (AVW). Whilst these methods provide an indicator of spectral quality, they are implemented solely to flag poor quality pixels to be removed from analysis altogether.

This chapter describes a new method to address these issues that not only identifies anomalies, but also uses these anomaly measures to select an optimal AC solution for each pixel. This method has the advantage of reducing the amount of data removed due to AC failure and allowing for constituent retrievals in coastal regions, where accurate estimations were previously not possible. In order to achieve this, a spectral matching approach was developed using all spectral information available between 412 nm and 645 nm (a total of 8 wavebands). This approach uses a standard Case 2 spectral LUT to compare to the image processed with several AC variants. In this study, the NASA standard AC (Bailey et al., 2010) and several variants of the MUMM AC with different aerosol reflectance ratios ( $\epsilon_m$ ) were used. The  $\epsilon_m$  parameter represents the multiple scattering aerosol reflectance ratio at 748 nm and 869 nm and is used to select the most appropriate aerosol optical model from a number of candidate models, which correspond to typical aerosol particle size distributions and discrete values of relative humidity (Ahmad et al., 2010). Once the appropriate model is determined, it is used to extrapolate the relative contribution of aerosols from the NIR to the shorter visible wavebands. The optimal AC for each pixel is determined by minimising divergence between the corrected satellite data and the range of simulated reflectance spectra in the LUT.

The per-pixel AC approach is implemented through the following:

1. The satellite data is processed several times, each with a different AC method applied.

2. For each AC iteration, the image is compared to a spectral look-up table (LUT) of simulated reflectance spectra representing a standard bio-optical model. The minimum difference value for each pixel is calculated, with corresponding optical constituent concentrations noted.
3. The minimum difference for each AC is compared on a per-pixel basis, with the smallest value indicating the optimal AC for that pixel, and simultaneously providing best estimate of optical constituent concentrations.

This approach to AC seeks to remove a large amount of anomaly associated with poor quality data. This is a crucial step in the development of an anomaly detection method to identify and characterise surface swarms of *C. finmarchicus* in optically complex waters, as it ensures analysis is being conducted on good quality spectral data. Thus, any remaining anomalies are more likely to be associated with in-water features that are not well characterised by a standard bio-optical model. This AC procedure will therefore be employed before the development of any spectral matching approach in future work on optically complex regions.

#### 4.2 The Gulf of Maine test image

The GoM MODIS image from the 17<sup>th</sup> June 2009 previously presented in Section 3.8 is used as the test image for this chapter. This image has a significant amount of optical complexity, from the coastal environment of the Bay of Fundy, out to optically clear open water at the southern edge. To test this method, pixels from three regions of interest (ROIs) were identified from the GoM image (Figure 4.1) that represented a coastal, in patch and open water region. The 'in patch' ROI includes the potential patch of *C. finmarchicus* that was identified by the application of the  $\Delta E_{2000}$  method to the image in the previous chapter. Individual spectra were extracted to represent the ROIs instead of an averaged area in order to investigate the performance of the algorithms on a per-pixel basis.

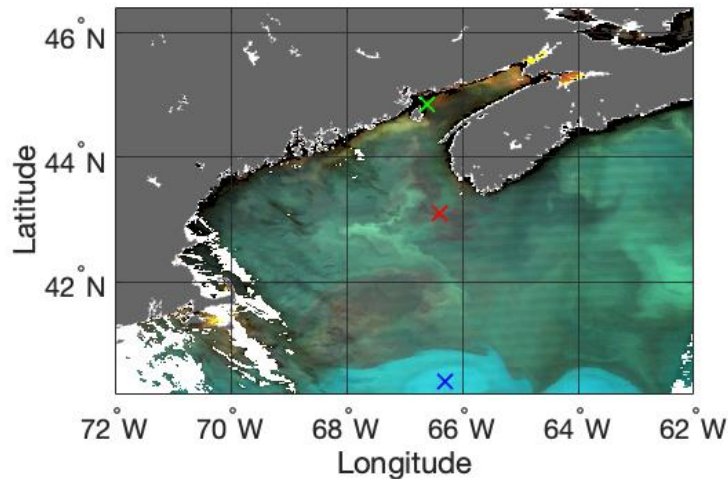


Figure 4.1 Standardised MODIS eRGB image from the 17<sup>th</sup> June 2009. The location of spectra used in analysis from the coastal (green), inside potential patch of *C. finmarchicus* (red) and open water (blue) regions of interest are denoted with a cross.

#### 4.3 Selection of an appropriate spectral matching technique

Many spectral matching metrics exist to quantify the similarity between a test spectrum and a reference spectrum. In order to ascertain the most suitable method to use for this application, two well established algorithms were tested on the GoM image. The LUT developed in the previous chapter from spectra simulated in Ecolight was modified to include  $R_{rs}$  spectra (instead of eRGB co-ordinates) with the 412 nm, 443 nm, 469 nm, 488 nm, 531 nm, 547 nm, 555 nm and 645 nm bands. This LUT contained a total of 1008 spectra, each with different CHL, MSS and CDOM concentration combinations, thus representing a standard Case 2 bio-optical model (constituent concentration specifications can be found in Section 2.3). The  $R_{rs}$  spectra for each pixel in the GoM image was compared to this Case 2 spectral LUT using the following spectral matching techniques.

The first algorithm applied was the widely used spectral information divergence (SID) algorithm, which calculates the statistical divergence to derive the similarity between reference spectra (i.e. LUT spectra) and test spectra (pixel spectra). It considers each pixel as a random variable and uses its spectral histogram to define

a probability distribution. The spectral similarity is a measure of the discrepancy of probabilistic behaviours between the spectra (Chang, 2000). SID was applied in MATLAB (2022b) using the Image Processing Toolbox's 'sid' function, where the SID value is calculated using the following equation:

$$SID(A, B) = \sum_{i=1}^N p_i \log\left(\frac{p_i}{q_i}\right) + \sum_{i=1}^N q_i \log\left(\frac{q_i}{p_i}\right) \quad (4.1)$$

where  $p_i$  and  $q_i$  are calculated as:

$$p_i = \frac{A_i}{\sum_{i=1}^N p_i} \quad (4.2a)$$

$$q_i = \frac{B_i}{\sum_{i=1}^N q_i} \quad (4.2b)$$

and  $N$  is the number of spectral intervals (in this case  $N = 8$ ).  $A$  ( $A_1, A_2, \dots, A_N$ ) and  $B$  ( $B_1, B_2, \dots, B_N$ ) denotes the reference and test spectral vectors respectively.

The second algorithm tested for suitability was the normalised spectral similarity score (NS<sup>3</sup>). NS<sup>3</sup> is an algorithm that combines the methods of Euclidean distance (or root mean square difference), which primarily measures differences in brightness or spectral magnitude (Gower, 1985) and spectral angle mapper (SAM), which is most sensitive to changes in the shape of the spectra (Kruse et al., 1993). Thus, NS<sup>3</sup> provides a measure of spectral similarity that takes into account both spectral angle and magnitude (Nidamanuri et al., 2011). NS<sup>3</sup> was also applied in MATLAB (2022b) using the Image processing toolbox's 'ns3' function, which utilise the following equations. First the Euclidean distance between two spectra is computed:

$$A_{\text{Euclidean}} = \sqrt{\frac{1}{N} \sum_{i=1}^N (t_i - r_i)^2} \quad (4.3)$$

where  $r$  and  $t$  are the reference and test spectra respectively. The SAM ( $\alpha$ ) is then calculated as:

$$\alpha = \cos^{-1} \left( \frac{\sum_{i=1}^C t_i r_i}{\sqrt{\sum_{i=1}^C t_i^2} \sqrt{\sum_{i=1}^C r_i^2}} \right) \quad (4.4)$$

Finally, the two are combined and the NS<sup>3</sup> score is computed as:

$$NS^3 = \sqrt{A_{\text{Euclidean}}^2 + (1 - \cos(\alpha))^2} \quad (4.5)$$

Both SID and NS<sup>3</sup> were primarily developed for use with hyperspectral data, where small changes in the spectral distribution could be important. However, for the coarser resolution multispectral data used in this project, small changes in spectral shape are not resolved. Therefore, a simpler approach of calculating the relative root mean square difference (RRMSD) between the reference and test spectra was also tested for suitability. This is a form of the Euclidean distance measure root mean square difference (RMSD), where the difference between the  $R_{rs}$  values being compared is scaled against the ‘actual’ value, in this case the pixel  $R_{rs}$  at each waveband interval. This removes the disproportionately large potential error associated with parts of the spectrum where overall signal is low (i.e. at the red end of the spectrum). RRMSD was calculated using the following equation:

$$RRMSD = \sqrt{\frac{\frac{1}{N} \sum_{i=1}^n (r_i - t_i)^2}{\sum_{i=1}^n (t_i)^2}} \quad (3.6)$$

where  $r$  and  $t$  represent the reference and test pixel spectra.

Spectral matching algorithms can often mathematically define a pair of spectra as nearly identical, whilst visual inspection reveals they are spectrally dissimilar. Therefore, to identify the optimal method for this application, the two best matches yielded from the inside potential patch and offshore ROI pixel spectra using SID,  $NS^3$  and RRMSD were compared (Figure 4.2). The coastal pixel spectra was excluded from this, as the 412 nm  $R_{rs}$  value is a negative number and therefore the resulting spectral match ups would be unreliable.

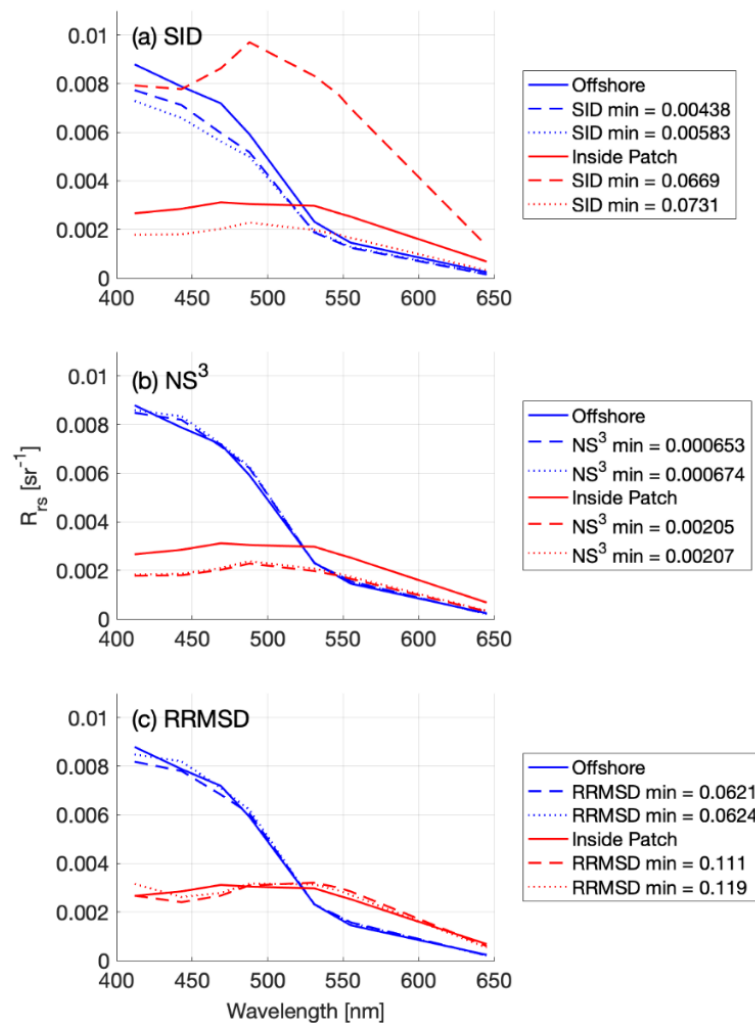


Figure 4.2 Two best spectral match ups for the inside patch (red) and offshore (blue) pixel spectra with the application of (a) spectral information divergence (SID), (b) normalised spectral similarity ( $NS^3$ ) and (c) relative root mean square difference (RRMSD).

The matchups derived from the SID algorithm (Figure 4.2a) were very visually different from the target pixel spectra, especially when compared to that of the other two methods. In particular, the mathematically closest SID match up to the inside patch spectrum was different both in terms of spectral magnitude and shape and appears to be less suitable than that of the second mathematically closest matchup derived from SID. Further, as SID is a computationally expensive method, it was excluded for this application.

The NS<sup>3</sup> algorithm performed better, especially with the open water pixel spectrum. The spectral magnitude of the two closest matchups from the inside patch spectra was smaller across the spectrum. However as this pixel is within the potential patch, it is not expected that optical closure can be achieved from a standard Case 2 bio-optical model alone. When comparing the results from NS<sup>3</sup> to RRMSD (Figure 4.2c), they appear similar, however RRMSD yielded a visually better spectral match within the potential patch, largely due to the similarity in spectral magnitude between the pixel and the matchup spectra. However, the spectral shape of the matchup spectra is dissimilar, especially in the blue/ green part of the spectrum, leading to a RRMSD value of greater than 0.1, or 10% if expressed as a percentage. Again, if this were indeed a surface aggregation of *C. finmarchicus*, some mis-match between the pixel and the standard Case 2 bio-optical model would be expected.

As both RRMSD and NS<sup>3</sup> performed similarly, and taking into consideration the fact that NS<sup>3</sup> requires a specialist MATLAB package and is more computationally expensive, the RRMSD method was chosen to perform this analysis. For the coarse spectral resolution data in this study, a method that provides matchups based on Euclidean distance, or spectral magnitude, appears optimal. However, if this method were to be applied to hyperspectral data, a method like NS<sup>3</sup> that provides equal weighting of Euclidean distance and spectral angle may be more appropriate. Therefore, the spectral matching approach utilised should be reviewed according to the spectral resolution of the data being tested.

#### 4.3.1 Testing the suitability of RRMSD for identifying optical anomalies

To test the performance of RRMSD as a method for identifying optical anomalies, it was compared to the Quality Water Index Polynomial (QWIP). QWIP is a metric that uses apparent visible wavelength (AVW) to identify spectra that fall outside of the general trends observed in optically deep waters (Dierssen et al., 2022). The AVW metric reduces a spectrum to a continuous variable representing the mean 'colour' of a spectrum (in nm) and is inherently correlated to spectral shape. QWIP represents a polynomial relationship between a spectrum's AVW and a normalised difference index (NDI) using red and green wavelengths. The QWIP score represents the distance of a datapoint above or below the QWIP (central tendency) and is scored with either a positive or negative value. The QWIP method was developed using a large global dataset representing blue, green and brown waters and was further tested with extensive field and satellite datasets.

The QWIP quality control method was applied to the GoM dataset. Firstly, AVW was calculated with wavebands 412 nm, 443 nm, 469 nm, 488 nm, 531 nm, 547 nm, 555 nm, 645 nm, 667 nm and 678 nm, using the equation:

$$AVW = \left( \frac{\sum_{i=1}^n R_{rs}(\lambda_i)}{\sum_{i=1}^n \frac{R_{rs}(\lambda_i)}{\lambda_i}} \right) \quad (3.7)$$

As QWIP was originally developed using hyperspectral data, the AVW calculated from the multispectral MODIS data in this study was translated to a hyperspectral equivalent AVW through the use of sensor specific polynomial offsets. The most up to date sensor specific offsets can be found in Vandermeulen (2022). QWIP is then calculated as:

$$QWIP = p_1 AVW^4 + p_2 AVW^3 + p_3 AVW^2 + p_4 AVW + p_5 \quad (3.8a)$$

where the five coefficients are given by:

$$p = (-8.399885 \times 10^{-9}, 1.715532 \times 10^{-5}, -1.301670 \times 10^{-2}, 4.357838 \times 10^0, -5.449532 \times 10^2) \quad (3.8b)$$

In order to calculate the QWIP score, the NDI is first calculated. For this application, the wavebands 488 nm and 667 nm were used:

$$NDI = \frac{(R_{rs}(667) - R_{rs}(488))}{(R_{rs}(667) + R_{rs}(488))} \quad (3.9)$$

Then the QWIP score is calculated as:

$$QWIP \text{ score} = NDI(488, 667) - QWIP \quad (3.10)$$

The resulting QWIP score provided an indication of the degree of spectral anomaly for each pixel. Following the procedure outlined in Dierssen et al. for application of the approach to satellite data, any pixel with an absolute QWIP score of 0.3 or greater would be flagged as poor quality data and removed from analysis. The QWIP score for each pixel in the GoM image was mapped and compared to the anomaly map created using the standard case two model and RRMSD spectral matching approach (Figure 4.3).

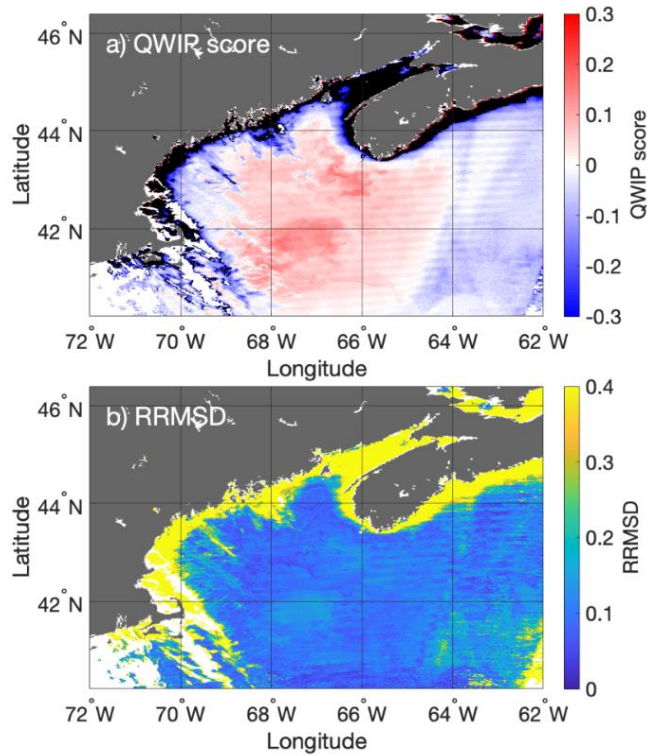


Figure 4.3 Comparison of the (a) quality water index polynomial (QWIP) score and (b) relative root mean square difference (RRMSD) methods of spectral anomaly detection. It is recommended that any pixel with an absolute QWIP score of 0.3 or greater (depicted in black in panel a) is removed from spectral analysis. This anomaly detection had been conducted on the Gulf of Maine image from 17<sup>th</sup> June 2009, and processed using standard atmospheric correction.

Comparison between the QWIP and RRMSD results for the GoM dataset indicate that these anomaly identification methods are behaving similarly. Both methods highlight significant anomaly along the coast, highlighting extensive coastal regions where data would be flagged for removal following QWIP protocol (the black pixels in Figure 4.3a generated a QWIP score of greater than 0.3). Further, whilst the two potential patches of *C. finmarchicus* (identified in the previous chapter by the  $\Delta E_{2000}$  method) are anomalous compared to surrounding waters, these patches are not being flagged as poor quality spectra by QWIP. The anomaly associated with these patches is also less apparent in the RRMSD method. The significant anomaly along

the coast is closely correlated to the negative spectra that were removed from the dataset in the Section 3.8 (Figure 3.12b). This suggests that the coastal anomaly is likely associated with AC failure, rather than driven by optically anomalous constituents. Overall, this suggests that RRMSD is a suitable method for detecting anomaly associated with AC failure.

#### 4.4 Atmospheric correction selection

This method does not rely on the development of a new AC algorithm, rather it provides a framework to identify a suitable solution out of established AC methods on a per-pixel basis. For this study, the NASA standard AC (Bailey et al., 2010), as well as eight variants of the MUMM AC (Ruddick et al., 2000) were applied to the GoM dataset using the software package SeaDAS (v 7.5.1). The MUMM AC algorithm is routinely used for estimating  $R_{rs}$  in turbid coastal waters and so was chosen to address the error in the coastal region of the dataset. It relies on assumptions of spatial homogeneity of the NIR band ratios for aerosol reflectance and water leaving reflectance. In particular, the assumption of a homogenous aerosol reflectance ratio ( $\epsilon_m$ ) limits the spatial extent to which the algorithm can be applied, as aerosol types tend to change over moderate spatial scales. To overcome this issue, the MUMM AC was applied seven different times using the SeaDAS processing tool 'l2gen', each with a different  $\epsilon_m$  value, varied between a typical range of 0.8 to 1.2 (Lavender et al., 2005). A total of 7 different  $\epsilon_m$  values were used: 0.8, 0.9, 1.0, 1.05, 1.1, 1.15 and 1.2.

##### 4.4.1 *The effect of atmospheric correction on spectral information*

In order to ascertain how each variant of AC impacts the spectral information in the GoM image, the 412 nm waveband was first investigated. The 412 nm waveband is the most affected by overcorrection due to AC failure, as aerosol reflectance has been extrapolated over a significant wavelength range, therefore resulting in an amplification of error at shorter wavelengths (Lavender et al., 2005). Analysis of the 412 nm waveband for each AC iteration indicates that  $R_{rs}$  values in the

NASA standard AC are especially low in coastal environments, with a lot of non-physical negative pixels, which are shown in black (Figure 4.4a). This suggests that the NASA standard AC is not performing well in this optically complex region, as expected. This correlates with the high QWIP score and RRMSD values that were apparent along the coast in the previous section (Figure 4.3). Additionally, it is clear that varying MUMM's  $\epsilon_m$  parameter has a significant impact in blue reflectance. A  $\epsilon_m$  of 1.2 (Figure 4.4b) behaves similarly to the NASA standard AC, resulting in a lot of negative values along the coast. As  $\epsilon_m$  is reduced,  $R_{rs}$  at 412 nm increases across the image, to the point that nearly all spatial variability is removed (Figure 4.4h). At an  $\epsilon_m$  value of 1.0, nearly all the negative 412 nm values have been removed, which is a significant improvement compared to the NASA standard. However, these uniformly high values are also likely to be erroneous, this points to the requirement for a per-pixel approach to AC across large images such as this, as opposed to blanket application.

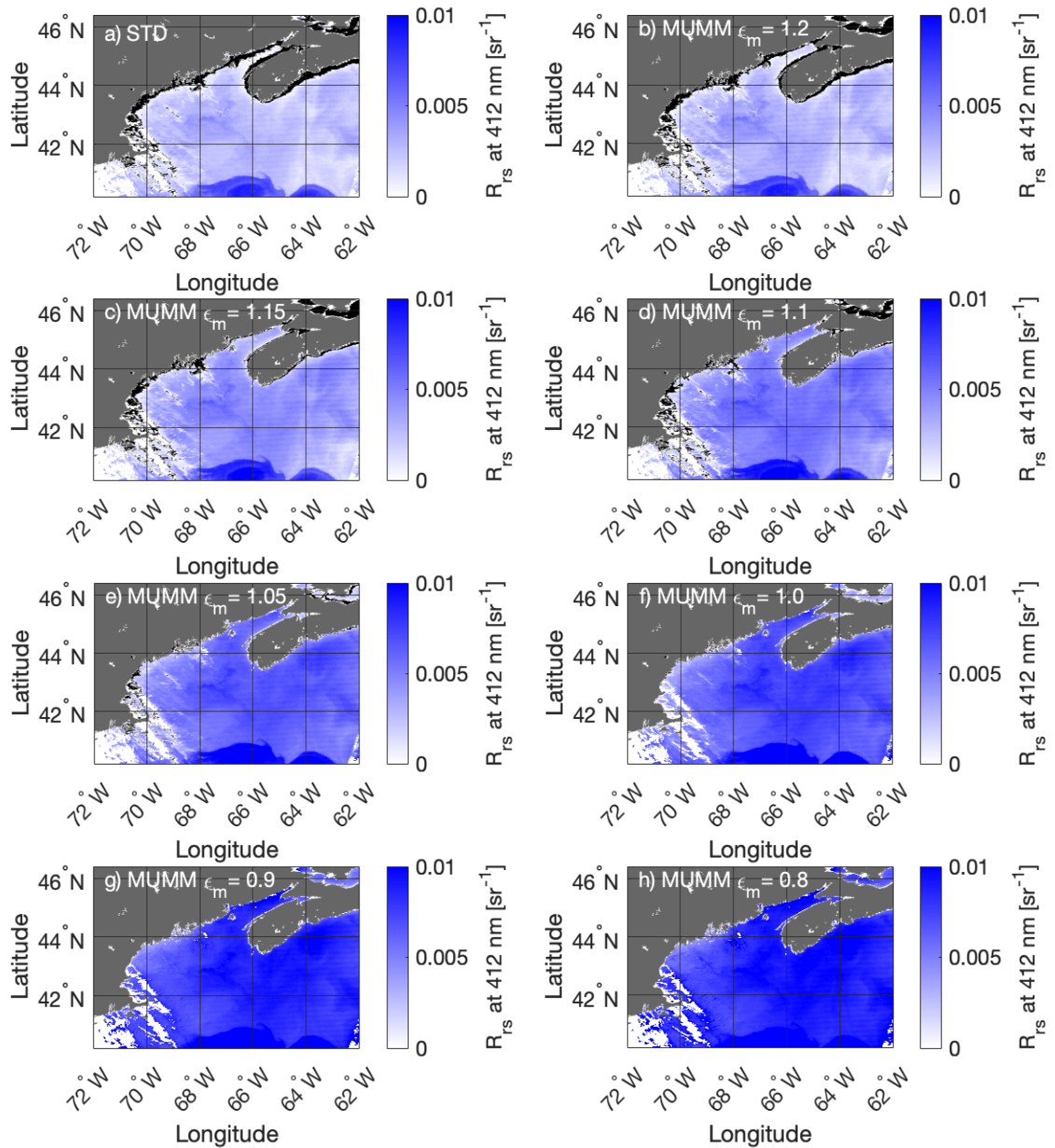


Figure 4.4 Remote sensing reflectance ( $R_{rs}$ ) values at 412 nm for the Gulf of Maine image processed using (a) the NASA standard atmospheric correction, as well as (b-h) 7 variants of the MUMM atmospheric correction, each with a different multiple scattering aerosol reflectance ratio ( $\epsilon_m$ ). Negative values are represented in black.

The impact of each AC variant on the spectra at the offshore (a), coastal (b) and inside patch (c) ROIs are presented in Figure 4.5. Across all three ROIs, the NASA standard AC produces the lowest reflectance spectra, with the standard coastal

spectra reaching a negative  $R_{rs}$  value at 412 nm (b). All variants of MUMM produce non-negative spectra and the  $R_{rs}$  spectral magnitude increases with decreasing  $\epsilon_m$  across all ROIs. Therefore, decreasing the reflectance ratio of aerosols decreases the overall contribution of aerosols to total TOA signal, resulting in an increase of the relative contribution of  $L_w$ , and therefore  $R_{rs}$ . In general, the AC procedure applied appears to have a significant impact on spectral magnitude across the spectrum. The impact on spectral shape is less significant, although the coastal and in patch ROIs see a change in spectral shape in the blue/ green, where the spectra appear to flatten out with decreasing  $\epsilon_m$ .

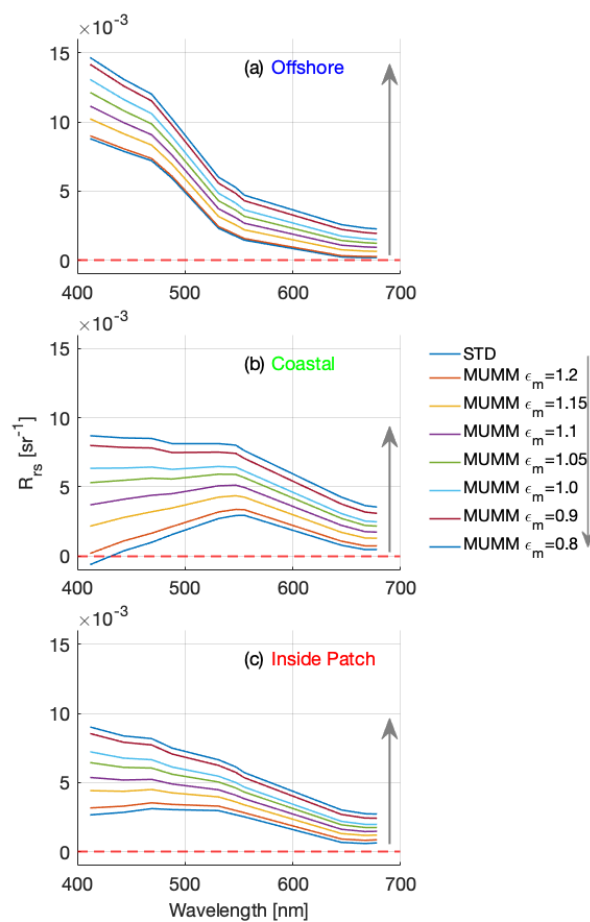


Figure 4.5 The impact of varying atmospheric correction methods in remote sensing reflectance ( $R_{rs}$ ) spectra in the (a) offshore, (b) coastal and (c) inside patch regions of interest. The arrow direction denotes the evolution from the NASA standard atmospheric correction, to the MUMM atmospheric correction with an aerosol reflectance ratio ( $\epsilon_m$ ) of 0.8.

This analysis highlights the sensitivity of satellite derived  $R_{rs}$  spectra to the aerosol model utilised and the AC procedure applied.  $R_{rs}$  spectra can vary significantly depending on the AC method selected, especially in the blue-green wavebands where the spectral matching algorithms developed in this project are largely operating. Therefore, selection of an appropriate AC method must first be conducted before any rigorous spectral analysis can take place.

#### 4.5 A per-pixel approach to atmospheric correction selection

Per-pixel comparison of AC to the standard Case 2 spectral LUT was carried out with the RRMSD matching algorithm described in Section 4.3. For each pixel, the eight variants of AC were compared to the 1008 simulated spectra and the minimum RRMSD value for each AC was extracted. The RRMSD values for each AC method were then compared on a per pixel basis and the minimum was considered the AC solution for that pixel.

The minimum RRMSD anomaly maps for each AC are presented in Figure 4.6. The RRMSD map associated with the 1.2  $\epsilon_m$  variant of MUMM (Figure 4.6b) is similar to that of the NASA standard AC (Figure 4.6a). High anomaly is present along the coast, with RRMSD values of greater than 0.4, or 40% as expressed as a percentage. This anomaly is likely associated with AC failure. However, offshore the anomaly is relatively low, with RRMSD values of 0.1 (10%) or less. This suggests that these AC variants are performing well offshore, and the spectra broadly correlate with a standard Case 2 model. As the  $\epsilon_m$  parameter decreases, the anomaly around the coast also decreases, suggesting that the MUMM AC with lower  $\epsilon_m$  performs better in these coastal regions than the NASA standard. At an  $\epsilon_m$  of 1.0 (Figure 4.6f), the exceedingly high anomaly around the coast has largely disappeared. However, the opposite is true offshore, where the anomaly increases with decreasing  $\epsilon_m$  values. As expected, the increasingly high anomaly offshore (Figure 4.6c-h) indicates that the MUMM AC is overcorrecting and therefore not suitable in those regions.

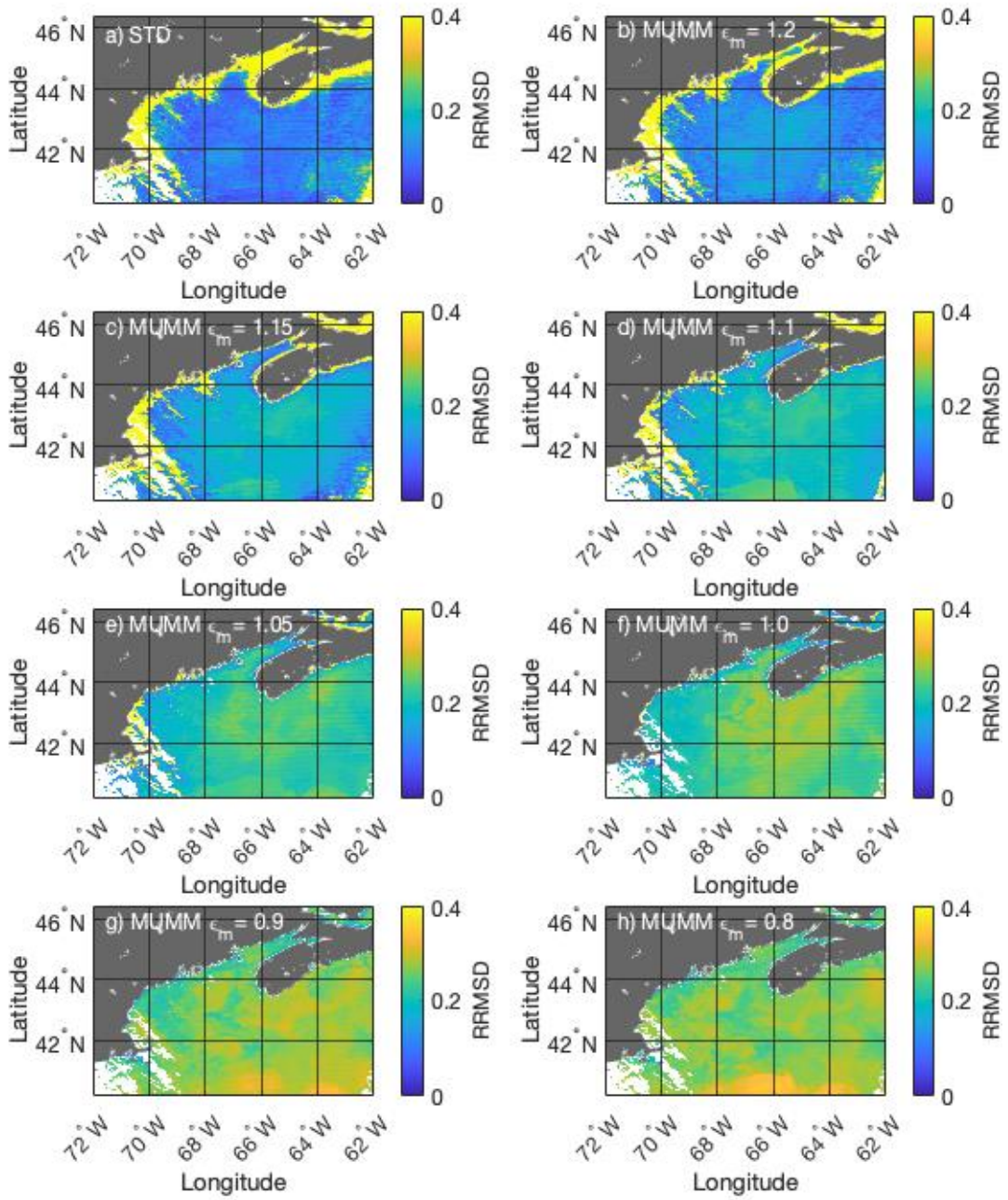


Figure 4.6 Gulf of Maine maps of minimum relative root mean square difference (RRMSD) for the comparison of (a) the NASA standard and (b-h) the MUMM atmospheric correction with varying the aerosol reflectance ratio ( $\epsilon_m$ ) parameter to the standard case two spectral look up table (LUT).

The index of the chosen AC variant for each pixel is presented in Figure 4.7a, along with the minimum RRMSD map for the comparison of all AC variants (Figure 4.7b), and the QWIP score for the newly corrected data (Figure 4.7c). The index highlights a distinct pattern in AC selection. In the offshore regions of the image, the NASA standard AC was selected. The MUMM AC was selected for the coastal regions, with decreasing  $\varepsilon_m$  values moving closer to the shoreline. This indicates that aerosol type changes with proximity to land, which is a reasonable expectation. However, a reduction in  $\varepsilon_m$  with proximity to shore is indicative of coarser aerosol models being selected closer to land, which is contrary to the general trend of fine mode particles (associated with anthropogenic origin) contributing more to the atmospheric composition in these regions relative to the open ocean (Ahmad et al., 2010). Whilst this result is somewhat surprising, it may be explained by the lack of parameterisation of strongly absorbing aerosols within the aerosol models used during the AC process (Ahmad et al., 2010). The effects of strongly absorbing aerosols, such as soot and dust, cannot be accounted for using the NIR bands typically used during the AC procedure. Despite this, strongly absorbing aerosols are likely influencing the signal, especially in the coastal environment, which are closer in proximity to the source of these particles. These strong absorbers would serve to flatten the aerosol reflectance spectrum, which would in turn reduce the  $\varepsilon_m$  value.

The only exception to this pattern is the south-easterly region of the image, where MUMM AC variants are being selected for open water. Some residual anomalies are still present in this region (Figure 4.7b), which indicates poor quality data on the outer perimeters of the image.

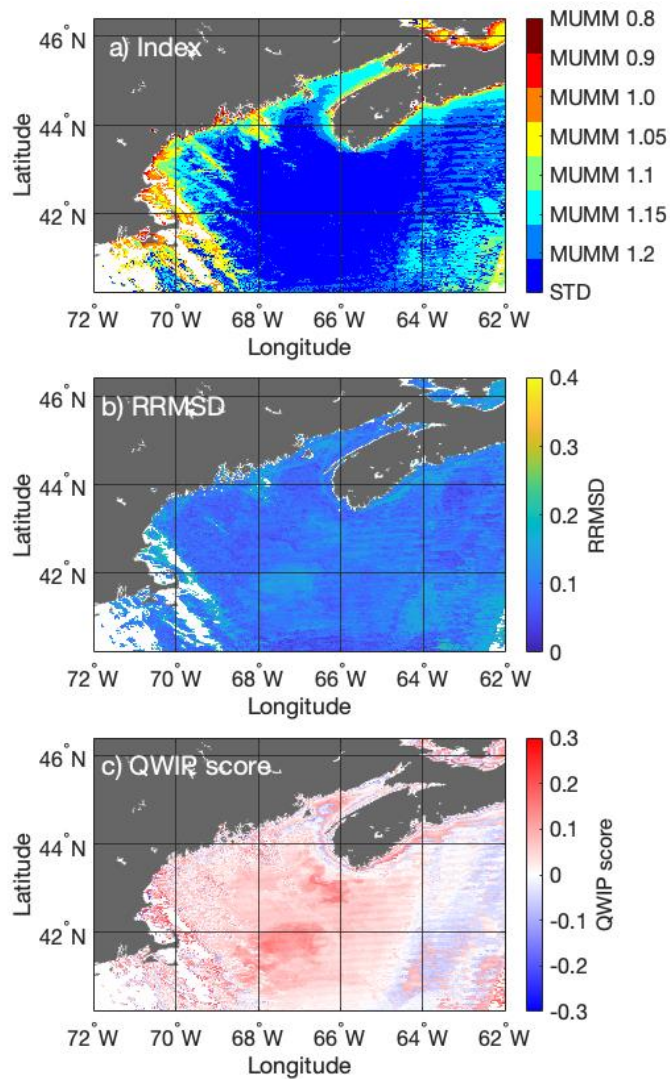


Figure 4.7 The Gulf of Maine (a) Index of atmospheric correction selection for each pixel and (b) relative root mean square difference (RRMSD) and (c) quality water index polynomial (QWIP) score for the corrected data.

The RRMSD map of the collated and fully corrected GoM image (Figure 4.7b) has considerably lower anomaly than the starting point of the NASA standard corrected image. Anomaly along the coast of 0.4 or greater (40%) has more than halved, with anomaly values in the coastal regions of the image within the same range as those in the optically clear regions. In general, the per-pixel approach out-performs any single AC method tested in this study.

Application of the QWIP score quality control method to the fully corrected GoM image (Figure 4.7c) shows a considerable improvement to that of the NASA standard AC (Figure 4.3a). QWIP scores have been reduced to well below an absolute value of 0.3, and therefore all of the data passes this quality control method according to the criteria outlined in Dierssen et al. (2022). There is, however, still some residual anomalies associated with the fully corrected GoM image, which is apparent in both the RRMSD and the QWIP score maps. One anomalous feature is present along the coast of Nova Scotia at the boundary of the standard and MUMM 1.2  $\epsilon_m$  AC selection. This anomaly is likely associated with the number of MUMM iterations used in this study. Decreasing the step size between  $\epsilon_m$  parameters may resolve this anomaly, however this would quickly become computationally expensive, and as the anomaly is satisfactorily low, the step-sizes were not altered.

A small anomaly signal that correlates with the potential *C. finmarchicus* patches identified through the  $\Delta E_{2000}$  method in the previous chapter (Figure 3.12b) is evident in the RRMSD map. However, this anomaly signal is not as strong as that generated by the QWIP score or indeed the  $\Delta E_{2000}$  anomaly signal generated in the previous chapter. The RRMSD anomaly map appears to have more background noise than the other two methods, which could be masking the *C. finmarchicus* associated anomaly. Excluding the matching metric used, the most significant difference between the  $\Delta E_{2000}$  and the RRMSD method is the amount of spectral information included in the matching process. The RRMSD method utilises 8 spectral wavebands, including those associated with aerosol properties that have a relatively low signal-to-noise ratio (SNR) (469 nm and 547 nm). In contrast, the  $\Delta E_{2000}$  method utilises only three wavebands. Therefore, some of the noise associated with the low SNR wavebands may be masking the in-water anomalies. Whilst including these wavebands is useful for the identification of appropriate AC, they may not be suitable for the identification of potential *C. finmarchicus* patches.

#### 4.5.1 Spectral matching generated constituent concentration estimates

Another key benefit of this AC method is the simultaneous constituent estimates of CHL, MSS and CDOM extracted through the spectral matching approach. Not only does this supply information on the bio-optical constituents in regions where data quality was previously too poor to derive retrievals, it also provides a form of sense check that the spectral matching technique is behaving appropriately. Figure 4.8 is the CHL (4.8a), CDOM (4.8b) and MSS (4.8c) concentration estimates derived from the optimal spectral match that determined the most suitable AC method for each pixel. Whilst there is no *in situ* validation data available for this particular image, the constituent concentrations appear reasonable. CHL correlates with the regions thought to contain *C. finmarchicus* patches, which is similar to the  $\Delta E_{2000}$  results for the GoM, as well as the Norwegian Sea. Further, relatively high MSS concentrations are reached in the Bay of Fundy. Some of this signal could be attributed to the drainage of the St. John and St. Croix rivers in this region. Additionally, the milky white feature in the centre of the image is also being attributed to MSS, similar to the  $\Delta E_{2000}$  results presented in the previous chapter. Again, as this feature is located in relatively open water, it is unlikely that this is the result of increased suspended sediment. This signal is more likely associated with a coccolithophore bloom, organisms that are encapsulated by white liths that scatter light. These organisms commonly bloom in the GoM at this time of year (Balch et al., 1991). However, due to the lack of coccolithophore IOP representation, the model is misattributing this to MSS, which also significantly scatters light.

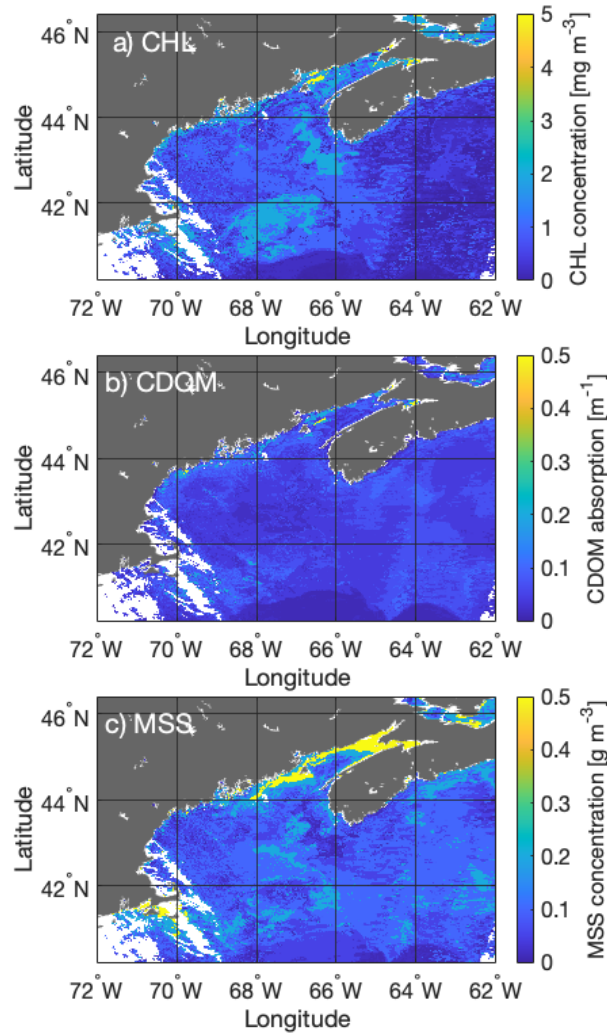


Figure 4.8 Constituent concentrations of (a) chlorophyll (CHL), (b) coloured dissolved organic matter (CDOM) and (c) material suspended sediment (MSS) required to reach minimum relative root mean square difference (RRMSD) values derived from the comparison of fully corrected satellite data and a standard case two bio-optical model.

#### 4.6 Conclusions

This chapter outlines a novel approach to the AC problem using a spectral matching algorithm. The method relies on relative root mean square difference (RRMSD) to compare simulated reflectance spectra representing a standard Case 2 bio-optical model to the satellite derived reflectance spectra with several variants of

AC applied to it. RRMSD provides a metric to identify the optimal AC method on a per pixel basis.

RRMSD was identified as a good method for flagging poor quality satellite reflectance spectra and behaves similarly to the QWIP method for spectral quality control outlined in Dierssen et al. (2022). However, this method differs from current quality control parameters such as Wei et al. (2016) and Dierssen et al. (2022), as it provides a solution to improve the data quality rather than eliminating it from analysis altogether. When this per-pixel approach was applied to the GoM image, data around the coast that was previously being flagged for removal by the QWIP score became of suitable quality for analysis. The resulting CHL, MSS and CDOM estimates derived from the spectral matching appear reasonable for this region, however no *in situ* validation data is available for this image. This is an important exercise that will form the foundation of future work.

Whilst for this application the RRMSD metric performs well, an alternative spectral matching algorithm may be more suitable under different circumstances. For example, with the imminent launch of NASA's PACE satellite, the use of hyperspectral data for ocean monitoring will likely become more commonplace. The application of this method to hyperspectral data may necessitate the use of a different metric such as NS<sup>3</sup>, as it is more sensitive to changes in spectral shape. This should be evaluated on a case by case basis.

This chapter does not present the development of a new AC algorithm, rather a framework to identify a suitable per-pixel solution out of well established AC methods. For this study, the NASA standard AC was used to address offshore data, whilst the MUMM AC with varying  $\epsilon_m$  values was used to address optically complex coastal waters. However, the user can easily alter the AC variants based on preferred algorithms already in use or the region of interest. For example, one of the major limitations of the MUMM AC method is the assumption of a homogenous aerosol reflectance ratio ( $\epsilon_m$ ) across the region (Ruddick et al., 2000). As a result, their recommendation is to use the MUMM method of AC over relatively small spatial scales. The method developed in this chapter overcomes this limitation and can be

used to analyse coastal/ inland waters over large spatial scales through the ability to select optimal AC on a per-pixel basis.

The outlined approach to AC selection provides good quality spectral information for the entirety of the GoM image, with reasonable estimates of CHL, MSS and CDOM. As this removes anomaly associated with AC failure, it allows for the identification of in-water optical anomalies, such as the occurrence of *C. finmarchicus* swarms. Whilst the RRMSD map of the fully corrected data has some residual anomaly that may be associated with *C. finmarchicus* patches, the anomaly map appears more noisy than the  $\Delta E_{2000}$  map generated in the previous chapter. This method utilises more wavebands, including those with a low SNR that are typically used for the identification of aerosols, which could cause complications when addressing in-water anomalies. Therefore, the following chapter will focus on the development of a spectral matching approach to identify *C. finmarchicus* swarms, which uses more carefully selected spectral information than the  $\Delta E_{2000}$  approach. This will be applied to the GoM image, corrected following the protocol described in this chapter, ensuring the analysis will be applied to good quality spectral data.

## 5 Development of a spectral matching approach to identify surface swarms of *C. finmarchicus* from satellite derived ocean colour data

### 5.1 Introduction

The previous chapter outlined the development of a method to identify spectral anomalies in ocean colour data associated with atmospheric correction (AC) failure. This spectral matching technique worked well for the optically complex Gulf of Maine (GoM) image from the 17<sup>th</sup> June 2009. It would follow that a similar method could identify in-water anomalies associated with deviance from the standard bio-optical model of CHL, MSS and CDOM. Therefore, the logical next step of this work is the development of a bio-optical anomaly technique with greater spectral resolution than that of the  $\Delta E_{2000}$  method first described in Chapter 3. A potential benefit of spectral matching over the  $\Delta E_{2000}$  approach is the inclusion of more spectral information, as eRGB colour matching is limited to the information in only three wavebands (443 nm, 488 nm and 555 nm). The inclusion of more wavebands could result in greater discrimination between optically similar constituents, such as CDOM and *C. finmarchicus* absorption, which have a broadly similar effect of absorbing in the blue/ green part of the spectrum (Figure 1.2c, Figure 1.4b). In addition to this, a spectral matching approach would not be constrained by any predetermined range. The  $\Delta E_{2000}$  approach requires the calculation of eRGB colour values associated with each reflectance spectrum in the LUT, as well as the eRGB colour values of each pixel in the target satellite image. These colour values are standardised using a global range of *in situ*  $R_{rs}$  values, collated by Valente et al. (2022). The upper range was determined by the 90<sup>th</sup> percentile of the range of *in situ* values for each band. Therefore, in regions comparable to the open ocean where blue reflectance will likely exceed the 90<sup>th</sup> percentile of *in situ* values, this range will have to be altered. In contrast, a spectral

matching method requires no ranges or data manipulation, and therefore can be easily applied across all oceanic environments.

However, the anomaly map associated with the spectral matching technique developed in Chapter 4 appeared relatively noisy and with no strong anomaly signal in the GoM image (Figure 4.7b). This contrasts with the findings from the application of  $\Delta E_{2000}$  to the GoM image in Figure 3.12b (which had the NASA standard AC method applied to it), which saw an anomalous feature off the coast of Nova Scotia and on the Georges Bank that was later attributed to *C. finmarchicus* absorption. The QWIP score quality control method (Dierssen et al., 2022) also identified these features as optically anomalous (Figure 4.7c). Therefore, there is a possibility that the inclusion of all 8 spectral wavebands from 412 nm to 645 nm does not provide sufficient weight to the *C. finmarchicus* feature, which only impacts part of the spectrum (with a peak in absorption at 480 nm). Additionally, the inclusion of atmospheric bands with low SNR could be introducing excess noise, which is further diluting the in-water anomaly signals associated with zooplankton.

This chapter outlines the development of a spectral matching approach to identify optical anomalies in the GoM image, atmospherically corrected using the method described in Chapter 4, and then tested on the Norwegian Sea subsene from 29<sup>th</sup> April 2017 (Figure 3.4c). First, the  $\Delta E_{2000}$  is applied to the pixel-specific atmospherically corrected GoM data, to allow for a point of comparison between the two methods. Then, the optimal number of wavebands for the spectral matching method to identify *C. finmarchicus* will be determined. Results of the spectral matching approach using relative root mean square difference (RRMSD) in the GoM will then be presented, along with results from the Norwegian Sea for the purposes of comparison with  $\Delta E_{2000}$ . The further development of an anomaly threshold will also be discussed. This chapter aims to compare the  $\Delta E_{2000}$  method for identification of bio-optical anomalies to a newly developed spectral matching method with increased spectral resolution, and assess the suitability for identifying surface swarms of *C. finmarchicus*.

## 5.2 $\Delta E_{2000}$ anomaly mapping on the Gulf of Maine dataset with pixel specific atmospheric correction applied

In order to allow comparison between the results generated by  $\Delta E_{2000}$  and those generated by a spectral matching method, the  $\Delta E_{2000}$  algorithm must first be applied to the pixel specific atmospherically corrected GoM image. In principle, this correction will have removed anomalies associated with AC failure and therefore any residual anomalies can be linked to in-water features. The  $\Delta E_{2000}$  algorithm was previously applied to the GoM image processed using the NASA standard AC, with the results are presented in Section 3.7. of this thesis. However, with the application of the per-pixel AC procedure, data around the coast that was previously of poor quality is now sufficient for spectral analysis, and therefore  $\Delta E_{2000}$  must be re-applied to investigate its performance in these optically complex coastal regions.

For this analysis, the eRGB colour values for each pixel of the corrected GoM image were first compared to the eRGB LUT derived from 1008 simulated  $R_{rs}$  spectra representing a standard Case 2 bio-optical model (first described in Section 3.4). The resulting minimum  $\Delta E_{2000}$  map is presented in Figure 5.1a. This was repeated using an eRGB LUT derived from 4410 simulated  $R_{rs}$  spectra that represented a standard Case 2 bio-optical model with the addition of *C. finmarchicus* absorption (Figure 5.1b). The details of this LUT can be found in Section 3.7. The *C. finmarchicus* concentration estimates derived from this colour matching technique are presented in Figure 5.1c.

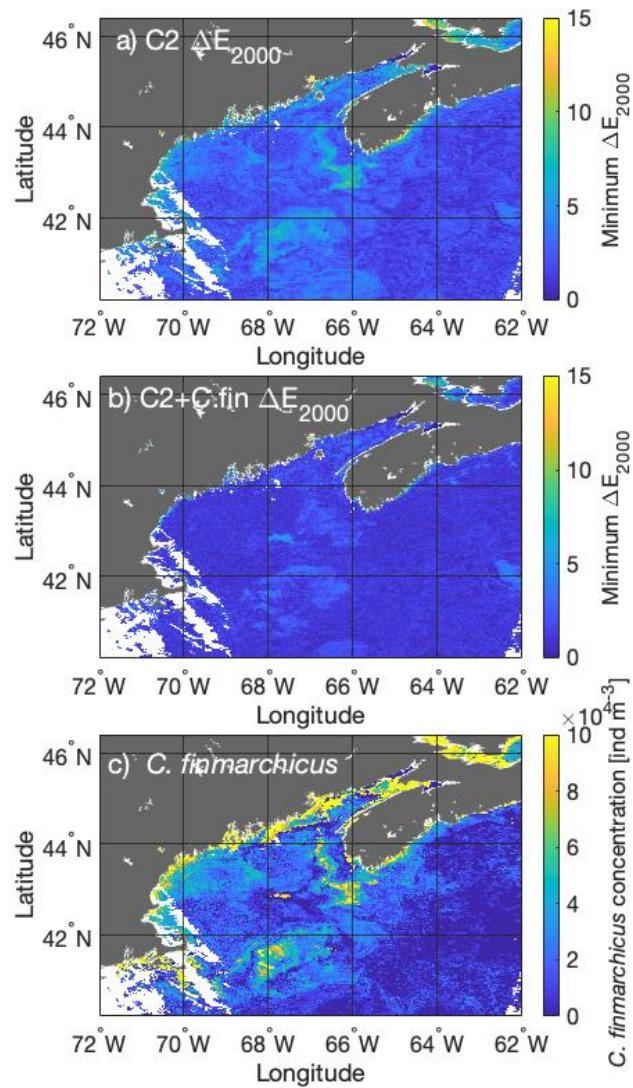


Figure 5.1 Minimum Delta E 2000 ( $\Delta E_{2000}$ ) map derived by comparing eRGB colour values from the Gulf of Maine MODIS image on 17<sup>th</sup> June 2009 to (a) a standard Case 2 bio-optical model and (b) a Case 2 bio-optical model with the addition of *C. finmarchicus* absorption. As well as (c) the estimated surface concentrations of *C. finmarchicus* produced from the minimum  $\Delta E_{2000}$  value for each pixel in the image (concentrations are expressed as individuals  $m^{-3}$ ). This data has been corrected using the per-pixel atmospheric correction approach outlined in Chapter 4.

The  $\Delta E_{2000}$  map produced with the standard Case 2 model (Figure 5.1a) highlights anomalous features south of Nova Scotia and on the Georges Bank,

associated with relatively high minimum  $\Delta E_{2000}$  values. This is consistent with the previous  $\Delta E_{2000}$  (Figure 3.12b) and QWIP score (Figure 4.7c) analysis and indicates that something other than the standard bio-optical model is impacting the optics of the water column in these regions. Additionally, whilst most of the previously unavailable coastal data show relatively low anomalies, some regions including the southeast coast of Nova Scotia, display high minimum  $\Delta E_{2000}$  values. When *C. finmarchicus* absorption is included in the model, the majority of anomalies are resolved in the region (Figure 5.1b). Interestingly, the relative anomaly of the feature in the centre of the GoM, associated with the milky white patch visible in the eRGB image (Figure 4.1), is higher than that of the standard Case 2 model. The *C. finmarchicus* concentrations associated with the best colour match up (Figure 5.1c) indicate concentrations of between 60,000-100,000 ind m<sup>-3</sup> within the patch off the coast of Nova Scotia and on the Georges Bank, which is consistent with previous  $\Delta E_{2000}$  analysis on the image with the NASA standard AC applied (Figure 3.13b). It is not surprising that the concentration maps agree well in these patches, as the per-pixel AC method largely selected the NASA standard AC in the offshore region of the image (Figure 4.7a). However, in the coastal region where data was previously not available, the map indicates high surface concentrations of *C. finmarchicus*. Whilst it is possible that there are high surface concentrations of *C. finmarchicus* along the coast, these high concentrations were not associated with any significant anomaly signal in the original Case 2 anomaly map (Figure 5.1a). This, along with the fact that these features appear to be tightly linked with the coast, suggest that that these high concentrations (100,000 ind m<sup>-3</sup> or greater) are erroneous. Considering their position, it is more likely that these features are associated with the optical complexity of the coastal zone. Again, the erroneous *C. finmarchicus* artefact in the centre of the image that is spatially correlated with the milky white patch in the eRGB image (Figure 4.1) is likely associated with a coccolithophore bloom. As there is currently no coccolithophore IOP information to include in the model, the signal is being misattributed to *C. finmarchicus*.

Assessing the bio-optical constituent concentrations required to reach optical closure (i.e. minimum  $\Delta E_{2000}$  values) provides more information on how the model works. A similar dataset has been presented in Section 3.7 (Figure 3.14), however constituent retrievals from the coastal regions of this image are also now available for analysis. Constituent concentrations generated from the standard Case 2 model (Figure 5.2a,c,e) appear reasonable, but are somewhat altered with the addition of *C. finmarchicus* (Figure 5.2b,d,f). In particular, MSS concentration estimates increase across the image, and especially in the Bay of Fundy, with the addition of *C. finmarchicus* absorption (Figure 5.2.e,f). The increase in MSS concentrations indicates a false optimisation procedure taking place during the colour matching process. This would account for the high concentrations of *C. finmarchicus* in the coastal regions, which were previously not associated with an anomalous signature when compared to a standard bio-optical model. In addition, it would explain the erroneous *C. finmarchicus* feature associated with the milky-white patch in the centre of the eRGB imagery. *C. finmarchicus* is represented in the model by only its absorption properties, whereas MSS has a strong scattering signal (Figure 2.3b). Therefore, when *C. finmarchicus* is being added to regions where it likely is not present, MSS is also being added to counter the absorption effect. Whilst this may numerically be a better colour match for the pixels, there was hardly any anomaly associated with these regions to begin with, which suggests that these areas can be relatively well-characterised using a standard bio-optical model with CHL, MSS and CDOM alone. Thus, the blanket application of the Case 2 with *C. finmarchicus* model may be inappropriate and a limitation of this methodology, particularly in optically complex environments like the GoM.

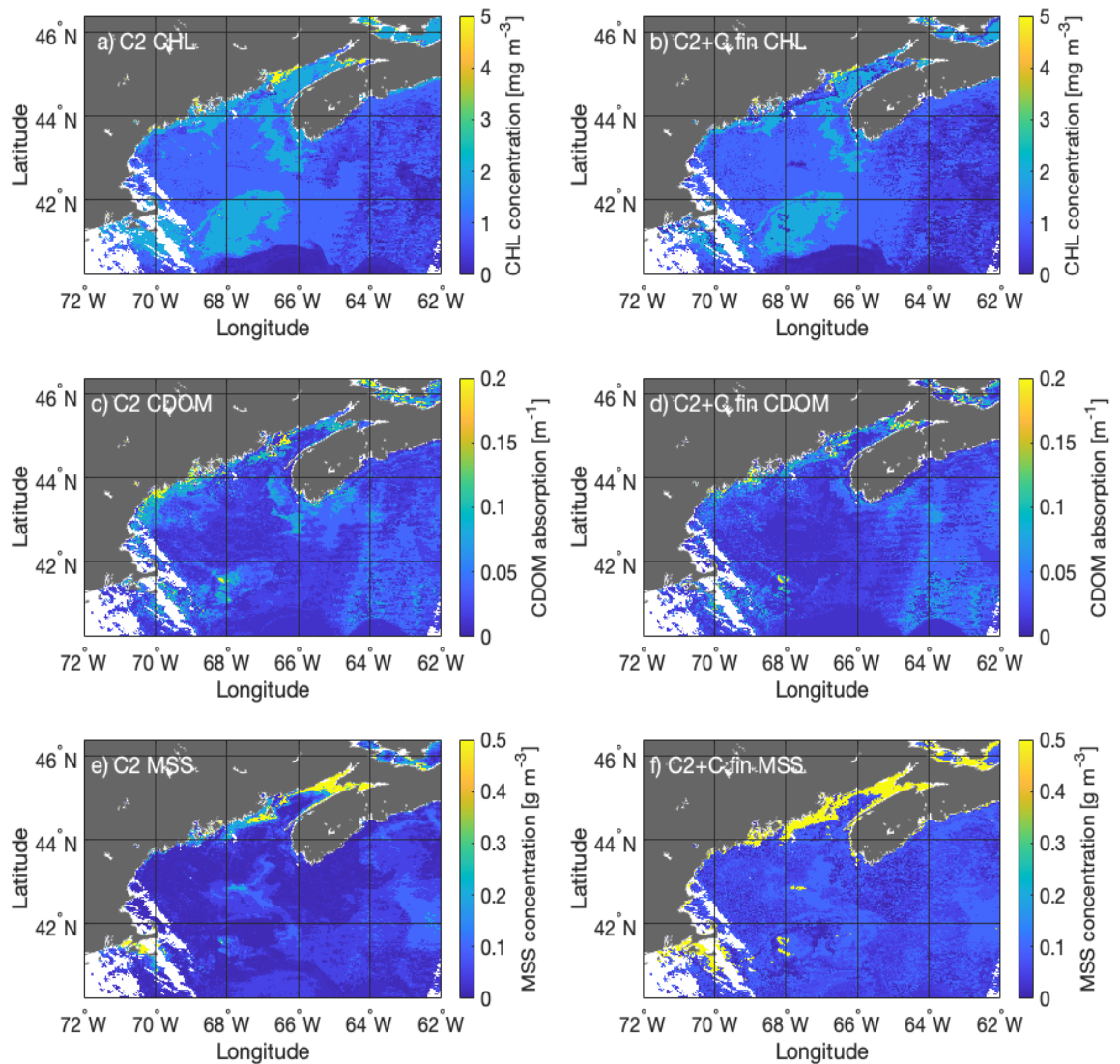


Figure 5.2 Estimated constituent concentrations required to reach minimum  $\Delta E_{2000}$  values with (a,c,e) a full Case 2 model and (b,d,f) a Case 2 model with the addition of *C. finmarchicus* absorption. This data has had the per-pixel atmospheric correction method applied to it, following the procedure outlined in Chapter 4.

Whilst the overall concentration estimates, especially those produced by the standard Case 2 model, look reasonable, there appears to be limitations associated with the  $\Delta E_{2000}$  approach. The issues of false optimisation become particularly prevalent in optically complex regions where a variety of potential solutions are available, and the addition of another constituent into the bio-optical model can further complicate things. It is possible that the inclusion of more spectral information

into the matching process will help to provide greater discrimination between the constituents, thereby reducing the erroneously high coastal *C. finmarchicus* retrievals that are seen here. The potential of a spectral matching approach to improve these retrievals will be explored in the following sections.

### 5.3 The development of an alternative spectral matching approach

#### 5.3.1 *Selection of optimal wavebands for anomaly mapping using a spectral matching approach*

MODIS Aqua data has 8 spectral wavebands available from 412 to 645 nm, which are: 412 nm, 443 nm, 469 nm, 488 nm, 531 nm, 547 nm, 555 nm and 645 nm. However, these wavebands have varying uses, which means their signal to noise ratio (SNR) also vary. Wavebands 469 nm, 547 nm and 645 nm are all primarily used for land, cloud and aerosol detection, and therefore have a much lower SNR than that of the other wavebands primarily utilised for ocean colour biogeochemical applications (Table 5.1). As a result, the inclusion of these bands in the spectral matching process might produce anomaly signals associated with noise. In addition to this, the 412 nm waveband can often be problematic for match up exercises, as this waveband is most sensitive to AC issues. Despite the per-pixel AC method removing the large majority of error due to AC failure, it is possible that a small amount of residual error associated with the 412 nm waveband may be prevalent. As a result, selection of appropriate wavebands for the purpose of identifying surface swarms of *C. finmarchicus* through spectral matching is critical.

Table 5.1 Spectral information available from MODIS Aqua data for the waveband range used in this study, along with the signal to noise ratio (SNR) requirement for each waveband.

$\lambda$ (nm)	Bandwidth (nm)	SNR	Primary use
412	405 - 420	880	Ocean colour/ Phytoplankton/ Biogeochemistry
443	438 - 448	838	Ocean colour/ Phytoplankton/ Biogeochemistry
469	459 - 479	243	Land/ Cloud/ Aerosol properties
488	483 - 493	802	Ocean colour/ Phytoplankton/ Biogeochemistry
531	526 - 536	754	Ocean colour/ Phytoplankton/ Biogeochemistry
547	545 - 565	228	Land/ Cloud/ Aerosol properties
555	546 - 556	750	Ocean colour/ Phytoplankton/ Biogeochemistry
645	620 - 670	128	Land/ Cloud/ Aerosol boundaries

In order to determine the optimal waveband configuration for the identification of *C. finmarchicus* associated in-water anomalies, the pixel spectra were compared to the standard Case 2 spectral LUT, varying the wavebands included in the match up process. The method used to quantify the best spectral match in this study is relative root mean square difference (RRMSD) and is fully described in Section 4.3. RRMSD is a measure of Euclidean distance, much like the foundation of the  $\Delta E_{2000}$  metric. A key benefit of RRMSD is the per-waveband scaling of the LUT  $R_{rs}$  to the satellite  $R_{rs}$  spectra, meaning disproportionately large error associated with relatively small signals (i.e. at the red end of the spectrum) will not skew results. Figure 5.3 displays the minimum RRMSD maps derived from the matching of all eight wavebands (412 nm, 443 nm, 469 nm, 488 nm, 531 nm, 547 nm, 555 nm and 645 nm) (Figure 5.3a), the matching of 7 wavebands with the removal of 412 nm (Figure 5.3b), the matching of 4 wavebands with the removal of 412 nm and the land/ aerosol and cloud bands (443 nm, 488 nm, 531 nm, 555 nm) (Figure 5.3c) and finally the

matching of 3 wavebands that match the wavebands used in the  $\Delta E_{2000}$  approach (443 nm, 488 nm and 555 nm) (Figure 5.3d).

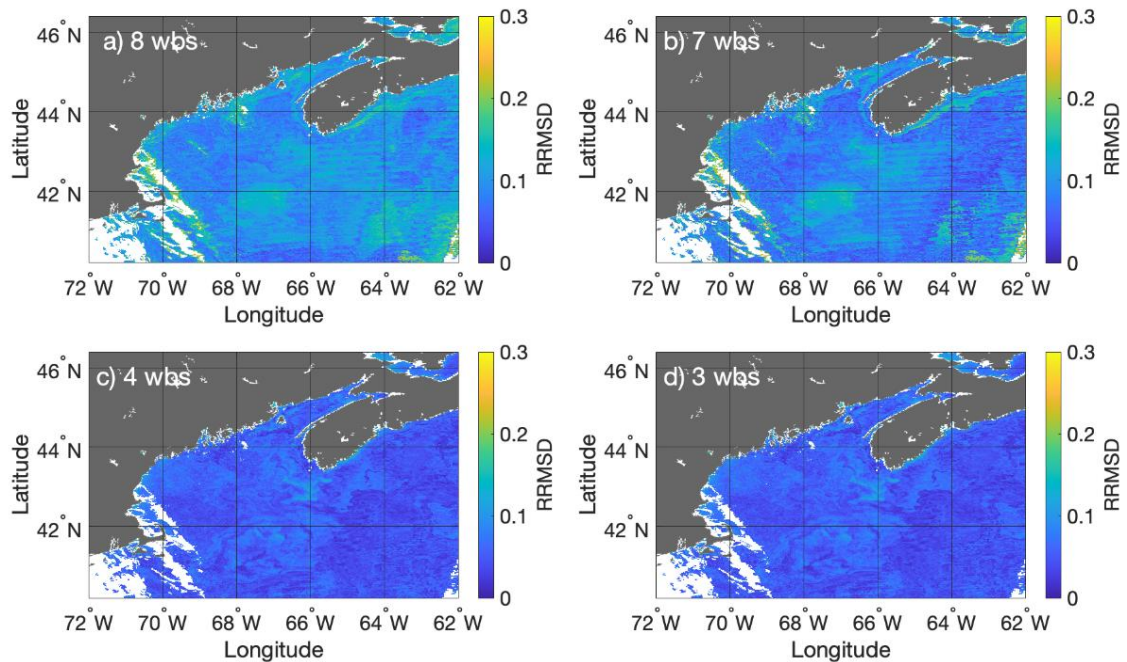


Figure 5.3 Minimum relative root mean square difference (RRMSD) maps for satellite spectral matching with a standard Case 2 bio-optical model using different spectral information. Spectral matching variants include (a) all 8 wavebands available (412, 443, 469, 488, 531, 547, 555 and 645 nm), (b) all wavebands except 412 nm (443, 469, 488, 531, 547, 555, 645 nm), (c) the ocean colour wavebands without 412 nm (443, 488, 531, 555, 645 nm) and (d) the three wavebands used in the  $\Delta E_{2000}$  approach (443, 488 and 555 nm).

To identify the optimal waveband selection for characterisation of in-water anomalies, the  $\Delta E_{2000}$  anomaly map was used as a benchmark (Figure 5.1a). The aim is to reduce as much residual noise in order to identify the same anomalous features as those evident in the  $\Delta E_{2000}$  derived anomaly map. These features, primarily the potential patch of *C. finmarchicus* off the coast of Nova Scotia, as well as that on the Geroges Bank, are corroborated as optically anomalous by the QWIP score method (Figure 4.7b) and are largely resolved with the addition of *C. finmarchicus* absorption using the  $\Delta E_{2000}$  approach. Therefore, when developing a method to identify in water anomalies, it is important that these features are sufficiently highlighted.

When the RRMSD spectral matching procedure is conducted using all eight wavebands from 412 nm to 645 nm, a significant amount of residual anomaly is still evident (Figure 5.3a). These anomalies appear to be associated with poor quality data at the edges of the image, persistent issues with cloud shadow, or small artefacts of the per-pixel AC selection. Whilst there is a signal associated with the potential *C. finmarchicus* patches off the coast of Nova Scotia and on the Georges Bank, the general noise in the image make differentiation between in-water anomalies and residual data quality issues difficult. This is only slightly improved with the removal of the 412 nm waveband (Figure 5.3b). The majority of anomalous features persist, with only a small difference in background noise. Once all of the low SNR wavebands associated with land and aerosol properties are removed (Figure 5.3c) the overall anomaly associated with the image is greatly reduced. Whilst there is an anomaly signal associated with the south Nova Scotia feature, it is less visually significant than that produced by the  $\Delta E_{2000}$  approach (Figure 5.1a). Additionally, the signal associated with the Georges Bank feature is comparatively weak. For a direct comparison between  $\Delta E_{2000}$  and RRMSD, spectral matching was also conducted using the same three wavebands as those used to calculate eRGB coo-ordinates in the  $\Delta E_{2000}$  method (443, 488 and 555nm) (Figure 5.3d). The exclusion of the 531 nm waveband appears to do very little in terms increasing the relative anomaly signal of the Georges Bank and south Nova Scotia features. Therefore, it can be determined that for anomaly associated with *C. finmarchicus* absorption, the 4 waveband RRMSD approach is the most suitable.

In terms of spectral resolution, the 4 waveband RRMSD approach is not much of an improvement on  $\Delta E_{2000}$ , which essentially relies on the information derived from 3 wavebands (443, 488 and 555 nm). However, increasing the number of wavebands included in the spectral matching process makes it more difficult to identify a *C. finmarchicus* associated signal. Not only does this allow for the inclusion of more noise, the increased spectral range may reduce the relative impact of *C. finmarchicus* on the RRMSD value. *C. finmarchicus* absorption is most significant between 450 and 520 nm, with a broad peak at 480 nm (Figure 1.4b). The inclusion of the 645 nm band may reduce the degree of relative difference in spectral information driven by *C.*

*finmarchicus*, as the copepod species does not absorb strongly in this part of the spectrum. As a result, a targeted waveband approach may be more suitable for the identification of surface swarms of *C. finmarchicus*.

### 5.3.2 Identification of in-water anomalies and estimation of *C. finmarchicus* concentrations in the Gulf of Maine

The spectral matching approach using wavebands 443, 488, 531 and 555 nm was applied to the GoM image, using both the Case 2 spectral LUT (1008 spectra) and the Case 2 LUT with the addition of *C. finmarchicus* absorption (4410 spectra). The minimum RRMSD map for the Case 2 model that was previously presented in Figure 5.3d is presented again in Figure 5.4a with a new colour bar scale for comparison with that of the Case 2 with *C. finmarchicus* LUT (Figure 5.4b). Whilst there is generally more noise associated with the RRMSD map compared to that of the equivalent  $\Delta E_{2000}$  approach (potentially due to the increased contrast that the eRGB imagery provides compared to  $R_{rs}$  data), the patch south of Nova Scotia has minimum RRMSD values of greater than 0.1, or 10% if expressed as a percentage. With the addition of *C. finmarchicus*, the anomaly map is improved (Figure 5.4c), however the relative anomaly of the feature in the centre of the image associated with the milky-white patch in the eRGB image increases. These results are similar to that of the  $\Delta E_{2000}$  approach (Figure 5.1a). The *C. finmarchicus* concentrations associated with the best spectral match appear similar to that generated through  $\Delta E_{2000}$ . High concentrations are associated with the Nova Scotia and Georges Bank features, with concentrations of up to 80,000 ind m<sup>-3</sup> within the patches. High *C. finmarchicus* concentrations are still present along the coast, although to a lesser extent than that of the  $\Delta E_{2000}$  method. Additionally, the erroneously high *C. finmarchicus* concentrations in the centre of the image associated with the milky-white patch is still evident, and generally larger than that produced by  $\Delta E_{2000}$ .

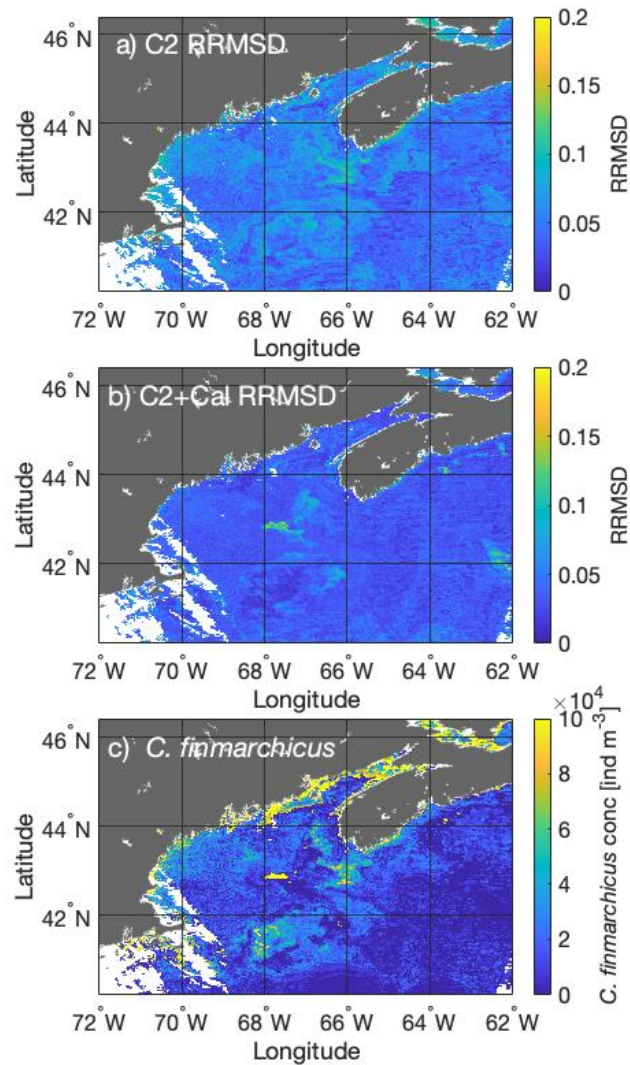


Figure 5.4 Minimum RRMSD map for spectral matching of the Gulf of Maine image with (a) a standard Case 2 spectral LUT and (b) a Case 2 spectral LUT with the addition of *C. finmarchicus* and (c) the *C. finmarchicus* concentrations estimates required to reach minimum RRMSD values.

The constituent concentration estimates required to reach minimum RRMSD values for the standard Case 2 spectral matching model (Figure 5.5a,c,e) and the Case 2 model with the addition of *C. finmarchicus* (Figure 5.5b,d,f) yields similar results to that of the  $\Delta E_{2000}$  approach. Again, the addition of *C. finmarchicus* absorption has the most significant impact on MSS concentrations, increasing along the coast and in the

milky-white feature associated with the potential coccolithophore bloom. Overall, the similarity between this and the  $\Delta E_{2000}$  approach suggests that the addition of the 531 nm waveband has very little overall impact in constituent discrimination.

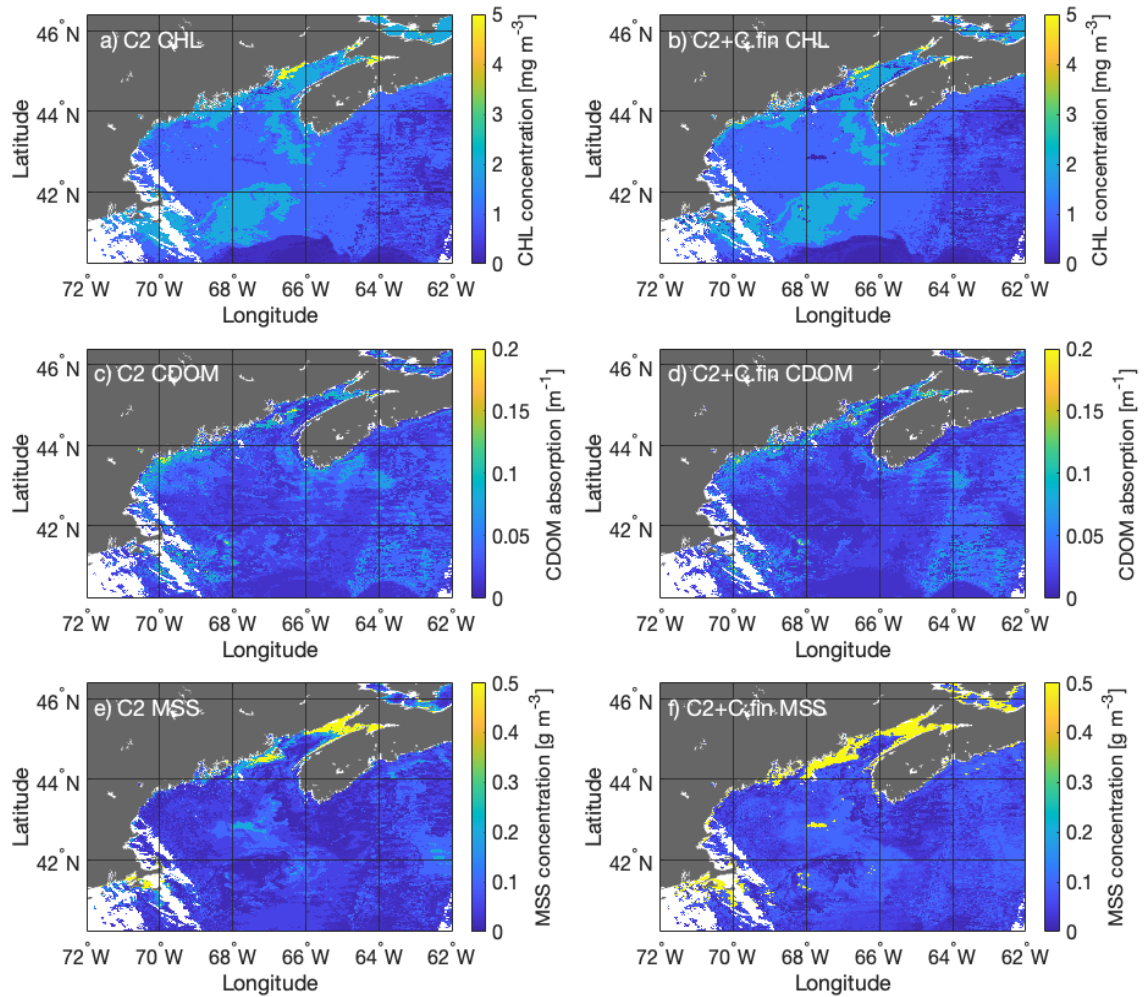


Figure 5.5 Constituent concentrations required to reach minimum RRMSD values with (a,c,e) the full Case 2 model and (b,d,f) the Case 2 model with the addition of *C. finmarchicus* absorption in the Gulf of Maine. Estimates are derived from the RRMSD 4 waveband spectral matching technique.

### 5.3.3 Application of spectral matching approach to the northern Norwegian Sea

The spectral matching approach was applied to the sub-scene from the northern Norwegian Sea from the 29<sup>th</sup> April 2017 (Figure 3.4c) for comparison in a less optically complex region where *in situ* data is available. This image was processed using the NASA standard AC, which appears to work relatively well across the image, with only small regions within the coastal fjords reaching high RRMSD values of 40% and over. This therefore allows for comparison with the  $\Delta E_{2000}$  results first presented in Chapter 3. Any pixels with negative spectra were removed from analysis. The four waveband RRMSD method was used to compare spectra from the northern Norwegian Sea to the standard Case 2 spectral LUT (1008) (Figure 5.6a) and a Case 2 spectral LUT with the addition to *C. finmarchicus* absorption (Figure 5.6b). In this analysis, the constrained Case 2 LUT with varying MSS and a total of 4410 unique spectra was utilised. The *C. finmarchicus* concentrations required to reach minimum RRMSD values for each pixel is presented in Figure 5.6c.

Again, results are similar to that of the  $\Delta E_{2000}$  approach, with relatively high minimum RRMSD values within the red patch (well over 0.1) (Figure 5.6a). This anomaly signal is largely resolved with the addition of *C. finmarchicus* absorption (Figure 5.6b). The anomaly signal associated with this red patch is stronger than that seen in the GoM, and the *C. finmarchicus* concentrations associated with it are generally higher than those seen in the GoM (Figure 5.6c). This is likely because the strong Norwegian Coastal Current in this region results in dense surface aggregations of *C. finmarchicus* in the Lofoten- Vesteralen (Dong et al., 2021). The *C. finmarchicus* concentration estimates derived from the spectral matching approach indicate high concentrations in the red patch, up to 150,000 individuals m<sup>-3</sup>. The very small number of residual anomalies associated with the coastal Fjords and the cloud cover suggest that AC has failed in these regions. This may be resolved in part with the per pixel AC method but is not significantly impacting spectral quality in the regions of interest.

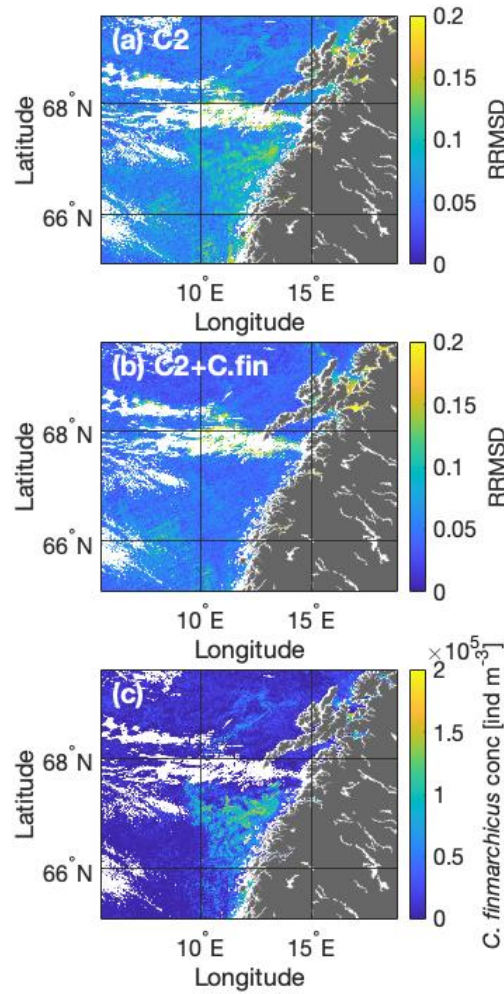


Figure 5.6 Minimum RRMSD map for spectral matching of the northern Norwegian Sea image (29<sup>th</sup> April 2017) with (a) a standard Case 2 spectral LUT and (b) a Case 2 spectral LUT with the addition of *C. finmarchicus* and (c) the *C. finmarchicus* concentrations estimates required to reach minimum RRMSD values. Data has been corrected using the NASA standard atmospheric correction.

The constituent concentrations required to reach minimum RRMSD values for spectral matching with a standard Case 2 model and a Case 2 model with the addition of *C. finmarchicus* absorption are presented in Figure 5.7. In the original  $\Delta E_{2000}$  analysis, the Case 2 LUT with the addition of *C. finmarchicus* had a static value  $0.03 \text{ g m}^{-3}$  for MSS, as MSS concentrations varied very little in the region. However, in this analysis,

the MSS was varied from between 0.01-1  $\text{g m}^{-3}$  to ensure the MSS constraint did not have a significant impact on constituent estimates. Despite this difference, concentration retrievals are very similar to that derived by the  $\Delta E_{2000}$  approach. When *C. finmarchicus* absorption is added to the model, CHL estimates within the patch increase, CDOM retrievals decrease and MSS remains stable. This all suggests that the RRMSD method is also behaving similarly to that of the  $\Delta E_{2000}$  approach in the northern Norwegian Sea.

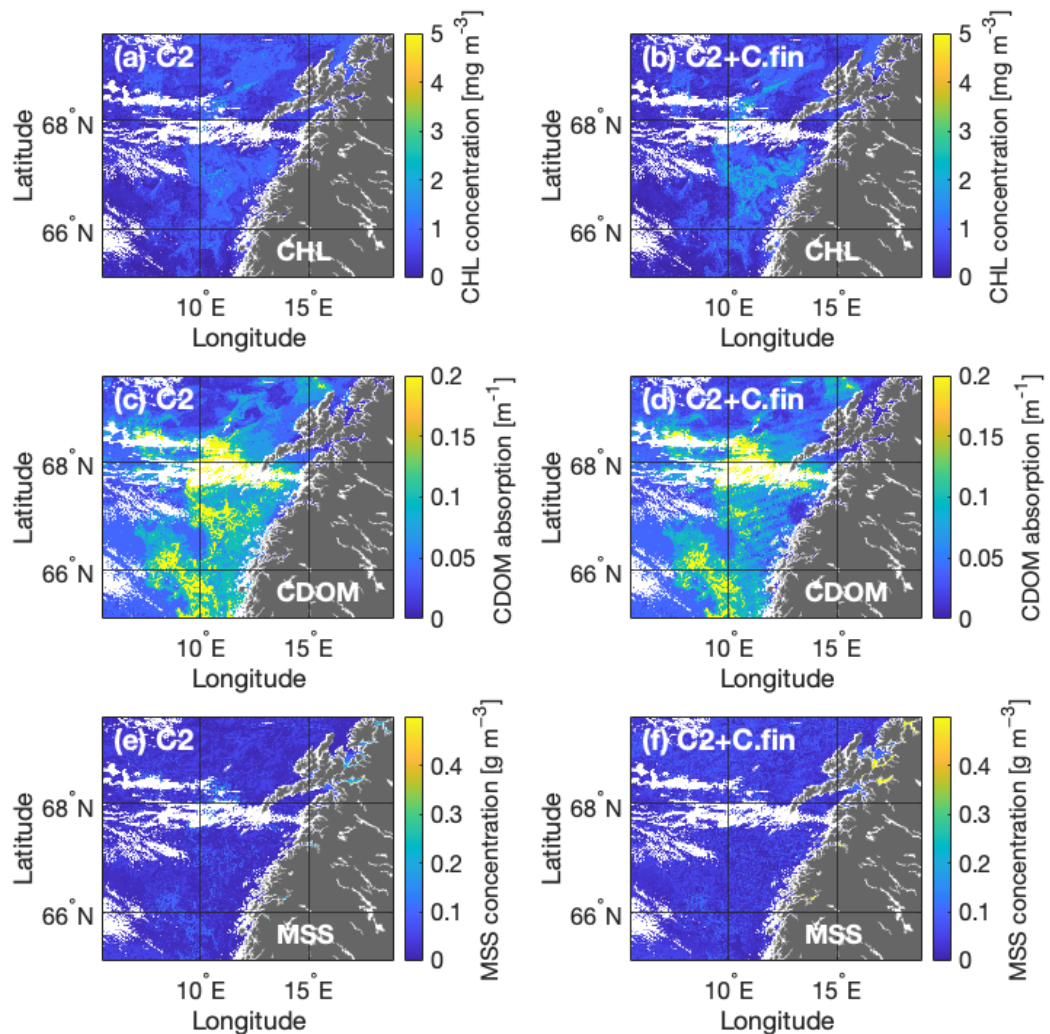


Figure 5.7 Constituent concentrations required to reach minimum RRMSD values with (a,c,e) the full Case 2 model and (b,d,f) the Case 2 model with the addition of *C. finmarchicus* absorption in the Northern Norwegian Sea. Estimates are derived from the RRMSD 4 waveband spectral matching technique. The data has been corrected using the NASA standard atmospheric correction.

#### 5.4 Comparison of *C. finmarchicus* concentration estimates derived from the $\Delta E_{2000}$ and the RRMSD spectral matching approaches

To compare *C. finmarchicus* concentration estimates from the  $\Delta E_{2000}$  and the RRMSD matching approach, difference maps were generated for both the GoM and the northern Norwegian Sea image (Figure 5.8).  $\Delta E_{2000}$  concentrations were taken away from concentrations derived from RRMSD and then normalised according to the maximum *C. finmarchicus* concentration value in the model. Therefore, in regions where the deviation of concentration estimates is at 1, RRMSD has estimated maximum concentrations of 150,000 ind m<sup>-3</sup> and the  $\Delta E_{2000}$  has generated estimates of 0. Conversely, in regions where the difference is -1, the  $\Delta E_{2000}$  approach has estimated concentrations of 150,000 ind m<sup>-3</sup>, whilst the RRMSD approach has estimated 0. The degree of divergence in concentration estimates between the two methods should be considered when assessing confidence in *C. finmarchicus* concentration retrievals. Generally, divergence in concentration estimates remains relatively low in the GoM (Figure 5.8a), with a mean divergence of -5,207 ind m<sup>-3</sup> and a median and mode divergence of 0 ind m<sup>-3</sup>. An overall negative mean divergence suggests the  $\Delta E_{2000}$  approach generates higher concentration estimates than that of RRMSD.

Slightly negative divergence is apparent within the south Nova Scotia and Georges Bank features. This suggests that the  $\Delta E_{2000}$  approach is estimating greater *C. finmarchicus* concentrations within the high concentration patches. Conversely, there is a large positive divergence in the centre of the image, suggesting the RRMSD approach is estimating high concentrations within this feature, whilst the  $\Delta E_{2000}$  approach is estimating concentrations close to 0 ind m<sup>-3</sup>. This provides further evidence that the high *C. finmarchicus* concentration estimates in this central feature are likely erroneous. Relatively high (positive and negative) divergence in the Bay of Fundy also indicate potential issues with *C. finmarchicus* concentrations in this region, associated with both  $\Delta E_{2000}$  and RRMSD.

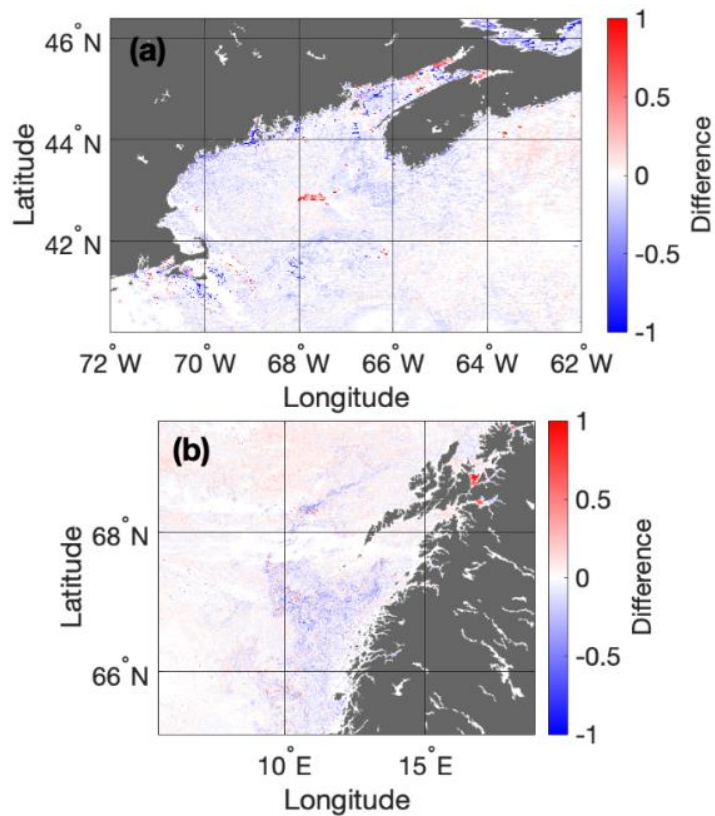


Figure 5.8 Normalised difference maps for the comparison of *C. finmarchicus* concentration estimates derived from the RRMSD spectral matching and the Delta E 2000 ( $\Delta E_{2000}$ ) colour matching approach (RRMSD- $\Delta E_{2000}$ ) in (a) the Gulf of Maine and (b) the northern Norwegian Sea.

A similar story is apparent in the northern Norwegian Sea, with generally low divergence in concentration estimates across the image (Figure 5.8b). The mean divergence between the two methods within the Norwegian Sea image is much smaller than that of the GoM at  $-88 \text{ ind m}^{-3}$ , whilst the median and the mode remains at  $0 \text{ ind m}^{-3}$ . Again, the negative mean aligns with the general trend of  $\Delta E_{2000}$  producing higher concentration estimates than RRMSD, with the smaller mean divergence likely associated with the relatively low optical complexity in this region. Within the red patch negative divergence is especially apparent, which again indicates that  $\Delta E_{2000}$  generally predicts higher *C. finmarchicus* concentrations than RRMSD in dense surface aggregations. Regions of high divergence in this image are

associated with the coastal Fjords, and are therefore likely AC artefacts, as this data has been corrected using the NASA standard AC method.

Whilst the RRMSD and  $\Delta E_{2000}$  generally agree on order of magnitude concentration estimates, RRMSD appears to consistently estimate lower concentrations within the surface *C. finmarchicus* patches compared to the  $\Delta E_{2000}$  approach. This corresponds with the lower anomaly signal produced by the RRMSD approach relative to  $\Delta E_{2000}$ . It is currently difficult to identify which method is closer to *in situ* concentrations, as evidence suggests that current ship-based methods of measuring *C. finmarchicus* concentrations *in situ* result in the under-estimation of population density due to animal evasion. However, comparison of the concentration estimates derived from these two methods provides a good amount of confidence in the order of magnitude estimates being generated.

#### 5.5 Establishment of an anomaly threshold for the targeted application of the *C. finmarchicus* model to ocean colour data

The blanket application of the *C. finmarchicus* model to address anomaly associated with the surface aggregations in the GoM has presented problems. Despite a relatively low  $\Delta E_{2000}$  anomaly signal along the coast with the application of the standard Case 2 model, high concentrations of *C. finmarchicus* were selected for these regions. Additionally, changes in Case 2 constituent concentrations, especially that of MSS, point to the occurrence of false optimisation in the model when *C. finmarchicus* is added. These problems persisted with the application of the RRMSD spectral matching approach to the GoM. However, the blanket application is not an issue when applied to the northern Norwegian Sea sub-scene. This suggests that in regions with a high degree of optical complexity, the addition of another bio-optical constituent can confound the retrievals.

One approach to overcome this issue is to apply a threshold of anomaly in order to target the application of non-standard bio-optical constituents to regions that are not well described by the standard bio-optical model. Thus, any pixels with an

anomaly value below the threshold will be considered 'solved' by the standard Case 2 model, and the CHL, MSS and CDOM values will remain the same. Only pixels with an anomaly value exceeding the implemented threshold will have the Case 2 model with *C. finmarchicus* applied, and constituent concentration estimates for these pixels will be derived from this more specialised model. Interestingly, this approach also allows for the possibility of several different solutions for each pixel, depending on the number of spectral matches that have a RRMSD value below the assigned threshold. This could result in a range of concentrations for each constituent rather than just one value derived from the best spectral match.

Whilst RRMSD has a less visually distinct anomaly signal relative to  $\Delta E_{2000}$ , the method is preferable as it can be applied to both Case 1 and Case 2 waters with very little data manipulation. Therefore in this section, the anomaly threshold was developed using the standard Case 2 minimum RRMSD map. The minimum RRMSD values of a small offshore area (denoted by the yellow box in Figure 5.9a, were averaged to determine the mean RRMSD value in a region where there is little optical complexity. Here, the only constraints on optical closure are most likely issues with the bio-optical model itself or any residual error associated with the satellite data, rather than the optical properties of the environment. Therefore, it can be assumed that this spectral matching approach will perform optimally in this region. The mean minimum RRMSD value calculated from the pixels in this offshore area was 0.053 (or 5% if expressed as a percentage). As a first attempt, the standard deviation of the minimum RRMSD values in this region (0.021) was multiplied by two and added to the mean to determine an anomaly threshold of 0.095. The pixels that exceed the RRMSD anomaly threshold are highlighted in yellow in Figure 5.9b. From this, it is evident that the majority of the 'red patch' south of Nova Scotia is of significant anomaly to have the *C. finmarchicus* specialist model applied to it. Conversely, the majority of the Georges Bank feature is considered 'solved' by the standard bio-optical model. In addition, whilst some residual anomalies around the coast remain, much of the coastal region is also well resolved by the standard bio-optical model. This largely eradicates the problem of erroneously high *C. finmarchicus* concentrations

along the coast. This suggests that whilst the anomaly maps generated by RRMSD spectral matching contain visually less distinct anomaly signals, numerically speaking the anomaly within the feature south of Nova Scotia is distinct enough to be highlighted as a region that requires the application of a specialist bio-optical model.

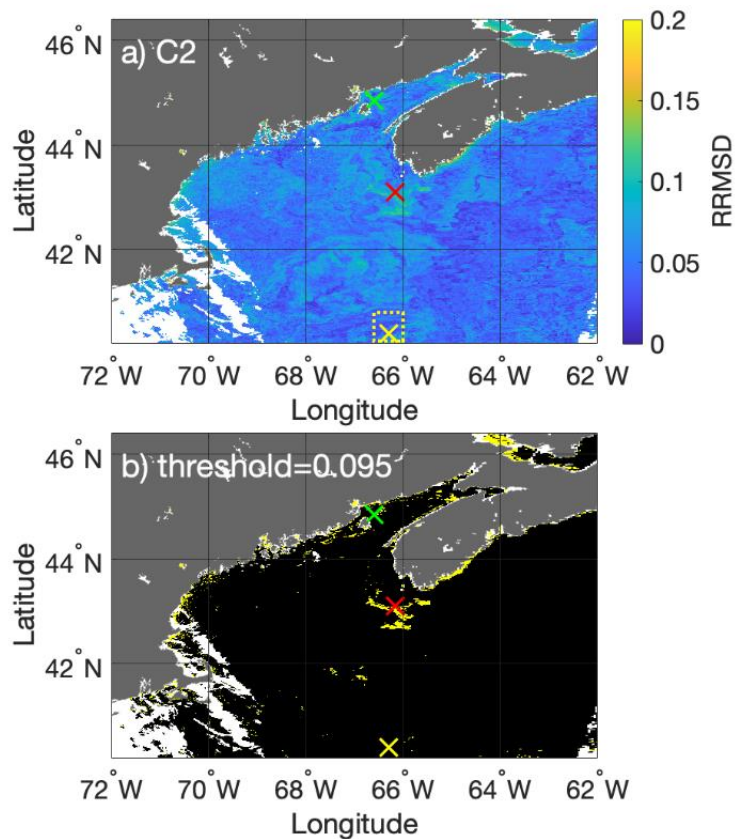


Figure 5.9 (a) Minimum RRMSD map for spectral matching of the Gulf of Maine (GoM) image with a standard Case 2 spectral LUT applied. The anomaly threshold of 0.095 was calculated using the mean value of the offshore area denoted by the yellow box (0.053) + 2 standard deviations (0.021). (b) Image of the GoM showing all pixels that exceed the anomaly threshold of 0.095 in yellow. All pixels that are 'solved' using a standard Case 2 model are represented in black. Pixels representing a coastal (green), in patch (red) and offshore (yellow) region are denoted by crosses.

Three pixels representing a coastal (green), in patch (red) and offshore (yellow) environment (Figure 5.9a) were tested with the anomaly threshold method. With the application of the standard Case 2 LUT containing 1008 unique spectra, both the coastal and offshore pixels are suitably solved. For the offshore pixel, four possible solutions have an RRMSD value of below 0.095, whilst for the coastal pixel, only two possible solutions achieve a RRMSD value of below the threshold. Conversely, the standard Case 2 spectral LUT does not provide any solution for the pixel in the patch, as the minimum generated RRMSD value was above the 0.095 anomaly threshold. Therefore, the Case 2 spectral LUT with the addition of *C. finmarchicus* absorption (a total of 4410 spectra) was applied to the in-patch pixel. With the application of this specialised model, a total of 37 solutions with RRMSD values below the threshold were generated, making the number of appropriate solutions much greater than that of the coastal and offshore pixels. The spectral solutions associated with each pixel tested are presented in Figure 5.10. What is immediately evident is that with the addition of *C. finmarchicus* into the model, very similar spectra are being produced with a variety of different constituent concentration combinations (Figure 5.10c). The number of possible solutions for the in-patch pixel illustrates that with increased bio-optical complexity, the spectral uniqueness of the LUT will likely be reduced. Table 5.2. summarises the constituent concentration ranges provided by all potential solutions for each pixel.

Table 5.2 Summary of possible solutions below the anomaly threshold for the offshore, coastal and in patch pixels using the Case 2 (C2) and Case 2 + *C. finmarchicus* (C2+Cal) bio-optical model.

Pixel ID	Model	Number of solutions	Av CHL ± 1SD [mg m <sup>-3</sup> ]	Av MSS ±1SD [g m <sup>-3</sup> ]	Av CDOM ± 1SD [m <sup>-1</sup> ]	Av Cal ± 1SD [ind m <sup>-3</sup> ]
Offshore	C2	4	0.05 ± 0.04	0.05 ± 0	0.01 ± 0	N/A
Coastal	C2	2	3.5 ± 1.5	0.13 ± 0.08	0.04 ± 0.03	N/A
In patch	C2+Cal	37	1.89 ± 0.31	0.06 ± 0.03	0.03 ± 0.02	60000 ± 31000

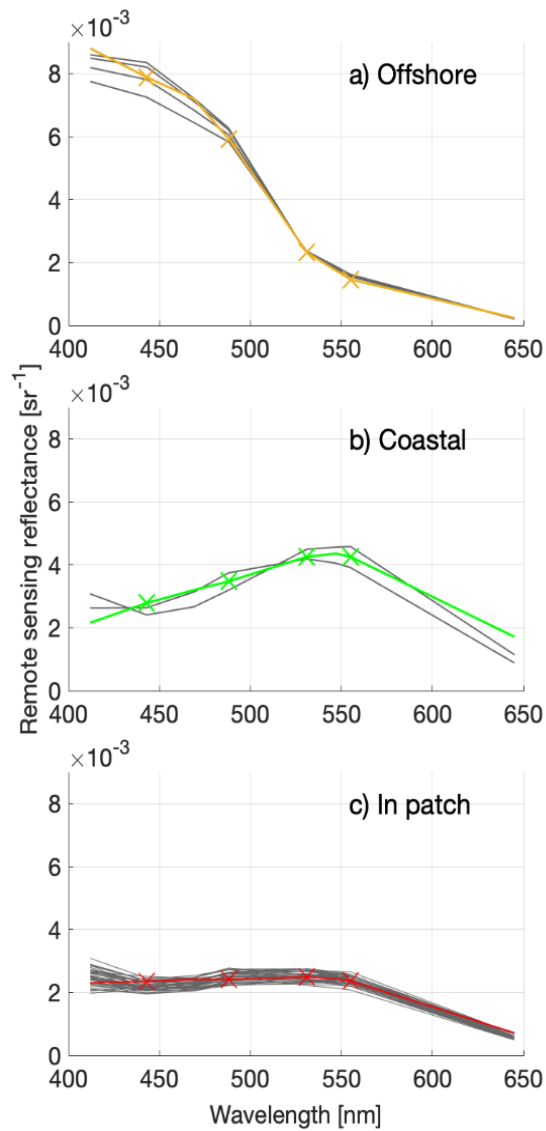


Figure 5.10 Satellite spectra for the (a) offshore, (b) coastal and (c) in patch pixels with all simulated spectral solutions for each pixel plotted in grey. The cross markers denote the location of the wavebands used in the spectral matching process.

The variation in constituent concentration estimates for the in-patch pixel is presented in Figure 5.11. Whilst possible CHL concentrations do not vary hugely (Figure 5.11a), MSS estimates are fairly evenly varied between 0.01 and 0.1  $\text{g m}^{-3}$  (Figure 5.11b). CDOM estimates vary between 0.01 and 0.07  $\text{m}^{-1}$ , with a broadly normal distribution in potential concentrations (Figure 5.11c). *C. finmarchicus* concentrations associated with in-patch spectral solutions show a wider spread than

any other constituent in the model, ranging from 10,000 ind m<sup>-3</sup> up to 120,000 ind m<sup>-3</sup> with a normal distribution around a mean value of 60,000 ind m<sup>-3</sup> (Figure 5.11d). It is evident from the *C. finmarchicus* distributions that the step-size in concentrations input into the model is influencing the variability. *C. finmarchicus* is more resolved in this model compared to CHL, MSS and CDOM which were all input in log space concentrations. Without prior knowledge of the impact of *C. finmarchicus* on  $R_{rs}$  signals, it was difficult to predict the appropriate concentration ranges to use in the model and as a result, *C. finmarchicus* were varied in a more linear fashion. This is likely influencing the high number of spectrally similar solutions for the in-patch pixel.

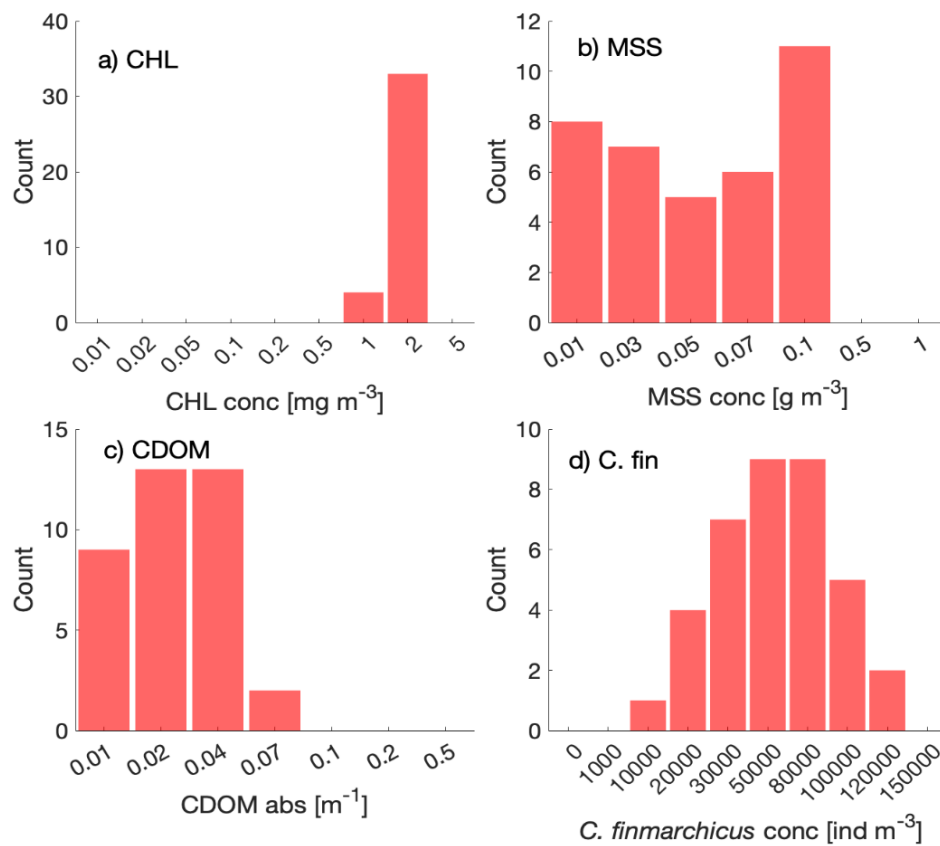


Figure 5.11 Constituent concentration estimates for the in patch pixel derived from all spectral match ups with a RRMSD value below the anomaly threshold of 0.095. Spectral matching was conducted using a Case 2 model with the addition of *C. finmarchicus* absorption.

As well as improving the erroneously high *C. finmarchicus* features observed after the previous blanket application of the specialised bio-optical model to optically complex regions, this method has the advantage of generating concentration range estimates on a per-pixel basis. This shifts the spectral matching technique from a deterministic approach, where concentration estimates are derived from the 'best' spectral match, to a probabilistic approach, where each pixel is assigned a range of plausible constituent concentrations. The final product generated from this approach would be a concentration map for each constituent, where each pixel is represented by the median concentration derived from all possible solutions.

## 5.6 Conclusions

This chapter describes the development of a spectral matching approach for the identification of *C. finmarchicus* from satellite derived ocean colour data. One of the aims of developing this approach was to improve on the  $\Delta E_{2000}$  anomaly detection method with the inclusion of more spectral information in the matching process, thereby improving the differentiation between the bio-optical constituents. However, indiscriminately increasing the number of spectral bands within the matching process did not aid in in-water anomaly detection. Likely the result of the inclusion of land/aerosol bands with low SNR, the minimum RRMSD map with the inclusion of all 8 MODIS wavebands (from 412 nm to 645 nm) lead to increased noise, and no significant signal from the potential patches of *C. finmarchicus*. Only when the spectral matching method was applied using 4 wavebands within the range that the  $\Delta E_{2000}$  method operates at (443 - 555 nm), was the noise reduced (generally below 10% RRMSD) and the anomaly signal visible. This suggests that waveband selection is not only important for the reduction of noise, but also targeted anomaly detection. *C. finmarchicus* absorption is most significant in the 430-550 nm range, thus the inclusion of the 645 nm waveband will reduce the relative impact of the copepod on spectral anomaly. Therefore, whilst the spectral matching approach does not afford significantly better spectral resolution relative to  $\Delta E_{2000}$ , it does allow for the flexibility

of waveband selection, depending on the constituent being targeted. For example, if a coccolithophore bloom was the target for detection, the inclusion of the 645 nm waveband may be desirable, as these organisms scatter strongly at the red-end of the spectrum.

The four waveband RRMSD spectral matching approach was identified as optimal for detecting surface swarms of *C. finmarchicus* and therefore was applied to the fully corrected GoM data, as well as the northern Norwegian Sea sub-scene. The constituent concentrations generated using the Case 2 and Case 2 model with the addition of *C. finmarchicus* were very similar to those produced by  $\Delta E_{2000}$  for both regions. Whilst this method generally worked well in the northern Norwegian Sea, the problem of erroneously high *C. finmarchicus* concentrations being assigned to pixels with a relatively low anomaly signal in the GoM persisted. This indicated that blanket application of the specialised Case 2 model with the addition of *C. finmarchicus* is not suitable for regions with a significant amount of optical complexity.

To overcome this, an anomaly threshold was developed that determined which pixels were 'solved' by a standard Case 2 model and which pixels require a more specialised model to achieve optical closure. When this protocol was tested on the chosen coastal, offshore and in patch pixels in the GoM image, both the coastal and offshore pixels were solved using the standard Case 2 model, with a varying range of possible constituent concentrations for each pixel. Conversely, the minimum RRMSD value of the in-patch pixel exceeded the anomaly threshold, thus requiring the specialised Case 2 model with the addition of *C. finmarchicus* absorption. This model yielded a total of 37 possible matches, giving a relatively broad range of possible concentration estimates for the pixel. Upon closer inspection of these concentration ranges, it became clear that the linear method of varying *C. finmarchicus* concentrations in the bio-optical model (as opposed to log space variation like the CHL, MSS and CDOM constituents) was influencing the variability and number of possible matches derived from the specialised model. For future work, it would be sensible to vary *C. finmarchicus* concentrations in log space, to reduce this variability and maintain spectral uniqueness in the LUT.

Whilst *in situ* validation is currently not available for the GoM image, the move from a deterministic to a probabilistic approach of extracting pixel-specific concentration estimates is likely to be more suited for establishing match ups with *in situ* data. Exact spatio-temporal match-ups are often extremely difficult to obtain and even when it can be achieved, a relatively small water sample (order of litres) is likely not wholly representative of the 1km<sup>2</sup> area covered by a single pixel. Therefore, determining a range of different constituent concentrations for each pixel provides a more realistic target for *in situ* validation. On a wider scale, a probabilistic approach would likely also benefit the continued developments of bio-optical models and data assimilation. For future work, the threshold approach will be applied across an image, with the final products being median constituent concentration estimates derived from all potential solutions of each pixel, along with an associated uncertainty product derived from the standard deviations for each pixel.

For the detection of *C. finmarchicus* specifically, it is important to consider the absorption measurements that are being used in this study. These absorption measurements were taken during the 2017 Sea Patches cruise and therefore should be somewhat representative of the Norwegian Sea population captured in the image on the 29<sup>th</sup> April 2017. However, there is currently no data on *C. finmarchicus* absorption properties in the Gulf of Maine. Whilst order of magnitude population estimates may hold between regions, there may be considerable variation in astaxanthin pigmentation between different populations. Further, astaxanthin levels can vary between individuals of the same population over relatively short time-scales, for reasons that are not currently understood (Vilgrain et al., 2023). Whilst this project makes the first attempt at identifying *C. finmarchicus* concentrations from space, a lot more work is needed to quantify the extent of pigmentation variation in these organisms, in order to account for that variance in future population estimates. A first attempt at looking at *C. finmarchicus* pigmentation variation is presented in the following chapter.

In general, whilst the  $\Delta E_{2000}$  and RRMSD approaches yield comparable results, there are many benefits to RRMSD that make it the favourable method for anomaly

identification. Unlike  $\Delta E_{2000}$ , no range is required to constrain the  $R_{rs}$  values in each waveband, as no visual element is required for analysis. This means that the spectral matching approach can be consistently applied to both coastal and open water environments, where reflectance values can vary significantly. Additionally, RRMSD allows for wavebands to be selected depending on the optical properties of the target constituent. The four waveband RRMSD approach worked well for the detection of *C. finmarchicus*, other wavebands may be more suitable for other organisms with different optical properties. As well as this, RRMSD is relatively simple and less computationally expensive than  $\Delta E_{2000}$ . All of this taken together, and with the development of an anomaly threshold to apply to images with significant optical complexity, the RRMSD spectral matching approach is the most practical method to carry forward into future work.

## 6 Experimental determination of the absorption properties of select zooplankton groups

### 6.1 Introduction

Ocean colour remote sensing signals are traditionally thought to be generated by mixtures of abundant yet relatively small particles (<100 µm), including algal material (CHL) and suspended sediments (MSS), as well as dissolved coloured materials (CDOM). As a result, extensive effort has been directed towards the optical characterisation of these constituents. However, this thesis, along with previous theoretical studies (Davies et al., 2021) has demonstrated the potential importance of larger ‘particles’ such as *C. finmarchicus* on the optical properties of the water column.

The global zooplankton biomass is dominated by the Crustacea groups Copepoda (including *Calanus finmarchicus*) and Eumalacostraca (including krill and amphipods), with copepods being the most abundant metazoan group of organisms on Earth (Schminke, 2007). Further, whilst the Cnidarians and Ctenophores (jellyfish and comb jellies) make up a relatively small proportion of the global biomass, surface swarms have reportedly been increasing in both size and frequency across the global coastal oceans (Purcell et al., 2007). All of these groups contain species that dwell in surface waters for part of their life cycle, with some, such as the Antarctic krill *Euphausia superba*, being regularly recorded in dense surface swarms (Harrison et al., 2020; E. J. Miller et al., 2019; Nicol, 2018). It would follow that, much like the surface swarms of *C. finmarchicus* that have been the focus of this thesis, these organisms may have the ability to influence surface reflectance signals to the extent that they could be visible from space.

The pigmentation in Crustacea are characterised by varying levels of carotenoid pigments. Of these carotenoid pigments, astaxanthin and canthaxanthin are the most dominant, with colours varying between yellow, orange, red and purple. These

pigments are thought to provide photo-protection for these organisms, amongst other ecological advantages (Vilgrain et al., 2023). Currently, little is known about the main drivers of inter and intra species pigmentation variation of zooplankton. Thus, gaining an understanding of the spectral absorption properties of these organisms will aid in both remote optical identification methods, as well as providing a greater understanding of the mechanisms of pigmentation variation within these groups.

IOP measurements of zooplankton have previously been a challenge, largely due to the bias of current measurement systems towards smaller particles as a result of generally small sample volumes. However, the Point Source Integrating Cavity Absorption Meter (PSICAM) has a cavity that holds nearly 400 ml of sample and measures absorption with a high degree of accuracy, free from scattering error (Röttgers et al., 2005). Following the serial addition method, zooplankton can be sequentially added to a seawater sample in order to determine a per-individual absorption spectra. This method was first utilised in Basedow et al. (2019) and the full methodology of this technique is described in Section 2.2.4.

Following from the previous work on measuring *C. finmarchicus* absorption in the Norwegian sea (Basedow et al., 2019) the main aim of this chapter is to begin to build a spectral absorption library for commercially and ecologically important zooplankton species that have the potential to influence satellite derived ocean colour signals. These spectra can then be implemented into the methodologies previously described in this thesis for the purposes of remote detection. Further, this chapter aims to investigate intra-species pigmentation variation, in order to understand how differences in the zooplankton assemblage could impact detection.

To achieve these aims, zooplankton samples were collected during a sampling trip to Loch Etive on 7<sup>th</sup> March 2022 and during the SFI Harvest cruise in the northern Norwegian Sea in June 2022. In addition to this, cultivated samples of micro jellyfish (*Aurelia aurita*) were obtained from the Marine Biological Association based in Plymouth. The spectral absorption properties of a total of 7 groups of zooplankton were measured in the PSICAM using the serial addition method. The zooplankton spectra were then incorporated into the radiative transfer model Ecolight to

determine their impact on  $R_{rs}$  signals. Finally, using the RRMSD anomaly threshold method described in Section 5.5., a concentration threshold of detection was calculated for each organism to determine the approximate surface concentration these organisms would need to reach to be identifiable from satellite derived ocean colour data.

## 6.2 Zooplankton sampling

### 6.2.1 *Loch Etive*

Live zooplankton samples were collected from Loch Etive in Scotland (Figure 6.1) on the 7<sup>th</sup> March 2022. Loch Etive is a regularly sampled sea loch on the west coast of Scotland that is of significant economic and ecological importance (Hicks, 2018). The loch is around 30 km in length and split into the upper and lower basin by a shallow sill called the Bonawe sill, which sits at 14 m depth. Loch Etive contains 96 categories of zooplankton, with a particularly large population of *C. finmarchicus* in the upper basin (Clark et al., 2012). Zooplankton samples were taken from the upper basin station RE5 (Figure 6.1), which is located at the deepest part of the loch, at depths of 146 m. Samples were collected using a WP2 plankton net with a 200  $\mu\text{m}$  mesh size (Hydro-Bios, GmbH, Germany) from 50 to 0 metres depth. Samples were sorted according to species, stored in water from Loch Etive and transported back to the laboratory. Here they were stored in a refrigerator at 5°C for a maximum of two days whilst the serial addition experiments were conducted.

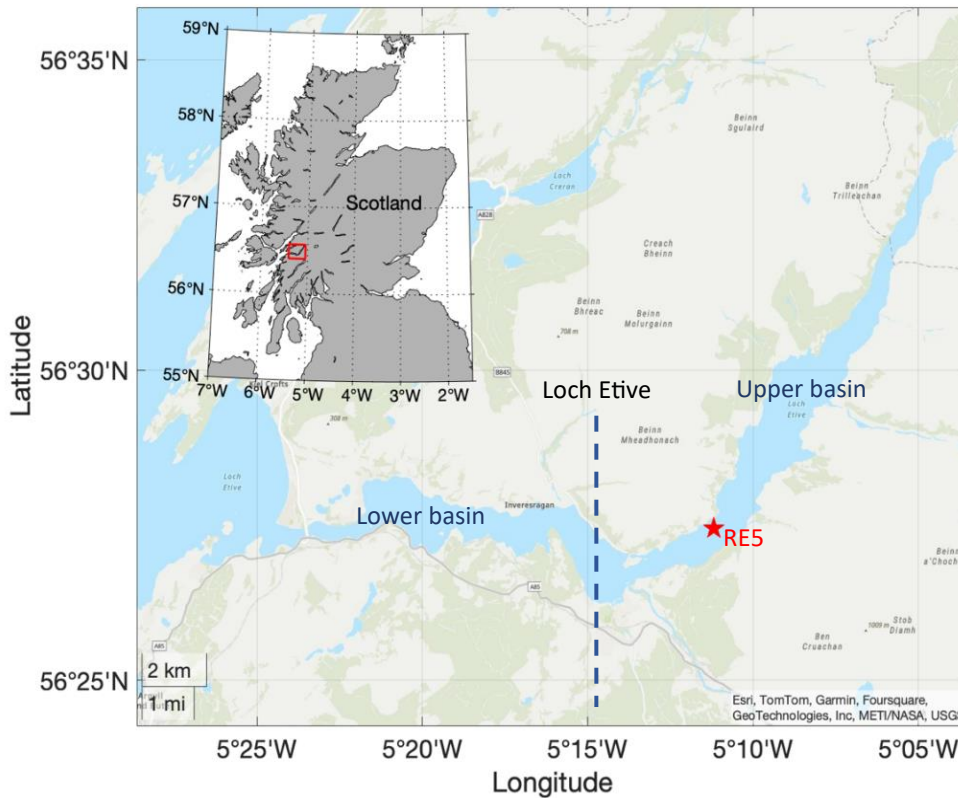


Figure 6.1 Map of Loch Etive, with the location of the sampled station RE5 denoted by a red star.

### 6.2.2 Northern Norwegian Sea (SFI Harvest)

Zooplankton samples were taken from the northern Norwegian Sea during the SFI Harvest cruise on board the R/V 'Helmar Hanssen' from 7<sup>th</sup> -14<sup>th</sup> June 2022. As the primary aim of this work was to make as many preliminary measurements of zooplankton absorption as possible, zooplankton samples were opportunistically taken largely from the upper 80 m across 5 different stations during the cruise (Figure 6.2). These samples were collected using three different types of plankton net: a MultiNet midi (0.25 m<sup>2</sup> opening, 180 µm mesh size, Hydrobios, Germany), as well as a Tucker Trawl (used primarily to collect krill samples) with a mouth opening of 1m<sup>2</sup>

and a 1000  $\mu\text{m}$  mesh size (Hydrobios, Germany). Once the samples were collected, the zooplankton were picked and sorted to genus level (and species level where possible). Once samples had been sorted, they were either measured directly or stored in a dark refrigerator at a temperature of 6°C until analysis was conducted. In all cases, samples were measured as closely to the time they were collected as possible. The maximum time the samples were left in the fridge before measurement was 6 hours.

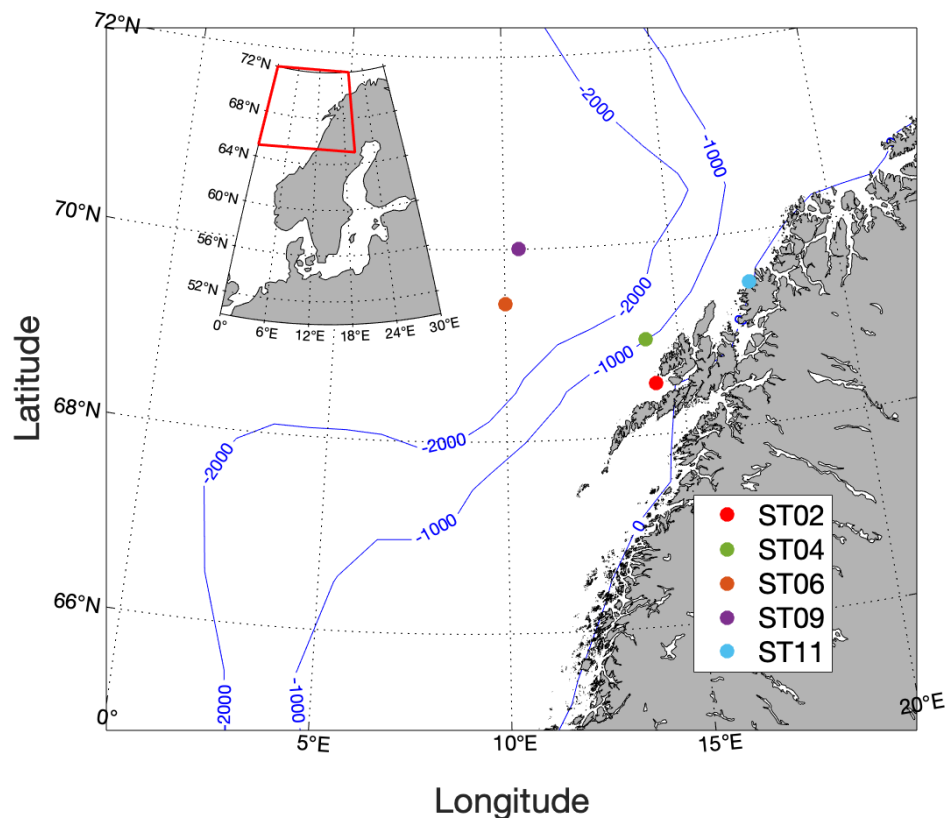


Figure 6.2 Map of stations sampled during the SFI Harvest cruise in the northern Norwegian Sea on board the R/V 'Helmar Hannsen' between 7th and 14th June 2022.

### 6.3 The absorption properties of select zooplankton groups

The absorption of several zooplankton samples obtained from the regions described above were measured using the PSICAM. These measurements were largely conducted using the serial addition method, which is fully described in

Section 2.2.4 but will be briefly outlined here for clarity. At each step of the experiment, a number of live zooplankton were sequentially added to filtered seawater, with purified MiliQ water providing a reference measurement. The number of individuals input at each step was dependent on the size and pigmentation of the organism being measured. Smaller organisms with little pigmentation required more individuals per addition to obtain a signal, whilst larger / more heavily pigmented organisms required fewer. Data were corrected for temperature and salinity effects following the protocol described by Lefering (2016). For each wavelength between 400 - 700 nm, a simple linear regression between the number of individuals and absorption at each wavelength produced the per- individual absorption spectra for each organism measured. The spectra were then divided by the volume of the PSICAM (384 ml) to get a concentration-specific absorption measurement. The number of measurements varied for each organism measured, largely due to sample availability and time constraints associated with handling live samples. Where good quality samples were available, at least three serial addition experiments were conducted for each organism. However, where this was not possible, as many experiments were conducted as the samples and time constraints allowed. Replicate experiments were always conducted on fresh samples.

### 6.3.1 *Calanus finmarchicus*

*C. finmarchicus* serial addition experiments were conducted for Loch Etive samples in March 2022 and northern Norwegian Sea samples during the SFI Harvest cruise in June 2022. A total of four serial additions were conducted for Loch Etive samples, with 7-15 individuals added during each step of the experiment (Figure 6.3 a,c,e,g). The high CDOM content of the Loch Etive resulted in high initial seawater absorption spectra, prompting the addition of more *C. finmarchicus* at each addition to ensure a distinguishable signal from the organisms. The relationship between absorption at 440 nm and the number of individuals at each step of the experiment shows a linear increase (Figure 6.3 b,d,f,h), which indicates the serial addition method

is working appropriately. Absorption at 440 nm increases from around 0.55 m<sup>-1</sup> with just seawater to over 0.74 m<sup>-1</sup> with the addition of 120 to 165 individuals.

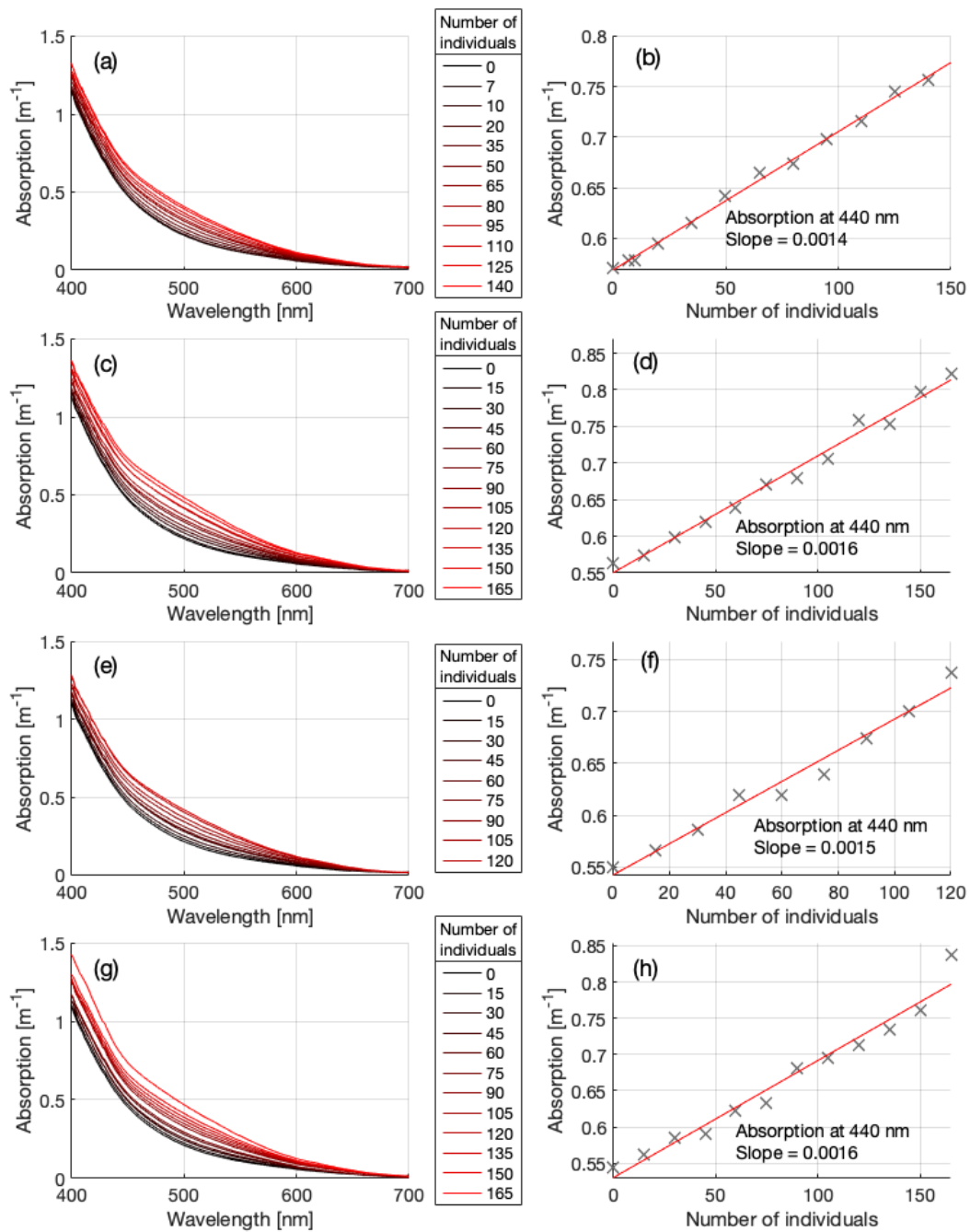


Figure 6.3 (a,c,e,g) Four *C. finmarchicus* serial addition experiments conducted on samples collected from Loch Etive on 7<sup>th</sup> March 2022 with (b,d,f,h) associated regression analysis between absorption and number of individuals at 440 nm. The slope of this regression represents the per-individual absorption value at 440 nm.

A total of two successful serial addition experiments were conducted using *C. finmarchicus* samples during the SFI cruise in June 2022. The samples used for these serial additions primarily consisted of C5 and adult *C. finmarchicus* and were taken from 80 to 0 m depth at station 9 (ST09) on 12<sup>th</sup> June 2022 (Figure 6.2). Whilst more samples were obtained during the cruise, it became apparent that rapid bleaching of the samples once removed from the water rendered them unrepresentative of the in-water population. Despite being kept in a dark refrigerator at 6 degrees (the same as the water temperature the samples were collected from), many of the *C. finmarchicus* samples would lose pigmentation in a matter of hours. Figure 6.4 shows a sample of *C. finmarchicus* freshly picked (a) and that sample after it had been left in the refrigerator overnight (approximately 10 and a half hours) (b). On one occasion, this rapid bleaching was observed to occur over a 3-hour period. The cause of this is unknown, as conditions within the refrigerator should have broadly matched those in the water column from which the samples were taken. Interestingly, this drastic bleaching over a short time period was not observed in either the Loch Etive samples, which were measured between 1-3 days after the samples were collected, or any other zooplankton groups measured during the SFI cruise. However, once this sample handling issue was identified, samples were picked and measured in the PSICAM as close to the time that they were taken from the water as possible.

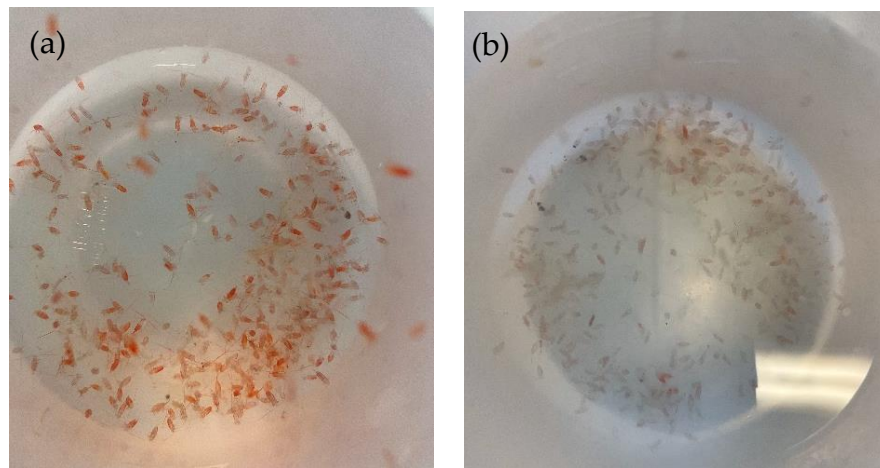


Figure 6.4 Two images of the same sample of *C. finmarchicus* obtained from station 9 during the SFI Harvoest cruise on 12<sup>th</sup> June 2022. Image (a) was taken at 10:39 pm, just after the sample had been collected and image (b) was taken at 9:10 am on the 13<sup>th</sup> June 2022, after the sample had been placed in a refrigerator at 6 degrees.

The two *C. finmarchicus* serial addition experiments were conducted at station 9 (ST09) during the SFI cruise are presented in Figure 6.5. During these experiments, seven or eight live individuals were added at each step. The initial seawater absorption measurement was much lower than that of Loch Etive, largely due to the relatively small amount of CDOM in the northern Norwegian Sea. In general, this population of *C. finmarchicus* appear to be having a larger impact on absorption relative to Loch Etive, which may be partly due to the lack of CDOM in the sample, as well as stronger absorption from these organisms. Absorption at 440 nm increases from just over 0.1 m<sup>-1</sup> to over 0.34 m<sup>-1</sup> with the addition of 64 and 68 individuals across both serial addition experiments.

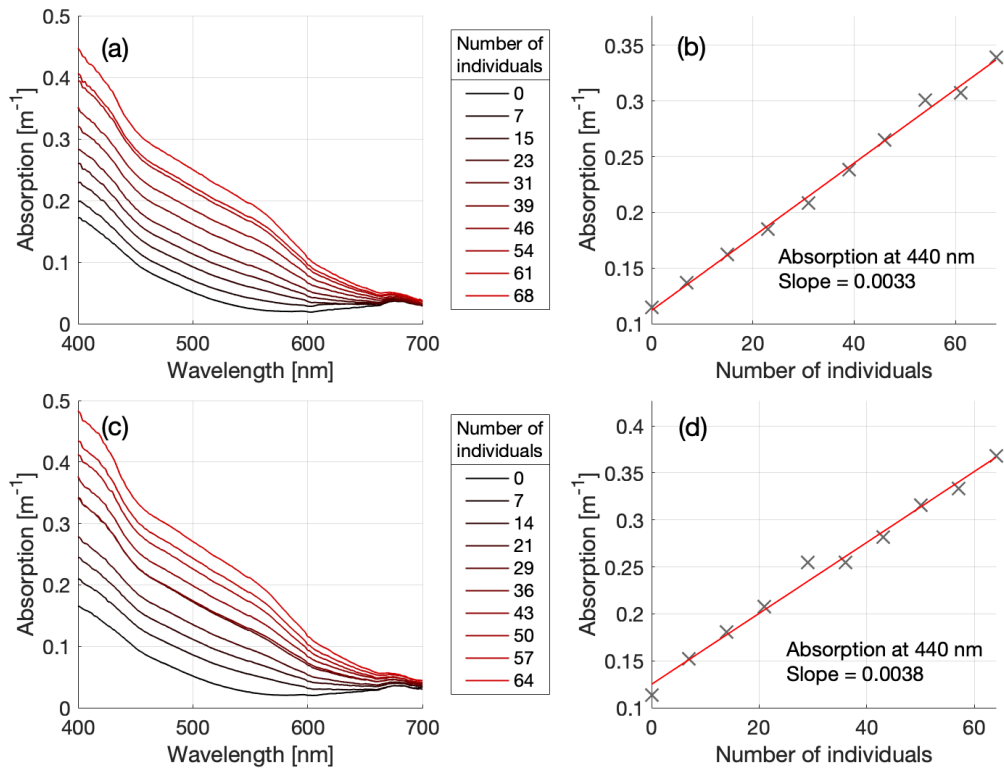


Figure 6.5 (a,c) Two *C. finmarchicus* serial addition experiments conducted at station 9 (ST09) on the 12<sup>th</sup> June 2022 during the SFI Harvest cruise in the northern Norwegian Sea, with associated (b, d) regression analysis between absorption and number of individuals at 440 nm. The slope of this regression represents the per-individual absorption value at 440 nm.

The per-individual absorption spectra derived from regression analyses of each serial addition from both Loch Etive and the SFI harvest cruise samples were then divided by the volume of the PSICAM (384 ml) to get a concentration-specific absorption spectrum. These spectra are presented in Figure 6.6, along with the concentration-specific absorption spectrum of *C. finmarchicus* that was measured during the SeaPatches cruise in 2017 for comparison. This spectrum was used for the *C. finmarchicus* modelling work previously presented in this thesis.

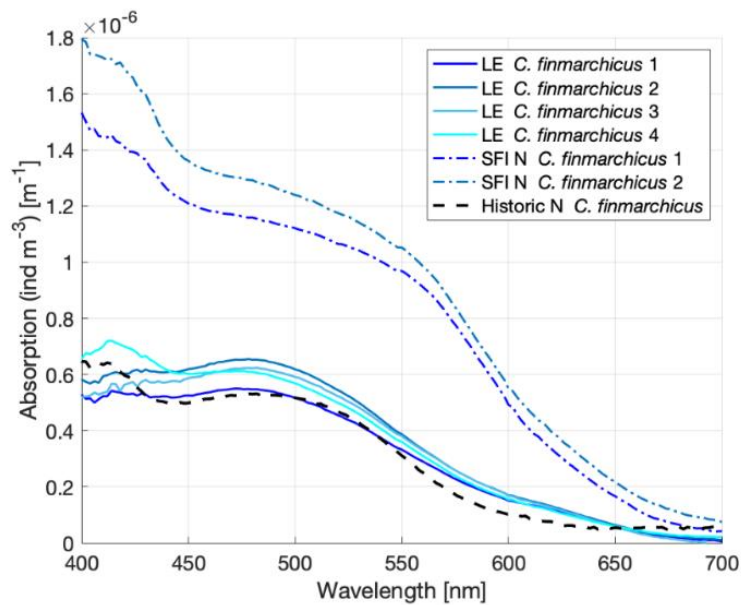


Figure 6.6 The per individual absorption spectra (per  $m^3$ ) derived from the four *C. finmarchicus* serial addition experiments conducted on samples from Loch Etive collected on 7<sup>th</sup> March 2022 (solid blue lines), as well as two conducted on samples from the Northern Norwegian Sea during the SFI Harvest cruise in June 2022 (dot-dashed lines). The black dashed line represents the historic *C. finmarchicus* absorption measurement taken during the Sea Patches cruise in May 2017, which has been plotted for comparison.

The *C. finmarchicus* absorption spectra derived from the serial addition experiments presented above show a large degree of variation between populations. The absorption spectra derived from the Loch Etive population appear to be very similar in both spectral shape and magnitude to that of the *C. finmarchicus* absorption measurement taken during the Sea Patches cruise of 2017. All spectra show the characteristic peak in absorption at around 480 nm, associated with the red pigment astaxanthin. However, these spectra differ considerably from those measurements taken during the SFI Harvest cruise in June 2022. These absorption spectra have a much greater absorption magnitude than that of the Loch Etive and historic Norwegian Sea measurement, as well as having a broader peak of absorption across the blue/ green part of the spectrum. Interestingly, some of the organisms measured during the SFI Harvest cruise had atypical pigmentation patterns. Generally,

astaxanthin is concentrated in the antennae of *C. finmarchicus*, with patches of the pigment also being associated with the urosome and lipid sac in the prosome (Figure 1.4a). However, as seen in Figure 6.4a, a large majority of the individuals sampled in Norway during June 2022 were almost entirely pigmented. Additionally, the *C. finmarchicus* samples collected during the June 2022 cruise appeared more orange in hue than the distinctly red samples taken from Loch Etive in March 2022. This is reflected in the broader peak of absorption across the blue/ green seen in the spectra from this population. Pigmentation also appeared to vary considerably within the Norwegian Sea population on a per-individual basis. Whilst variation in pigmentation between populations was expected, the degree of variation and its subsequent impact on absorption properties was an important result that has to be considered when modelling these populations in future work.

The primary driver of pigmentation variation within *C. finmarchicus* is unknown, largely due to lack of clarity on the primary ecological function of pigmentation in these organisms (Vilgrain et al., 2023). These results suggest that geography does not play a significant factor, as the Loch Etive absorption spectra and the Norwegian Sea spectra from May 2017 look very similar. Conversely, the two Norwegian Sea spectra measured in 2017 and 2022 differ greatly. A possible explanation for the variation in the Norwegian Sea 2022 population relative to the other measurements is the difference in the light field in the northern Norwegian Sea in June. The SFI Harvest cruise took place during 24 hour daylight between the 7<sup>th</sup> and 13<sup>th</sup> June 2022, whilst the Sea Patches cruise took place between the 28<sup>th</sup> April and 4<sup>th</sup> May 2017. During this time of year, the sun still sets and the region experiences total darkness for around 4-5 hours. Further, Loch Etive always experiences day-night cycles, as it is not far north enough to be exposed to 24 hour daylight/ darkness. One of the leading hypotheses to explain pigmentation in these organisms is the ability for astaxanthin to provide photoprotection against oxidative damage of the lipid sac, caused by sunlight (Vilgrain et al., 2023). Following this line of thought, it could be hypothesized that at times of the year when the sun does not set below the horizon, the astaxanthin content of these organisms may increase in response to increased

exposure to light in general and potentially UV in particular. However, it is clear that a lot more work needs to be done to test this hypothesis, as well as quantify the extent of pigmentation variation in *C. finmarchicus* on different spatio-temporal scales.

### 6.3.2 *Calanus hyperboreus*

*Calanus hyperboreus* is another species of copepod primarily found in the Arctic ocean. Whilst *C. finmarchicus* dominate the copepod biomass in the Norwegian basin, *C. hyperboreus* are also important organisms, especially in regions that are heavily influenced by cold Arctic waters. As a sister species of *C. finmarchicus*, they appear visually very similar, also containing the red pigment astaxanthin. However, the main distinguishing factor between these species is the considerable size difference. Adult *C. finmarchicus* typically range between 2-4 mm, whilst *C. hyperboreus* are much larger, ranging between 5-7 mm in length. As a larger, more nutrient dense organism, they represent an important food source for many Arctic and sub-Arctic fish populations (Conover, 1988). These organisms typically inhabit a temperature niche with maximum abundances in the northern Norwegian Sea being found to occur at water temperatures between 1-2°C (Strand et al., 2020). As a result, they are considered an important indicator species in climate change studies, and so understanding the potential for remote detection of these organisms is important. These organisms have a similar life cycle to *C. finmarchicus* and can be found from surface waters to depths of up to 5,000 m during over-wintering periods, so surface detection is possible depending on the abundances required to impact a satellite ocean colour signal.

Relatively few *C. hyperboreus* individuals were collected throughout the cruise and as a result only one serial addition experiment could be conducted. These individuals were sampled from the top 80 m at ST09 on 12<sup>th</sup> June 2022. As these organisms are much larger than *C. finmarchicus*, only four individuals were required at each step of the experiment in order to achieve a signal. The *C. hyperboreus* serial addition, as well as the regression between number of individuals and absorption

signal are presented in Figure 6.7. The addition of *C. hyperboreus* seems to have a sizeable impact on the seawater absorption signal, with absorption at 440 nm going from  $0.11 \text{ m}^{-1}$  to around  $0.37 \text{ m}^{-1}$  with the inclusion of 36 individuals (Figure 6.7b).

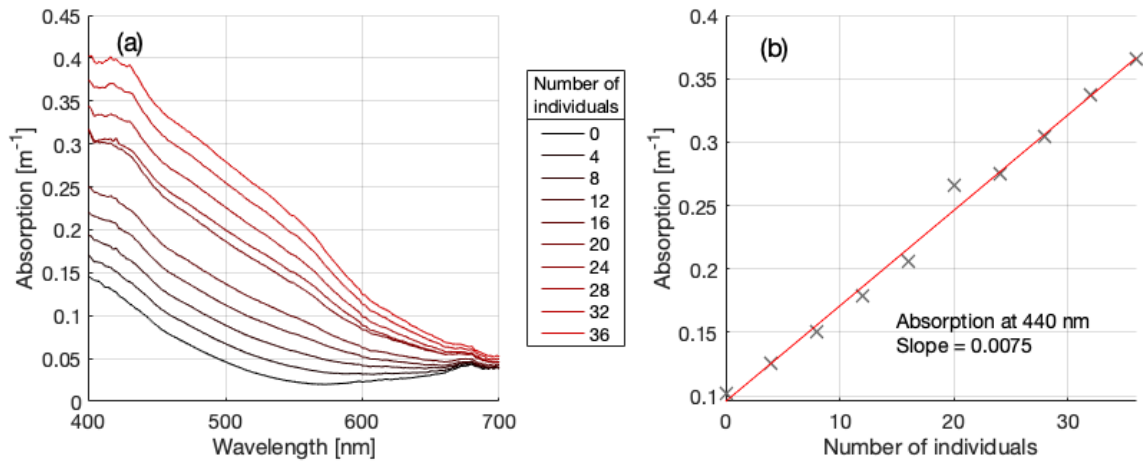


Figure 6.7 (a) *C. hyperboreus* serial addition experiment conducted at station 9 on 12<sup>th</sup> June 2022 during the SFI Harvest cruise in the Northern Norwegian Sea, with associated (b) regression analysis between absorption and number of individuals at 440 nm. The slope of this regression represents the per-individual absorption value at 440 nm.

The resulting concentration specific per-individual absorption spectra of *C. hyperboreus* is plotted in Figure 6.8. The spectral shape is comparable to that of the Norwegian Sea *C. finmarchicus* spectra (Figure 6.8), with a relatively broad peak in absorption across the blue/ green part of the spectrum, with a reduction in absorption towards the red end.

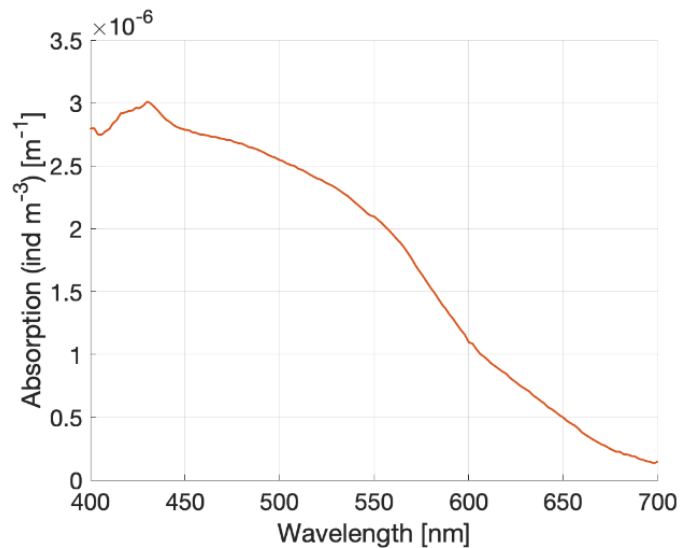


Figure 6.8 The concentration specific per-individual absorption spectra (per  $m^3$ ) derived from the *C. hyperboreus* serial addition experiment conducted on samples from station 9 (ST09) on 12<sup>th</sup> June 2022 during the SFI Harvest cruise in the Norwegian Sea in June 2022.

### 6.3.3 *Paraeuchaeta norvegica*

*Paraeuchaeta norvegica* is a carnivorous copepod species that range from 5- 11 mm in length at maturity and are prevalent in the North Atlantic and Arctic oceans. Much like the other copepod species presented, these organisms are largely transparent but contain carotenoid pigments, most notably astaxanthin. These organisms live throughout the water column, usually at greater depths in winter and early spring, with shallower distributions in the summer and autumn months (Vestheim et al., 2005). Larger individuals within a population, especially mature females with attached egg sacs, remain at greater depths than smaller individuals. This is thought to reduce the risk of predation from visual predators at the surface, as larger individuals will have greater energy reserves and can therefore prioritise predator avoidance over feeding in the surface waters (Vestheim et al., 2005).

The *P. norvegica* sample used in this study was taken from Loch Etive on 7<sup>th</sup> March 2022. Within the Loch Etive sample, which was taken from 50 to 0 m depth,

both mature ovigerous females and smaller non-ovigerous individuals were present. Therefore, the serial addition experiments were partitioned into larger female *P. norvegica* with egg sacs, and smaller *P. norvegica* individuals without egg sacs. The serial addition experiments of both female *P. norvegica* with eggs and smaller *P. norvegica* without eggs are presented in Figure 6.9. The serial addition experiments and absorption measurements at 440 nm indicate that the larger *P. norvegica* with the egg sacs have a more significant influence on the absorption signal than the smaller individuals, which was expected as the individuals in this sample were larger and the egg sacs were relatively large and dark in colour.

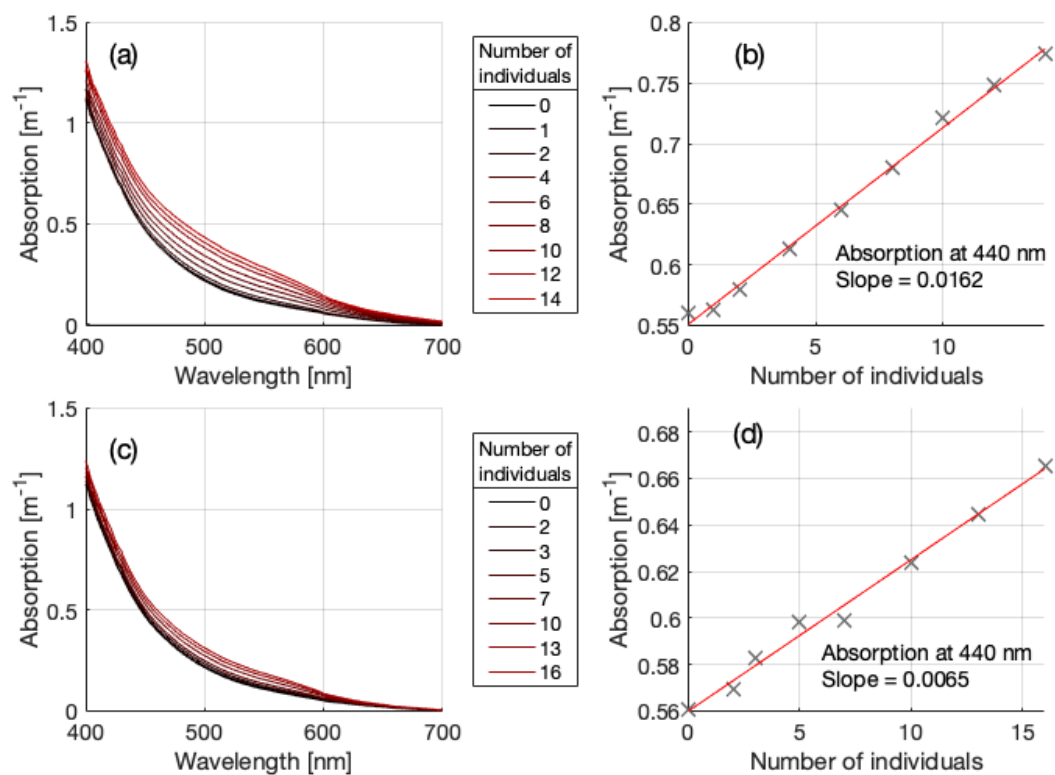


Figure 6.9 *P. norvegica* serial addition experiments conducted at Loch Etive on 7<sup>th</sup> March 2022. Serial addition experiments were divided into (a) larger females with egg sacs and (c) smaller individuals, with associated (b and d) regression analysis between absorption and number of individuals at 440 nm. The slope of this regression represents the per-individual absorption value at 440 nm.

The concentration specific per-individual absorption spectra of the *P. norvegica* samples illustrates the difference in absorption properties between the larger females with egg sacs attached and the smaller individuals (Figure 6.10). The magnitude of the mature *P. norvegica* females with egg sacs is almost three times greater than that of the smaller *P. norvegica* individuals at 440 nm. Interestingly, despite the presence of the dark egg sacs, the predominant signal from the mature female *P. norvegica* still appears to be associated with the astaxanthin pigment, as absorption peaks at 480 nm. However, relative to the spectral shapes of the other zooplankton species measured thus far, the absorption at the red end of the spectrum is stronger. This signal is likely associated with the dark, almost black, eggs within the egg sac. Conversely, the smaller *P. norvegica* individuals have nearly no absorption at the red end of the spectrum, likely due to the absence of eggs within this sample. Whilst the dominant feature of the absorption spectra of the smaller individuals also appears to be associated with the astaxanthin pigment, the peak at 480 nm is not as pronounced as that derived from the mature females with eggs.

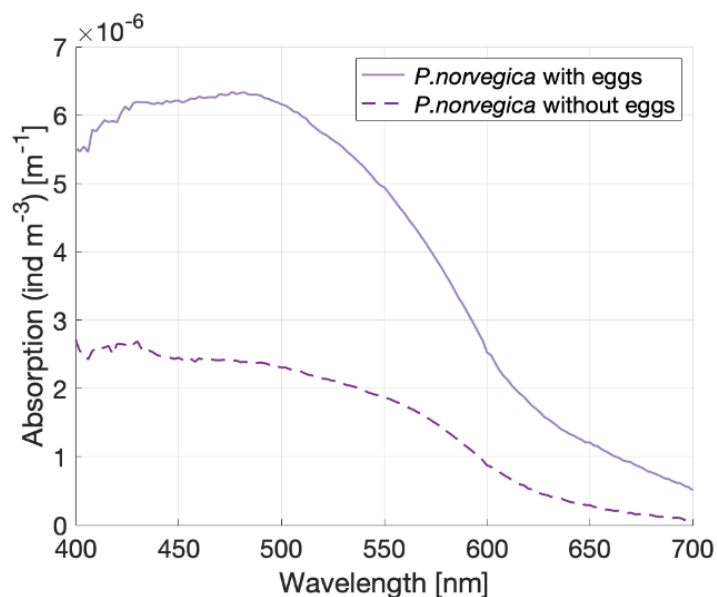


Figure 6.10 The per individual absorption spectra (per m<sup>3</sup>) derived from the *P. norvegica* serial addition experiment conducted on samples from Loch Etive collected on 7<sup>th</sup> March 2022. The

*solid line represents the absorption spectra from mature females with an attached egg sac and the dashed line represents smaller individuals without an egg sac.*

Generally, these results illustrate the potential variation in absorption spectra between individuals of the same species within the same population but at different stages of the life cycle. This highlights the need for work to be done on fully characterising pigmentation variation within zooplankton species.

#### 6.3.4 *Meganyctiphanes norvegica*

*Meganyctiphanes norvegica* are a species more commonly known as northern krill. These organisms are present in the North Atlantic and sub-Arctic environments and can reach up to 4 cm in body length. The adult *M. norvegica* measured in this study were collected from station 11 (ST11) (Figure 6.2) at 300 m depth on 13<sup>th</sup> June 2022 during the SFI harvest cruise in the Northern Norwegian Sea (Figure 6.11). Typically, these organisms are found at depth, but have been recorded swarming at the surface within the Bay of Fundy, turning the surface waters ‘a vivid red’ colour that was visible from both a boat and helicopter (Nicol, 1984, 1986). Like the copepod species sampled in this study, *M. norvegica* contain a number of carotenoid pigments, including astaxanthin. As a result, these organisms have the potential to influence satellite derived ocean colour signals. *M. Norvegica* play an important ecological role in the northern hemisphere, not only as a contributor to the biological carbon pump, but also as a food source for groundfish, squid, baleen whales and seabirds (Tarling et al., 2010). Thus, being able to remotely monitor these populations over large spatio-temporal scales would provide important insights into ecosystem health and potentially inform management strategies.



Figure 6.11 Image of *M. norvegica* sample retrieved from 300 m depth on 13<sup>th</sup> June 2022 during the SFI Harvest cruise in the northern Norwegian Sea.

In the southern hemisphere, the krill species *Euphausia superba*, otherwise known as Antarctic krill, fulfils a similarly important ecological role as the main prey source for many top predators. However, the Southern Ocean is also home to some of the largest krill fisheries in the world, with *E. superba* as the target species (Botterell et al., 2023). As these species are critical in the Southern Ocean ecosystem, careful monitoring and management of these populations is of vital importance to ensure this species is not irrevocably over-exploited. Whilst *E. superba* are larger than their northern counterparts, reaching up to 6 cm in size, they are visually similar in appearance, and also contain red pigment astaxanthin. Thus, whilst samples of *E. superba* were not available for this work, it reasonable to infer that absorption spectra of *M. norvegica* could provide some understanding of the potential of remotely monitoring krill populations in the Southern Ocean, where ship-based sampling can be notoriously challenging.

A problem was encountered when the serial addition method was applied to the *M. norvegica* samples. At certain points throughout the measurement process, the absorption signal would inexplicably jump, leading to erroneously high absorption measurements. This was unlikely to be related to the stability of the fibre optic connections, which is the most common source of instability, as these were regularly checked. Further, this issue was not prevalent when measuring any of the other samples. As these organisms were considerably larger and much more mobile than the others measured, it is possible that they were disrupting the uniformity of the light field within the cavity. During the measurement processes, these organisms were continually moving around the PSICAM. Therefore, it is possible that one or more of the individuals moved directly under the sensor and/ or the light source, resulting in an anomalous jump in the absorption measurement.

However, as these organisms were so large and pigmented, their absorption signal could be measured on an individual basis. This approach is, in fact, advantageous as it provides more information on the variation in pigmentation and absorption properties between individuals within the same sample. To accommodate this, the data processing procedure was adapted to yield absorption measurements from the attempted serial additions. At each addition, one live organism was added on a step-wise basis to filtered seawater. However, instead of regression analysis determining the per-individual absorption at each wavelength, the absorption spectrum at each step in the experiment was subtracted from the spectrum of the previous step, and the erroneous measurements were excluded from analysis. As only one individual was added to the experiment at a time, this provided a per-individual absorption spectrum. Following this processing method, a total of 11 absorption spectra of adult *M. norvegica* were collected. The mean concentration-specific absorption spectra and standard deviation is plotted in Figure 6.12.

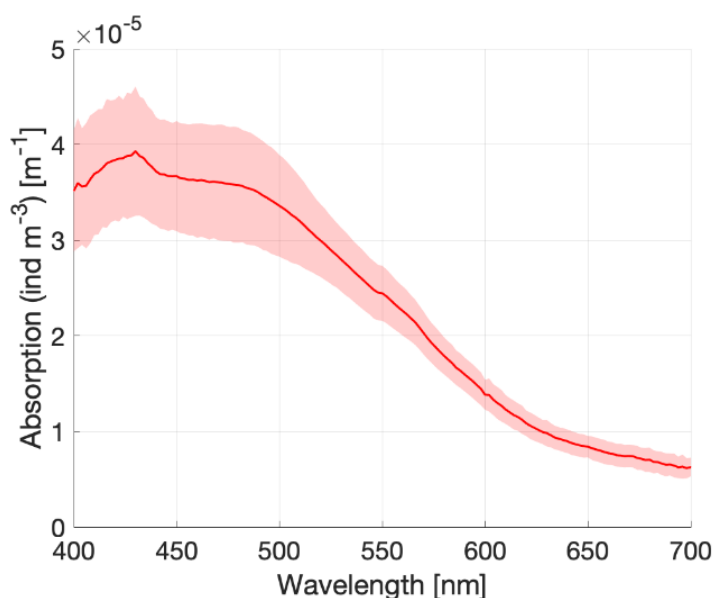


Figure 6.12 The mean per individual absorption spectra (per  $m^3$ ) of *M. norvegica* on samples from station 11 of the SFI Harvest cruise in the northern Norwegian Sea collected on 13<sup>th</sup> June 2022. The mean is derived from 11 individual absorption spectra and the shaded area represents  $\pm 1$  standard deviation from the mean.

The *M. norvegica* absorption spectral shape looks very comparable to the other species measured in this study, with the characteristic absorption peak at 480 nm associated with astaxanthin. In addition, this spectrum shows absorption in the red end, likely due to the black eyes of *M. norvegica* that will absorb across the spectrum.

#### 6.3.5 *Limacina* spp.

*Limacina* is a genus of pteropod, commonly referred to as sea butterflies, that are ubiquitous in the ocean. These organisms are up to 6 mm in length, have calcium carbonate shells of aragonite and are semi-transparent with a darkly pigmented body. Pteropods are typically located in the upper portion of the water column (0-150 m), with maximum abundances above 50 m depth (Maas et al., 2020). Due to their abundance and calcium carbonate shells, these organisms play an important role in the carbonate pump in polar environments, and are a good indicator species for ocean

acidification. The samples collected in this study were taken from the upper 30 m at station 2 (ST02), the shelf station 4 (ST04) and station 6 (ST06) between 8<sup>th</sup> and 11<sup>th</sup> June 2022 on the SFI cruise in the northern Norwegian Sea and largely consisted of the cold water species *Limacina retroversa*, with the potential of a few *Limacina helicina* included.

Three *Limacina* serial addition experiments were conducted throughout the SFI harvest cruise on samples from ST02, ST04 and ST06 (Figure 6.2). At each step, 3 to 4 of the organisms were sequentially added to the filtered seawater sample. It appears from the serial addition experiments that, unlike the other species measured in this study, the inclusion of *Limacina* into the seawater sample results in a proportional increase in absorption across the entire spectrum (Figure 6.13 a,c,e).

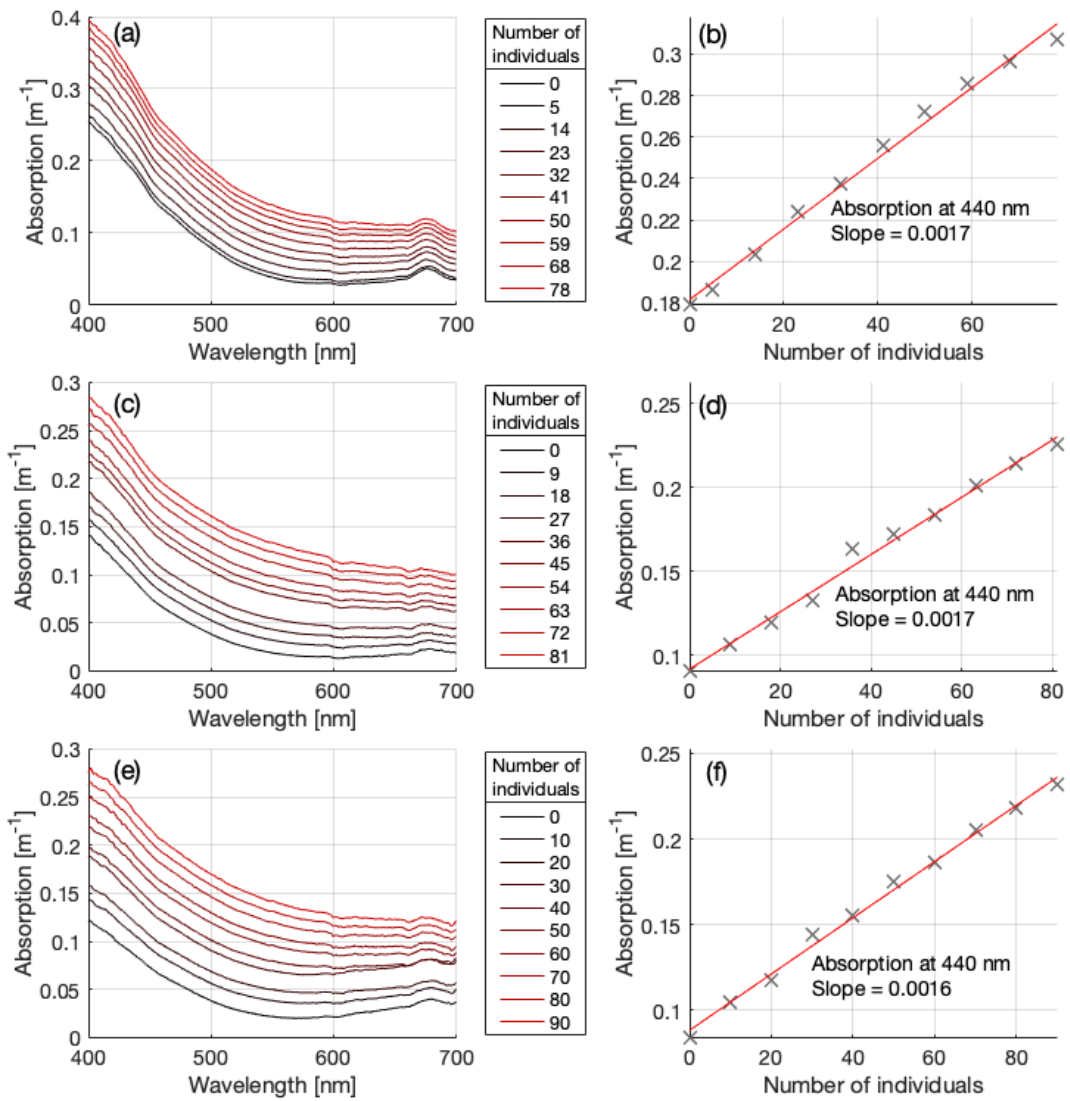


Figure 6.13 *Limacina* spp. serial addition experiments conducted on samples from (a) station 2 on the 8<sup>th</sup> June 2022 (c) station 4 on 9<sup>th</sup> June 2022 and (e) station 6 on 10<sup>th</sup> June 2022 during the SFI Harvest cruise in the northern Norwegian Sea. (b, d and f) represent regression analysis between absorption and number of individuals at 440 nm. The slope of this regression represents the per-individual absorption value at 440 nm.

The resulting absorption spectra for each of the *Limacina* serial additions are relatively featureless in spectral shape, and appear to absorb fairly evenly across the spectrum, with only a very slight reduction in the red wavebands (Figure 6.14). This is likely due to the dark brown/ black colouration of the body. Whilst measuring the

absorption of these organisms means it is now possible to model their impact on ocean colour remote sensing signals, without any clear spectral signature it would be extremely difficult to identify surface populations of *Limacina* from satellite imagery alone.

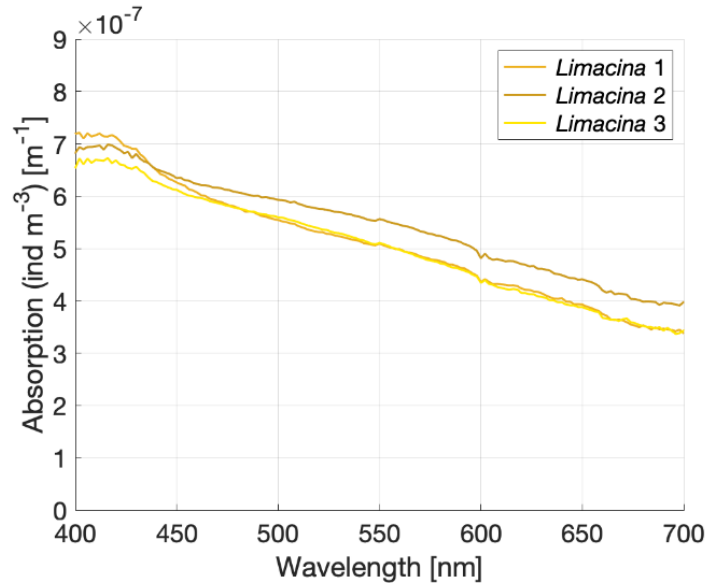


Figure 6.14 The per individual absorption spectra (per  $m^3$ ) derived from the three *Limacina* serial addition experiments conducted on samples from station 2 (*limacina* 1) station 4 (*limacina* 2) and station 6 (*limacina* 3) during the SFI Harvest cruise in the northern Norwegian Sea in June 2022.

### 6.3.6 *Parathemisto* spp.

*Parathemisto* is a genus of carnivorous amphipod that are most prevalent within the cold waters of the high latitudes. Here, these organisms are third in numerical abundance within the holoplanktonic zooplankton assemblage, behind copepods and krill. *Parathemisto* species live over wide depth ranges, and have been recorded to exhibit near- surface swarming behaviour during the reproductive phase, which occurs in summer (Dunbar, 1946; Havermans et al., 2019; Kim & Oliver, 1989). The *Parathemisto* spp measured in this experiment were sampled from the upper 30 m at ST02, ST04 and ST06 between 8<sup>th</sup> and 11<sup>th</sup> June during the SFI Harvest cruise in

the northern Norwegian Sea. These organisms were uniformly a dark purple/ brown in colour and are pictured for visual reference in Figure 6.15.



Figure 6.15 Image of a *Parathemisto* sample taken from station 4 (ST04) on 9<sup>th</sup> June 2022 during the SFI Harvest cruise in the northern Norwegian Sea.

A total of three *Parathemisto* spp serial addition experiments were conducted, and are presented in Figure 6.16. For each addition, 3-4 organisms were added to the sample. Similar to that of the *Limacina* serial additions, the addition of *Parathemisto* to the seawater sample appears to proportionally increase the absorption signal across the spectrum.

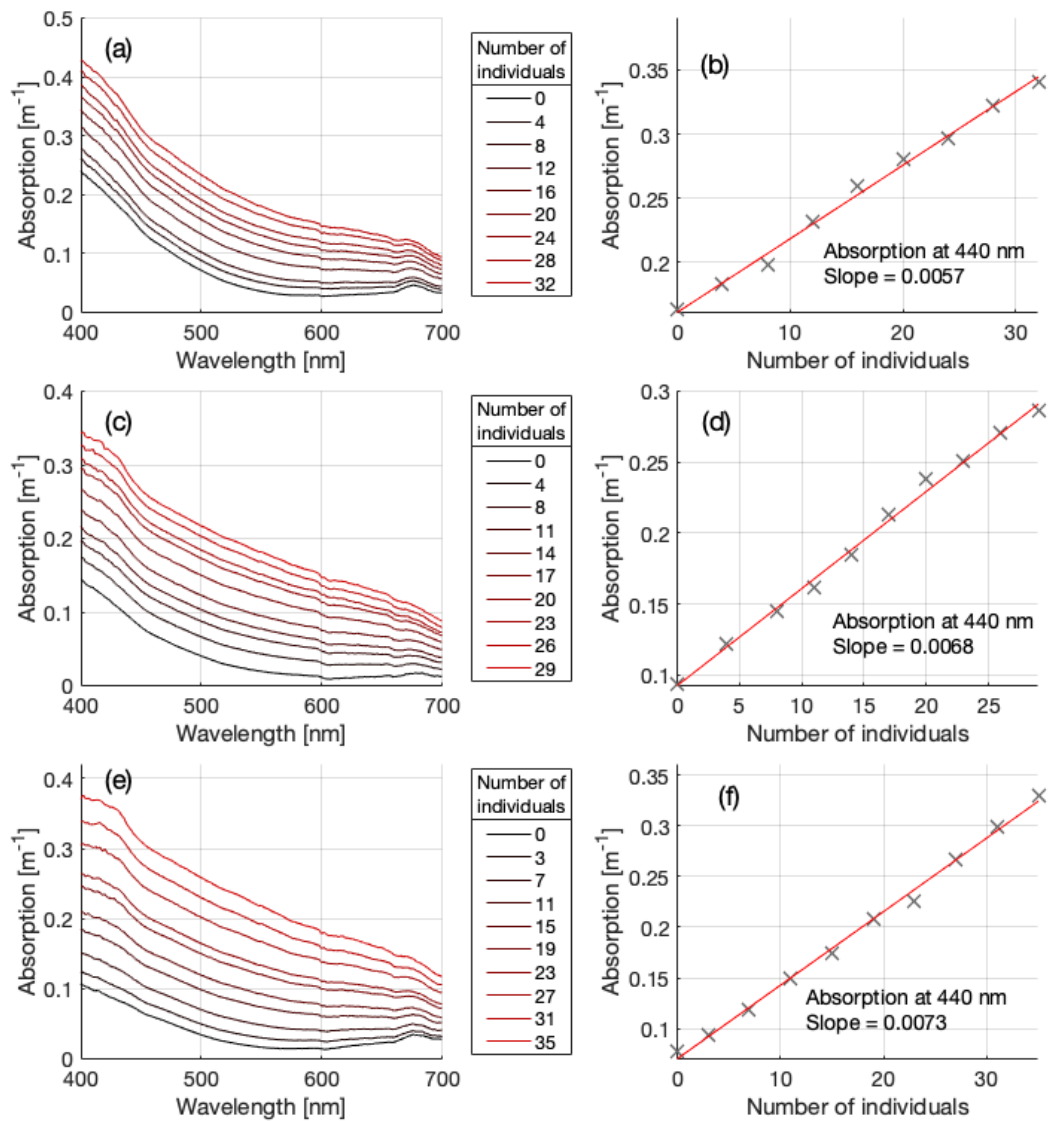


Figure 6.16 *Parathemisto* spp. serial addition experiments conducted on samples from (a) station 2 on the 8<sup>th</sup> June 2022 (c) station 4 on 9<sup>th</sup> June 2022 and (e) station 6 on 10<sup>th</sup> June 2022 during the SFI Harvest cruise in the northern Norwegian Sea. (b, d and f) represent regression analysis between absorption and number of individuals at 440 nm. The slope of this regression represents the per-individual absorption value at 440 nm.

Again similar to *Limacina*, each of the serial additions for *Parathemisto* spp. yielded a relatively featureless spectrum with no distinctive spectral features (Figure 6.17). The magnitude of absorption is reduced moving toward the red end of the spectrum, nevertheless these organisms still absorb in the red wavebands. As

identification from ocean colour requires the presence of a somewhat discernible spectral signature to distinguish a particular group of organisms, these darkly coloured zooplankton do not appear to be good candidates for remote detection.

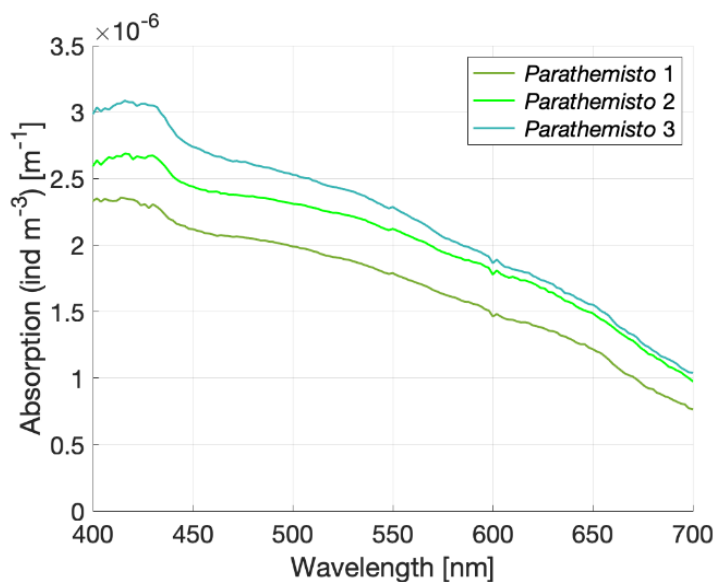


Figure 6.17 The per individual absorption spectra (per  $m^3$ ) derived from the three *Parathemisto* serial addition experiments conducted on samples from ST02, ST04 and ST06 during the SFI Harvest cruise in the northern Norwegian Sea in June 2022.

### 6.3.7 *Aurelia aurita*

*Aurelia aurita* are a species of Cnidarian more commonly known as moon jellyfish. They are typically found in coastal temperate seas, where large scale bloom events are becoming increasingly common. Several hypotheses for this global increase in jellyfish blooms have been put forward, including over-fishing leading to the removal of natural jellyfish predators, the warming climate leading to faster growth and reproduction, and the increase of nutrient run-off from agriculture creating more low oxygen oceanic dead-zones in which jellyfish thrive (M. E. C. Miller & Graham, 2012; Purcell et al., 2007). These blooms have caused a number of issues for human activity in recent years, most notably in the fishing industry, where these

events are interfering with aquaculture operations, as well as serving as predators and effective competitors for commercially fished species (Purcell et al., 2007). Small jellyfish and the tentacles of larger jellyfish can enter aquaculture pens, irritating the fish gills, eventually leading to suffocation and death. Natural fish stocks are also being depleted due to increased competition from the jellyfish blooms depleting resources. Monitoring and predicting the occurrence of these jellyfish blooms is therefore of considerable importance in order to mitigate these issues. However, this remains a challenge, largely due to an incomplete understanding of population processes (Goldstein & Steiner, 2020). Thus, being able to remotely identify and track these organisms over large spatio-temporal scales would provide more information on the topic and help inform bloom forecasting models. These organisms are, however, almost entirely transparent and therefore may not produce a strong enough absorption signal to allow for remote identification from ocean colour.

Unlike the previously described samples, the *A. aurita* measured in this study were taken from laboratory cultivated samples. These samples were cultivated by the Evolution of Early Branching Metazoans Research Group at the Marine Biological Association in Plymouth. These samples consisted of *A. aurita* organisms within the ephyra and medusa stage and were up to 2 cm in size (Figure 6.18). Despite being nearly entirely transparent on an individual basis, a pink/ orange hue was evident when the organisms aggregated.



Figure 6.18 Image of cultivated *A. aurita* ephyra/ medusa sample used for serial addition experiments. Samples were cultivated by the Evolution of Early Branching Metazoans Research Group at the Maine Biological Association in Plymouth, UK.

One serial addition experiment was carried out for the cultivated *A. aurita* on 29th March 2022. At each addition, 2-3 live *A. aurita* were added to a filtered seawater collected from Loch Etive on the 7th March 2022 (Figure 6.19). Results from the serial addition clearly indicate that despite being largely transparent, the addition of *A. aurita* into the sample did increase the absorption at 440 nm. This points to the possibility of these organisms influencing the optics of the water column if occurring in sufficiently large concentrations.

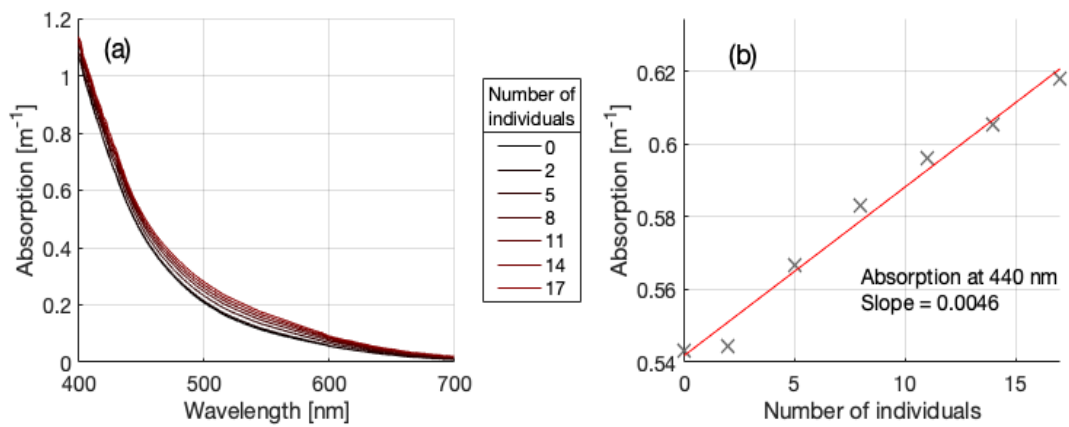


Figure 6.19 (a) Serial addition of the cultivated *A. aurita* sample and (b) regression analysis between absorption and number of individuals at 440 nm. The slope of this regression represents the per-individual absorption value at 440 nm.

The concentration-specific absorption spectrum derived from this serial addition is presented in Figure 6.20. This result shows a broad absorption peak at 480 nm, with a similar shape to the previous astaxanthin- rich species in this study. However, as *A. aurita* are generally transparent in colour, it is more likely that this feature is associated with what these organisms were fed. This was a laboratory cultivated sample, which was regularly fed on *Artemia*, or brine shrimp. These brine shrimp can contain various keto-carotenoid pigments, including  $\beta$ -carotene, canthaxanthin and small amounts of astaxanthin. These pigments give *Artemia* they're orange- red colour, and would explain the similarity in spectral signature between these organisms and the Crustacea in this study.

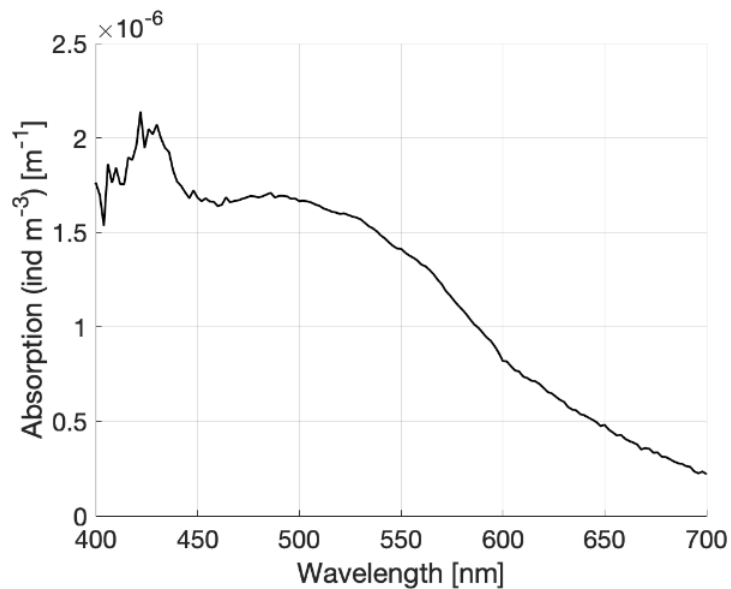


Figure 6.20 The per individual absorption spectra (per  $m^3$ ) derived from cultivated *A. aurita* serial addition experiment.

As this serial addition experiment was conducted on laboratory cultivated samples rather than natural ones, it is likely that these results are not truly representative of a natural population. The absorption properties of these organisms appear to be influenced by the prey they consume, and therefore in nature their absorption will likely vary according to the composition of the zooplankton assemblage. Whilst these results suggest that seemingly ‘transparent’ species such as *A. aurita* could produce an absorption signal strong enough to influence surface reflectance signals (in dense aggregations), more work defining the absorption properties of natural samples is required in order to provide an accurate representation of *in situ* populations.

#### 6.3.8 Comparison of zooplankton spectral absorption properties

The absolute and normalised absorption spectra for the zooplankton measured in this study are compared in Figure 6.21 a and b respectively. The majority of these organisms absorb on the same order of magnitude per unit concentration, with the exception of northern krill (*M. norvegica*) (Figure 6.21a). The spectra were

normalised using maximum scaling method, where the absorption at each wavelength was divided by the maximum absorption value in the spectrum. These organisms have a much stronger absorption signal than any of the other species measured and therefore considerably lower concentrations of *M. norvegica* will be required to influence surface reflectance signals. This is likely because *M. norvegica* are significantly larger than the other organisms measured in this study, and therefore contain more absorbing pigment. The mature *P. norvegica* with eggs appear to be the next strongest absorbers, also likely due to the larger size of individuals in this sample, as well as the large dark egg sacs.

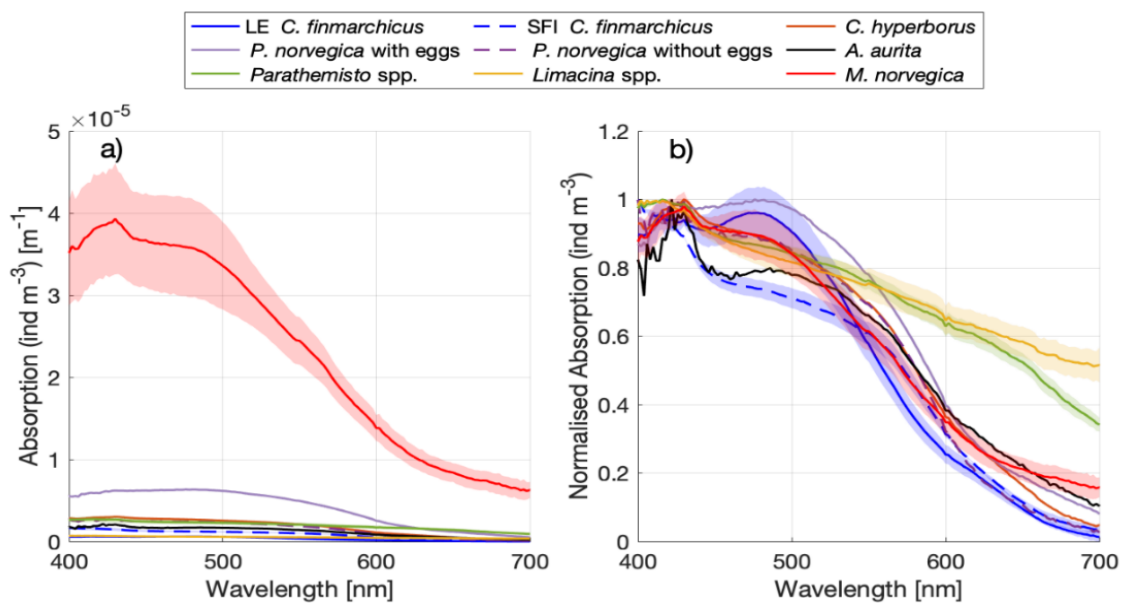


Figure 6.21 . Comparison of (a) absolute and (b) normalised absorption spectra of all the zooplankton groups in this study. Species with multiple absorption spectra are represented by the mean with the shaded region depicting  $\pm 1$  standard deviation.

Comparison of the spectral shapes of all zooplankton measured in this study indicates these organisms have very similar absorption properties (Figure 6.21b). Across the copepods (*C. finmarchicus*, *C. hyperboreus*, *P. norvegica*) and krill (*M. norvegica*), the absorption signal is dominated by the varying levels of carotenoid pigments, most notably astaxanthin. The absorption spectra of all these organisms

peak at around 480 nm, which coincides with the astaxanthin absorption peak. However, some groups (such as the Loch Etive *C. finmarchicus*) have a narrower absorption peak, whilst others (such as the *M. norvegica*, *C. hyperboreus* and SFI Norwegian Sea *C. finmarchicus*), exhibit broader absorption peaks across the blue/green part of the spectrum. This could be related to the varying concentrations of carotenoids in these groups, resulting in organisms that range from red to orange in colour. This absorption feature was also present in the ephyra/ medusa stage moon jellyfish (*A. aurita*), which had been laboratory grown and fed on carotenoid containing brine shrimp (*Artemia*). The only organisms that did not share these spectral features were the darker amphipods (*Parathemisto* spp) and sea butterflies (*Limacina* spp). These individuals had fairly featureless absorption spectra, making any form of remote identification of these species using ocean colour very challenging.

As the absorption properties of the majority of these organisms are dominated by astaxanthin and other carotenoid pigments, it would not be possible to remotely differentiate between these groups. Thus, prior knowledge of the zooplankton assemblage within a region of interest is required before remote identification can take place. Indeed, it may not be possible to distinguish these zooplankton species from algal species containing red pigments as well. One potential consequence of this could be the occurrence of false positives for red tide algorithms in the case of high concentrations of e.g. *C. finmarchicus*.

#### 6.4 Modelled impact of zooplankton on remote sensing reflectance signals

To ascertain the impact of each group of zooplankton measured in this study on  $R_{rs}$  signals, the measured concentration-specific absorption spectra of each group were input into the radiative transfer model Ecolight (version 5.2.) at varying concentrations. For groups with more than one absorption spectrum, the average absorption spectrum was calculated. A CHL concentration of  $1.7 \text{ mg m}^{-3}$  and a CDOM absorption (at 440 nm) measurement of  $0.06 \text{ m}^{-1}$  were chosen as initial concentrations,

as these were the average values measured during the 2017 Sea Patches cruise. Whilst CHL and CDOM concentrations remained the same throughout the simulations, the concentrations of each group of zooplankton were varied over 0, 10, 100, 1000, 10000, 25000, 50000, 75000 and 100000 individuals  $\text{m}^{-3}$ . This provided a sensitivity analysis for the effect of these zooplankton groups on satellite derived  $R_{rs}$  signals. The modelled spectra for each of the zooplankton groups are presented in Figure 6.22.

To quantify the effect of each organism, the relative root mean square difference (RRMSD) between the initial  $R_{rs}$  spectrum with no zooplankton and each  $R_{rs}$  spectrum modelled with increasing zooplankton was calculated. First described in Chapter 5, the RRMSD spectral matching approach for identifying swarms of *C. finmarchicus* included the application of an anomaly threshold (Section 5.5) to target the application of non-standard bio-optical constituents to regions not well described by a standard bio-optical model. The calculated RRMSD values for each of the modelled spectra, along with the RRMSD threshold, is also presented in Figure 6.22.

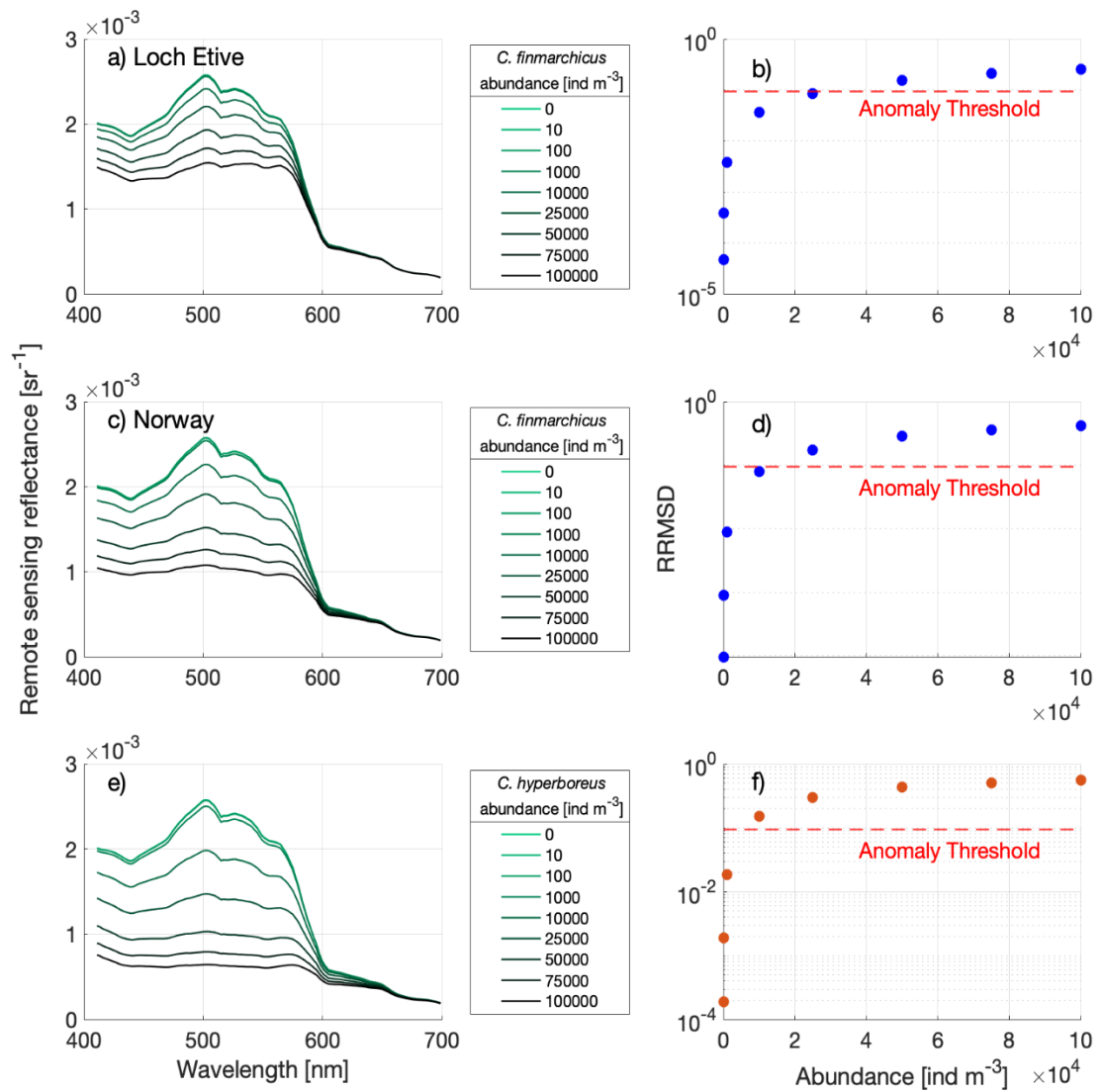


Figure 6.22 Modelled remote sensing reflectance spectra with increasing concentrations of (a, c) *C. finmarchicus*, (e) *C. hyperboreus*, (g, i) *P. norvegica*, (k) *M. norvegica*, (m) *A. aurita*, (o) *Parathemisto* spp. and (q) *Limacina* spp., with associated (b, d, f, h, j, l, n, p, r) relative root mean square difference values for comparison between each modelled spectrum with the initial spectrum where no zooplankton were present.

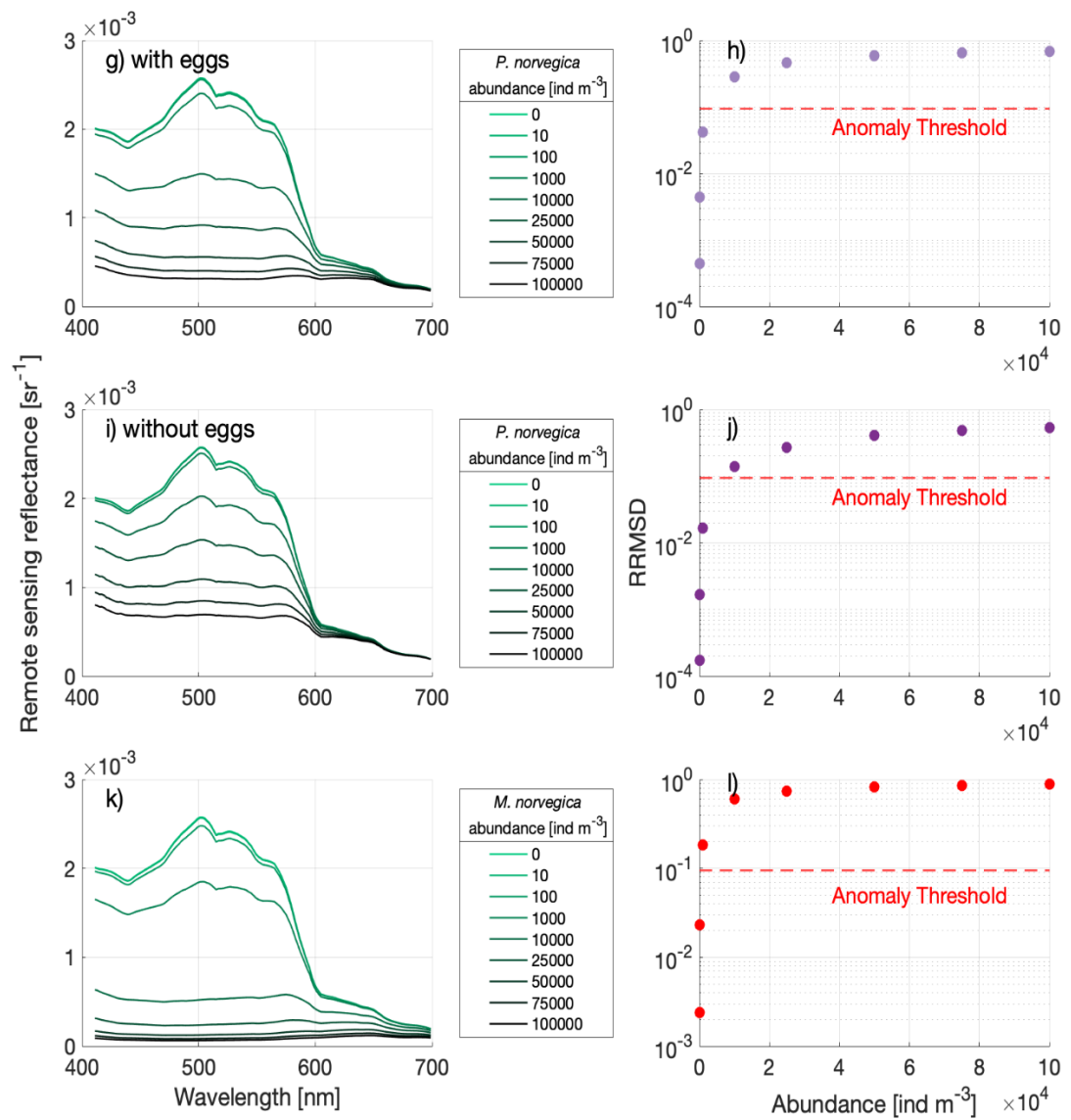


Figure 6.22 continued...

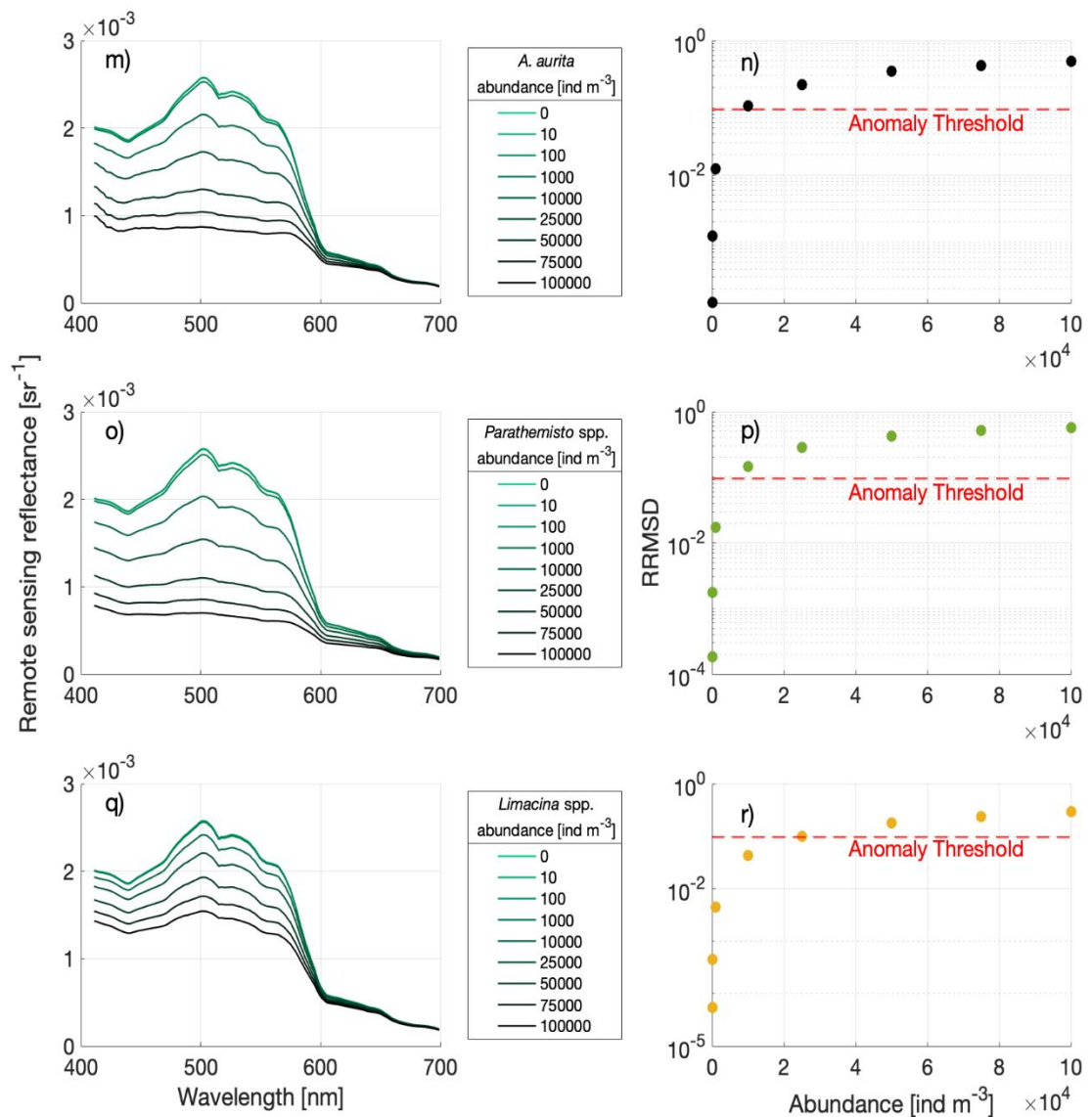


Figure 6.22 continued...

Overall, all zooplankton groups have a broadly similar effect of reducing  $R_{rs}$  magnitude, most notably in the blue/ green part of the spectrum. This is a natural consequence of modelling their optical impact as only involving additional absorption. As well as this, RRMSD values increase across all group with the addition

of increasing concentrations of the organism. This suggests that the RRMSD methodology is suitable for detection of zooplankton aggregations. Comparison between the Loch Etive (a and b) and the northern Norwegian (c and d) populations of *C. finmarchicus* illustrate that the difference in pigmentation and composition between individuals of the same species could have a considerable impact on  $R_{rs}$ . The Norwegian *C. finmarchicus* suppress reflectance signals much more effectively than the Loch Etive population, and the anomaly threshold is reached with the inclusion of fewer individuals in the model. Comparison of the *P. norvegica* individuals with eggs (Figure 6.22 g and h) and without eggs (Figure 6.22 i and j) shows a similar story, with the more mature *P. norvegica* population with eggs reducing reflectance to a greater extent than that of the smaller individuals without eggs. These results point to the importance of prior knowledge of the zooplankton assemblage before remote detection can be attempted, as well as increased effort to determine the degree of pigmentation variation and its drivers in these species.

The northern krill (*M. norvegica*) (Figure 6.22 k and l) have the most significant impact on modelled reflectance signals across the spectrum, resulting in a completely flat spectrum with the addition of 100,000 ind m<sup>-3</sup>. Considering *in situ* *M. norvegica* swarm concentration estimates reached up to 770,000 individuals m<sup>-3</sup> in the Bay of Fundy (Nicol, 1986), these are plausible natural concentrations. Further, the RRMSD analysis indicates that far lower concentrations of these organisms would be sufficient to have a noticeable impact on reflectance signals. Given the sheer size difference between these organisms and the others measured in this study, this is an expected result. The moon jellyfish (*A. aurita*) absorption signal is surprisingly effective at drawing down the  $R_{rs}$  signal (Figure 6.22 m), which indicates the possibility of being able to detect these organisms remotely. However, it is important to remember that these organisms were laboratory cultivated and therefore not necessarily representative of natural populations.

#### 6.4.1 Concentrations of zooplankton required to reach the RRMSD threshold of optical anomaly

Modelling the effects of zooplankton concentrations on reflectance spectra facilitates an estimation of surface abundances required to influence reflectance signals in a way that is significant enough to be identified from satellite imagery. The zooplankton concentration at which the RRMSD value increases beyond the anomaly threshold of 0.095 (first determined in Section 5.5) is the concentration required to produce a signal that would be identified as ‘optically anomalous.’ In this case, optically anomalous refers to a region of the satellite imagery that is not well described by a standard bio-optical model of CHL, MSS and CDOM alone. As a result, the zooplankton groups that aggregate in concentrations lower than their specific threshold concentration may not produce a signal strong enough to be identifiable through satellite imagery. The concentration at which each group reached the RRMSD threshold of 0.095 was linearly interpolated from the modelled data presented in Figure 6.22 using MATLAB (R2023b) and is presented to 2 significant figures in Table 6.1.

Table 6.1 Concentrations of each zooplankton group required to produce a strong enough signal to be identified through satellite imagery.

Organism	Concentration at which RRMSD threshold is reached [ind m <sup>-3</sup> ]
Loch Etive <i>C. finmarchicus</i>	28000
Norwegian (SFI) <i>C. finmarchicus</i>	12000
<i>C. hyperboreus</i>	6200
Mature <i>P. norvegica</i> with eggs	3000
Small <i>P. norvegica</i>	6800
<i>M. norvegica</i>	490
<i>Parathemisto</i> spp.	6400
<i>Limacina</i> spp.	24000
<i>A. aurita</i>	8900

The concentrations of *C. finmarchicus* required to produce a strong enough signal to be identified through satellite imagery varied considerably between the two populations modelled. The Loch Etive *C. finmarchicus* required 16,000 ind m<sup>-3</sup> more

than that of the Norwegian population to reach the anomaly threshold of 0.095. This disparity emphasises the importance of prior understanding of the zooplankton assemblage being targeted. This difference is considerable enough to suggest the possibility of multiple *C. finmarchicus* models that can be used depending on the region/ time of study and the assemblage being targeted. However, as there are currently only absorption spectra from three different populations (2017 Sea Patches spectra from northern Norwegian Sea, 2022 SFI Harvest spectra from northern Norwegian Sea and Loch Etive spectra), two of which are very similar in both spectral shape and magnitude, it is difficult to know if the Norwegian SFI Harvest spectra are anomalous results. General trends dictate that more highly pigmented zooplankton populations are found at higher latitudes/ altitudes (Hansson & Hylander, 2009), and whilst the northern Norway site constitutes a high latitude region at 68 °N- 70 °N, the measurement from the same region during the Sea Patches 2017 cruise suggests relatively low pigmentation within the population. Relatively little is currently known about the drivers of variation, which makes choosing a suitable *C. finmarchicus* model difficult without corresponding *in situ* measurements. Therefore, more work on characterising the extent of variation in *C. finmarchicus* pigmentation is crucial to establish the model requirements for the remote detection of these organisms.

Whilst the detection thresholds for both populations of *C. finmarchicus* are considerably lower than the concentration estimations generated in Chapters 3 and 5 (up to 180,000 ind m<sup>-3</sup> within the patches), they are still on the high end in comparison to current *in situ* swarm abundance estimates from the literature (for example, swarm abundance estimates within the GoM region are presented in a literature review assembled by Ross et al. (2023)). This may suggest that concentrations this high do not often naturally occur in the ocean. However, it is important to remember that the traditional techniques may be underestimating populations due to animal evasion. Therefore, it is possible that patches of these densities may occur far more frequently than the current literature suggests. It has already been established that less invasive measurement techniques (such as a sail buoy mounted acoustic sensor) can record *C. finmarchicus* densities of up to 165,000 individuals m<sup>-3</sup> within the Norwegian Sea

(Bandara et al., 2022). Therefore, with a detection threshold of 28,000 ind m<sup>-3</sup>, *C. finmarchicus* surface swarms such as these are likely to be well resolved using ocean colour signal.

Comparison of the density thresholds derived from the two different samples of *P. norvegica* show a similar story of variation. More than double the number of small *P. norvegica* were required to reach the concentration threshold relative to the mature *P. norvegica* individuals with eggs. This illustrates the importance of considering the life stages of a target species when attempting remote identification to ensure greater accuracy of concentration estimates. This was a first attempt at quantifying the effect of zooplankton demography on pigmentation and absorption properties, and more work needs to be done to better understand this phenomenon.

Concentration thresholds for *Limacina* spp. and *Parathemisto* spp. were comparable to that of the other species measured, indicating a potential for remote detection using satellite signals. However, as they have a broadly featureless absorption spectrum, their impact will be fairly uniform across the reflectance signal. As a result, it would be easier for the model to confuse these organisms for other optically important standard constituents, especially that of CDOM. As a result, remote identification of these organisms would be difficult, and would require a comprehensive *in situ* IOP measurements of the region being studied that overlap with the satellite data, as well as observations of surface aggregations of these organisms for a targeted approach. This would likely negate the utility of remote identification.

*M. norvegica* required by far the smallest concentration of individuals in order to reach the detection threshold, which is a positive result in terms of potential for remote identification of krill swarms through ocean colour. Nicol (1986) recorded small scale, visually identifiable surface swarms of *M. norvegica* in the Bay of Fundy that reached densities of 770,000 ind m<sup>-3</sup>. These concentrations were remotely determined from aerial photography and contrasted with minimally invasive *in situ* 'bag sampled' concentration estimates, which reached a maximum of 41,000 ind m<sup>-3</sup>, as well as traditional net sampled concentrations of only 6 ind m<sup>-3</sup>. Taking into account

these abundances, it is possible that natural populations could reach the determined detection threshold of 490 ind m<sup>-3</sup> and therefore be identified remotely. Additionally, the difference in concentration estimates derived from the three techniques used in Nicol (1986) further demonstrates the potential for animal evasion to influence concentration estimates. The remote (helicopter camera) and minimally invasive (bag sampling) methods yielded concentration estimates that were orders of magnitude greater than the more invasive net sampling method. Other studies have also identified and investigated krill evasion behaviour, demonstrating that these highly mobile organisms, in particular larger members of the population, can evade net capture (Brierley, 1999; Everson & Bone, 1986; Hill et al., 1996). The evasion behaviour of krill was also found to be more significant at the surface, where there is lots of light and krill can visually detect sampling nets (Hill et al., 1996). This further highlights the need for development of non-invasive *in situ* sampling techniques to provide surface concentration estimates that are free from evasion bias and are more representative of natural concentrations.

A lot of the interest regarding remote detection of krill is concentrated on the Southern Ocean, which supports the largest krill fisheries in the world and where *in situ* population monitoring is difficult due to the challenging conditions of the region. In the Southern Ocean, *E. superba* are the dominant krill species and are generally larger than their northern counterparts. Therefore, it is possible than even lower densities would be required to produce an identifiable signal through ocean colour. The range of *E. superba* swarm densities vary considerably in the literature, with acoustic estimates in the Scotia Sea ranging from 3-81 ind m<sup>-3</sup> but reaching up to 1650 ind m<sup>-3</sup> (Fielding et al., 2012). However, visual estimates have exceeded these values by two orders of magnitude, ranging between 25,000 to 64,000 ind m<sup>-3</sup> (Hamner & Hamner, 2000). Further, *in situ* measurements of *E. superba* swarms in the Southern Ocean have reached spatial scales of up to 100 km<sup>2</sup>, meaning they would be resolvable using 1km<sup>2</sup> resolution satellite data. Consequently, it is likely that some of these high concentration events will be visible through satellite imagery. This is a good first attempt at understanding the absorption properties of krill, and provides a strong

indication that remote sensing of krill swarms from ocean colour signals is feasible. However, more work is needed to characterise krill absorption properties, especially in the Antarctic species *E. superba*, which are of significant biological and economic interest globally.

## 6.5 Uncertainties associated with the PSICAM serial addition approach

When analysing the zooplankton absorption spectra derived from the PSICAM serial addition approach, there are two main sources of uncertainty that should be considered, the first of which being instrument specific uncertainty associated with the PSICAM. High sensitivity (associated with long optical pathlengths) and absence of systematic scattering error means the PSICAM could be considered the current state of the art for absorption determination and has even been used as a reference to correct other absorption measurements (Lefering, Röttgers, et al., 2016; McKee et al., 2013; Röttgers et al., 2013). Despite this, there are uncertainties associated with the PSICAM, which have been well characterised by Lefering et al. (2018). As PSICAM absorption measurements are highly sensitive to changes in the reflectivity of the cavity walls, the calibration process represents the largest source of uncertainty for the PSICAM. Lefering et al. (2018) found this to be highly wavelength and sample dependent, where absolute differences in reflectivity measurements lead to ~6% deviation from mean absorption in the blue/ green wavelengths. This quantification was based on standard PSICAM measurement protocol, which requires calibration measurements to be conducted in triplicate throughout the measurement process (Kirk, 1997). However, there is potential that this approach could introduce greater uncertainty. Using this approach, the calibration is conducted using one (triplicate) reflectivity measurement. Whilst the triplicate determination ensures a degree of precision, the accuracy of this measurement cannot be resolved. For example, it is possible that the calibration procedure may be subject to error due to issues such as bubbles or water quality, leading to an erroneous reflectivity measurement. To overcome this, this chapter employed an alternative approach, where the PSICAM

was calibrated regularly and each reflectivity measurement was added to an existing database. Obviously erroneous measurements were excluded and a median reflectivity measurement was used to calibrate the samples. As the reflectivity measurements within the database showed very little variability, with no obvious trends or step changes, it is likely that this is more representative of the system. This method will likely reduce the uncertainty associated with variability in reflectivity.

Lefering et al. (2018) also determined both the precision and accuracy of the PSICAM instrument. By averaging all of the standard deviations of the total non-water absorption measurements (in triplicate), a value of 1.7% was estimated. Again, it was found that precision was wavelength dependent, although between the wavelengths of 500 to 700 nm, it remained relatively constant. As there is no real independent measure of truth for PSICAM, the accuracy was determined by comparing the absorption measurements generated by two independently operated instruments. Again, the accuracy was sample dependent, with percentage RMSE values calculated at 6% for CDOM samples and 12.6% for particulate non-water absorption measurements. This variability is likely associated with the lack of homogeneity associated with sub-samples of water containing particulate material. Accuracy was also wavelength dependent, with maximum variability reached at the extreme ends of the spectrum, where absorption is high (due to both water and CDOM absorption) leading to low light intensity within the cavity. This results in artefacts associated with straylight becoming more significant at lower intensities. For this reason, this study only included wavelengths between 400 and 700 nm. Whilst the Lefering et al. (2018) uncertainty estimates cannot be directly applied to the work in this chapter, as the samples being analysed are very different and uncertainty in PSICAM measurements are highly dependent on the sample, they can provide a general picture that can serve as a guide when interpreting the results.

The second source of uncertainty that should be considered when using the serial addition approach to measure zooplankton is the sample handling procedure. Pigmentation is an extremely plastic trait and can change in a matter of hours. An example of this is shown in Figure 6.4 where the *C. finmarchicus* sample completely

bleached overnight, despite being kept in a fridge at a similar temperature to that of the water from which they were taken. The reason behind this bleaching is unknown, however it may be due to the stress associated with being handled. Once this phenomenon was observed, samples in this study were processed as close to the time they were collected as possible. However, this was not the case for the sample taken from Loch Etive, which were processed over the course of two days. Whilst none of the other samples appeared to visually change to the same degree as the SFI *C. finmarchicus*, it is possible that this phenomenon may still have influenced the absorption spectra to an unknown degree. If any of the other zooplankton samples did undergo bleaching, it would mean the absorption spectra resulting from these samples would be lower than natural populations. Further work to understand this trait is required to fully characterise the potential error associated with it.

## 6.6 Conclusions

This chapter presents the first set of measurements of the absorption properties of 7 ecologically and commercially important zooplankton species. These absorption spectra form the beginning of a spectral library of zooplankton that can be utilised for modelling purposes and remote identification. In addition, these spectra provide a greater understanding of pigmentation and its variation in these species. Previously, pigmentation has been understudied in comparison to other functional traits, likely due to the typical sample preservation strategies (e.g. ethanol and formaldehyde) resulting in unreliable colour information. With the PSICAM serial addition technique presented in this chapter, it is now possible to directly measure the absorption of these live organisms quickly and without the need for preservation measures.

Comparison of the zooplankton spectra showed that whilst the magnitude of absorption varied between species (as well as within species), the spectral signatures were broadly similar. Broad absorption features across the blue/ green part of the spectrum that peaked at 480 nm were evident in all but two species measured. This

480 nm peak is consistent with the absorption of astaxanthin, which was expected as this is the most prevalent carotenoid pigment in Crustacea. Some of these peaks were broader (*M. norvegica* and *C. hyperboreus*), likely influenced by other carotenoid pigments with slightly different absorption properties, and some were narrower (Loch Etive *C. finmarchicus*). However, this difference in spectral signature was not distinctive enough to remotely distinguish these species. These results imply that the *C. finmarchicus* model developed in this thesis is likely sensitive to all astaxanthin containing zooplankton. As well as this, the strong influence of astaxanthin on the absorption properties of these organisms could result in false positives due to other astaxanthin containing organisms present in surface waters, such as phytoplankton red tides. As a result, it is important to have prior information of the plankton assemblage in the study region before attempting remote identification.

Despite this, the spectral magnitude of absorption did vary considerably, both within and between the species measured. For example, the *C. finmarchicus* absorption measured in June 2022 in the northern Norwegian Sea was considerably stronger than that measured in the same region in April 2017. In addition, the absorption peak was generally broader. This suggests that the June 2022 populations had greater pigmentation, as well as a greater proportion of other carotenoid pigments influencing their absorption properties. Whilst there are several hypotheses to explain pigmentation in these organisms (Vilgrain et al., 2023), the primary driver of this variation in pigmentation is unknown. As the June 2022 sample was taken during 24 hour sunlight, it is possible that this increase in pigmentation is triggered by increased light levels as carotenoids provide UV protection for these organisms (Vilgrain et al., 2023). This would also explain why the spring 2017 *C. finmarchicus* absorption spectra were so similar to the Loch Etive spectra from March 2022. However, without the collection of more absorption spectra from this region at different times of the year, this cannot be definitively concluded.

Another interesting observation of this study was the bleaching that occurred within the northern Norwegian Sea *C. finmarchicus* samples when placed in a cold, dark refrigerator. In some cases, this considerable alteration in colour took place

within an hour. This phenomenon only occurred in the June 2022 northern Norwegian Sea *C. finmarchicus* samples, and was not seen in the Loch Etive *C. finmarchicus* or indeed any of the other zooplankton species measured. This observation served to illustrate the general plasticity of pigmentation within *C. finmarchicus* and the possibility of considerable variation over very small spatio-temporal scales.

In addition to this, *P. norvegica* displayed a considerable difference in absorption at different life stages, with the mature *P. norvegica* with eggs having a stronger absorption signal relative to the smaller *P. norvegica* individuals. In fact, the smaller individuals required more than double the concentrations to reach the detection threshold. This illustrates the importance of considering the structure of the zooplankton assemblage being targeted.

Generally, these results highlight the need for more measurements of the absorption properties of keystone zooplankton species. In this preliminary work, a high degree of variation is already evident, especially in magnitude of absorption. Therefore, it is important to appropriately characterise the degree of this intra-species variation to ensure more accurate modelled population estimations. This will require experiments that span different seasons, as well as separation of zooplankton samples into different life-stages. With this information, it will be possible to select an absorption spectrum to incorporate into the model that is appropriate for a particular species, based on the time of year and location of the study.

When the impact of each zooplankton species on modelled  $R_{rs}$  spectra was tested, it illustrated that all organisms could impact reflectance signals if present in sufficient concentrations. The concentration thresholds for detection varied between (as well as within) species, and appeared to be broadly correlated with the size of the organisms. Whilst this result is encouraging, remote detection is not contingent on absorption signal alone. As well as being concentrated enough to produce a signal, aggregations will have to cover a significant spatial scale. For example, the spatial resolution of the MODIS Aqua satellite data used in this thesis is 1 km<sup>2</sup>. If these organisms aggregate on smaller, more localised scales, then they will likely not be

resolved through satellite imagery. In addition, all of the other restrictions associated with satellite detection apply here, including light availability, cloud cover and optical depth. Thus, the behaviour, life cycle and location of these populations will also influence the likelihood of remote detection.

This study demonstrated significant scope for the remote identification of krill swarms. At an estimated detection threshold of only 490 individuals  $\text{m}^{-3}$  for *M. norvegica*, the feasibility of remote detection is high. The application of this method to the Antarctic krill species *E. superba* is of particular interest, due to its commercial importance, and the challenges associated with *in situ* sampling in the Southern Ocean. However, without direct measurements of the absorption properties of these organisms, remote identification is not possible. Therefore, characterising the absorption of this species is crucial for the implementation of this technique.

Similarly, an unexpected result of this chapter was the signal derived from the ephyra and medusa stage *A. aurita* samples. It is widely known that these moon jellyfish are transparent, and so the absorption peak across the blue/ green part of the spectrum was of great interest. As this feature was similar to the other organisms measured in this study, it was determined that it could be attributed to their food source. These organisms were cultivated in a laboratory and fed on *Artemia*, a carotenoid containing arthropod more commonly known as brine shrimp. Thus, in order to fully understand the potential for remote identification of harmful jellyfish swarms, measurements of the absorption properties of natural populations is required.

Finally, whilst this chapter contributes significantly to the understanding of the optical properties of zooplankton, these spectra do not represent a complete IOP profile. At present, there is no instrumentation to measure the backscattering of these organisms. Theoretical studies suggest that backscattering will have a negligible impact on the signal relative to absorption (Davies et al., 2021). In fact, using Mie Theory modelling, Davies et al. determined approximations of maximum contributing particle diameters for absorption, which was greater than 10,000  $\mu\text{m}$ , which then dropped to 2,000  $\mu\text{m}$  for scattering and only 150  $\mu\text{m}$  for backscattering.

All of the organisms studied here have particle diameters that well exceed 150  $\mu\text{m}$ , and therefore it is assumed that their overall contribution to bulk  $b_b$  signals will be insignificant. Despite this, future work on testing this assumption and determining the full IOP profile of these organisms will hopefully provide a more holistic understanding of their impact on ocean colour signals.

## 7 Conclusions

Ultimately, this thesis aimed to explore the possibility of remote identification of zooplankton from satellite derived ocean colour signals. Zooplankton are keystone organisms within the marine environment, representing a crucial link between primary production and higher order predators. They also represent an important economic resource, providing a nutritional food source for many commercially harvested fish species, as well as certain zooplankton species being fished directly to produce health supplements for human consumption. Despite this considerable interest, it is difficult to map zooplankton populations using traditional ship-based techniques, largely due to their patchy population dynamics. In this context, ocean colour remote sensing represents a useful tool for the provision of wide scale spatio-temporal monitoring of surface population distributions. The work presented in this study demonstrated the feasibility of ocean colour remote sensing as a means of zooplankton detection and detailed the development of remote methods for the identification and characterisation of surface zooplankton swarms.

### 7.1 Summary of key findings

Traditionally, the contribution of larger (millimetre sized) particles to the bulk IOPs of the water column has largely been overlooked by the marine optics community. This is because it was generally assumed that larger particles are not present in sufficient concentrations to influence ocean colour. However, along with anecdotal evidence that zooplankton can visually alter the colour of surface waters (Bullen, 1913; Nicol, 1984; Sars, 1903) and theoretical evidence that larger particles could influence bulk IOPs, particularly spectral absorption (Davies et al., 2021), the prospect of high concentration zooplankton ‘swarms’ influencing satellite derived  $R_{rs}$  became increasingly apparent. The first attempt to determine the impact of zooplankton on satellite  $R_{rs}$  was conducted by Basedow et al. (2019) in the northern Norwegian Sea. The Basedow et al. study found relatively high *in situ* surface

concentrations of the zooplankton species *Calanus finmarchicus* were recorded at the same time a distinctly red feature was captured on a satellite image of the sample area. The first chapter of this thesis follows on from the initial work conducted by Basedow et al. (2019), presenting a method to identify and quantify surface concentrations of *C. finmarchicus* in the northern Norwegian Sea from eRGB imagery. The methodology broadly followed a two-step approach, where the eRGB coordinates of each pixel were first compared to an eRGB co-ordinate LUT, generated from a total of 1008 simulated reflectance spectra representative of a standard Case 2 bio-optical model. The quantitative comparison was made using the metric  $\Delta E_{2000}$ . The output of this colour matching algorithm was a map of relative anomaly, with high minimum  $\Delta E_{2000}$  pixels indicating regions of the image that were not well described by a standard bio-optical model. This process is then repeated and the image is compared to a specialised LUT, derived from spectra representing a Case 2 model with the addition of a *C. finmarchicus* absorption component. Comparison of the two anomaly maps provided an indication of the extent to which the anomalies evident in the first step was influenced by *C. finmarchicus* absorption. When the Norwegian Sea image was compared to the standard Case 2 LUT, the red feature previously identified by Basedow et al. as a potential *C. finmarchicus* patch was highlighted as anomalous relative to surrounding waters. However, with the addition of *C. finmarchicus* absorption, this anomaly was largely resolved. This provided evidence that the optical properties of this extensive red feature could potentially be explained by the presence of *C. finmarchicus*.

Further, the concentrations of *C. finmarchicus* required to reach optical closure for each pixel were extracted and mapped, providing an order of magnitude estimation of surface concentrations within the region of interest. This is the first time zooplankton concentrations have been directly determined from satellite imagery. Within the identified red feature, surface concentrations of *C. finmarchicus* reached up to 180,000 ind m<sup>-3</sup>, which was an order of magnitude greater than the concentrations measured *in situ*. This was an important finding that pointed to a potential *in situ* sampling issue associated with animal evasion. Net evasion is a behaviour that is well

documented within highly mobile krill populations (Hill et al., 1996; Nicol, 1986). However, despite knowledge that small copepod species such as *C. finmarchicus* undergo DVM, during which they can swim hundreds of metres, evasion behaviour within these groups is less studied. Further, another northern Norwegian Sea study conducted by Bandara et al. (2022) found similar abundance magnitudes (up to 165,000 ind m<sup>-3</sup>) using a non-invasive acoustic sensor attached to a sailbouy. Thus, mismatches between abundance estimates generated by invasive net sampling procedures and that of less invasive techniques, provides evidence of potential evasion behaviour within *C. finmarchicus* populations that should be taken into account when devising *in situ* sampling regimes for these organisms.

Chapter 3 also presents a 'proof of concept' study, where the colour mapping method was applied to the optically complex Gulf of Maine (GoM) to identify *C. finmarchicus* within the region. Whilst a possible *C. finmarchicus* feature was identified, some issues associated with the GoM image were highlighted. Firstly, there were some small artefacts within the imagery that were likely being misattributed to *C. finmarchicus* absorption. This could be due to the considerable amount of optical complexity within the image. However, the most notable issue that arose from the GoM imagery was that when all negative spectra were flagged and removed, a lot of coastal data were eliminated. This was likely due to failure of the NASA standard atmospheric correction (AC) in the optically complex coastal region. This raised questions surrounding the general quality of spectral data within the GoM image. As high quality spectral  $R_{rs}$  is critical for the application of any matching technique derived from spectral data, this issue was addressed in the following chapter.

Chapter 4 presented a solution to the AC of large swath imagery that spans both Case 1 and Case 2 waters. Here, a suitable AC scheme was selected on a per-pixel basis, using a spectral matching approach with all available satellite wavebands between 412 nm and 645 nm. A standard Case 2 spectral LUT was compared to the GoM image, which had been processed several times, each with a different variant of an established AC scheme applied. The AC that yielded the lowest root mean square difference (RRMSD) value when compared to all spectra in the LUT was selected as

the AC solution for that pixel. Critically, this solution allows for data that were previously flagged for removal due to poor quality to be utilised for analysis. As a result, reasonable retrievals of CHL, MSS and CDOM were obtained from the coastal regions of the image. Most importantly for the aims of this thesis, this method ensured the satellite data was of sufficient quality for spectral matching algorithms to be applied. Whilst this conceptually simple method achieved encouraging results, the multiple processing iterations required make this method computationally expensive. Further, *in situ* validation on constituent concentration retrievals has yet to be achieved. This is an important exercise that will form the foundation of future work.

With the establishment of a method to correct poor quality spectral  $R_{rs}$  data in optically complex coastal regions, it was then possible to develop an alternative spectral matching approach for the identification of *C. finmarchicus* from satellite data in Chapter 5. The rationale for further methodological development followed that the inclusion of more spectral information relative to the eRGB colour matching approach (which utilised information from only three wavebands) could lead to better discrimination between the modelled optical constituents. However, during the development process, it became apparent that the inclusion of more spectral information could lead to increased residual noise within the data. This noise can potentially be attributed to two factors: the inclusion of more 'land' bands with low SNR and the dilution of statistical significance of astaxanthin related anomaly. The second factor is arguably the most important, as astaxanthin absorbs most effectively within the 400-550 nm range, with a peak at around 480 nm. Therefore, the inclusion of wavebands outside this range could considerably reduce the relative impact of *C. finmarchicus* associated anomaly on the total anomaly signal.

As a result, it was concluded that waveband selection should be targeted according to the optical properties of the constituent being identified. For the case of *C. finmarchicus*, four wavebands between 443 nm and 555 nm yielded optimal results. Once the optimal waveband configuration for the detection of *C. finmarchicus* was established, the spectral matching approach could then be applied to the image. This

followed the two-step approach first developed in Chapter 3, where the image would first be compared to a LUT representing a standard Case 2 bio-optical model, followed by comparison with a Case 2 model with the addition of *C. finmarchicus*. The key difference being instead of an eRGB co-ordinate LUT, the LUT was derived from the simulated  $R_{rs}$  spectra. The quantitative comparison was conducted using RRMSD, the same metric used in Chapter 4 to select AC.

This approach identified the same optical anomalies as the colour matching method and produced similar *C. finmarchicus* concentration estimates within the previously identified patch. However, concentrations of *C. finmarchicus* along the coast appeared unusually high, despite being associated with a low anomaly signal with the application of a standard Case 2 model. This pointed to a false optimisation issue, where regions already well described by a standard Case 2 model were erroneously including *C. finmarchicus* absorption and altering the concentrations of the other bio-optical constituents to provide marginally better optical closure. This highlighted a general limitation of the application of this algorithm to optically complex waters. To overcome this, an anomaly threshold was developed to identify pixels that require the application of specialised bio-optical models to achieve optical closure. The RRMSD values of a small section in the open water region of the image, where the standard bio-optical model was likely to work the best, was averaged and with the addition of 2 standard deviations a threshold of 0.095 (or 9.5% difference) was established. When this threshold was applied, it identified the suspected *C. finmarchicus* patch as optically anomalous, whilst determining the majority of coastal data to be suitably described by the standard Case 2 model, which matched well with the original eRGB approach. Therefore, it was determined that an anomaly threshold worked well to target anomalous pixels for specialised bio-optical model application in optically complex waters.

Whilst comparison of the colour matching and spectral matching approach indicates that the two methods yield similar results, the spectral matching approach has many benefits that make it optimal for anomaly identification. Most notably, the spectral matching approach can be universally applied to both open ocean and coastal

environments with vastly different reflectance values. This differs from the colour matching method, where there is a requirement for  $R_{rs}$  data at each waveband to be constrained in order to achieve visual standardisation. As well as this, the method has the flexibility of waveband selection for targeted bio-optical constituent identification, making it useful for a wide range of bio-optical constituents. As a result, future studies will utilise the spectral matching approach to identify optically anomalous constituents from ocean colour data.

The work presented in this thesis demonstrates good potential for zooplankton to influence ocean colour signals. As a result, it became increasingly important to determine the spectral IOPs of other key groups of pelagic zooplankton within the marine environment. Thus, the final results chapter of this thesis details the first attempt (at the time of writing) to characterise the spectral absorption properties of seven key groups of zooplankton. Concentration specific absorption spectra of zooplankton from the classes Crustacea (copepods, krill and amphipods), Gastropoda (sea butterflies) and Scyphozoa (ephyra/ medusa stage moon jellyfish) were determined in a PSICAM, using a serial addition method. Further, the absorption of some groups, including *C. finmarchicus*, were measured multiple times to begin to determine the degree of variability in spectral absorption within a species. Generally, the spectral properties of all zooplankton groups appeared broadly similar, with all but two groups presenting an absorption peak around 480 nm, consistent with the carotenoid pigment astaxanthin. The similarity in spectral signatures suggests that it may be difficult to distinguish different species remotely and some knowledge of the plankton assemblage within the region of interest will be required. The signal magnitude did vary however, both between and within species, meaning the concentration required to influence remote sensing signals varies with species. The anomaly threshold developed in Chapter 5 was used to establish estimates of concentrations required to influence  $R_{rs}$  signals to detectable levels. Modelled  $R_{rs}$  spectra with increasing concentrations of each zooplankton group were compared to a spectrum without any zooplankton to determine a RRMSD value for each modelled concentration, and the concentration that reached the anomaly

threshold RRMSD value of 0.095 was linearly interpolated. Despite being on the high end of *in situ* concentration ranges, many organisms did reach the satellite detection threshold with concentrations that have previously been recorded *in situ*, thereby demonstrating the feasibility of remote detection of different zooplankton species through ocean colour. Further, with evidence of animal evasion influencing abundance measurements derived from invasive *in situ* sampling, it is possible that current *in situ* estimates are not truly representative of natural concentrations.

With regards to *C. finmarchicus* specifically, considerable variation in absorption was evident between different populations. Whilst the varying spectra would likely produce similar order of magnitude population estimates, the concentrations required to reach the detection threshold varied by a factor of 2. This highlights the need for future work on characterising pigmentation variation in these organisms, as with measurements from only three separate populations, this study cannot distinguish between variability and an anomalous result.

Whilst Chapter 6 presents important information on the spectral absorption properties of several zooplankton groups, currently there is no information available on the spectral backscattering properties of these organisms. Absorption has been found to be the most important SIOP for particles of this size class (Davies et al., 2021) and therefore is likely to have the most significant overall contribution to the optical signal from these organisms. Despite this, spectral backscattering may still contribute to the overall signal received by satellite sensors and therefore should be the focus of future work to provide a complete understanding of the impact of these organisms on ocean colour signals.

Taken all together, the work presented in this thesis provides evidence that high concentration aggregations of zooplankton can be identifiable from satellite derived ocean colour signals. In fact, this thesis presents methods to extract order of magnitude concentration estimates from satellite imagery. Ocean colour remote sensing presents a powerful monitoring tool for these keystone organisms, as traditional ship-based methods cannot match the extensive spatio-temporal coverage provided by satellite data. Zooplankton are critical organisms within the marine food

web, providing a vital link between primary production and higher order consumers, such as commercially harvested fish species and larger charismatic marine mammals. In addition to this, zooplankton play an important role in the marine biological pump, increasing the efficiency of carbon capture and storage within the ocean (Figure 1.3). Further, with short life cycles and physiological processes highly sensitive to temperature, zooplankton make excellent bio-indicators for climate change. As a result, the methods developed in this thesis to exploit satellite derived datasets as a means of zooplankton monitoring present an invaluable resource for better understanding the marine environment. However, a key limitation of satellite imagery is the inability to resolve zooplankton populations at depth. Further, due to the similarity in spectral properties, it may be difficult to remotely distinguish between different groups of zooplankton. Therefore, satellite remote sensing should be used in conjunction with *in situ* measurements, to ensure a holistic approach to population monitoring.

More generally, this study highlights the importance of considering larger particles and their influence on the bulk IOPs of the water column. The methods presented in this study are broadly applicable and can be utilised to identify any constituent that deviates from the standard Case 2 bio-optical model, including other large particles such as fish eggs or larvae. The main requirement is accurate SIOP information for target constituents. As a result, facilitation of the development of IOP instrumentation that can accurately resolve the relative contribution of larger particles to the bulk optical properties of the marine environment is critical.

## 7.2 Future directions

As the contribution of zooplankton and other large particles to the optical properties of the water column has traditionally been overlooked by the scientific community, relatively little work on the optics of this group has been carried out. This represents a sizeable gap within the literature and as a result there is considerable scope for development within this field. This thesis details the first attempt to

characterize the impact of different zooplankton groups on ocean colour  $R_{rs}$  and quantify zooplankton populations from space. Looking forward, a number of avenues for future development have been revealed that will improve our ability to detect zooplankton and other large particles from ocean colour data.

### 7.2.1 *Development of remote detection methods and application to other zooplankton and large particles*

To continue applying the remote detection approaches described in this thesis, some refinement is required. Most importantly, rigorous testing of the current Ligurian Sea bio-optical model used to build the LUTs is needed to ensure it is sufficiently representative of a standard Case-2 environment. This will be achieved by finding matchups of processed satellite imagery with *in situ* measurements of the optical constituents in both the Norwegian Sea and the GoM. When applying the methods to new regions, matchups with any available *in situ* data will be attempted to ensure the assumption that the LUTs are broadly representative of the global ocean is robust. Further, a non-linear version of the bio-optical model, which takes into account the packaging effect, will also be compared to the current linear approach to ascertain which model best represents the natural environment.

To further ensure the longevity of the methods developed throughout this thesis, they will be adapted for application to other satellite ocean colour sensors. MODIS was chosen in this study over comparable instruments such as VIIRS and the European Space Agency's (ESA) Sentinel 3 Ocean and Land Colour Instrument (OLCI), as it provided data with higher spectral resolution in the visible region pre-2016. However, as MODIS is soon to be decommissioned, it is important to modify the methods developed in this thesis to be used with other ocean colour instruments. This is easily achieved, as the simulated  $R_{rs}$  spectra used to build the LUTs in this work are hyperspectrally resolved. Therefore, selection of the appropriate wavebands for each instrument is all that is required before the spectral matching process can take place. As a result, these methods are easily applicable to any satellite mounted

ocean colour instrument, which could allow for even greater insight moving forward. For example, whilst OLCI has good spectral resolution, with 9 wavebands in the VR (compared to MODIS's 8), the real benefit is the instrument's greatly increased spatial resolution of 300 m. This could allow for the detection of smaller-scale, more localised swarms of zooplankton than is currently possible with MODIS's 1 km resolution data. Another instrument that may lead to greater insight within this field is NASA's first hyperspectral satellite PACE. This significant increase in resolution could allow for the detection of finer spectral features, which may help to better discriminate between optical constituents, including different zooplankton groups with similar spectral properties.

The work presented in this thesis demonstrated the importance of larger particles on the bulk IOPs of the marine environment. With this in mind, it is important to build on the work presented in Chapter 6 and focus efforts on characterisation of the optical properties of other large particles that are ubiquitous within the marine environment. Continuing with the PSICAM approach, measuring the absorption properties of other species, such as the Southern Ocean krill species *E. superba* and natural populations of micro jellyfish, will allow for the application of the detection methods described in this work to these zooplankton groups, both of which are ecologically and commercially important. With respect to the krill species *E. superba*, which represent a globally significant economic and biological resource, this will allow for more extensive monitoring of stock levels for management purposes.

Indeed, preliminary work on applying the colour matching method to *E. superba* in the Southern Ocean has been conducted, with promising initial results. A British Antarctic Survey (BAS) research cruise conducted between 15<sup>th</sup> January and 23<sup>rd</sup> February 2016 off the South Orkney Islands recorded the presence of large swarms of krill in the surface waters between the 7<sup>th</sup> and 15<sup>th</sup> February 2016. Figure 7.1a shows a MODIS eRGB image of the area from the 15<sup>th</sup> February 2016, with the extent of the cruise indicated by the red dotted line. There is a clear red feature evident within the cruise extent, which was highlighted as optically anomalous when the  $\Delta E_{2000}$  algorithm was applied to it (Figure 7.1b). As no absorption measurements of

this krill species are currently available, it is not possible to determine if this anomaly is caused by *E. superba* swarms. However, as a preliminary study, *C. finmarchicus* absorption was added to the model to account for this anomaly, which was used as a proxy for astaxanthin absorption, as both *C. finmarchicus* and *E. superba* contain this pigment. With the addition of this astaxanthin component, the anomaly within the feature was resolved (Figure 7.1c). This provides evidence that an astaxanthin containing organism is likely influencing the optical signal within this feature. However, in order to attempt to estimate *E. superba* abundance using images such as this, future work on the absorption characterisation of natural *E. superba* populations is critical.

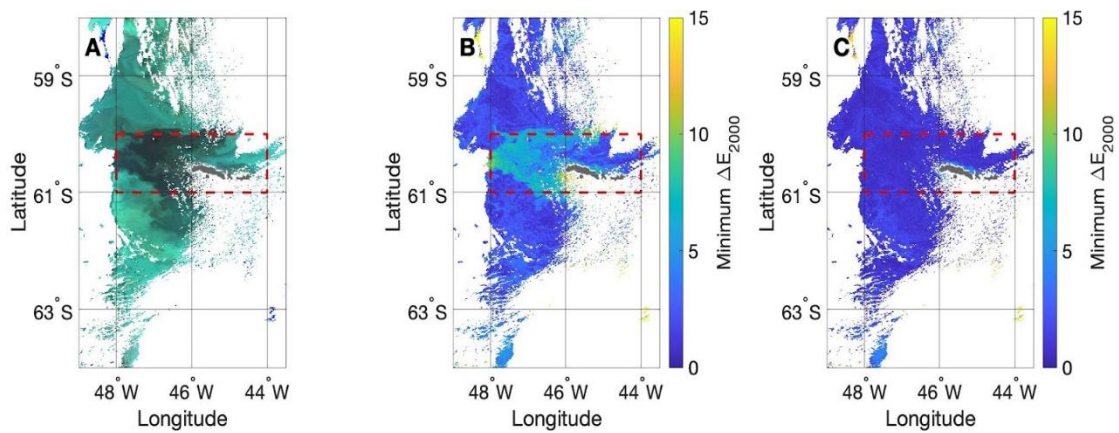


Figure 7.1 (a) MODIS Enhanced RGB image of the South Orkney Islands from 15<sup>th</sup> February 2016, showing an extensive red feature in the same region that a British Antarctic Survey (BAS) lead research cruise (cruise extent indicated by red dotted line) recorded large surface swarms of *E. superba*. (b) The red feature was highlighted as optically anomalous when compared to a standard Case 2 model. (c) This anomaly was resolved with the addition of an astaxanthin absorbing component into the model.

The application of satellite detection techniques to micro jellyfish populations could aid in minimising the harmful impact jellyfish blooms can have on coastal fisheries and tourism globally. Despite being largely transparent organisms, the work presented in this thesis illustrates that micro-jellyfish have the potential to influence

ocean colour signals. However, as the organisms measured in this study were cultivated in a laboratory and the signal appeared to be driven by their food source, it is important to characterise the absorption properties of natural jellyfish populations. With this information, the feasibility of remote detection of harmful jellyfish blooms *in situ* will become apparent. Similarly, measuring the spectral absorption of other large particles that may be present in surface waters, such as fish eggs and larvae, will contribute to our understanding of the optical impact of this particle size class. Further, the remote detection of fish eggs/ larvae would be particularly useful, as providing information on the spatial extent/ concentration of fish spawning events could considerably improve stock assessments for the fishing industry. Generally, the continued expansion of spectral libraries to include the spectral absorption of large particles will allow for the application of the remote detection methods presented in this thesis for critical organisms within this size class.

#### 7.2.2 *Application of methods for remote detection of phytoplankton functional types*

The methods described throughout this thesis are widely applicable and therefore can be utilised for other optically anomalous constituents. One potential application for the spectral matching framework is the distinction of Phytoplankton Functional Types (PFTs) from ocean colour data. Whilst satellite detection of chlorophyll-*a* as a proxy for phytoplankton biomass has revolutionised understanding of global phytoplankton dynamics, it does not fully capture the complex nature of phytoplankton assemblages. PFTs represent a classification system of phytoplankton based on their ecological roles within the marine environment and can provide considerable insight on ecosystem health and functioning, as well as biogeochemical cycling (Nair et al., 2008). Remote detection of PFTs have been the focus of the scientific community within recent years, with the development of many different approaches to remote PFT identification (Sathyendranath et al., 2014). Of the approaches that utilise optical characteristics to distinguish PFT signals, many rely on empirical relationships between different PFTs and *in situ* observations of

chlorophyll, as well as other auxiliary pigments. With further development of the spectral matching approach described in this thesis, concentration estimates of PFTs with distinct optical signatures, for example highly scattering coccolithophores, could potentially be obtained directly from reflectance data. However, the application of these methods to PFT identification first requires the accurate determination of PFT SIOPs, including both absorption and backscattering coefficients. With focused efforts on determining the spectral characteristics of different PFTs, as well as how these characteristics change within species/ functional types, better characterisation of these groups from space may be achieved.

### 7.2.3 *Characterisation of variability in spectral absorption within zooplankton species*

Another key finding of this thesis was the considerable degree of variability in absorption properties between individuals within the same species. Careful characterisation of this variability, as well as its potential causes, is critical for the improvements of remote population concentration estimates. The study of pigmentation variation between individuals has largely been overlooked, likely the result of the intrinsic plasticity of this functional trait and the difficulties associated with pigment extraction and sample handling (Vilgrain et al., 2023). However, the PSICAM approach facilitates relatively fast, highly sensitive absorption measurements to be made on live natural populations. This could be a powerful tool for testing the impact of different variables such as life stage, exposure to light and food availability on pigmentation of these organisms. This would not only provide biological information on a previously understudied functional trait, but also better parameterisation of pigmentation for modelling and detection purposes. Additionally, this would aid in the development of a robust variance product associated with remote concentration estimates, which would provide a measure of confidence to ensure the quality and reliability of concentration outputs.

#### 7.2.4 Characterisation of the spectral scattering properties of zooplankton

The work in this thesis has demonstrated the novel use of the PSICAM to ascertain the spectral absorption properties of zooplankton. As Davies et al. (2021) theoretically demonstrated, this is the most critical SIOP for larger particles. However, to obtain a more complete SIOP profile and fully characterise the contribution of zooplankton to ocean colour, their backscattering properties must be determined. Unfortunately, current *in situ* instrumentation is bias towards smaller, more numerically abundant particles, which means there is currently no scope to directly measure the backscattering properties of this particle size class. The development of *in situ* instrumentation that has the ability to resolve the optical properties of larger particles is therefore vital for the advancement of this field.

In the meantime, Mie Theory could be used as an alternative approach to obtain a crude theoretical estimate of scattering. However, as Mie Theory describes the scattering properties of spherical particles and zooplankton are typically not spherical, it is likely that estimates derived from this method will not be representative of natural populations. Another method of deriving backscattering estimates is to utilise an inverse solution method using radiometric measurements. The most common relationship to express underwater  $r_{rs}$  as a function of IOPs is represented in Gordon et al. (1988) as:

$$r_{rs}(\lambda) = \sum_{i=1}^2 G_i(\lambda) \left[ \frac{b_b(\lambda)}{a(\lambda) + b_b(\lambda)} \right] \quad (7.1)$$

Where the  $G(\lambda)$  coefficients represent the combined influence of illumination conditions and geometry, sea surface properties and the shape of the marine VSF. The  $r_{rs}$  can then be converted to above surface  $R_{rs}$  as observed from satellite imagery, using relationships such as those defined in Lee et al. (2002). From relationships such as these, radiometric  $R_{rs}$  measurements can be converted into bulk  $a$  and  $b_b$  estimates, which can then be partitioned into different optical constituents. However, this

method will require *in situ* sampling of a surface swarm zooplankton, which could be difficult to achieve in practice as these organisms exhibit extremely patchy distributions. Another alternative is to obtain radiometric measurements from laboratory cultivated samples, although it is likely that these samples would not be wholly representative of natural populations.

As both previous theoretical studies (Davies et al., 2021) and this thesis has demonstrated, larger particles can significantly contribute to the bulk optical properties of the water column. As a result, it is important for the marine optics community to focus on the development of instrumentation that has the capacity to fully characterise the IOPs of particles of this size class. However, as outlined above, there are a number of avenues to obtain some estimate of the backscattering properties of large particles such as zooplankton in the absence of direct measurements, which can be explored in future work.

#### 7.2.5 *In situ* zooplankton monitoring and characterisation of evasion behaviour

In order to validate zooplankton concentrations estimates derived from space, *in situ* abundance measurements are required. As a first step, resources such as the CPR may provide some information on zooplankton abundances that can be used for validation purposes. However, an important issue first identified in Chapter 3 was the order of magnitude difference in concentration estimates of *C. finmarchicus* between *in situ* measurements and those derived from satellite signals. It was hypothesised that this deviation could be the result of animal evasion behaviours, as unlike the other optically significant constituents in marine waters, zooplankton can swim over considerable distances and are responsible for the greatest migration of biomass in the world (Hays, 2003). Net evasion behaviour has previously been recorded and studied in highly mobile krill organisms, providing evidence of the active evasion of these organisms from net sampling (Brierley, 1999; Everson & Bone, 1986; Hill et al., 1996; Nicol, 1986). This behaviour was also recorded to increase towards the surface, where there is lots of light that allow krill to visually detect nets

(Hill et al., 1996). Despite this, there has been little study on the impact of net sampling on the behaviours of smaller zooplankton species such as *C. finmarchicus*. However, considering the evidence of mismatch between satellite and *in situ* observations of *C. finmarchicus* presented in Chapter 3 of this thesis, it is clear that evasion behaviour should be considered when sampling these organisms *in situ*. Therefore, to ensure the availability of accurate *in situ* population measurements for ground truthing purposes, it is important to quantify this evasion behaviour and encourage the development of new technologies that facilitate less invasive sampling techniques.

Quantification of evasion behaviours would allow for a correction factor to be applied to historic abundance measurements. Instead of simply classifying historic measurements as incorrect, this would increase data availability, which is of vital importance when trying to provide *in situ* match ups for satellite-based studies. This could potentially be achieved by mounting cameras to nets and/or on the bow of a ship, in order to capture evasion behaviour. Similarly, cameras attached to drones or autonomous platforms could be used to detect any evasion behaviour when nets/sensing instruments are deployed. Research ships themselves may cause considerable disturbance to zooplankton populations, which means all ship-based sampling techniques could be affected by animal evasion. To overcome this, sampling should occur as far away from the ship as possible. The continued use and further development of newer autonomous imaging technologies such as the Zooglider, Imaging FlowCytobot and Underwater Vision Profiler (UVP-6) will contribute to the goal. Further, floating frames with mounted radiometric instruments could be tethered to a research vessel with floating rope and allowed to drift as far from the vessel as possible. This would allow for radiometric measurements to be made in relatively undisturbed waters. There has also been some success with the use of acoustic sensors mounted on a floating sailbuoy for characterising populations, with Bandara et al. (2022) measuring *C. finmarchicus* concentrations of up to 165,000 individuals  $\text{m}^{-3}$  in the Norwegian Sea. Whilst acoustic sensors cannot resolve surface concentrations due to considerable noise at the surface, continued monitoring of

zooplankton populations in this capacity could be used in conjunction with other methods for ground truthing purposes.

#### 7.2.6 *Development of the per-pixel atmospheric correction method*

In a more general context, the per-pixel AC selection method presented in Chapter 4 represents significant potential for the retrieval of high quality ocean colour data from optically complex environments. This method not only provides corrected  $R_{rs}$  spectra, but also CHL, MSS and CDOM products that can span optically clear open ocean and optically complex coastal waters. However, before this method can be implemented on a larger scale, further testing and development is necessary. Firstly, rigorous *in situ* validation exercises must be conducted, where the satellite derived CHL, MSS and CDOM products will be compared to *in situ* measurements for ground truthing. For this, concentration retrievals from differing oceanic environments will be compared, to identify any regions where this method may break down.

Following this, the methodology requires considerable streamlining for operational use. Whilst conceptually simple, the multi-step approach first presented in Chapter 4 is computationally expensive and requires multiple processing iterations to achieve optimal results. This makes the method less attractive for batch processing exercises and broader practical applications. To overcome this, there is potential for the development of an artificial neural network (NN) approach, where a training dataset is constructed using the methodology described in Chapter 4. The NN would therefore output appropriately corrected spectral  $R_{rs}$  data, as well as CHL, MSS and CDOM products in an optimised manor. However, NNs require extensive training datasets, which must contain a lot of data points that are appropriately representative of the oceanic environments it will be applied to. This will greatly increase the generalisation capabilities of the NN and reduce the risk of model overfitting based on a biased training dataset. As satellite data has global coverage, data availability should not be an issue. However, the sheer number of satellite images required to develop a globally applicable NN would make the training process both

computationally and time intensive. Despite this, once the NN has been adequately trained, the application of this method would be much quicker than that of the manual processing method outlined in Chapter 4. As a result, whilst this approach has its disadvantages, it could represent a powerful tool to aid in the accessibility of this promising per-pixel approach to AC of ocean colour data.

## 8 References

- Ahmad, Z., Franz, B. A., McClain, C. R., Kwiatkowska, E. J., Werdell, J., Shettle, E. P., & Holben, B. N. (2010). New aerosol models for the retrieval of aerosol optical thickness and normalized water-leaving radiances from the SeaWiFS and MODIS sensors over coastal regions and open oceans. *Applied Optics*, 49(29), 5545. <https://doi.org/10.1364/AO.49.005545>
- Bailey, S. W., Franz, B. A., & Werdell, J. P. (2010). Estimation of near-infrared water-leaving satellite ocean color data processing. *Optics Express*, 18(7), 7521–7527.
- Balch, W. M., Holligan, P. M., Ackleson, S. G., & Voss, K. J. (1991). Biological and optical properties of mesoscale coccolithophore blooms in the Gulf of Maine. *Limnology and Oceanography*, 36(4), 629–643. <https://doi.org/10.4319/lo.1991.36.4.0629>
- Bandara, K., Basedow, S. L., Pedersen, G., & Tverberg, V. (2022). Mid-summer vertical behavior of a high-latitude oceanic zooplankton community. *Journal of Marine Systems*, 230. <https://doi.org/10.1016/j.jmarsys.2022.103733>
- Basedow, S. L., McKee, D., Lefering, I., Gislason, A., Daase, M., Trudnowska, E., Egeland, E. S., Choquet, M., & Falk-Petersen, S. (2019). Remote sensing of zooplankton swarms. *Scientific Reports*, 9(1). <https://doi.org/10.1038/s41598-018-37129-x>
- Behrenfeld, M. J., Gaube, P., Della Penna, A., O'Malley, R. T., Burt, W. J., Hu, Y., Bontempi, P. S., Steinberg, D. K., Boss, E. S., Siegel, D. A., Hostetler, C. A., Tortell, P. D., & Doney, S. C. (2019). Global satellite-observed daily vertical migrations of ocean animals. *Nature*, 576(7786), 257–261. <https://doi.org/10.1038/s41586-019-1796-9>
- Bengil, F., McKee, D., Beşiktepe, S. T., Sanjuan Calzado, V., & Trees, C. (2016). A bio-optical model for integration into ecosystem models for the Ligurian Sea. *Progress in Oceanography*, 149, 1–15. <https://doi.org/10.1016/J.POCEAN.2016.10.007>
- Berge, J., Geoffroy, M., Daase, M., Cottier, F., Priou, P., Cohen, J. H., Johnsen, G., McKee, D., Kostakis, I., Renaud, P. E., Vogedes, D., Anderson, P., Last, K. S., & Gauthier, S. (2020). Artificial light during the polar night disrupts Arctic fish and zooplankton behaviour down to 200 m depth. *Communications Biology*, 3(1). <https://doi.org/10.1038/s42003-020-0807-6>
- Botterell, Z. L. R., Lindeque, P. K., Thompson, R. C., & Beaumont, N. J. (2023). An assessment of the ecosystem services of marine zooplankton and the key threats to their provision. In *Ecosystem Services* (Vol. 63). Elsevier B.V. <https://doi.org/10.1016/j.ecoser.2023.101542>
- Brewin, R. J. W., Hardman-Mountford, N. J., Lavender, S. J., Raitos, D. E., Hirata, T., Uitz, J., Devred, E., Bricaud, A., Ciotti, A., & Gentili, B. (2011). An intercomparison of bio-optical techniques for detecting dominant

- phytoplankton size class from satellite remote sensing. *Remote Sensing of Environment*, 115(2), 325–339. <https://doi.org/10.1016/j.rse.2010.09.004>
- Brierley, A. S. (1999). A comparison of Antarctic euphausiids sampled by net and from geothermally heated waters: insights into sampling bias. *Polar Biology*, 22, 109–144.
- Brown, C. W., & Podestá, G. P. (1997). Remote sensing of coccolithophore blooms in the Western South Atlantic ocean. *Remote Sensing of Environment*, 60(1), 83–91. [https://doi.org/10.1016/S0034-4257\(96\)00140-X](https://doi.org/10.1016/S0034-4257(96)00140-X)
- Buiteveld, H., Hakvoort, J., & Donze, M. (1994). Optical properties of pure water. *Ocean Optics XII*, 2258, 174–183.
- Bullen, G. (1913). Mackerel and Calanus. *Nature*, 91, 531.
- Carder, K. L., Chen, F. R., Cannizzaro, J. P., Campbell, J. W., & Mitchell, B. G. (2004). Performance of the MODIS semi-analytical ocean color algorithm for chlorophyll-a. *Advances in Space Research*, 33(7), 1152–1159. [https://doi.org/10.1016/S0273-1177\(03\)00365-X](https://doi.org/10.1016/S0273-1177(03)00365-X)
- Chang, C.-I. (2000). An information-theoretic approach to spectral variability, similarity, and discrimination for hyperspectral image analysis. *IEEE Transactions on Information Theory*, 46(5).
- Chen, S., Zhang, T., & Hu, L. (2014). Evaluation of the NIR-SWIR atmospheric correction algorithm for MODIS-Aqua over the Eastern China Seas. *International Journal of Remote Sensing*, 35(11–12), 4239–4251. <https://doi.org/10.1080/01431161.2014.916051>
- Clark, K. A. J., Brierley, A. S., & Pond, D. W. (2012). Composition of wax esters is linked to diapause behavior of *Calanus finmarchicus* in a sea loch environment. *Limnology and Oceanography*, 57(1), 65–75. <https://doi.org/10.4319/lo.2012.57.1.0065>
- Conover, R. J. (1988). Comparative life histories in the genera *Calanus* and *Neocalanus* in high latitudes of the northern hemisphere. *Hydrobiologia*, 167, 127–142.
- Cram, D. L., Agenbag, J. J., Hampton, I., & Robertson, A. A. (1979). SAS Protea Cruise, 1978; The general results of the acoustics and remote sensing study, with recommendations for estimating the abundance of krill (*Euphausia superba* Dana). In *S. Afr. J. Antarct. Res* (Vol. 9).
- Davies, E. J., Basedow, S. L., & McKee, D. (2021). The hidden influence of large particles on ocean colour. *Scientific Reports*, 11(1). <https://doi.org/10.1038/s41598-021-83610-5>
- Dierssen, H. M., Vandermeulen, R. A., Barnes, B. B., Castagna, A., Knaeps, E., & Vanhellemont, Q. (2022). QWIP: A Quantitative Metric for Quality Control of Aquatic Reflectance Spectral Shape Using the Apparent Visible Wavelength. *Frontiers in Remote Sensing*, 3. <https://doi.org/10.3389/frsen.2022.869611>
- Dippner, J. W., & Krause, M. (2013). Continuous plankton recorder underestimates zooplankton abundance. *Journal of Marine Systems*, 111–112, 263–268. <https://doi.org/10.1016/j.jmarsys.2012.09.009>
- Dong, H., Zhou, M., Hu, Z., Zhang, Z., Zhong, Y., Basedow, S. L., & Smith, W. O. (2021). Transport Barriers and the Retention of *Calanus finmarchicus* on the

- Lofoten Shelf in Early Spring. *Journal of Geophysical Research: Oceans*, 126(8). <https://doi.org/10.1029/2021JC017408>
- Drira, Z., Kmiha-Megdiche, S., Sahnoun, H., Tedetti, M., Pagano, M., & Ayadi, H. (2018). Copepod assemblages as a bioindicator of environmental quality in three coastal areas under contrasted anthropogenic inputs (Gulf of Gabes, Tunisia). *Journal of the Marine Biological Association of the United Kingdom*, 98(8), 1889–1905. <https://doi.org/10.1017/S0025315417001515>
- Druon, J.-N., Hélaouët, P., Beaugrand, G., Fromentin, J.-M., Palialexis, A., & Hoepffner, N. (2019). Satellite-based indicator of zooplankton distribution for global monitoring. *Scientific Reports*, 9(1), 4732. <https://doi.org/10.1038/s41598-019-41212-2>
- Dunbar, M. J. (1946). On *Themisto libellula* in Baffin Island Coastal Waters. *Journal of the Fisheries Research Board of Canada*, 6e(6), 419–434. <https://doi.org/10.1139/f42-050>
- Eilertsen, K. E., Mæhre, H. K., Jensen, I. J., Devold, H., Olsen, J. O., Lie, R. K., Brox, J., Berg, V., Elvevoll, E. O., & Østerud, B. (2012). A wax ester and astaxanthin-rich extract from the marine copepod *Calanus finmarchicus* attenuates atherosclerosis in female apolipoprotein E-deficient mice. *Journal of Nutrition*, 142(3), 508–512. <https://doi.org/10.3945/jn.111.145698>
- Emberton, S., Chittka, L., Cavallaro, A., & Wang, M. (2016). Sensor capability and atmospheric correction in ocean colour remote sensing. *Remote Sensing*, 8(1). <https://doi.org/10.3390/rs8010001>
- Everson, I., & Bone, D. G. (1986). Effectiveness of the RMT8 System for Sampling Krill (*Euphausia superba*) Swarms. In *Polar Biol* (Vol. 6).
- Falk-Petersen, S., Mayzaud, P., Kattner, G., & Sargent, J. R. (2009). Lipids and life strategy of Arctic *Calanus*. In *Marine Biology Research* (Vol. 5, Issue 1, pp. 18–39). <https://doi.org/10.1080/17451000802512267>
- Ferrari, G. M., & Tassan, S. (1999). A method using chemical oxidation to remove light absorption by phytoplankton pigments. *Journal of Phycology*, 35(5), 1090–1098. <https://doi.org/10.1046/j.1529-8817.1999.3551090.x>
- Fielding, S., Watkins, J. L., Collins, M. A., Enderlein, P., & Venables, H. J. (2012). Acoustic determination of the distribution of fish and krill across the Scotia Sea in spring 2006, summer 2008 and autumn 2009. *Deep-Sea Research Part II: Topical Studies in Oceanography*, 59–60, 173–188. <https://doi.org/10.1016/j.dsr2.2011.08.002>
- Frouin, R. J., Franz, B. A., Ibrahim, A., Knobelspiesse, K., Ahmad, Z., Cairns, B., Chowdhary, J., Dierssen, H. M., Tan, J., Dubovik, O., Huang, X., Davis, A. B., Kalashnikova, O., Thompson, D. R., Remer, L. A., Boss, E., Coddington, O., Deschamps, P. Y., Gao, B. C., ... Zhai, P. W. (2019). Atmospheric Correction of Satellite Ocean-Color Imagery During the PACE Era. *Frontiers in Earth Science*, 7. <https://doi.org/10.3389/feart.2019.00145>
- Goldstein, J., & Steiner, U. K. (2020). Ecological drivers of jellyfish blooms – The complex life history of a ‘well-known’ medusa (*Aurelia aurita*). *Journal of Animal Ecology*, 89(3), 910–920. <https://doi.org/10.1111/1365-2656.13147>

- Gordon, H. R. (1978). Removal of atmospheric effects from satellite imagery of the oceans. *Applied Optics*, 17(10), 1631–1636.
- Gordon, H. R., & Wang, M. (1994). Retrieval of water-leaving radiance and aerosol optical thickness over the oceans with SeaWiFS: a preliminary algorithm. *Applied Optics*, 33(3), 443–452.
- Gower, J. C. (1985). Properties of Euclidean and Non-Euclidean Distance Matrices. *Linear Algebra and Its Applications*, 67, 81–97.
- Hamner, W. M., & Hamner, P. P. (2000). Behavior of Antarctic krill (*Euphausia superba*): schooling, foraging, and antipredatory behavior. *Canadian Journal of Fisheries and Aquatic Sciences*, 57(S3), 192–202.
- Hansson, L. A., & Hylander, S. (2009). Effects of ultraviolet radiation on pigmentation, photoenzymatic repair, behavior, and community ecology of zooplankton. *Photochemical and Photobiological Sciences*, 8(9), 1266–1275. <https://doi.org/10.1039/b908825c>
- Harrison, L. M. K., Goetz, K., Cox, M. J., & Harcourt, R. (2020). A Southern Ocean archipelago enhances feeding opportunities for a krill predator. *Marine Mammal Science*, 36(1), 260–275. <https://doi.org/10.1111/mms.12645>
- Havermans, C., Auel, H., Hagen, W., Held, C., Ensor, N. S., & A. Tarling, G. (2019). *Predatory zooplankton on the move: Themisto amphipods in high-latitude marine pelagic food webs* (pp. 51–92). <https://doi.org/10.1016/bs.amb.2019.02.002>
- Hays, G. C. (2003). A review of the adaptive significance and ecosystem consequences of zooplankton diel vertical migrations. In *Hydrobiologia* (Vol. 503).
- Hicks, N. (2018). *Loch Etive MASTS Case Study Workshop Report*.
- Hill, H. J., Trathan, P. N., Croxall, J. P., & Watkins, J. L. (1996). A comparison of Antarctic krill *Euphausia superba* caught by nets and taken by macaroni penguins *Eudyptes chrysolophus*: evidence for selection? *Marine Ecology Progress Series*, 140, 1–11.
- Holm-Hansen, O., & Huntley, M. (1982). Feeding Requirements of Krill in Relation to Food Sources. *Journal of Crustacean Biology*, 4, 156–173. <https://www.jstor.org/stable/27920094>
- Hu, C., Feng, L., Lee, Z., Franz, B. A., Bailey, S. W., Werdell, P. J., & Proctor, C. W. (2019). Improving Satellite Global Chlorophyll a Data Products Through Algorithm Refinement and Data Recovery. *Journal of Geophysical Research: Oceans*, 124(3), 1524–1543. <https://doi.org/10.1029/2019JC014941>
- Hu, C., Lee, Z., & Franz, B. (2012). Chlorophyll a algorithms for oligotrophic oceans: A novel approach based on three-band reflectance difference. *Journal of Geophysical Research: Oceans*, 117(1). <https://doi.org/10.1029/2011JC007395>
- Iwasa, Y. (1982). Vertical migration of zooplankton: A game between predator and prey. *The American Naturalist*, 120(2), 171–180. <https://about.jstor.org/terms>
- Jennings, S., Mélin, F., Blanchard, J. L., Forster, R. M., Dulvy, N. K., & Wilson, R. W. (2008). Global-scale predictions of community and ecosystem properties from simple ecological theory. *Proceedings of the Royal Society B: Biological Sciences*, 275(1641), 1375–1383. <https://doi.org/10.1098/rspb.2008.0192>
- John, E. H., Batten, S. D., Harris, R. P., & Hays, G. C. (2001). Comparison between zooplankton data collected by the Continuous Plankton Recorder survey in the

- English Channel and by WP-2 nets at station L4, Plymouth (UK). *Journal of Sea Research*, 46(3–4), 223–232. [https://doi.org/10.1016/S1385-1101\(01\)00085-5](https://doi.org/10.1016/S1385-1101(01)00085-5)
- Kenney, R. D., & Wishner, K. F. (1995). The South Channel Ocean Productivity Experiment. In *Continental Shelf Research* (Vol. 15, Issue 5).
- Kim, S. L., & Oliver, J. S. (1989). Swarming benthic crustaceans in the Bering and Chukchi seas and their relation to geographic patterns in gray whale feeding. *Canadian Journal of Zoology*, 67(6), 1531–1542. <https://doi.org/10.1139/z89-218>
- Kirk, J. T. O. (1997). Point-source integrating-cavity absorption meter: theoretical principles and numerical modeling. *Applied Optics*, 36(24), 6123–6128.
- Kruse, F. A., Lefkoff, A. B., Boardman, J. W., Heidebrecht, K. B., Shapiro, A. T., Barloon, P. J., & Goetz, A. F. H. (1993). The spectral image processing system (SIPS)-interactive visualization and analysis of imaging spectrometer data. *Remote Sensing of Environment*, 44(2–3), 145–163. [https://doi.org/10.1016/0034-4257\(93\)90013-N](https://doi.org/10.1016/0034-4257(93)90013-N)
- Lavender, S. J., Pinkerton, M. H., Moore, G. F., Aiken, J., & Blondeau-Patissier, D. (2005). Modification to the atmospheric correction of SeaWiFS ocean colour images over turbid waters. *Continental Shelf Research*, 25(4), 539–555. <https://doi.org/10.1016/j.csr.2004.10.007>
- Leathers, R. A., Downes, T. V., & Davis, C. O. (2000). Analysis of a point-source integrating-cavity absorption meter. *Applied Optics*, 39(33), 6118–6127.
- Lee, Z., Carder, K. L., & Arnone, R. A. (2002). Deriving inherent optical properties from water color: a multiband quasi-analytical algorithm for optically deep waters. *Applied Optics*, 41(27), 5755. <https://doi.org/10.1364/AO.41.005755>
- Lefering, I. (2016). *Characterisation of a Point-Source Integrating Cavity Absorption Meter for applications in optical oceanography*. University of Strathclyde .
- Lefering, I., Bengil, F., Trees, C., Röttgers, R., Bowers, D., Nimmo-Smith, A., Schwarz, J., & McKee, D. (2016). Optical closure in marine waters from in situ inherent optical property measurements. *Optics Express*, 24(13), 14036. <https://doi.org/10.1364/oe.24.014036>
- Lefering, I., Röttgers, R., Utschig, C., Twardowski, M. S., & McKee, D. (2018). Measurement uncertainties in PSICAM and reflective tube absorption meters. *Optics Express*, 26(19), 24384. <https://doi.org/10.1364/OE.26.024384>
- Lefering, I., Röttgers, R., Weeks, R., Connor, D., Utschig, C., Heymann, K., & McKee, D. (2016). Improved determination of particulate absorption from combined filter pad and PSICAM measurements. *Optics Express*, 24(22), 24805. <https://doi.org/10.1364/OE.24.024805>
- Lerebourg, C. J.-Y., Pilgrim, D. A., Ludbrook, G. D., & Neal, R. (2002). Development of a point source integrating cavity absorption meter. *Journal of Optics A: Pure and Applied Optics*, 4.
- Liu, H., Wu, B., Liu, Y., Huang, M., & Xu, Y. (2013). A discussion on printing color difference tolerance by CIEDE2000 color difference formula. *Applied Mechanics and Materials*, 262, 96–99. <https://doi.org/10.4028/www.scientific.net/AMM.262.96>
- Lo Prejato, M., McKee, D., & Mitchell, C. (2020). Inherent Optical Properties-Reflectance Relationships Revisited. *Journal of Geophysical Research: Oceans*, 125(11). <https://doi.org/10.1029/2020JC016661>

- Loveday, B. R., & Smyth, T. (2018). A 40-year global data set of visible-channel remote-sensing reflectances and coccolithophore bloom occurrence derived from the Advanced Very High Resolution Radiometer catalogue. *Earth System Science Data*, 10(4), 2043–2054. <https://doi.org/10.5194/essd-10-2043-2018>
- Luo, M. R., Cui, G., & Rigg, B. (2001). The development of the CIE 2000 colour-difference formula: CIEDE2000. *Color Research & Application*, 26(5), 340–350. <https://doi.org/10.1002/col.1049>
- Maas, A. E., Lawson, G. L., Bergan, A. J., Wang, Z. A., & Tarrant, A. M. (2020). Seasonal variation in physiology and shell condition of the pteropod *Limacina retroversa* in the Gulf of Maine relative to life cycle and carbonate chemistry. *Progress in Oceanography*, 186. <https://doi.org/10.1016/j.pocean.2020.102371>
- Madsen, S. J., Nielsen, T. G., Tervo, O. M., & Söderkvist, J. (2008). Importance of feeding for egg production in *Calanus finmarchicus* and *C. glacialis* during the Arctic spring. *Marine Ecology Progress Series*, 353, 177–190. <https://doi.org/10.3354/meps07129>
- Mahesh, R., Saravanakumar, A., Thangaradjou, T., Solanki, H. U., & Raman, M. (2018). A regional algorithm to model mesozooplankton biomass along the southwestern Bay of Bengal. *Environmental Monitoring and Assessment*, 190(4), 246. <https://doi.org/10.1007/s10661-018-6578-6>
- Marcus, N. (2004). An Overview of the Impacts of Eutrophication and Chemical Pollutants on Copepods of the Coastal Zone. *Zoological Studies*, 43(2), 211–217. <http://www.sinica.edu.tw/zool/zoolstud/43.2/211.pdf>
- Marine Zooplankton Colloquium 2. (2001). Future marine zooplankton research- a perspective. *Marine Ecology Progress Series*, 222, 297–308.
- Mathisen, A., & Macaulay, M. C. (1983). The Morphological Features of a Superswarm of Krill *Euphausia superba*. *Memoirs of National Institute of Polar Research*, 27, 153–164.
- McCarry, C. L., Basedow, S. L., Davies, E. J., & McKee, D. (2023). Estimating Surface Concentrations of *Calanus finmarchicus* Using Standardised Satellite-Derived Enhanced RGB Imagery. *Remote Sensing*, 15(12), 2987. <https://doi.org/10.3390/rs15122987>
- McKee, D., Piskozub, J., Röttgers, R., & Reynolds, R. A. (2013). Evaluation and Improvement of an Iterative Scattering Correction Scheme for in situ Absorption and Attenuation Measurements. *Journal of Atmospheric and Oceanic Technology*, 30(7), 1527–1541. <https://doi.org/10.1175/JTECH-D-12-00150.1>
- McKee, D., Röttgers, R., Neukermans, G., Calzado, V. S., Trees, C., Ampolo-Rella, M., Neil, C., & Cunningham, A. (2014). Impact of measurement uncertainties on determination of chlorophyll-specific absorption coefficient for marine phytoplankton. *Journal of Geophysical Research: Oceans*, 119(12), 9013–9025. <https://doi.org/10.1002/2014JC009909>
- Melle, W., Runge, J., Head, E., Plourde, S., Castellani, C., Licandro, P., Pierson, J., Jonasdottir, S., Johnson, C., Broms, C., Debes, H., Falkenhaus, T., Gaard, E., Gislason, A., Heath, M., Niehoff, B., Nielsen, T. G., Pepin, P., Stenevik, E. K., & Chust, G. (2014). The North Atlantic Ocean as habitat for *Calanus finmarchicus*:

- Environmental factors and life history traits. *Progress in Oceanography*, 129(PB), 244–284. <https://doi.org/10.1016/j.pocean.2014.04.026>
- Meyer-Gutbrod, E. L., Greene, C. H., Davies, K. T. A., & Johns, D. G. (2021). *Ocean regime shift is driving the collapse of the North Atlantic Right Whale population*. 34(3), 22–31. <https://doi.org/10.2307/27051387>
- Miller, E. J., Potts, J. M., Cox, M. J., Miller, B. S., Calderan, S., Leaper, R., Olson, P. A., O'Driscoll, R. L., & Double, M. C. (2019). The characteristics of krill swarms in relation to aggregating Antarctic blue whales. *Scientific Reports*, 9(1). <https://doi.org/10.1038/s41598-019-52792-4>
- Miller, M. E. C., & Graham, W. M. (2012). Environmental evidence that seasonal hypoxia enhances survival and success of jellyfish polyps in the northern Gulf of Mexico. *Journal of Experimental Marine Biology and Ecology*, 432–433, 113–120. <https://doi.org/10.1016/j.jembe.2012.07.015>
- Mobley, C. D. (1994). Optical Properties of Water. In C. D. Mobley & R. W. Preisendorfer (Eds.), *Light and Water: Radiative Transfer in Natural Waters*. Academic Press.
- Mobley, C. D. (2022). *The Oceanic Optics Book* (C. D. Mobley, Ed.). International Ocean Colour Coordinating Group (IOCCG).
- Moore, T. S., Dowell, M. D., & Franz, B. A. (2012). Detection of coccolithophore blooms in ocean color satellite imagery: A generalized approach for use with multiple sensors. *Remote Sensing of Environment*, 117, 249–263. <https://doi.org/10.1016/j.rse.2011.10.001>
- Morel, A., & Prieur, L. (1977). Analysis of variations in ocean color. *Limnology and Oceanography*, 22(4), 709–722. <https://doi.org/10.4319/lo.1977.22.4.0709>
- Nair, A., Sathyendranath, S., Platt, T., Morales, J., Stuart, V., Forget, M.-H., Devred, E., & Bouman, H. (2008). Remote sensing of phytoplankton functional types. *Remote Sensing of Environment*, 112(8), 3366–3375. <https://doi.org/10.1016/j.rse.2008.01.021>
- Neveux, J. (2008). Bio-optical properties of the marine cyanobacteria *Trichodesmium* spp. *Journal of Applied Remote Sensing*, 2(1), 023503. <https://doi.org/10.1117/1.2839036>
- Nicol, S. (1984). Population structure of daytime surface swarms of the euphausiid *Meganyctiphanes norvegica* in the Bay of Fundy. In *Source: Marine Ecology Progress Series* (Vol. 18, Issue 3).
- Nicol, S. (1986). Shape, size and density of daytime surface swarms of the euphausiid *Meganyctiphanes norvegica* in the Bay of Fundy. In *Journal of Plankton Research* (Vol. 8). <https://academic.oup.com/plankt/article/8/1/29/1607998>
- Nicol, S. (2018). Oceans of Krill. In *The Curious Life of Krill; A Conservation Story from the Bottom of the World* (pp. 1–15).
- Nidamanuri, R. R., Zbell, B., & Nidamanuri, R. R. (2011). Normalized Spectral Similarity Score (NS3) as an Efficient Spectral Library Searching Method for Hyperspectral Image Classification. *IEEE Journal of Selected Topics in Applied Earth Observations and Remote Sensing*, 4(1), 226–240. <https://doi.org/10.1109/JSTARS.2010.2086435>

- Nowicki, M., DeVries, T., & Siegel, D. A. (2022). Quantifying the Carbon Export and Sequestration Pathways of the Ocean's Biological Carbon Pump. *Global Biogeochemical Cycles*, 36(3). <https://doi.org/10.1029/2021GB007083>
- Ohman, M. D., Davis, R. E., Sherman, J. T., Grindley, K. R., Whitmore, B. M., Nickels, C. F., & Ellen, J. S. (2019). Zooglider: An autonomous vehicle for optical and acoustic sensing of zooplankton. *Limnology and Oceanography: Methods*, 17(1), 69–86. <https://doi.org/10.1002/lom3.10301>
- Olson, R. J., & Sosik, H. M. (2007). A submersible imaging-in-flow instrument to analyze nano-and microplankton: Imaging FlowCytobot. *Limnology and Oceanography: Methods*, 5(6), 195–203. <https://doi.org/10.4319/lom.2007.5.195>
- O'Reilly, J. E., & Werdell, P. J. (2019). Chlorophyll algorithms for ocean color sensors - OC4, OC5 & OC6. *Remote Sensing of Environment*, 229, 32–47. <https://doi.org/10.1016/j.rse.2019.04.021>
- Pedersen, A. M., Vang, B., & Olsen, R. L. (2014). Oil from calanus finmarchicus - Composition and possible use: A review. *Journal of Aquatic Food Product Technology*, 23(6), 633–646. <https://doi.org/10.1080/10498850.2012.741662>
- Picheral, M., Catalano, C., Brousseau, D., Claustre, H., Coppola, L., Leymarie, E., Coindat, J., Dias, F., Fevre, S., Guidi, L., Irisson, J. O., Legendre, L., Lombard, F., Mortier, L., Penkerch, C., Rogge, A., Schmechtig, C., Thibault, S., Tixier, T., ... Stemmann, L. (2022). The Underwater Vision Profiler 6: an imaging sensor of particle size spectra and plankton, for autonomous and cabled platforms. *Limnology and Oceanography: Methods*, 20(2), 115–129. <https://doi.org/10.1002/lom3.10475>
- Pollina, T., Larson, A. G., Lombard, F., Li, H., Le Guen, D., Colin, S., de Vargas, C., & Prakash, M. (2022). PlanktoScope: Affordable Modular Quantitative Imaging Platform for Citizen Oceanography. *Frontiers in Marine Science*, 9. <https://doi.org/10.3389/fmars.2022.949428>
- Pope, R. M., & Fry, E. S. (1997). Absorption spectrum 380-700 nm of pure water. II. Integrating cavity measurements. *Applied Optics*, 36(33), 8710–8723.
- Purcell, J. E., Uye, S. I., & Lo, W. T. (2007). Anthropogenic causes of jellyfish blooms and their direct consequences for humans: A review. In *Marine Ecology Progress Series* (Vol. 350, pp. 153–174). <https://doi.org/10.3354/meps07093>
- Raitsos, D. E., Lavender, S. J., Maravelias, C. D., Haralabous, J., Richardson, A. J., & Reid, P. C. (2008). Identifying four phytoplankton functional types from space: An ecological approach. *Limnology and Oceanography*, 53(2), 605–613. <https://doi.org/10.4319/lo.2008.53.2.0605>
- Ratnarajah, L., Abu-Alhaja, R., Atkinson, A., Batten, S., Bax, N. J., Bernard, K. S., Canonico, G., Cornils, A., Everett, J. D., Grigoratou, M., Ishak, N. H. A., Johns, D., Lombard, F., Muxagata, E., Ostle, C., Pitois, S., Richardson, A. J., Schmidt, K., Stemmann, L., ... Yebra, L. (2023). Monitoring and modelling marine zooplankton in a changing climate. In *Nature Communications* (Vol. 14, Issue 1). Nature Research. <https://doi.org/10.1038/s41467-023-36241-5>
- Richardson, A. J. (2008). In hot water: zooplankton and climate change. *ICES Journal of Marine Science*, 65(3), 279–295. <https://academic.oup.com/icesjms/article/65/3/279/787309>

- Ross, C. H., Runge, J. A., Roberts, J. J., Brady, D. C., Tupper, B., & Record, N. R. (2023). Estimating North Atlantic right whale prey based on *Calanus finmarchicus* thresholds. *Marine Ecology Progress Series*, 703, 1–16. <https://doi.org/10.3354/meps14204>
- Röttgers, R. (2011). *Documentation operation procedures PSICAM*.
- Röttgers, R., Häse, C., & Doerffer, R. (2007). Determination of the particulate absorption of microalgae using a point-source integrating-cavity absorption meter: Verification with a photometric technique, improvements for pigment bleaching, and correction for chlorophyll fluorescence. *Limnology and Oceanography: Methods*, 5(1), 1–12. <https://doi.org/10.4319/lom.2007.5.1>
- Röttgers, R., McKee, D., & Woźniak, S. B. (2013). Evaluation of scatter corrections for ac-9 absorption measurements in coastal waters. *Methods in Oceanography*, 7, 21–39. <https://doi.org/10.1016/j.mio.2013.11.001>
- Röttgers, R., Schönfeld, W., Kipp, P.-R., & Doerffer, R. (2005). Practical test of a point-source integrating cavity absorption meter: the performance of different collector assemblies. *Applied Optics*, 44(26), 5549–5560.
- Ruddick, K. G., Ovidio, F., & Rijkeboer, M. (2000). Atmospheric correction of SeaWiFS imagery for turbid coastal and inland waters. *Applied Optics*, 39(6), 897–912.
- Sars, G. O. (1903). *An Account of the Crustacea of Norway: Copepoda, Calanoida* (Vol. 4). Christiania A. Cammermeyer.
- Sathyendranath, S., Aiken, J., Alvain, S., Barlow, R., Bouman, H., Bracher, A., Brewin, R. J. W., Bricaud, A., Brown, C. W., Ciotti, A. M., Clementson, L., Craig, S. E., Devred, E., Hardman-Mountford, N., Hirata, T., Hu, C., Kostadinov, T. S., Lavender, S., Loisel, H., ... Uitz, J. (2014). Phytoplankton Functional Types from Space. *Reports of the International Ocean Colour Coordinating Group (IOCCG)*, 15, 1–156. [www.ioccg.org](http://www.ioccg.org)
- Schminke, H. K. (2007). Entomology for the copepodologist. *Journal of Plankton Research*, 29(SUPPL. 1). <https://doi.org/10.1093/plankt/fbl073>
- Schroeder, T., Behnert, I., Schaale, M., Fischer, J., & Doerffer, R. (2007). Atmospheric correction algorithm for MERIS above case-2 waters. *International Journal of Remote Sensing*, 28(7), 1469–1486. <https://doi.org/10.1080/01431160600962574>
- Sharma, G., Wu, W., & Dalal, E. N. (2005). The CIEDE2000 Color-Difference Formula: Implementation Notes, Supplementary Test Data, and Mathematical Observations. *Col Res Appl*, 30, 21–30. <https://doi.org/10.1002/col>
- Shi, W., & Wang, M. (2009). An assessment of the black ocean pixel assumption for MODIS SWIR bands. *Remote Sensing of Environment*, 113(8), 1587–1597. <https://doi.org/10.1016/j.rse.2009.03.011>
- Shi, W., & Wang, M. (2012). Satellite views of the Bohai Sea, Yellow Sea, and East China Sea. *Progress in Oceanography*, 104, 30–45. <https://doi.org/10.1016/j.pocean.2012.05.001>
- Shulenberg, E. (1983). Superswarms of antarctic krill (*Euphausia superba* Dana). *Antarctic Journal*, 18, 194–197.
- Shutler, J. D., Grant, M. G., Miller, P. I., Rushton, E., & Anderson, K. (2010). Coccolithophore bloom detection in the north east Atlantic using SeaWiFS:

- Algorithm description, application and sensitivity analysis. *Remote Sensing of Environment*, 114(5), 1008–1016. <https://doi.org/10.1016/j.rse.2009.12.024>
- Steinmetz, F., Deschamps, P.-Y., & Ramon, D. (2011). Atmospheric correction in presence of sun glint: application to MERIS. *Optics Express*, 19(10), 9783–9800.
- Strand, E., Bagøien, E., Edwards, M., Broms, C., & Klevjer, T. (2020). Spatial distributions and seasonality of four Calanus species in the Northeast Atlantic. *Progress in Oceanography*, 185. <https://doi.org/10.1016/j.pocean.2020.102344>
- Strömberg, K. H. P., Smyth, T. J., Allen, J. I., Pitois, S., & O'Brien, T. D. (2009). Estimation of global zooplankton biomass from satellite ocean colour. *Journal of Marine Systems*, 78(1), 18–27. <https://doi.org/10.1016/j.jmarsys.2009.02.004>
- Tarling, G. A., Ensor, N. S., Fregin, T., Goodall-Copestake, W. P., & Fretwell, P. (2010). *An Introduction to the Biology of Northern Krill (Meganyctiphanes norvegica Sars)* (pp. 1–40). <https://doi.org/10.1016/B978-0-12-381308-4.00001-7>
- Tarling, G. A., & Fielding, S. (2016). Swarming and Behaviour of Antarctic Krill. In V. Siegel (Ed.), *Biology and Ecology of Antarctic Krill* (pp. 279–319). Springer . <http://www.springer.com/series/10290>
- Tarling, G. A., Klevjer, T., Fielding, S., Watkins, J., Atkinson, A., Murphy, E., Korb, R., Whitehouse, M., & Leaper, R. (2009). Variability and predictability of Antarctic krill swarm structure. *Deep-Sea Research Part I: Oceanographic Research Papers*, 56(11), 1994–2012. <https://doi.org/10.1016/j.dsr.2009.07.004>
- Tarling, G. A., & Thorpe, S. E. (2017). Oceanic swarms of antarctic krill perform satiation sinking. *Proceedings of the Royal Society B: Biological Sciences*, 284(1869). <https://doi.org/10.1098/rspb.2017.2015>
- Valente, A., Sathyendranath, S., Brotas, V., Groom, S., Grant, M., Jackson, T., Chuprin, A., Taberner, M., Airs, R., Antoine, D., Arnone, R., Balch, W. M., Barker, K., Barlow, R., Bélanger, S., Berthon, J. F., Beşiktepe, Ş., Borsheim, Y., Bracher, A., ... Zibordi, G. (2022). A compilation of global bio-optical in situ data for ocean colour satellite applications – version three. *Earth System Science Data*, 14(12), 5737–5770. <https://doi.org/10.5194/essd-14-5737-2022>
- Vestheim, H., Kaartvedt, S., & Edvardsen, B. (2005). State-dependent vertical distribution of the carnivore copepod *Pareuchaeta norvegica*. *Journal of Plankton Research*, 27(1), 19–26. <https://doi.org/10.1093/plankt/fbh144>
- Vilgrain, L., Maps, F., Basedow, S., Trudnowska, E., Madoui, A., Niehoff, B., & Ayata, S.-D. (2023). Copepods' true colours: pigmentation as an indicator of fitness. *Ecosphere*. <https://doi.org/10.5281/zenodo.7671742>
- Wang, M. (2007). Remote sensing of the ocean contributions from ultraviolet to near-infrared using the shortwave infrared bands: simulations. *Applied Optics*, 46(9), 1535–1547.
- Wang, M., & Shi, W. (2005). Estimation of ocean contribution at the MODIS near-infrared wavelengths along the east coast of the U.S.: Two case studies. *Geophysical Research Letters*, 32(13), 1–5. <https://doi.org/10.1029/2005GL022917>
- Wei, J., Lee, Z., & Shang, S. (2016). A system to measure the data quality of spectral remote-sensing reflectance of aquatic environments. *Journal of Geophysical Research: Oceans*, 121(11), 8189–8207. <https://doi.org/10.1002/2016JC012126>

- Weng, F., Choi, T., Cao, C., & Zhang, B. (2017). Reprocessing of SUOMI NPP VIIRS sensor data records and impacts on environmental applications. *IEE International Geoscience and Remote Sensing Symposium*, 293–296.
- Wiborg, K. F. (1976). Fishery and commercial exploitation of *Calanus finmarchicus* in Norway. In *J. Cons. int. Explor. Mer* (Vol. 36, Issue 3). Fevrier. <https://academic.oup.com/icesjms/article/36/3/251/639243>
- Zaneveld, J. R., & Pegau, W. S. (1993). Temperature-dependent absorption of water in the red and near-infrared portions of the spectrum. *Limnology and Oceanography*, 38(1), 188–192.
- Zhang, M., Carder, K., Muller-Karger, F. E., Lee, Z., & Goldgof, D. B. (1999). Noise Reduction and Atmospheric Correction for Coastal Applications of Landsat Thematic Mapper Imagery detection techniques for noise reduction. *Remote Sensing for the Environment*, 70, 167–180.
- Zhang, X., Hu, L., & He, M.-X. (2009). Scattering by pure seawater: Effect of salinity. *Optics Express*, 17(7), 5698–5710.